The University of British Columbia

FACULTY OF GRADUATE STUDIES

PROGRAMME OF THE

FINAL ORAL EXAMINATION

FOR THE DEGREE OF

DOCTOR OF PHILOSOPHY

of

ERLAND MAXWELL SCHULSON

B.A.Sc. (Hons.), The University of British Columbia

THURSDAY, JANUARY 4, 1968 AT 3:30 P.M.

IN ROOM 201, METALLURGY BUILDING

COMMITTEE IN CHARGE

Chairman: B.N.Moyls

C.A. Brockley D.L. Williams
L.C. Brown N.R. Risebrough
E. Teghtsoonian D. Tromans

External Examiner: Dr. R.E. Smallman
Department of Physical Metallurgy and
Science of Materials
The University of Birmingham
Birmingham, England

Research Supervisor: Dr. E. Teghtsoonian

THE PLASTICITY OF β 'AuZn SINGLE CRYSTALS

ABSTRACT

Single crystals of the CsCl type intermetallic compound β 'AuZn were prepared and tested in tension over a wide range of temperatures, strain rates and orientations for three compositions, Au-rich (51.0 at .% Au), stoichiometric and Zn-rich (51.0 at.% Zn).

Slip surfaces are generally non-crystallographic planes in the zone of the slip direction [001], and are temperature, strain rate and orientation sensitive. A model based on thermally activated sessile-glissile transformations of screw dislocations has been proposed to explain non-crystallographic slip.

Multi-stage work-hardening is observed over the temperature range $0.2 \lesssim T/T_m \lesssim 0.35$. In stage I the work-hardening rate is low ($\mu/1000$ to $\mu/5000$) but rises sharply during stage II ($\theta_{II} \sim \mu/500$). Stage III is characterized by a rapidly decreasing hardening rate coincident with the onset of profuse large-scale cross-slip. Surface slip line studies revealed that the end of easy glide is coincident with the onset of localized slip on non-crystallographic planes in the [100] zone.

Thin foil electron microscopy was carried out on critically chosen crystallographic sections from annealed and deformed crystals. At the beginning of stage I clusters of edge dislocation dipoles were revealed, forming walls perpendicular to the glide plane. The dislocation density of the walls increases during easy glide.

During testing at intermediate temperatures ($\sim .3$ to $.4\ T_m$) serrated yielding was detected in non-stoichiometric crystals and was attributed to

dislocation-solute atom interactions.

Under special testing conditions ($77^{\circ}K$ or near $\langle 001 \rangle$ orientations) slip occurs in $\langle 111 \rangle$ directions. The associated work-hardening rates are very high and ductility is low.

Thermal activation studies were made to determine the dislocation mechanism responsible for the temperature sensitivity of yield in stoichiometric crystals below $\sim 220^{\circ}K$. Activation volume measurements are consistent with both the Peierls-Nabarro and cross-slip mechanisms below $\sim 150^{\circ}K$.

GRADUATE STUDIES

Field of Study: Physical Metallurgy

Metallurgical Thermodynamics	C.S. Samis
Structure of Metals	E. Teghtsoonian
Advanced Physical Metallurgy	E. Teghtsoonian L.C. Brown
Diffusion	L.C. Brown
Electron Microscopy	D. Tromans

Related Studies:

Quantum Theory of Solids	R. Haering
Theory of Plasticity	H. Ramsey

THE PLASTICITY OF β' AuZn SINGLE CRYSTALS

by

ERLAND MAXWELL SCHULSON

B.A.Sc., University of British Columbia, 1964

A THESIS SUBMITTED IN PARTIAL FULFILMENT OF

THE REQUIREMENTS FOR THE DEGREE OF

DOCTOR OF PHILOSOPHY

in the Department

of

METALLURGY

We accept this thesis as conforming to the
required standard

THE UNIVERSITY OF BRITISH COLUMBIA

December, 1967

In presenting this thesis in partial fulfilment of the requirements for an advanced degree at the University of British Columbia, I agree that the Library shall make it freely available for reference and Study. I further agree that permission for extensive copying of this thesis for scholarly purposes may be granted by the Head of my Department or by his representatives. It is understood that copying or publication of this thesis for financial gain shall not be allowed without my written permission.

Department of Metallurgy

The University of British Columbia
Vancouver 8, Canada

Date April 1, 1968

Supervisor: Dr. E. Teghtsoonian

ABSTRACT

Single crystals of the CsCl type intermetallic compound β'AuZn were prepared and tested in tension over a wide range of temperatures, strain rates and orientations for three compositions, Au-rich (51.0 at.% Au), stoichiometric and Zn-rich (51.0 at.% Zn).

Slip surfaces are generally non-crystallographic planes in the zone of the slip direction [001], and are temperature, strain rate and orientation sensitive. A model based on thermally activated sessile-glissile transformations of screw dislocations has been proposed to explain non-crystallographic slip.

Multi-stage work-hardening is observed over the temperature range $0.2 \lesssim T/T_m \lesssim 0.35$. In stage I the work-hardening rate is low ($\mu/1000$ to $\mu/5000$) but rises sharply during stage II ($\theta_{II} \sim \mu/500$). Stage III is characterized by a rapidly decreasing hardening rate coincident with the onset of profuse large-scale cross-slip. Surface slip line studies revealed that the end of easy glide is coincident with the onset of localized slip on non-crystallographic planes in the [100] zone.

Thin foil electron microscopy was carried out on critically chosen crystallographic sections from annealed and deformed crystals. At the beginning of stage I clusters of edge dislocation dipoles were revealed, forming walls perpendicular to the glide plane. The dislocation density of the walls increases during easy glide.

During testing at intermediate temperatures ($\sim .3$ to $.4\ T_m$) serrated yielding was detected in non-stoichiometric crystals and was attributed to dislocation-solute atom interactions.

Under special testing conditions (77°K or near <001> orientations) slip occurs in <111> directions. The associated work-hardening rates are very high and ductility is low.

Thermal activation studies were made to determine the dislocation mechanism responsible for the temperature sensitivity of yield in stoichiometric crystals below ~220°K. Activation volume measurements are consistent with both the Peierls-Nabarro and cross-slip mechanisms below ~150°K.

ACKNOWLEDGEMENT

The author gratefully acknowledges the advice and encouragement given by his director, Dr. E. Teghtsoonian. Helpful discussions with various members of the faculty and fellow graduate students are also acknowledged. Financial assistance was received from the International Nickel Company of Canada Limited in the form of a post-graduate fellowship.

TABLE OF CONTENTS

THE PLASTICITY OF β' AuZn SINGLE CRYSTALS

TABLE OF CONTENTS (continued)

TABLE OF CONTENTS (continued)

TABLE OF CONTENTS (continued)

LIST OF FIGURES

LIST OF FIGURES (continued)

LIST OF FIGURES (continued)

LIST OF FIGURES (continued)

LIST OF TABLES

1. INTRODUCTION AND OBJECTIVES

Intermetallic compounds can be defined as intermediate phases in binary or higher order metal - metal systems. Such compounds may possess long range order at all temperatures in the solid state or undergo an order-disorder transformation at a critical temperature above which the compound adopts a nearly random structure. In the latter case, short range order persists in a decreasing degree up to the melting point. When highly ordered, intermetallic compounds have lower symmetry than the corresponding disordered alloy, leading to extra reflections, termed superlattice reflections, in their diffraction patterns.

The four most common superlattices in which the crystal structure does not change upon the formation of long range order are shown in Figure 1 and their common names, corresponding disordered structure and examples of each are given in Table 1. The most frequently occurring super-

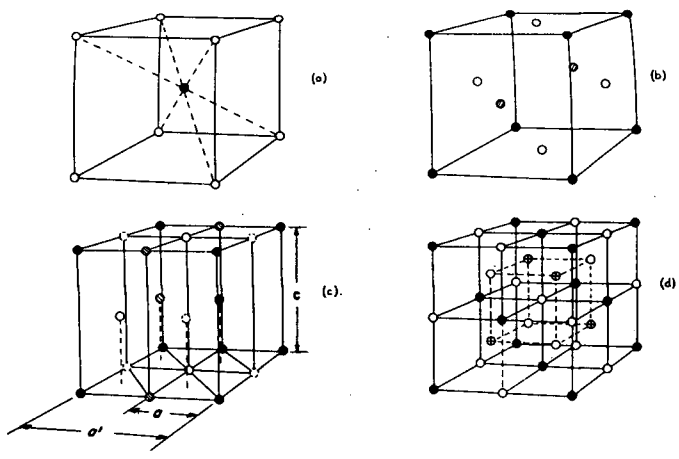

Figure 1. Common types of superlattices in which crystal structure does not change upon the formation of long-range order: (a) B2, (b) Ll_2 (c) DO_{19} (d) DO_3. (after Stoloff and Davies[113])

lattice type is the B2 or CsCl type structure which takes the form of two interpenetrating simple cubic lattices. The symmetry of the B2 structure is

lowered from a bcc in which all sites are equivalent to a simple cubic in which the (0, 0, 0) and (1/2, 1/2, 1/2) sites are different. The consequence of reduced symmetry is that two types of regionsmay occur within a crystal: where the A atoms and B atoms are in their respective α (0,0,0) and β (1/2, 1/2, 1/2) sites and where the A and B atoms interchange sites such that A occupy β sites and B occupy α sites. The boundary between two such regions will contain bonds between like atoms and will be a surface of higher energy. The regions are known as antiphase domains (APD) and the boundary as an antiphase boundary (APB). Because a stable domain structure requires at least four sublattices, Bragg[114] suggested that APB's in the B2 structure(having two sublattices) which form during an ordering process should disappear as a result of domain growth. Recent transmission electron microscopy studies on the B2 compound NiAl[115] (ordered up to its melting point) led to the conclusion that APD's do not exist in annealed or deformed samples, substantiating Bragg's suggestion. In similar studies APB's have been detected in the B2 compound β-brass quenched from above the critical ordering temperature.[116,117] However, experiments were not carried out to determine whether or not the APB's would disappear on prolonged annealing.

The second most common superlattice type is the $L1_2$ structure, related to fcc in much the same way as the B2 superlattice is to bcc. The face centered sites are occupied by A atoms and the corner sites by B atoms. Symmetry is again lowered to simple cubic and antiphase domains can exist since of the four initially equivalent sites (0,0,0), (0, 1/2, 1/2), (1/2, 0, 1/2) and (1/2, 1/2, 0), any one may be occupied by a B atom and the other three by A atoms. APB's have been detected in $L1_2$ compounds Cu_3Au[118,119,120] and Ni_3Mn[121]. Less commonly observed superlattices are the DO_3 and DO_{19} types. The most complex is the DO_3 type which is built up of eight bcc unit cells and may be considered as being composed of four inter-

TABLE 1

Common Superlattices

Structure Type	Common Name	Disordered Structure	Examples	
$L2_0$ or B2	CsCl	bcc	CuZn	AgMg
			AgZn	NiAl
			AuZn	CuAl
			AuCd	FeAl
			AgCd	FeCo
			NiTi	
Ll_2	Cu_3Au	fcc	Cu_3Au	Ni_3Fe
			Au_3Cu	Ni_3Al
			Ni_3Mn	Pt_3Fe
			Ir_3Cr	
DO_3	Fe_3Al	bcc	Fe_3Al	Fe_3Be
			Fe_3Si	Cu_3Al
DO_{19}	Mg_3Cd	hcp	Mg_3Cd	Ti_3Al
			Cd_3Mg	Ni_3Sn

penetrating fcc lattices. For the DO_{19} structure, the ordered unit cell may be compared to four unit cells of the disordered hcp structure.

In some instances ordering also effects a change in crystal structure. The most common superlattice of this type is typified by the CuAu structure in which alternate layers of Cu and Au atoms form on (001) planes of the fcc disordered solution, distorting it into a fct structure. The fourfold axis of symmetry is normal to the alternating planes of Au and Cu atoms and the axial ratio is usually between 0.9 and 1.0. Other examples of the fct ordered structure (classified as Ll_0 type superlattice) are CoPt, FePt and FePd.

Deformation studies on intermetallics have centered almost wholly on the behaviour of polycrystalline material under various conditions

of temperature, strain rate, grain size, defect structure created by departure from stoichiometry and degree of long range order. In a comprehensive treatment of the subject prior to 1959, Westbrook[122] reviewed a large number of papers devoted to fabrication, testing procedures and the properties of very high melting point compounds as well as a few concerned with surface slip line structure and antiphase boundary observations. General interest in associated dislocation structure and behaviour was not apparent at that time. In recent years with the improvement of fabrication and testing techniques and the advent of sophisticated transmission electron microscopy contrast theory, much progress has been made from both the experimental and theoretical approaches in understanding the plastic behaviour and fracture of intermetallics. Also many papers have appeared in the literature relating strength and degree of long-range order.

In their recently published review, Stoloff and Davies[113] point out that the mechanical behaviour of alloys that form superlattices at a critical temperature below the melting point can be understood mainly in terms of changes in dislocation configuration with degree of order. The ordered materials deform by the movement at relatively low stresses of superlattice dislocations which consist generally of closely spaced pairs of unit dislocations. Since the dislocations are constrained to move as a group to preserve the ordered arrangement of the lattice, cross slip is hindered thereby leading to high work-hardening rates (Cu_3Au[123,124] FeCo[125]) and brittle fracture (FeCo[126,127]). Decreasing the degree of long range order brings about an increase in the separation of superlattice partials which can explain the peak in yield stress manifested near the critical ordering temperature by many superlattices (Cu_3Au,[76] FeCo,[125,127] CuZn[75,128] and Fe_3Al[127,129,130]). Variations in long range order, however, cannot explain similar intermediate-temperatures strengthening effects in alloys

ordered up to the melting point (AgMg,[101] Ni_3Al[131,132,133] and NiAl[134]). The resolution of this phenomenon necessitates detailed single crystal studies.

In CsCl type superlattices (including intermetallic compounds as well as ionic materials such as CsI and CsBr) a distinction may be made between compounds on the basis of slip direction. When bonding is of ionic character, electrostatic forces prevent like ions from becoming nearest neighbors and $\langle 001 \rangle$ slip occurs, but when bonding is of metallic character and the two kinds of "ions" that alternate along close packed rows are practically indifferent to their neighbors, $\langle 111 \rangle$ slip occurs. The polycrystalline mechanical consequence of slip direction is reflected in the extreme brittleness of the "ionic" compounds compared to the relative ductility of the "metallic" compounds. Further discussion of slip modes in CsCl type superlattices with direct reference to the literature will appear in the appropriate sections of the thesis.

Perhaps the major obstacle in the path of more widespread industrial use of intermetallics is their extreme brittleness at low temperatures. Origin of brittleness in AgMg[135], NiAl[135] and NiGa[136] has been attributed to the segregation of interstitial impurities to grain boundaries. Grain boundary contamination, however, cannot be the only reason for brittleness. In NiAl for instance, single crystal studies[25,29] show that slip occurs on $\{110\}\langle 001 \rangle$ systems. Since there are only three independent $\{110\}\langle 001 \rangle$ modes[29], general polycrystalline ductility is not possible, and hence, even in the absence of grain boundary contamination, NiAl would be brittle at low temperatures. This example illustrates the value of single crystal studies in uncovering the nature of the deformation behaviour of intermetallics.

The object of the work presented in the thesis was to study the

plastic deformation of an intermetallic compound in single crystal form. The B2 compound β' AuZn was chosen for three reasons:

(1) The moderate and congruent melting temperature of 725°C would ease the preparation of homogeneous single crystals;

(2) The solubility range from 47.5 to 52.0 at. % Au, Figure 2, would permit an evaluation of the effects of deviations from stoichiometry on the plastic behaviour;

(3) The crystal structure is relatively simple and remains highly ordered to the melting point,[107,137] thereby simplifying subsequent analysis of the results.

Because the work represents one of the first deformation studies of intermetallic crystals, the thesis is not limited to the investigation of a single phenomenon. Instead the effects were noted of a wide range of variables that include temperature, strain rate, orientation and deviations from stoichiometry. Justification for the project stems from an academic interest in the fundamental deformation behaviour of ordered alloys.

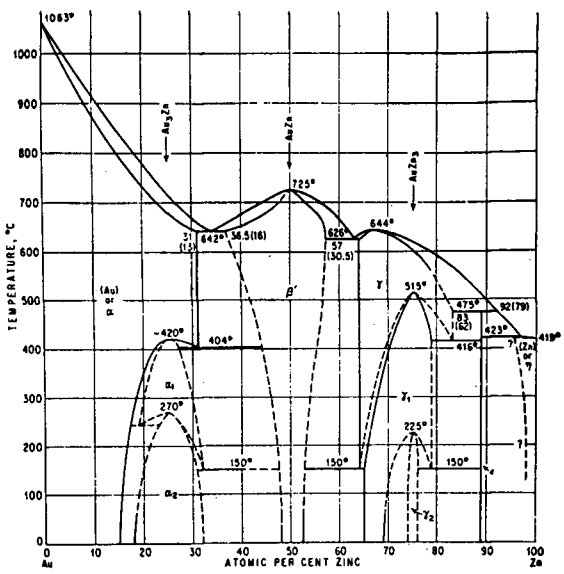

Figure 2. Equilibrium diagram for the Au-Zn system.

2. DEFORMATION CHARACTERISTICS OF β' AuZn SINGLE CRYSTALS

2.1 EXPERIMENTAL PROCEDURE

2.1.1 Alloy Preparation and Crystal Growth

The gold and zinc used in this investigation was of 99.999% purity and was supplied by the Cominco Ltd., Trail, B.C. in the form of gold splatter and one-half inch diameter zinc rod. Alloys weighing approximately 75 grams were prepared by encapsulating gold and zinc of accurately weighed amounts under reduced pressure in 11 mm. diameter carefully cleaned (H_2SO_4-Cr_2O_3 hot solution) quartz tubes then fusing at 800°C. The melts were repeatedly agitated to ensure thorough mixing then quenched in cold water to minimize segregation on solidification. To remove the de-zinced surface zone, castings were electrochemically polished in 5% KCN solution (12 volts, approximately $1\frac{1}{2}$ amp/cm^2, 40°C). The piped end was cropped off each casting.

The billets were reduced to 0.108 inch wire first by hot swaging at 300°C to 0.163 inch rod then cold drawing to the final size. The wire was straightened while held in the die by heating with a propane torch after the final draw. Segments to be grown into single crystals approximately 16 inches in length, were thoroughly cleaned (degreased, abraded, and electrochemically polished in 5% KCN solution), charged into pre-cleaned, close fitting 0.113 inch quartz quills then sealed under reduced pressure. Single crystals were grown in the standard Bridgman manner by superheating the melt 50°C to 775°C then lowering the charge at 7cm/hr. through a temperature gradient of 25°C/cm. The quartz sheaths were subsequently removed in HF. Crystal orientations were determined at three points along their lengths from back-reflection Laue X-ray diffraction

patterns. It was found that this technique yielded crystals bearing random axial orientations and that a common orientation could be preserved by adopting a standard seeding technique.

During preliminary investigations of the crystal growth conditions, it was found that crystals having smooth surfaces would be obtained only if the wire were closely charged into the silica quills. Loose fitting charges yielded crystals with severely cavitated surfaces.

Crystals were analyzed for composition variations resulting from solidification, for interstitial content, and for trace element impurities. The analytical procedure and results are reported in Appendix 1. For the purposes of obtaining fairly uniform compositions, only the first two-thirds of as-grown crystals was accepted. Because the actual composition was quite close to the composition intended on alloying, all compositions stated in the thesis will refer to the initial alloy composition.

2.1.2 Tensile Specimen Preparation

"Dumb-bell" shaped tensile specimens, Figure 3, were prepared by carefully machining single crystals in a jewellers lathe. The gauge diameter was reduced from 0.113 inch to 0.090 inch through a series of cuts less than 0.0005 inch deep. Specimens were subsequently hand-polished in the lathe with well-lubricated 0 and 3/0 emery papers.

Machining damage was evaluated and the results are reported in Appendix 2. It was found that damage was minimized upon removing 0.005 inch from the abraded surface. Non-ellipitical cross-sections and taper-free gauge sections were effected by rapidly rotating and repeatedly turning the specimen end for end during polishing. Gauge diameters were accurate

to $\pm$0.0005 inch. Machining damage was completely eliminated by subsequently annealing specimens in evacuated pyrex capsules at 300°C for one hour.

2.1.3 Testing Procedure

Experiments were performed by straining specimens in a Floor Model Instron tensile machine at strain rates varying from 2.5×10^{-4}/sec to 2.5×10^{-2}/sec and temperatures ranging from 77°K to 488°K. Load-elongation curves were autographically recorded during straining. Liquid testing environments accurate to $\pm$2° included nitrogen (77°K), oxygen (90°K), petroleum ether cooled with nitrogen (133 to 293°K) and heated silicone oil (293 to 488°K).

Specimen dimensions were carefully measured using a Gaertner travelling microscope with a 10X eyepiece. Diameters, accurate to $\pm$0.0005 inch were averaged from six reading along the gauge section and across two perpendicular diameters.

Specimens were successfully gripped in a self-aligning pin-chuck and threaded collet system, Figure 4.

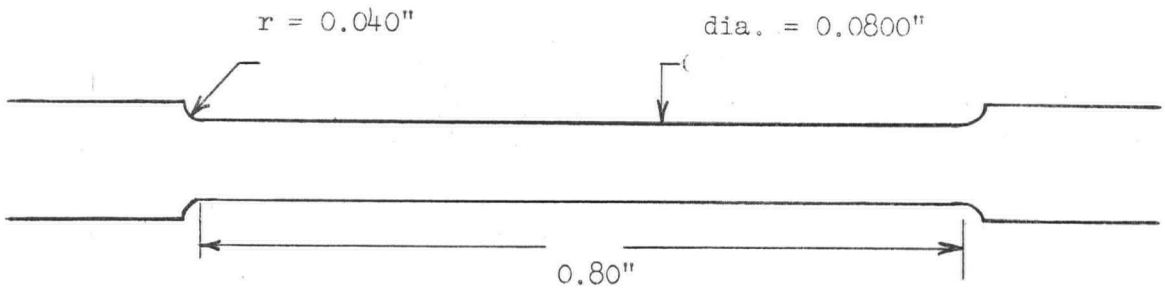

Figure 3. Diagram of a tensile specimen.

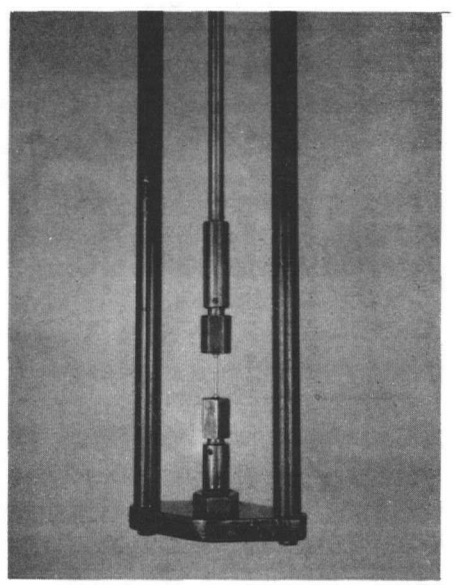

Figure 4. Showing specimen gripping arrangement. (Hex-nuts soldered onto pin-chucks)

2.2 GENERAL DESCRIPTION OF THE SHEAR STRESS-SHEAR STRAIN CURVES

2.2.1 Experiments

Specimens of three compositions (Au-rich = 51.0 at.% Au, Stoichiometric = 50.0 at.% Au and Zn-rich = 49.0at.% Au) oriented near the centre of the standard stereographic triangle were prepared and tested in tension at temperatures from 77°K to 488°K. Cross-head speed was constant at 0.05 inch per minute corresponding to a strain-rate of 2.5×10^{-3}/sec. Experiments were also performed to determine the effects of strain rate and orientation on the room temperature deformation behaviour of 51.0 at.% Au-crystals. Excluding the strain rate study, all tests were done in duplicate and found to be reproducible in most cases to within five percent.

An IBM computer was programmed to calculate resolved shear-stresses and shear-strains from equations presented in Appendix 3. For these calculations it was necessary to know the slip system operative under the experimental conditions investigated. A thorough analysis of deformation modes is presented in section 2.4 of the thesis where it is shown that for specimens oriented within the [001]-[101] - [111] stereographic triangle, slip occurs on planes belonging to the [001] zone, except for orientations very near the [001] corner where [111] zonal planes become operative. The results of the slip mode study have been incorporated in the computations of resolved shear stress and shear strain.

2.2.2 Definition of Work Hardening Parameters

A schematic resolved shear-stress shear-strain curve typical of crystals oriented near the centre of the primary stereographic triangle and deformed at room temperature is shown in Figure 5. The curve will be divided

according to a scheme given by Mitchell et al.[1] Stage 0, a region of decreasing hardening rate is followed by two stages of linear hardening, I and II, then by a second region of decreasing hardening rate, stage III.

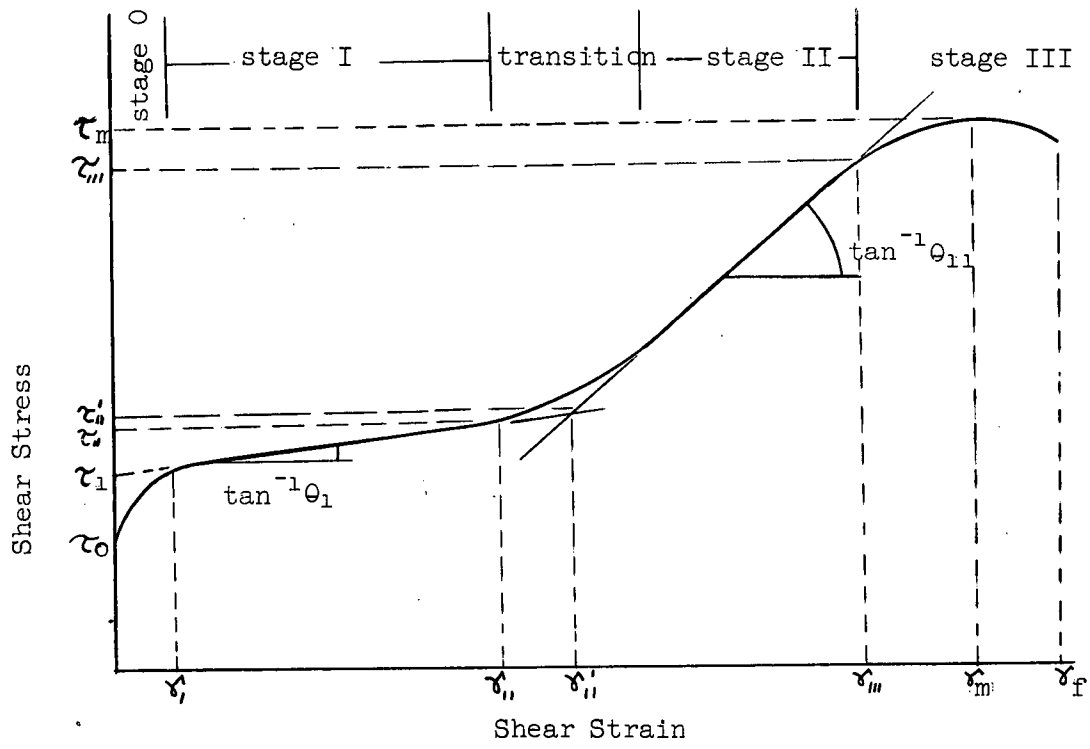

Figure 5. Schematic resolved shear stress-shear strain curve.

τ_o is defined as the yield stress at the first detectable departure from linearity; τ_I is the initial flow stress obtained by extrapolating stage I to zero strain. Stresses τ_{II}, τ_{II}' and τ_{III} correspond to shear strains γ_{II}, γ_{II}' and γ_{III}; τ_m is defined as the maximum flow stress. Total ductility is given as γ_f. The work-hardening rate in stage I is defined as $\Theta_I = \frac{\tau_{II} - \tau_I}{\gamma_{II}}$ and during stage II as $\Theta_{II} = \frac{\tau_{III} - \tau_{II}'}{\gamma_{III} - \gamma_{II}'}$.

2.2.3 Temperature and Strain Rate Dependence

The temperature dependence of the shear stress-shear strain

curves for the Au-rich, stoichiometric and Zn-rich crystals is illustrated in Figures 6, 7 and 8 respectively. In the range of intermediate temperatures from approximately 200 to 350°K it can be seen that the flow curves are very similar to those classically observed for face-centered cubic metals[2,3,4] and those more recently reported for body-centered cubic metals.[1,5,6,7,8,9,10,11] A low work-hardening, easy glide stage I is followed by a higher work-hardening stage II region. Total ductility is very large (~300% shear strain). As the temperature is either increased or decreased, the length of stage I is decreased until a parabolic type of flow curve is obtained; ductility is also reduced in both cases. Similar temperature effects have been observed in Nb,[1] Ta[9] and Fe[11] single crystals. The extent of stage II and III decrease and increase respectively with increasing temperature above approximately 293°K. At temperatures below approximately 150°K, rapid hardening is terminated in brittle fracture, while at temperatures greater than approximately 375°K, initial hardening is followed by general work-softening until chisel-edge type ductile fracture occurs. Over the temperature range in which stage III flow occurs, the maximum flow stress decreases with increasing temperature.

In the range of intermediate temperatures stage 0 tends to decrease with increasing temperature. This is particularly noticeable for the Au-rich crystals, Figure 6. It is also apparent that the slow transition zone between stages I and II tends to decrease with increasing temperature.

The effect of strain rate on the room temperature plasticity of Au-rich crystals is shown in Figure 9. It is apparent that over the range of strain rates investigated 2.5×10^{-4} to 2.5×10^{-2}/sec, the general flow behaviour is rather strain rate insensitive. There is, however, an effect on stage II hardening which will be discussed accordingly in section 2.5.1.

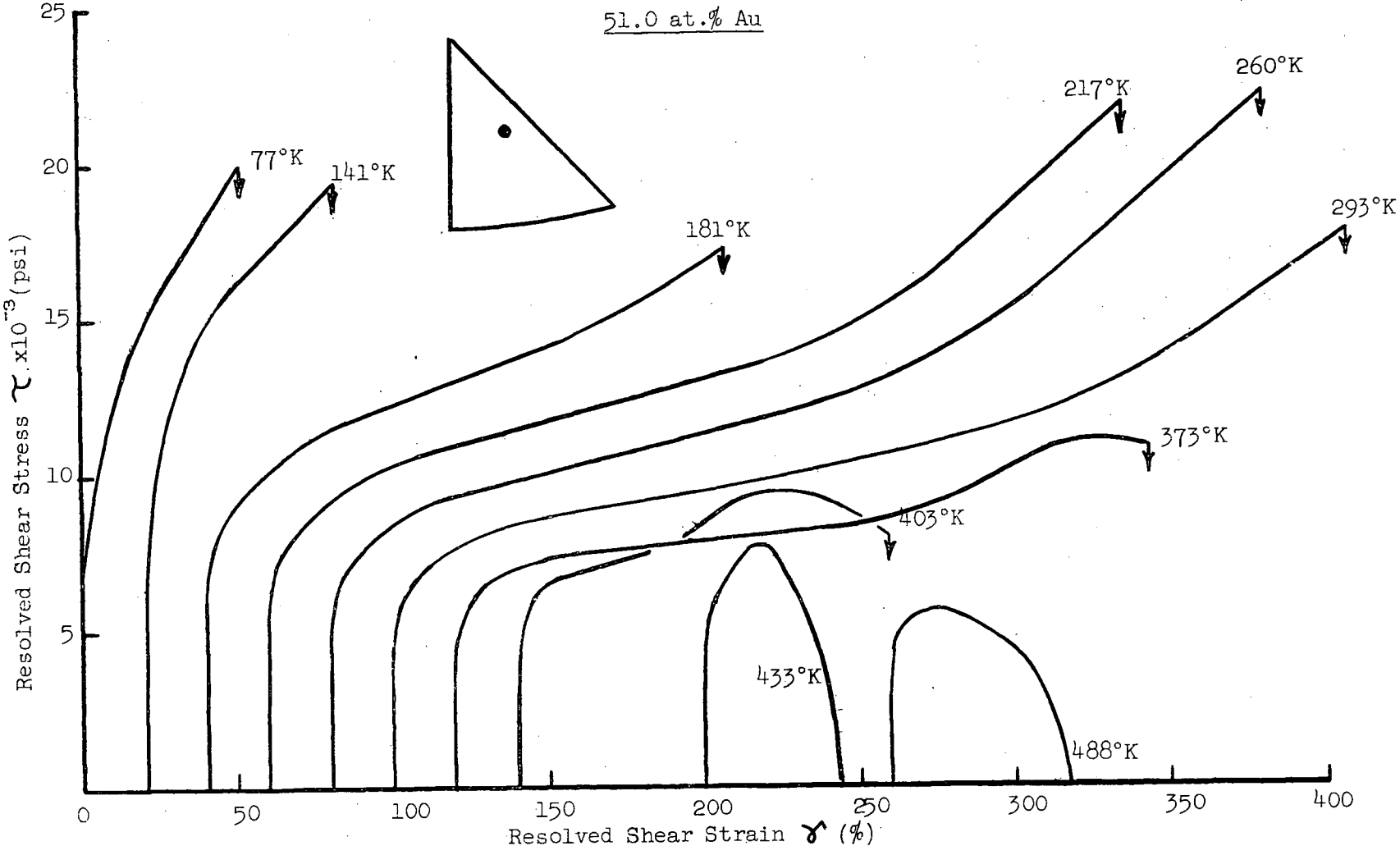

Figure 6. Resolved shear stress-shear strain curves of Au-rich β'AuZn crystals as a function of temperature between 77°K and 488°K. ($\dot{\gamma}$ = 2.5 x 10^{-3}/sec)

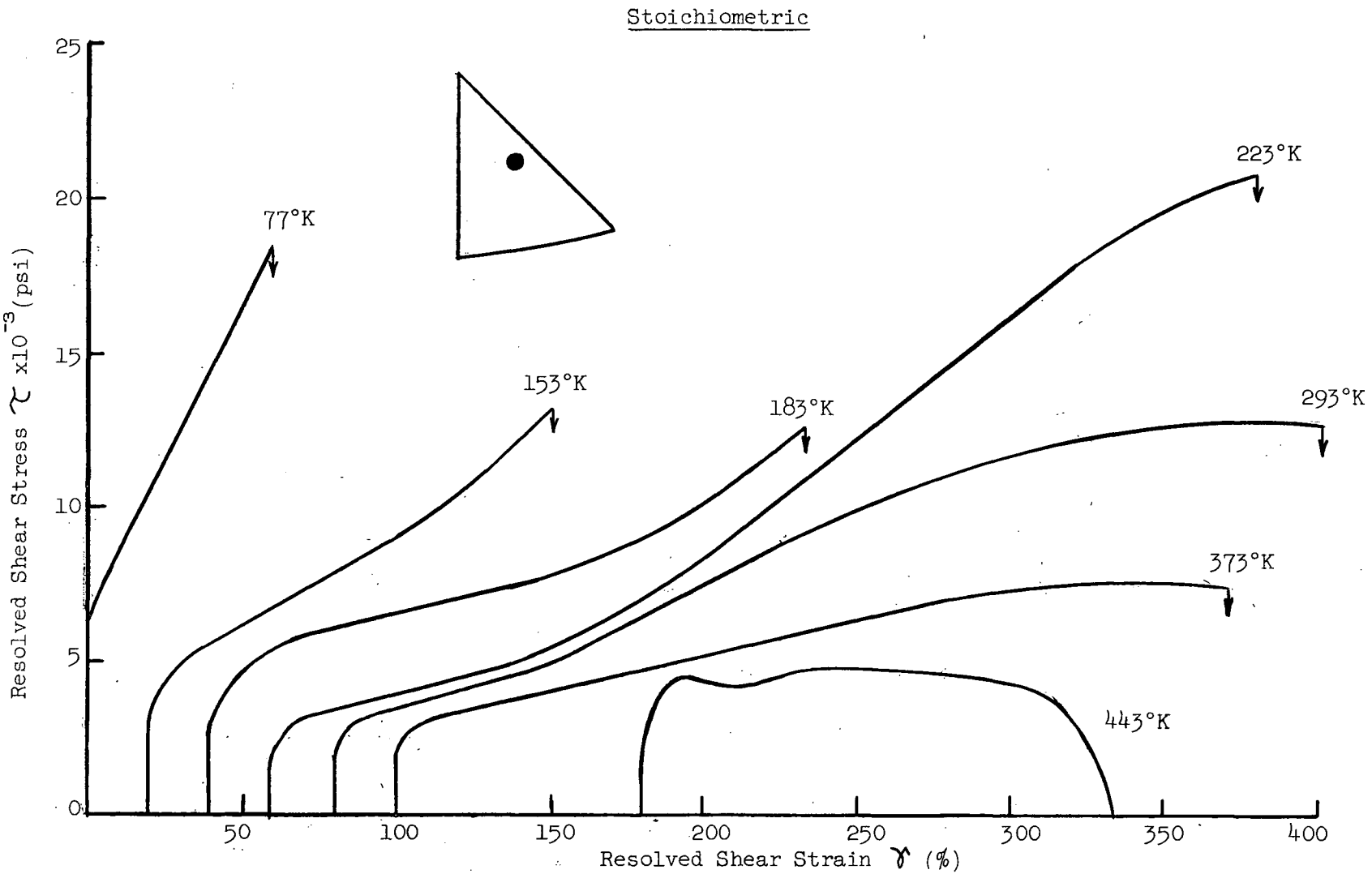

Figure 7. Resolved shear stress-shear strain curves of stoichiometric β' AuZn crystals as a function of temperature between 77°K and 443°K. ($\dot{\gamma} = 2.5 \times 10^{-3}$/sec)

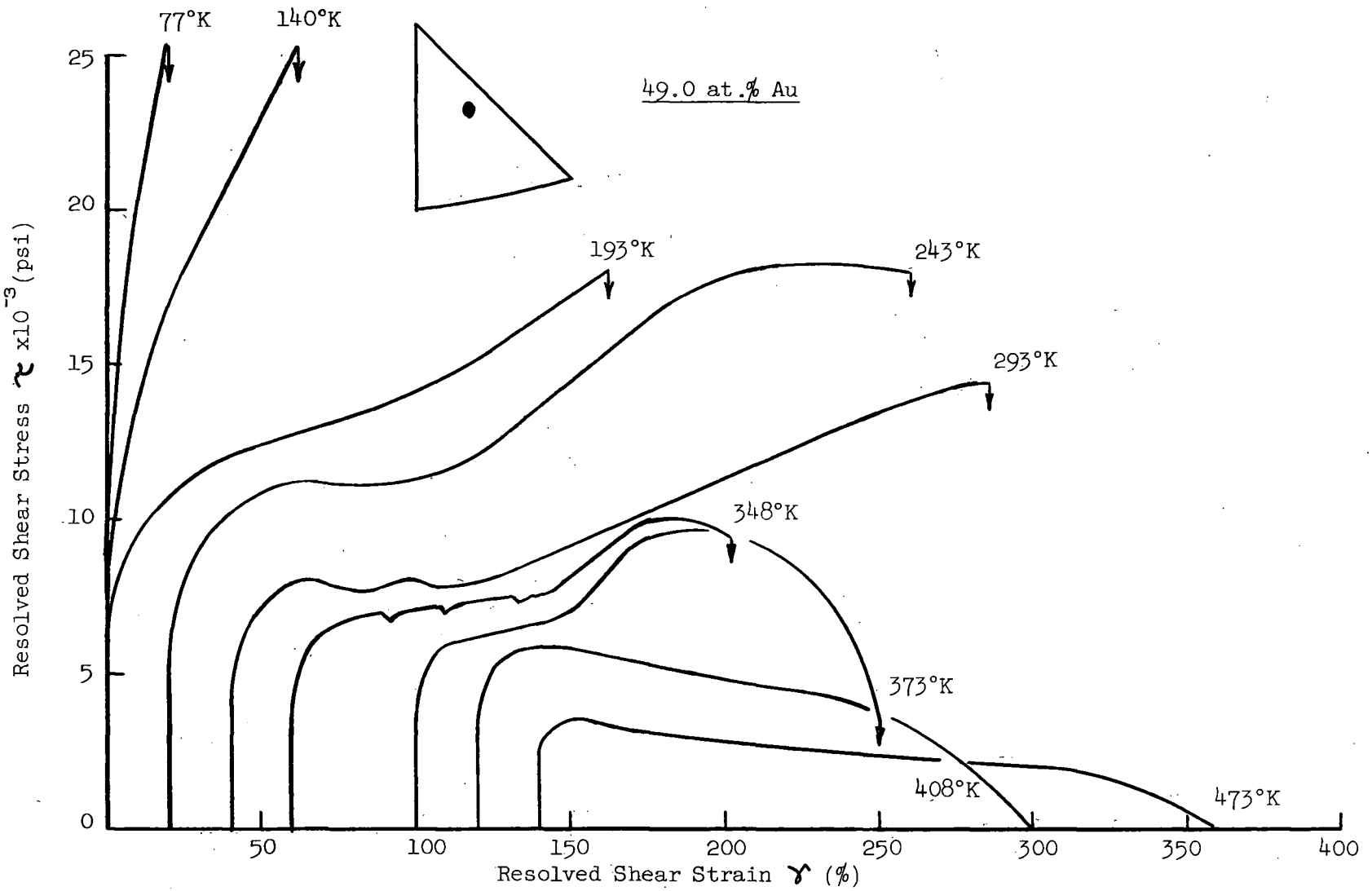

Figure 8. Resolved shear stress-shear strain curves of Zn-rich β' AuZn crystals as a function of temperature between 77°K and 473°K. ($\dot{\gamma}$ = 2.5 x 10^{-3}/sec)

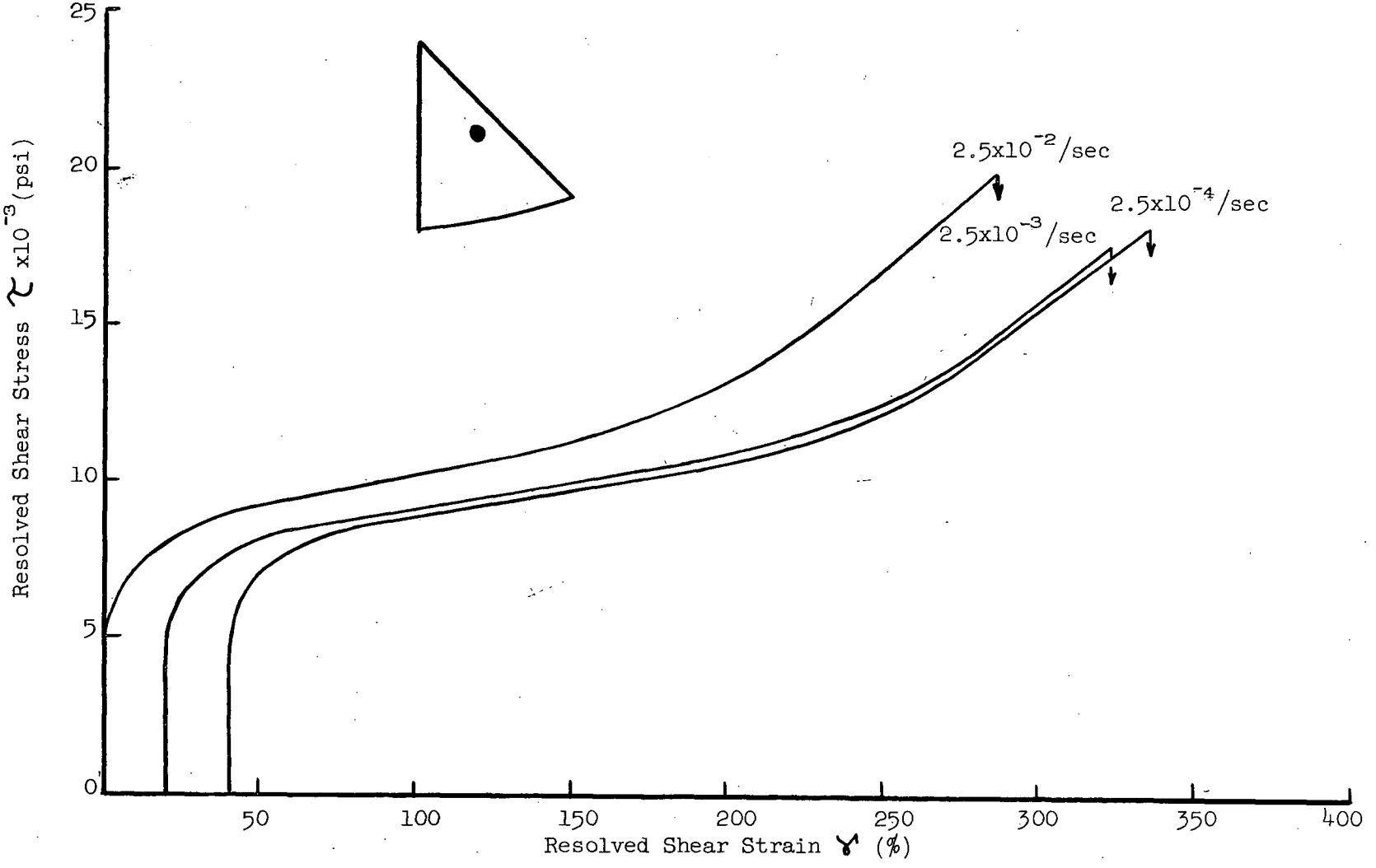

Figure 9. Resolved shear stress-shear strain curves of Au-rich β'AuZn crystals as a function of strain rate from 2.5 x 10^{-4}/sec to 2.5 x 10^{-2}/sec. (T = 293°K)

2.2.4 Effect of Deviations from Stoichiometry

To illustrate the effect of deviations from stoichiometry on the shear stress-shear strain curves at 77°K, 223°K, 293°K and 373°K, curves from Figures 6, 7 and 8 are superimposed on Figure 10, where the shortened notation +Au, St. and +Zn refer to the Au-rich, stoichiometric and zinc-rich compositions respectively. It can be seen that at all temperatures, yield and flow stresses are higher for the non-stoichiometric material with approximately equal hardening on both sides of stoichiometry, similar to the behaviour of polycrystalline AuZn,[12] AgMg,[13] NiAl[14,81] and Cu_3Au.[15] It appears that the difference in flow stress between stoichiometric and non-stoichiometric material is more pronounced during easy glide. In the intermediate temperature range deviations from stoichiometry increased the length of stage I, with the most pronounced lengthening occurring for the Au-rich crystals. Similar stage I lengthening has been observed with increasing Zn content in α-brass[16] and in Ni-Co alloys.[17] It is observed, too, that stage III begins at lower temperatures for the stoichiometric crystals.

It is also evident during straining at intermediate temperatures that flow in Zn-rich crystals occurs in a wavy manner prior to the high hardening rate, stage II region (for instance, at 293°K and 348°K, Figure 8). Wave "frequency" and "height" were observed to increase and decrease respectively with increasing temperature then disappear just above ~348°K. By carefully observing the specimen during straining at room temperature, it could be seen that each "wave" was coincident with localized one dimensional thinning within the gauge section. Once the gauge section was uniformly thinned, stage II hardening began. Stoichiometric and Au-rich crystals deformed uniformly throughout the gauge at all temperatures.

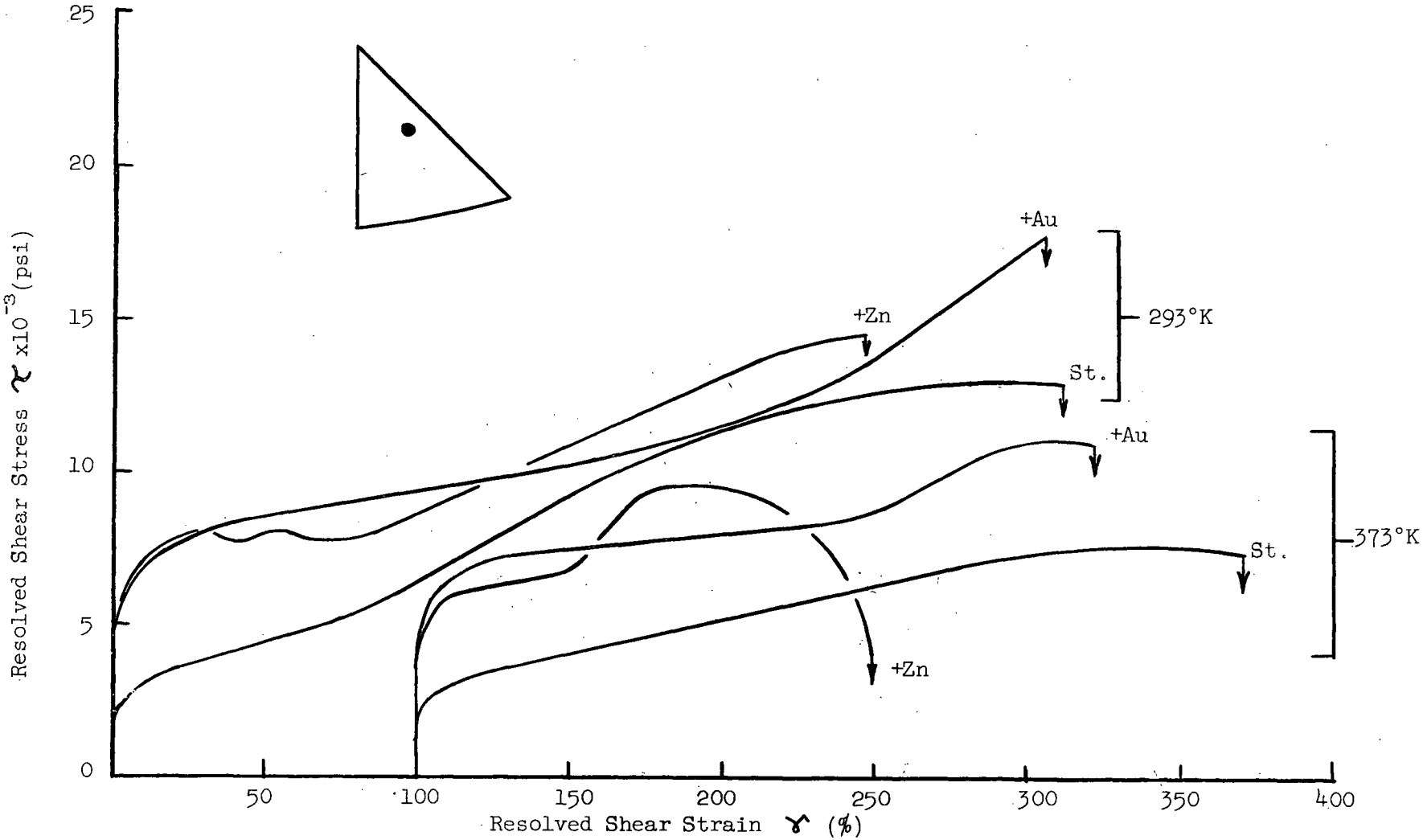

Figure 10.1. Resolved shear stress-shear strain curves of β'AuZn crystals as a function of composition at 293°K and 373°K.

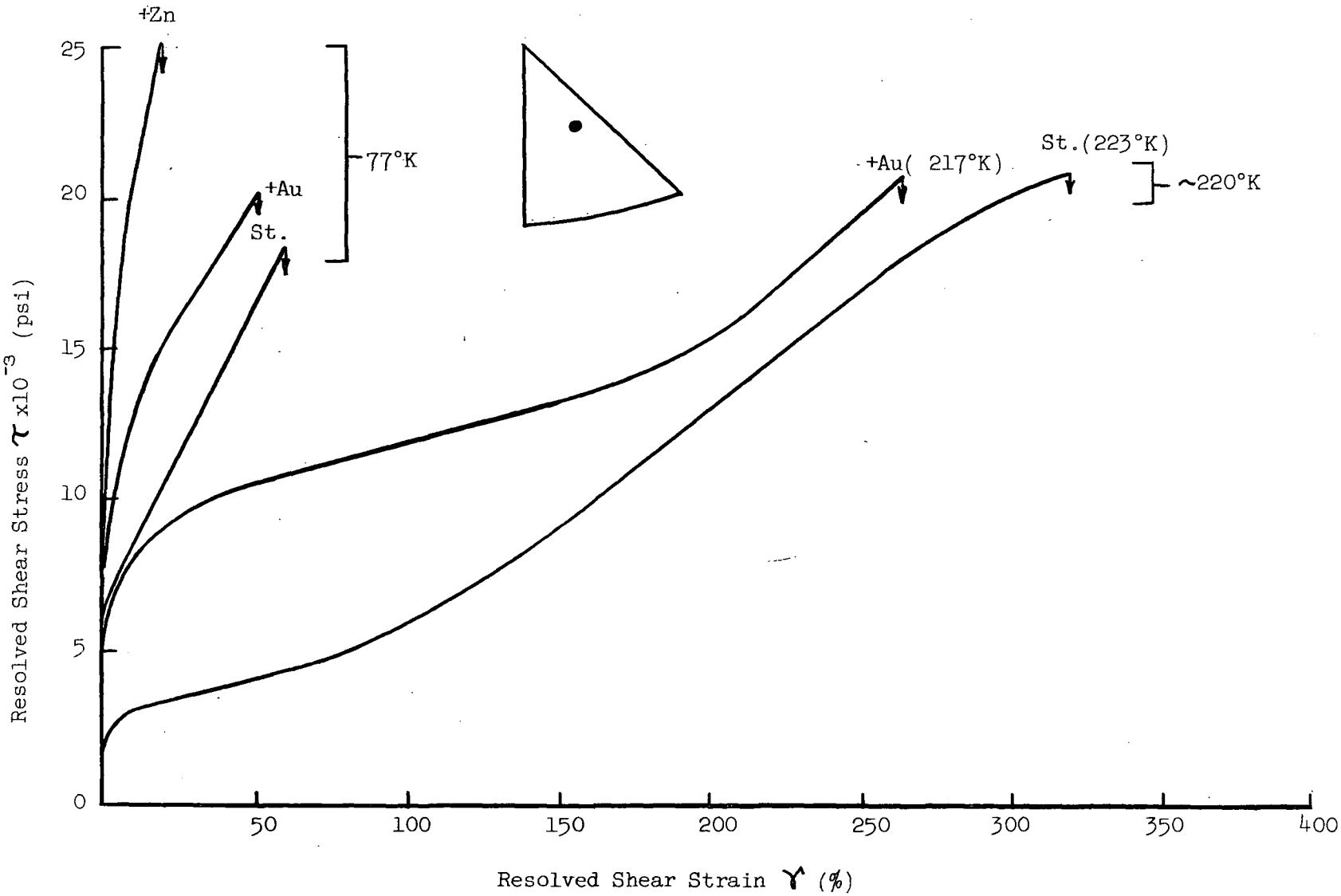

Figure 10.2. Resolved shear stress-shear strain curves of β' AuZn crystals as a function of composition at 77°K and ~ 220°K.

It appears that work-hardening rates during stage I and II are not greatly affected by deviations from stoichiometry, but at 77°K the initial hardening rate appears to be higher for the non-stoichiometric crystals.

Deviations from stoichiometry seem to have little effect on total ductility, except at 77°K where Zn-rich material is considerably less ductile, similar to polycrystalline AuZn behaviour.[12] It is possible that Zn-rich material undergoes a low temperature phase transformation similar to that reported in polycrystalline AuZn[18] which could account for the relative brittleness. Because the transformation temperature decreases with increasing Au, stoichiometric and Au-rich crystals may retain the parent structure at 77°K. Upon metallographic examination of deformed crystals, no unusual markings were observed on the surface of the brittle Zn-rich crystals. The possibility of transformation induced brittleness was not further investigated during the course of this work.

2.2.5 Orientation Dependence

The orientation dependence of the stress-strain curves is shown in Figure 11. Within the stereographic triangle it is apparent that as the position of the specimen axis is varied from the [001] - [111] boundary towards the centre, the flow curve changes from two stages of linear hardening to three-stage hardening at the expense of both stages I and II. The work hardening rate Θ_1 appears unchanged but Θ_{II} decreases slightly. With increasing distance from the [101] - [111] boundary, both stages I and II and the transition region are shortened and total ductility is decreased. This behaviour is somewhat analogous to the orientation dependence of easy glide in fcc single crystals[3] and bcc niobium[1] where the extent of easy

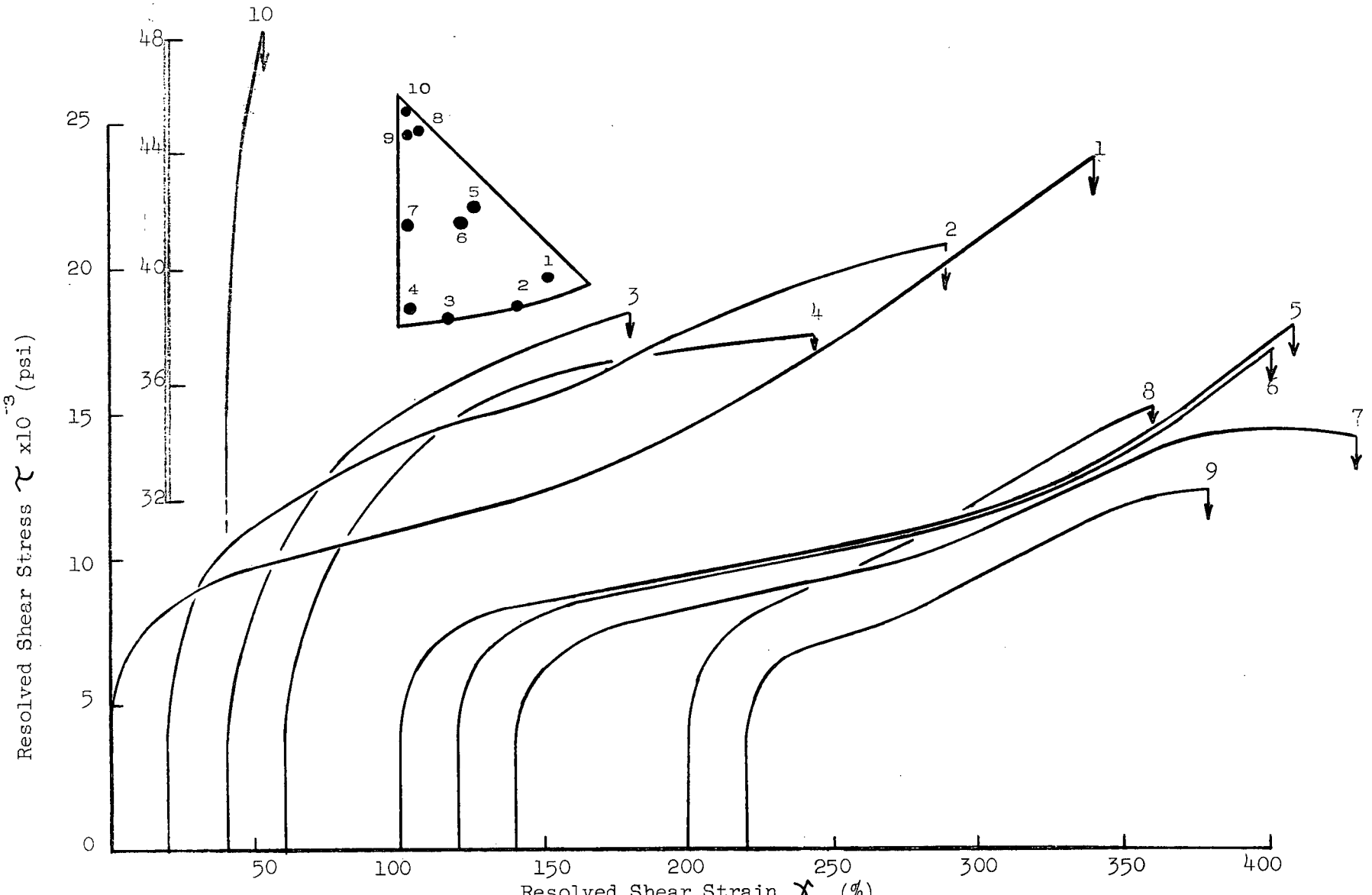

Figure 11. Resolved shear stress-shear strain curves of Au-rich β' AuZn crystals as a function of orientation. (T = 293°K; $\dot{\gamma} \sim 2.5 \times 10^{-3}$/sec)

glide decreases as the orientation approaches the symmetry boundaries [001]-[111] and [001]-[101] respectively.

Whereas specimens oriented well within the stereographic triangle give rise to multi-stage work-hardening curves, those oriented along the [101]-[111] boundary near the [101] corner display parabolic type hardening, and near [111], semi two-stage hardening. Curves from these orientations are very much like the most commonly observed flow curves for bcc single crystals[19-24] and that observed for the bcc ordered alloy NiAl deformed in compression along the [101] direction.[25]

An exception to the general multi-stage behaviour for orientations within the triangle has been observed very near the [001] corner (orientation 10 Figure 11). Plastic flow is characterized by an extremely high hardening rate and fracture occurs after very little deformation, somewhat similar to the low temperature behaviour of AuZn single crystals.

2.3 SERRATED FLOW

2.3.1 Occurrence

An interesting feature disclosed by tensile tests, not shown in Figures 6, 7, 8, 9 and 11 is the serrated nature of the plastic flow in non-stoichiometric crystals at intermediate temperatures. The same phenomenon has been reported by Causey[12] during room temperature deformation of polycrystalline β' AuZn. Au-rich crystals displayed serrated load-elongation curves from 260°K to 403°K and Zn-rich crystals from 293°K to 408°K. (These temperatures must be taken as approximate limits; i.e. Au-rich crystals, for instance, when tested at 260°K display serrated flow curves whereas at 217°K show smooth curves; at high temperature serrations are observed at 403°K but not at 433°K.)

A typically serrated resolved shear-stress shear-strain curve is shown schematically in Figure 12. Serrations begin after a few percent pre-strain in the stage 0 region and become fully developed at the onset of stage I. The critical strain, γ_c in Figure 12, necessary for the first jerk was observed to decrease with increasing temperature and decreasing strain rate, Table 2. During stage I, the amplitude and frequency of the load-drops fluctuate slightly, but on the average remain approximately constant. It was also observed that both the frequency and amplitude increase slightly with increasing temperature. Perhaps the most striking observation is that the amplitude is decreased abruptly during the transition region. During stage II the amplitude is greatly reduced and the frequency tends to zero near the onset of stage III. No serrations are observed during stage III deformation.

Well-defined serrated yielding was observed during stage I deformation for Au-rich crystals at all orientations within the stereo-

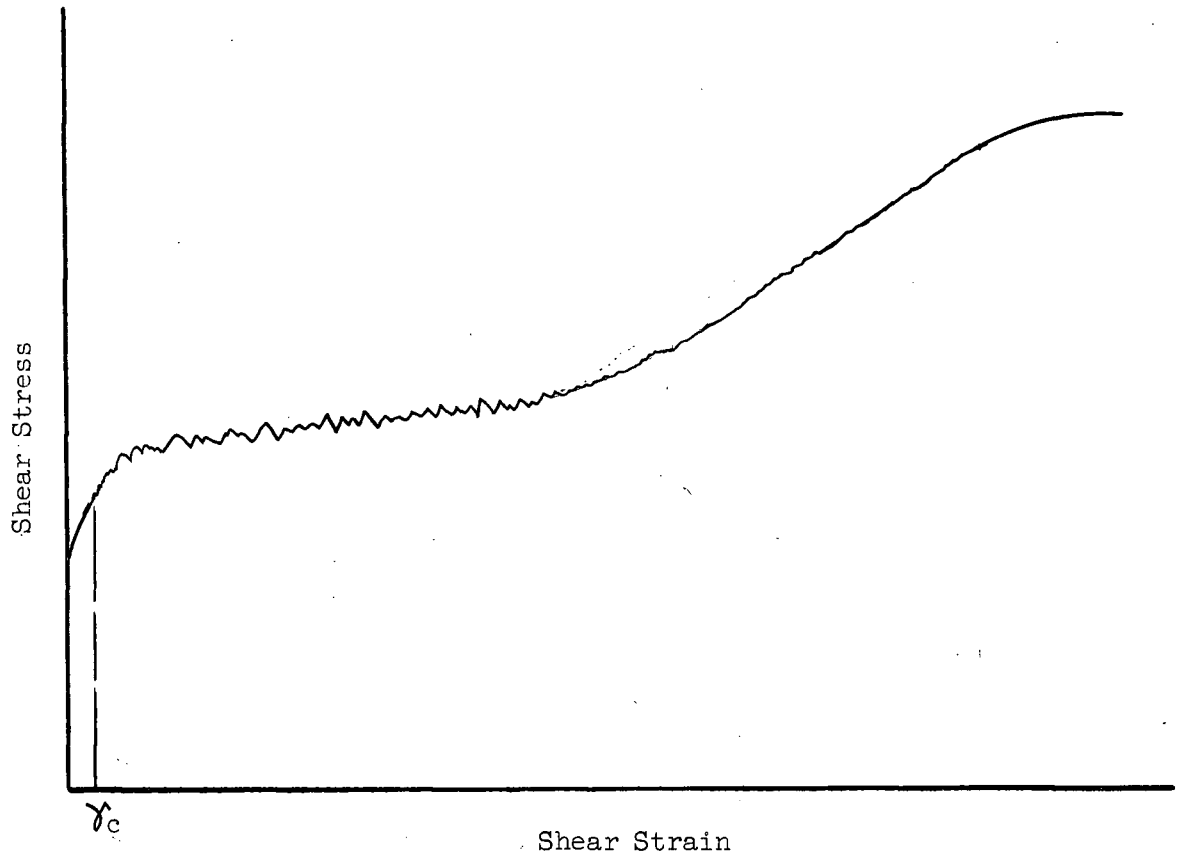

Figure 12. Schematic representation of a serrated flow curve typical for non-stoichiometric crystals tested around 300°K. γ_c is the critical strain before first jerk.

TABLE 2

Showing the Variation in Critical Strain with Temperature and Strain Rate for Non-stoichimetric β' AuZn Crystals

Composition	Test No.	Temp. °K	Strain Rate $\dot{\gamma}$/sec	Critical Strain γ_c
51.0 at.% Au	84	260	2.5×10^{-3}	0.17 - 0.23
"	85	"	"	0.20 - 0.26
"	60	293	"	0.07 - 0.13
"	61	"	"	0.07 - 0.13
"	75	373	"	0.02 - 0.06
"	76	"	"	0.02 - 0.05
"	82	403	"	0.018
"	83	"	"	0.016
49.0 at.% Au	89	293	2.5×10^{-3}	0.09 - 0.11
"	90	"	"	0.07 - 0.11
"	103	348	"	0.04 - 0.06
"	104	"	"	0.04 - 0.06
"	91	373	"	0.03 - 0.04
"	92	"	"	0.03 - 0.04
"	105	408	"	0.016
51.0 at.% Au	112	293	2.5×10^{-4}	0.05 - 0.07
"	110	"	2.5×10^{-2}	0.20 - 0.28

graphic triangle except near the [001] apex where fracture occurred after very little deformation (section 2.2). For orientations along the [101]-[111] boundary, however, minor serrations were observed after very little prestrain (2% shear strain) but were not detected past the high hardening region, disappearing at shear strains greater than approximately 50%. This behaviour is identical with the stage II damping out and stage III absence of serrated flow reported above.

A strain rate cycling experiment was performed at room temperature on an Au-rich (51.0 at % Au) crystal by cycling the cross-head speed of the Instron between 0.002 to 0.20 inch per minute, corresponding to a strain rate variation from 1×10^{-4}/sec to 1×10^{-2}/sec. Part of the strain-rate-change flow curve was photographed and is shown in Figure 13. It can be seen that both the amplitude and frequency of the serrations decrease with increasing strain rate.

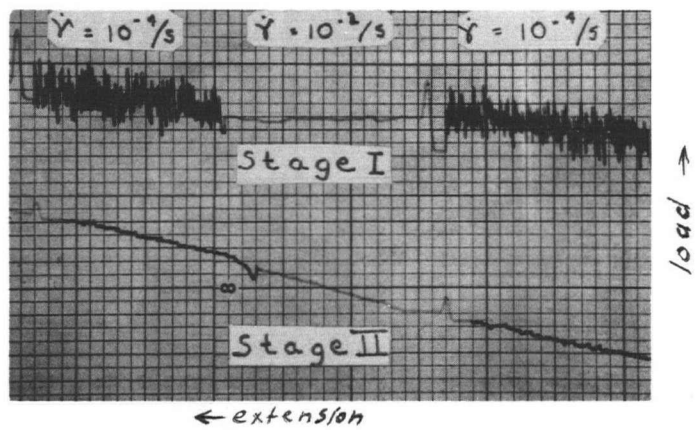

Figure 13. Photograph of segments of a serrated load-elongation curve during stage I and stage II deformation.

Metallographic examination of an Au-rich specimen strained well into stage I revealed a very even distribution of strain markings throughout the gauge which coincided with the operative slip plane. Since the strain markings would not reappear when electro-chemically polished in 5% KCN and etched in the same solution (for one minute at 1.5 V potential), they were assumed to be slip traces.

From these observations it appears that three conditions must be met for the occurrence of well-defined serrated flow in β' AuZn single crystals:

(1) The composition must deviate from stoichiometry;

(2) The resolved shear stress-shear strain curve must display a well-developed easy glide region;

(3) The test temperature must lie within a critical range centered approximately about 325°K which is equivalent to 0.33 T_m where T_m is the absolute melting point.

2.3.2 Origin

Serrated flow has been observed during plastic deformation of many intermetallic compounds of various superlattice types. During compression testing from 77°K to 350°K Fe_3Be single crystals (DO_3 superlattice) undergo continual mechanical twinning, giving rise to serrated flow curves.[72] Load drops during tensile experiments have been detected in the B2 compounds NiTi[67] and Cu-saturated (60 at % Cu) β-brass crystals[74] and were attributed to strain-induced transformations. During tensile deformation at intermediate temperatures, serrated yielding observed in non-stoichiometric AgMg[13] (B2) and NiAl[14] (B2) and in crystals of β-brass[75] (B2) and Cu_3Au[76] ($L1_2$) was attributed to dislocation-solute

atom interactions, commonly termed the Portevin-LeChetelier effect.[77] It is believed that the present phenomenon can also be explained in terms of solute interactions with moving dislocations. Since serrated yielding was restricted to non-stoichiometric compositions, it appears that the solutes interacting are either excess Au or Zn atoms. Causey[12] has shown that a substitutional type defect structure exists on both sides of stoichiometry suggesting that the segregating species diffuses through a vacancy-type mechanism. The interaction mechanism will be discussed in the next section.

2.3.3 Dislocation-Solute Atom Interaction

It is generally believed that plastic deformation may increase the density of mobile dislocations ρ according to the empirical relationship:

$$\rho = K_1 \gamma^m \tag{1}$$

where γ is the plastic shear strain and K_1 and m are constants. During deformation at a constant strain rate $\dot{\gamma}$, the product of the average dislocation velocity v and mobile dislocation density remains constant, according to:

$$\dot{\gamma} = \rho b v \tag{2}$$

where b is the Burgers vector of the mobile dislocations. Therefore v is a decreasing function of γ. Under suitable conditions of temperature and strain rate, the dislocation velocity approaches a critical value v_c (at a critical strain γ_c), sufficiently low to enable solute atoms to segregate towards the mobile dislocations; the strain fields of the segregating species and the dislocation interact, atmospheres are formed and the dislocation is either slowed down or pinned. The critical conditions for pinning were first expressed by Cottrell[79] in the relationship:

$$v_c = \frac{4D}{I} \tag{3}$$

where D is the self-diffusion coefficient of the segregating species and I is the atmosphere radius. In order to maintain the applied strain rate, the velocity of the unrestricted dislocations must increase, necessitating a localized increase in stress. At a sufficiently high stress level, the pinned dislocations either break-away from their atmospheres and/or fresh dislocations are generated. At this point, the first load drop occurs. The process of solute locking followed by dislocation break-away and/or generation is repeated during subsequent deformation, giving rise to the observed serrated flow curve.

From this description of serrated yielding, the experimentally observed effects of temperature, strain rate and strain can be explained. Because of the marked effect of temperature on diffusion coefficients, $v > \frac{4D}{I}$ at low temperatures for all strains beyond yield. Because of the low D values, atmospheres are not formed around mobile dislocations, motion is not impeded and consequently serrated yielding does not occur. At high temperatures $\frac{4D}{I} > v$ at all strains and atmospheres are formed, but because of the larger D values, move along with dislocations and do not impede their motion. In the intermediate temperature range where serrated flow occurs, v_c increases proportional to the increase in D with temperature necessitating decreasing values of prestrain before first jerk.

To understand the effect of strain rate on the critical strain, equation (3) is rewritten by incorporating equation (2) and equating I to 4b, to give:[82]

$$\gamma_c = D\beta \tag{4}$$

Because vacancy-type defects are created during initial straining the value of D is believed to increase according to:[80]

$$D = a^2 \upsilon Z C e^{-Q/kT} \tag{5}$$

where a is the lattice parameter, ν the Debye frequency, Z the coordination number, C the concentration of vacancy-type defects created during straining, Q the activation energy for motion of the segregating species, k the Boltzmann constant, and T the absolute temperature. The parameter C is given by the empirical relationship:[83]

$$C = K_2 \gamma^n \tag{6}$$

where K_2 and n are constants. By substituting (6) into (5) and (1) into (4), it is seen that at constant temperature:[78]

$$\gamma_c^{(n+m)} = K_3 \dot{\gamma}_c \tag{7}$$

where K_3 is a constant. It is immediately apparent from (7) that the critical strain increases with strain rate, in line with the experimental observations.

In discussing strain rate effects on amplitude and frequency of serrations, one must be careful to distinguish between true strain rate effects and apparent strain rate effects. Apparent effects are noted directly from the autographically recorded load-elongation curves, and are recorded in the thesis. It is quite possible that at high strain rates, because of poor pen response on the testing machine, a stress drop which is coincident with a burst of dislocations will not be detected. Consequently, an apparent large decrease in amplitude with strain rate does not necessarily mean that the number of dislocations released or generated per burst has been greatly reduced. Because of the uncertainty in relating the apparent with the true effect, strain rate dependence on serrated flow will not be discussed further.

During stage I deformation, the serration amplitude remains relatively constant, suggesting that an equilibrium exists between the mobile dislocation density and the vacancy-type defect concentration.

During stage II, however, because of increased dislocation-dislocation interactions (section 2.5.2), the defect production rate is increased upsetting the equilibrium. Diffusion rates may then be large enough to allow atmospheres to move with dislocations which would account for the gradual decay of serrated yielding. Some basis for this belief is derived from the following rough calculations. Assuming that the mobile dislocation density at the end of stage I is $\sim 10^{9}/cm^{2}$, the average dislocation velocity v' necessary to maintain the applied strain rate of $\sim 10^{-3}$/sec was calculated from equation (2) to be $v' \sim 10^{-4}$ cm/sec where b was taken as 3×10^{-8} cm. Furthermore, assuming that the defect concentration C as a function of strain may be given roughly as $C \sim 10^{-4} \gamma^{111}$, then the diffusion coefficient D' at the end of easy glide calculated from equation (5) is given as $D' \sim 10^{-11}$ cm^2/sec, where a was taken as 3×10^{-8} cm, γ as 1, Z as 8, υ as 10^{13}/sec and Q as ~ 0.25 ev. (see next section). On substituting D' into equation (3) and letting $I = 4b^{82}$, it is seen that $\frac{4D}{I} \sim 10^{-3}$ cm/sec and therefore somewhat greater than v', consistent with the suggestion that atmospheres diffuse along with moving dislocations at the end of stage I. It must be emphasized that these calculations are only crude approximations since they are based on the questionable assumption that $\rho_{mobile} \sim 10^{9}/cm^{2}$ and that $C \sim 10^{-4}\gamma$ at large strains. Since specimens oriented along the [101]-[111] boundary deform by multiple slip (section 2.4.5.3) the explanation based on an increased vacancy production rate can probably account for the greatly reduced amplitude of serrations for these orientations.

2.3.4 Segregating Species

The problem remains to identify the segregating species. An analysis will be carried out to determine the activation energy of motion, Q, with the view that knowledge of such a parameter is valuable in this regard. Although successful in estimating Q, the analysis does not permit an unambiguous identification of the species. Since the variation

in γ_c with $\dot{\gamma}$ was not determined for Zn-rich crystals, the energy Q will be evaluated for Au-rich crystals only.

By equating D in equations (4) and (5) and substituting equation (1) and (6) for ρ and C respectively, it can be shown that at constant strain rate:

$$\gamma_c^{m+n} = K_4 e^{Q/kT} \qquad (8)$$

where K_4 is constant. The sum (m + n) may be obtained by plotting $\log_{10} \gamma_c$ against $\log_{10} \dot{\gamma}_c$ (equation 7) and reciprocating the slope. Because of difficulties in obtaining accurate values of γ_c from load-elongation curves, it was decided to plot the range of strain, Table 2, in which γ_c fell, Figure 14, where the bracketed points locate the critical strain range. At strains less than those depicted by the lower brackets, serrations were not detected whereas at strains greater than those specified by the upper brackets, serrated flow had definitely begun. To determine the value (m + n) from the points in Figure 14, two extreme lines were drawn and the corresponding slopes measured then reciprocated to give an average value of (m + n) with a deviation term. It was found that $(m+n)=3.6 \pm 0.9$, comparable with the values 2.2 ± 0.1 and 1.9 ± 0.2 determined for Cu-Sn[71] and Cu-Zn[84] alloys respectively.

It is now possible to determine Q from the slope of the graph $\ln \gamma_c$ against the reciprocal of the absolute temperature, Figure 15. Again, the critical strain range is plotted and the bracketed points have the same significance as described above. To determine the slope from the points in Figure 15, the two-extreme line technique was again used, then to obtain the maximum and minimum, and hence most probable activation energy, the highest and lowest slopes were multiplied by the highest and lowest (m + n) values. The most probable activation energy Q obtained in

Figure 14. Showing the variation in Critical Strain γ_c with Critical Strain Rate $\dot{\gamma}_c$ (T = 293°K; 51.0 at.% Au)

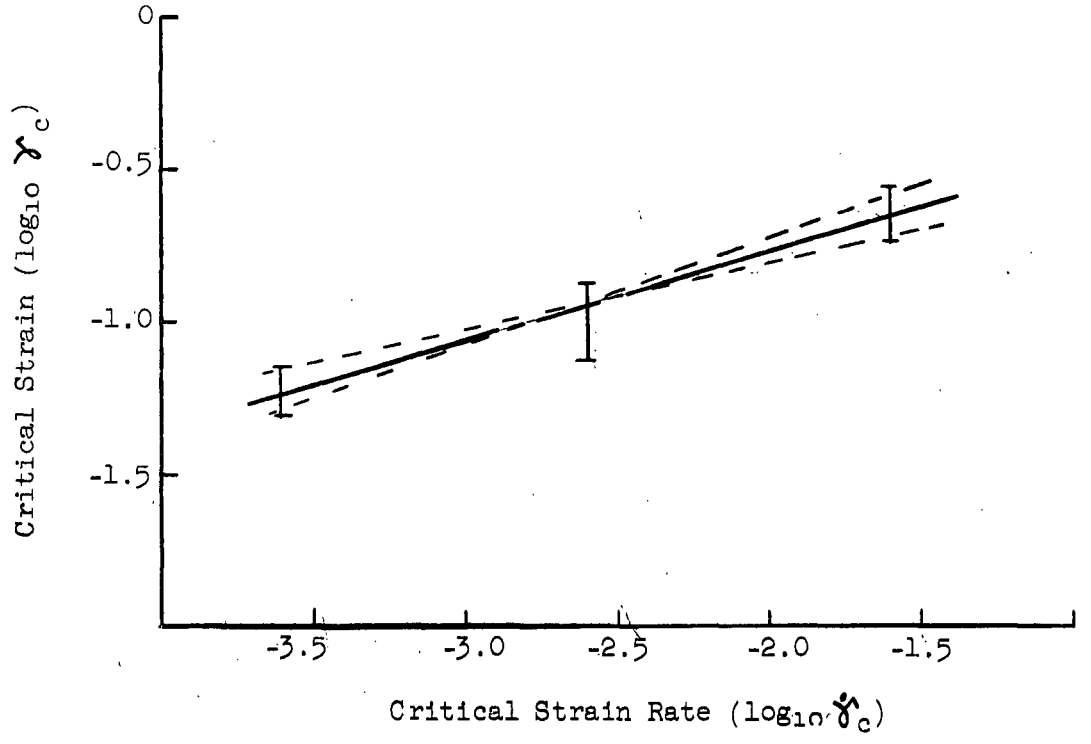

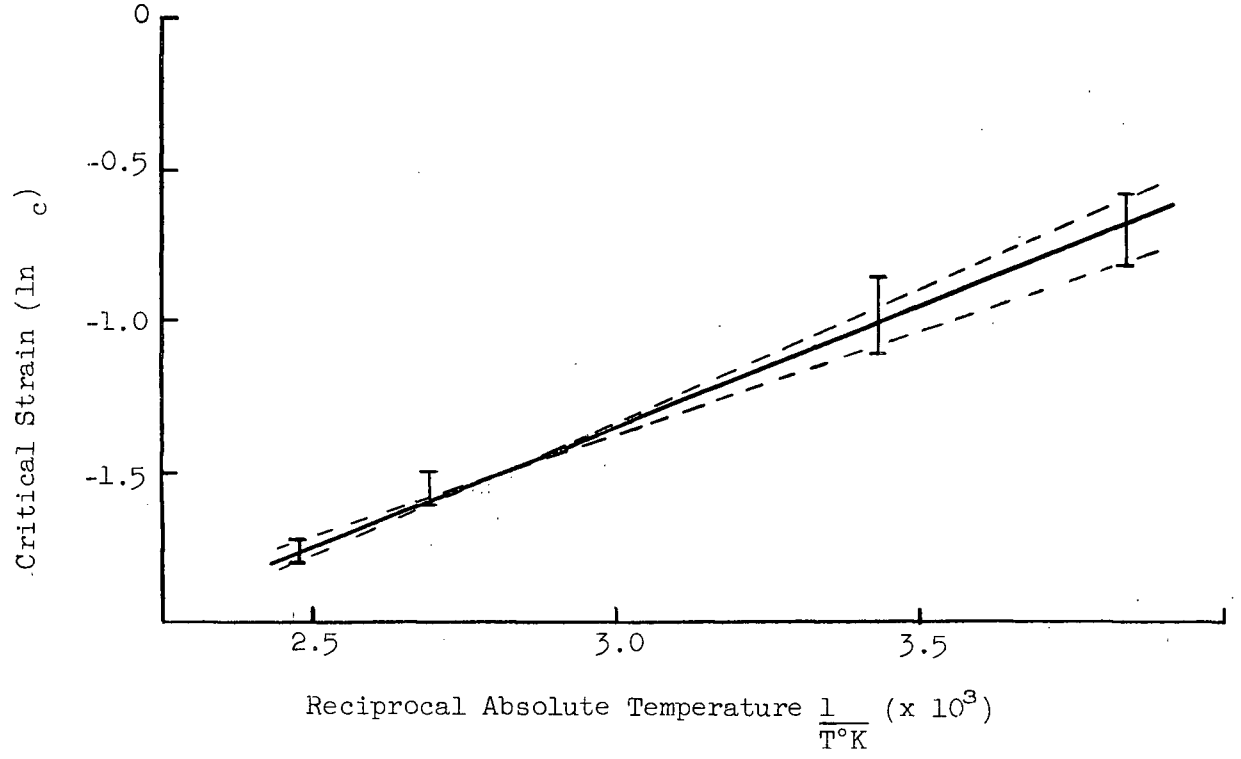

Figure 15. Showing the effect of temperature on critical strain ($\dot{\gamma}$ = 2.5 x 10^{-3}/sec, 51.0 at.%Au)

this way was found to be:

$$Q = 0.26 \pm 0.08 \text{ ev.}$$

The activation energy for motion of vacancies in material of the same composition was given by Mukherjee et al[85] as 0.47 ± 0.05 ev., determined from isothermal annealing studies on quenched-in defects in 3 mm. diameter single crystals. It is apparent that the energy for motion of vacancies does not fall within the range determined for the present activation energy.

Due to the paucity of data in the literature listing the activation energies for the motion of defects in intermetallic compounds in general, and AuZn in particular, it is impossible at this juncture to associate $Q = 0.26 \pm 0.08$ ev. with the motion of any defect species. The identity of the segregating species, therefore, remains unknown.

2.4 DEFORMATION MODES

2.4.1 Introduction

The operative slip systems in CsCl type superlattices are strongly dependent on the degree of ionic bonding between the component atoms. In considering the question how large must the ordering energy be to change the slip direction from the usual bcc "metallic" <111> type to the "ionic" <001> type, Rachinger and Cottrell[26] (RC) begin with Nabarro's[27] postulation that <111> slip should not occur unless the total a <111> dislocation dissociates into two superlattice partial dislocations according to:

$$a\langle 111\rangle = \frac{a}{2}\langle 111\rangle + \frac{a}{2}\langle 111\rangle \qquad (9)$$

Nabarro's postulation is based on the fact that total a <111> dislocations are able to dissociate into three perfect a <001> type dislocations with no change in elastic energy, and consequently, an applied stress that acts strongly on one of the three a <001> components will move this component independent of the others. RC point out that even if dissociation (9) occurs, <001> slip may still be favourable if the stacking fault energy linking the two superlattice partials is high enough so that their equilibrium spacing is only ~a, one lattice spacing. The critical factor, then, in determining whether or not <111> slip occurs is the critical stacking fault energy ω_c above which, <001> is the favoured mode and below which the equilibrium separation of the partials is greater than a so that <111> is favoured. As a quantitative criterion, RC assume that ω_c exerts a force on the dislocation equal to the theoretical shear strength of the lattice, and hence may be expressed as:

$$\omega_c = \alpha\mu\, b \qquad (10)$$

where $\alpha\mu$ is the theoretical shear strength ($\alpha \sim 1/30$) and b is the Burgers vector. Giving typical values of 3×10^{11} dynes/cm^2 and 2.5×10^{-8}cm

to μ and b respectively, ω_c was calculated as ~ 250 ergs/cm^2. Then considering the atomic density on (110) planes $\sqrt{2}/a^2$ and that each atom forms bonds with two nearest neighbours in parallel layers, RC calculate that on the nearest neighbour bond approximation:

$$V_{AB} - \frac{1}{2}(V_{AA} + V_{BB}) = -\omega_c \frac{a^2}{2\sqrt{2}} \approx -.06 \text{ ev.} \qquad (11)$$

which is the critical ordering energy per atomic bond, equivalent to a charge of only ± 0.1 electron on each "ion". They conclude that since ionic character as small as this is quite possible, even in highly "metallic" alloys, <100> should be the common mode of slip in CsCl type structures.

In an attempt to evaluate their hypothesis, RC studied slip modes in several CsCl compounds and compared the slip direction with that expected on the basis of bond type. In compounds undergoing an order-disorder reaction, $\frac{kT_c}{4}$ was taken as a measure of the ordering energy per bond,[28] where T_c is the ordering temperature in degrees Kelvin. Their results are given in Table 3. For the ionic compounds noted, <100> is the slip direction, as predicted. For CuZn, <111> slip was observed, again in agree-

TABLE 3

Slip Systems in CsCl Type Compounds

(Rachinger and Cottrell[26])

Compound	Plane	Direction	Bond Character	
			T_c (°K)	Ordering Energy (ev.) $= kT_c/4$
CuZn	110	111	738	0.015
AgMg	321	111	1093 (Tm.p.)	0.023
TlBr, TlI, TlCl				
TlBr, LiTl, MgTl	110	001	ionic compounds	
AuZn	110	001	998 (Tm.p.)	0.022
AuCd	110	001	900 (Tm.p.)	0.020

ment with their hypothesis, since the low ordering energy of 0.015 ev. is less than the critical energy 0.06 ev. But, slip directions <001> in the compounds AuZn and AuCd appear to invalidate the hypothesis since the ordering energies are less than 0.06 ev. However, as RC point out, the fact that AuCd and AuZn are ordered up to their melting points suggests that the use of T_{mp} as T_c in computing the ordering energy probably results in a figure less than the true value.

Ball and Smallman[29] (BS) have recently reported slip systems in the B2 compound NiAl to be of the form {110}<001>. Since NiAl, like AuCd, AgMg and AuZn, is ordered up to its melting point, BS calculated that the ordering energy per atomic bond $\left(\text{from the relationship } \frac{kT_{mp}}{4}\right)$ is 0.04 ev, somewhat less than the critical 0.06 ev. for <100> slip according to RC.[26] BS conclude that the RC criterion fails again to satisfactorily predict slip modes in CsCl type compounds. The problem of slip systems in CsCl compounds is then reconsidered in terms of the dislocation elastic energy E which is given by the relationship derived by Foreman:[30]

$$E = \frac{Kb^2}{4\pi} \ln \frac{R}{r_o} \qquad (12)$$

where R and r_o are the outer and inner cut-off radii respectively, b the Burgers vector and K the energy factor which is a function of the elastic constants c_{11}, c_{12}, c_{44} and the direction cosines α, β, γ of the dislocation line with respect to the cube axis. Energy factors for screw dislocations lying along <111> directions have been calculated by Head[32] and for screws along <100> and <110> as well as edges lying along <100> and <110>, by Foreman.[30] Since the relative mobility S (i.e. the ratio of the stress required to move a dislocation to that necessary to make the atomic planes move rigidly over one another) of the lower energy dislocations in possible glide planes will determine their rate of multiplication and

hence the predominant slip system, the S values of the lower energy dislocations must also be compared. Eshelby[33] has proposed an equation to determine S:

$$S = 4\pi \frac{\zeta}{b} e^{\frac{-2\pi\zeta}{b}} \qquad (13)$$

where ζ is the width of the dislocation and can be calculated from the expression:[33]

$$\frac{\zeta}{b} = \frac{1}{2} \frac{K}{\mu} \frac{d}{b} \qquad (14)$$

where K is the energy factor, μ the shear modulus in the slip direction on the glide plane and d the spacing between the glide planes.

To compare the experimentally observed slip modes in some CsCl compounds with those predicted by the elastic energy-dislocation mobility criterion, BS calculated E and S for screw and edge dislocations lying along ⟨111⟩, ⟨101⟩ and ⟨100⟩directions in CuZn, NiAl and CsBr. For comparison the author calculated the corresponding terms for similar dislocation arrangements in the iso-structural compound AuZn. The lowest energy configurations, the relative mobilities and the experimentally determined slip modes are given in Table 4.

Although a ⟨100⟩appears to be the most favourable total dislocation in CuZn, BS show that a⟨111⟩ dissociates into two $\frac{a}{2}$⟨111⟩ superlattice partials having total energy lower than that for the a⟨100⟩ dislocation. The predicted system {110} ⟨111⟩is therefore consistent with experimental results. In CsBr, energetically both {110}⟨001⟩and {100}⟨001⟩are possible systems, but because of the favourable mobility term, {110} ⟨001⟩is predicted, again in agreement with experiment. Clearly, ⟨001⟩ is the favourable slip direction in NiAl and the energetics suggest that slip should occur on {100} planes. However, because the mobility term

TABLE 4

Comparison of Line Energies E and Mobilities S of Low Energy Dislocations in CuZn, NiAl, CsBr (after Ball and Smallman[29]) and AuZn

Slip System		Ref.	Compound	Plane	Burgers Vector	Dislocation Character	$E^* \times 10^{-4}$ (ergs/cm)	S
110	111	26	CuZn	010	100	e	3.24	.723
				110	111	s	4.4	.7
				110	110	s	4.4	.086
				110	100	e	4.86	.626
110	001	29	NiAl	100	100	e	7.69	.71
				110	100	e	8.83	.513
				110	100	s	9.29	.46
				100	100	s	9.29	.67
110	001	26	AuZn	100	100	e	2.3	.431
				110	100	e	2.64	.276
				110	110	s	2.78	.426
				110	100	s	3.0	.482
110	001	70	CsBr	110	100	s	.825	.46
				100	100	s	.825	.67

E^* = line energy where $\frac{1}{4\pi} \ln \frac{R}{r_o}$ is taken as unity.

e = edge dislocation
s = screw dislocation

is more favourable on {110} planes, the predicted system is {110} <001> consistent with the experimental observations. In AuZn as well, <001> is clearly the preferred slip direction. Since mobility appears to dominate in low energy configurations, {110} <001> is the predicted slip system, in agreement with the results of Rachinger and Cottrell[26] and consistent with the observations to be presented in sections 2.4.3 and 2.4.4 of the thesis.

The latest discussion of slip systems in CsCl type compounds suggests that the atom size ratio R_A/R_B may be an important factor governing

the choice of slip system. Lautenschlager et al[34] grouped B2 compounds into three classes:

A, mainly ionic with some degree of covalent bonding;

B, metallically bonded and reinforced by a strong covalent component;

C, wholly metallic with a slight covalent tendency.

In class A, ionic characteristics are believed to dominate the slip direction and <001> is the preferred mode, while in class C, an orientation criterion dominates and on the basis of Schmid factor calculations for the systems {110} <111>, {211} <111>, {321} <111>, {110}<110>, {110}<001>and {100} <001>, the most favoured slip direction is along <111>. (It must be pointed out that the orientation criterion necessarily assumes that the critical resolved shear stress is the same on all possible slip systems.) In class B, though, Lautenschlager et al state that R_A/R_B governs the choice of slip mode. The criterion for classifying a particular compound was not stated.

Hard sphere CsCl models were constructed[34] and the effect of atom size ratio from 1.000 to 0.732 (i.e. range in which CsCl structure is stable[35]) on the choice of slip system was evaluated in the following manner. Choosing either <100>, <110> or <111> as the slip direction, possible slip planes were either accepted or rejected if the maximum displacement normal to the shear plane, $d_\perp$ were less than or greater than 0.3a, where a is the lattice parameter. The only systems fulfilling this criterion were {100}<001>, {110}<001>, {110}<110>, {110}<111>, {211}<111>and {321}<111>. For a specific R_A/R_B ratio, the most favourable system from these six possibilities is associated with the smallest $d_\perp$ value. On this basis it was shown that <111> is the favourable slip direction as $\frac{R_A}{R_B}$ tends to 1.000 while <001> is preferred when the ratio tends to 0.732. For values

between 1.000 and 0.732, however, the $d_\perp$ criterion is less discriminative in its choice for slip direction. Also, it appears that the $d_\perp$ criterion is not able to distinguish unambiguously between the possible slip planes in the <111> or <001> zone.

A second important deformation mode that is often encountered in bcc metals and alloys is that produced by mechanical twinning. Upon ordering, however, Laves[41] pointed out that a crystal may lose its twinning ability. Marcinkowski and Fisher[42] considered the number of nearest neighbor A-B bonds broken and A-A and B-B bonds formed during mechanical twinning in a CsCl type compound, assuming the twin mechanism to be that invariably observed in bcc lattices, namely {211} <111>. Unlike the case for slip, a suitable pair of dislocations that might create a twin without leading to any subsequent disorder does not exist, because if the $\frac{a}{6}$<111> twin dislocation dissociates or combines with another, the necessary atom movements for twin formation would not be provided. Consequently the stress necessary to move the twinning dislocation, and thereby disorder the lattice, is believed to be very high. Marcinkowski and Fisher conclude therefore that <111> slip is generally preferable to twinning in the B2 lattice. In alloys that exhibit <001> slip, twinning on the {211} <111> system is probably even less likely than in systems undergoing <111> slip.

As noted, considerable information is available on the deformation modes in the various CsCl type intermetallic compounds. However, no detailed account has appeared in the literature concerning the effects of temperature, strain rate and crystal orientation (on deformation modes). Such a study has been carried out during the course of the present investigation with the view that such information would aid in understanding the general deformation characteristics of β'AuZn and possibly elucidate the underlying dislocation mechanisms responsible for the observed behaviour.

2.4.2 Procedure

For the purposes of trace analysis, highly polished flat surfaces were prepared by spark-machining square cross-sections on the 3mm. diameter crystals over a 2 cm. gauge length then electrochemically removing approximately 0.004 inch from the eroded surface in fresh 5% KCN solution. All specimens were subsequently encapsulated under reduced pressure and annealed one hour at 300°C to remove any slight residual strains that may have been incurred from the spark-machining operation. All specimens were examined under the optical microscope prior to straining. In the experiments designed to study temperature effects on deformation modes, the same pair of crystallographic faces were exposed on all specimens. This procedure is, of course, not possible when studying orientation effects.

In determining the orientation dependence of the slip plane, specimens were strained in tension until well-defined strain markings could be seen under the optical microscope. Shear strains from 5 to 10 percent were found to be adequate. For metallographic examination, specimens were supported in a specially designed "jig" then examined under green-filtered oblique lighting using a Reichert metallograph. Strain markings on adjacent surfaces were carefully paired, noted and then photographed. The orientation of the surfaces examined was determined from back-reflection Laue X-ray patterns taken after straining. To minimize experimental errors extreme care was taken to align the crystal face parallel to the X-ray film plane. The operative slip plane was determined by a two-surface trace analysis according to a procedure given by Barrett[43]. Reproducibility was found to be within three degrees.

2.4.3 Definitions

In studying slip systems it was useful to characterize the

orientation of the specimens by the angles ξ and χ in the manner first proposed by Taylor,[44] shown in Figure 16, and recently employed in similar studies on Ta,[48] Nb[45] and Fe-Si alloys.[46,47] Accordingly, ξ is the angle between the slip direction $\bar{b}$ (shown later to be [001]) and the tensile axis σ and χ is the angle between a reference plane in the [001] zone, taken as (110), and the maximum resolved shear stress plane M in the zone, which is normal to the plane containing $\bar{b}$ and σ. In Figure 16, ψ is defined as the angle between the macroscopic slip plane and the reference plane (110) and will subsequently be termed the slip plane parameter.

2.4.4 Slip Direction

The Burgers vector of the mobile dislocations was determined from changes in crystal orientation caused by plastic deformation since it can be shown[49] that the direction in the glide plane to which the longitudinal axis moves is the slip direction. The changes in orientation for a slightly Au-rich crystal (~50.3 at % Au) during deformation at 77°K, 140°K, 293°K, 398°K and 473°K are shown in Figure 17. The corresponding load-elongation curves are also shown so that a rough idea may be gained of the amount of strain induced prior to each re-orientation. It is evident that the specific direction of specimen axis re-orientation is temperature dependent. At 77°K, two experiments were performed from which slightly different results were obtained. It is observed that the specimen axis in one case rotated towards [100] throughout deformation (Figure 17.1.a) but in the second case rotated toward [100] initially then towards [001] during the later stages of deformation (Figure 17.1.b). In both cases the specimen axis followed a great circular route to either [100] or [001]. During straining at temperatures 140°K, 298°K and 398°K (Figure 17.2.a; Figure 17.3.a; Figure 17.4.a) the specimen axis rotated directly towards [001]

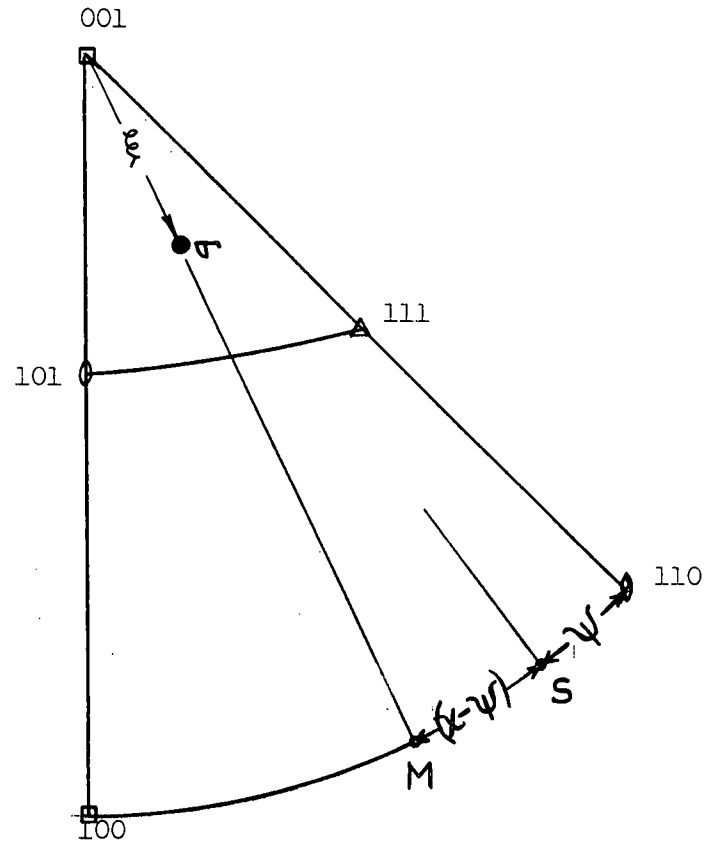

Figure 16. A (001) stereographic projection showing the parameters characterizing the specimen orientation and the slip plane relative to (110).

ξ = angle between slip direction [001] and tensile axis σ.

χ = angle between the (110) reference plane and most highly stressed plane (of pole M) in the [001] zone.

ψ = slip plane parameter; angle between the (110) reference plane and the observed slip plane of pole S.

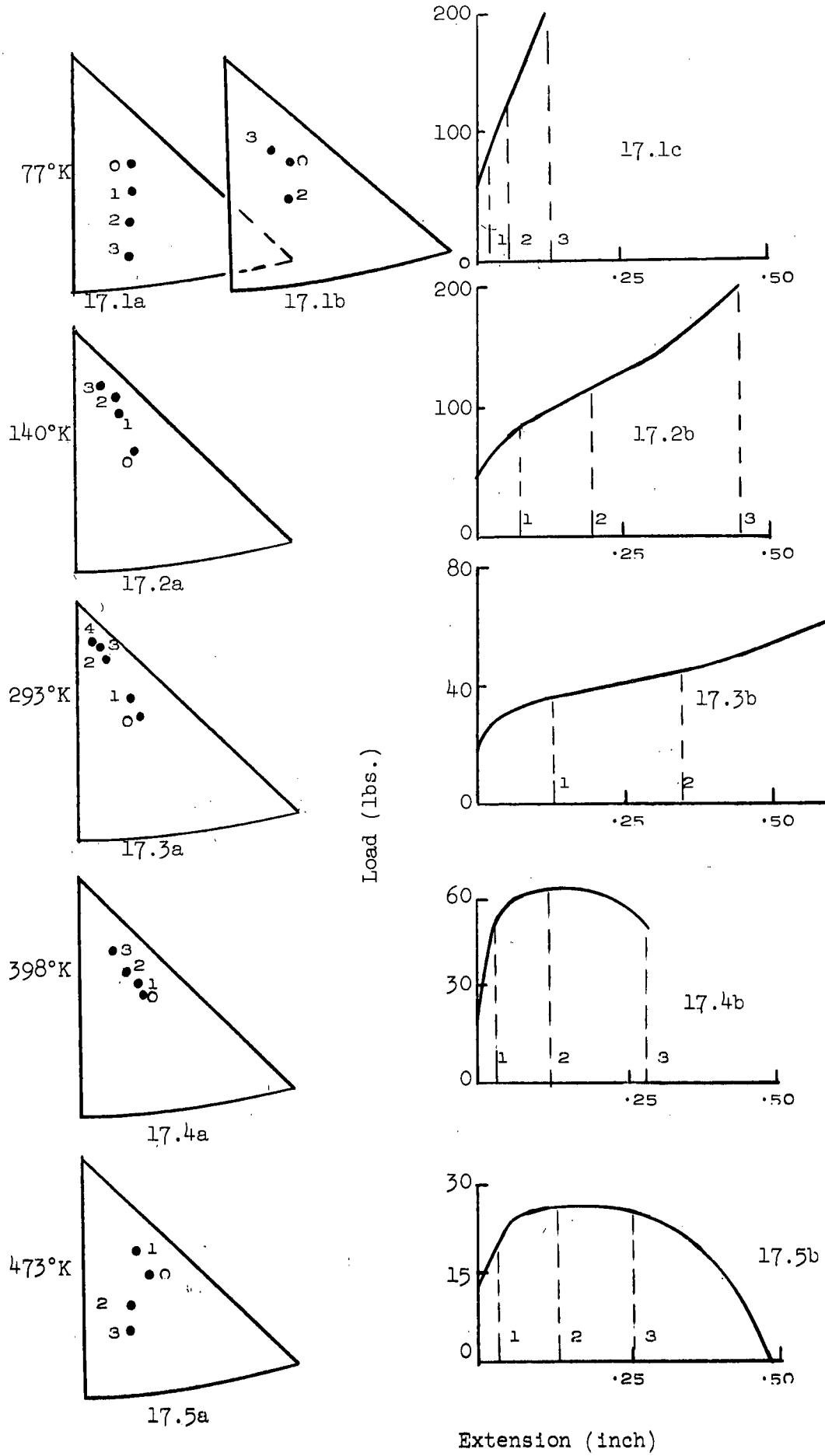

Figure 17. Stereographic representation of specimen axis reorientation during plastic deformation as a function of temperature. (0 denotes initial orientation)

throughout deformation, while at 473°K (Figure 17.5.a) towards [001] initially then towards [100].

From these results, it could be inferred that the re-orientation along two directions during straining is indicative of a change in the operative slip system. Slip systems have been studied during deformation and the results are reported in section 2.5.2 where it is shown that the most prominent system at 473°K changes during deformation. At this juncture, it may be concluded that the most prominent slip direction in β'AuZn is the <001> type, in agreement with the observations of Rachinger and Cottrell[26] and the predictions based on elasticity theory given in section 2.4.1.

2.4.5 Primary Slip Planes

2.4.5.1 Temperature Dependence

The primary slip plane dependence on temperature from 77°K to 473°K was investigated for two orientations within the stereographic triangle, Figure 18, using slightly Au-rich (~50.3 at % Au) crystals. Typical slip traces from orientation 1 observed at low magnification are shown in Figure 19, and at high magnification, Figure 20. The high magnification structures were obtained from transmission electron microscopy studies of replicated surfaces using chromium-shadowed carbon replicas taken from cellulose-acetate impressions of the crystal surfaces.

It is seen that slip traces on faces A are generally short and wavy while those on faces B are long and relatively straight. This difference is particularly evident in Figure 20. Since the operative slip direction above 77°K is [001], it was possible to calculate that the inclination of the slip vector to faces A and B(which were oriented from back-reflection photographs) is 28° and 10° respectively. The short wavy traces, therefore,

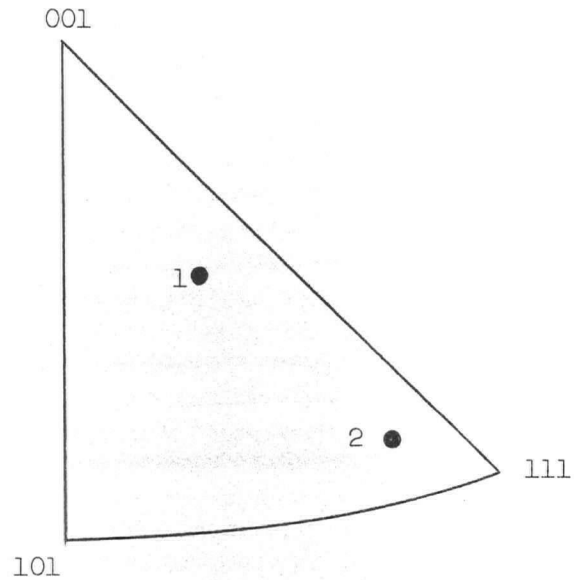

Figure 18. Crystal orientations used in slip plane-temperature study.

20.A

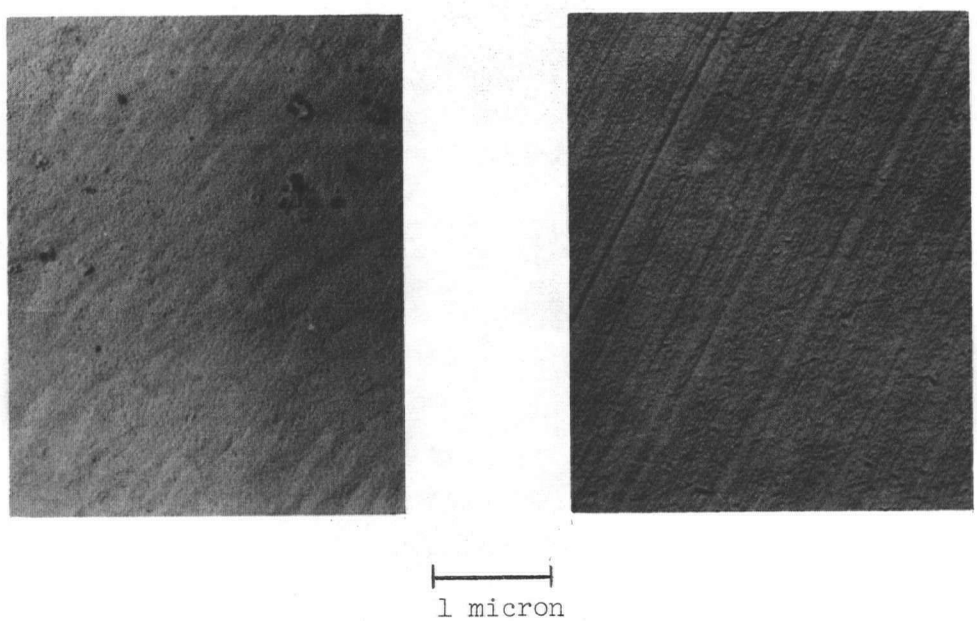

20.B

Figure 20. Replicas of surface slip traces on orthogonal faces A and B.

19.A.1

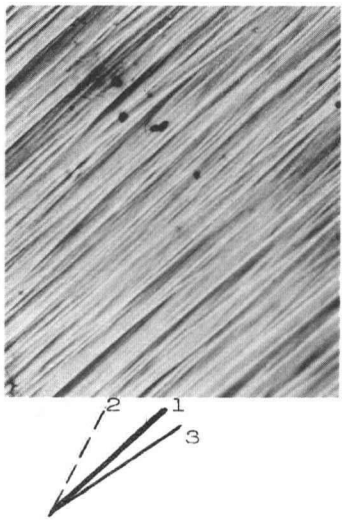

77°K

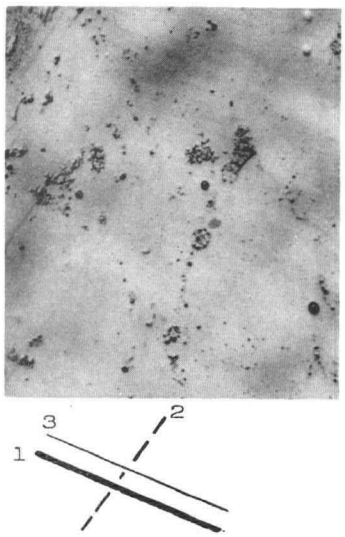

19.B.1

19.A.2

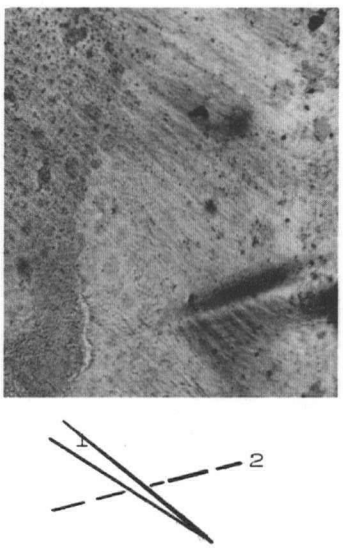

293°K

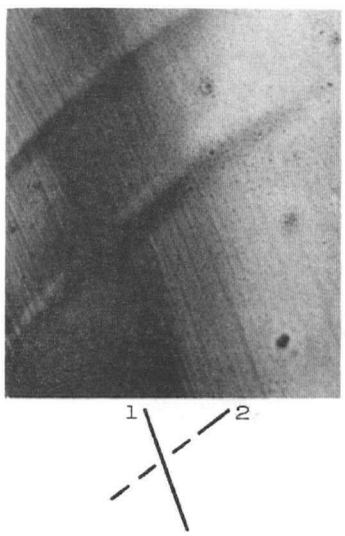

19.B.2

19.A.3

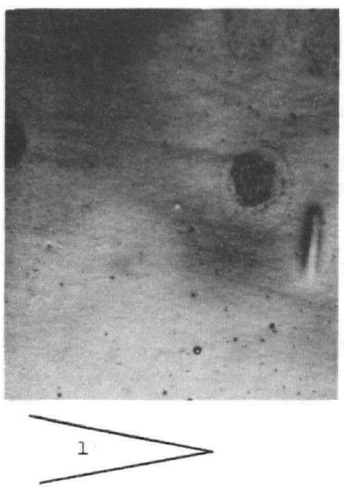

473°K

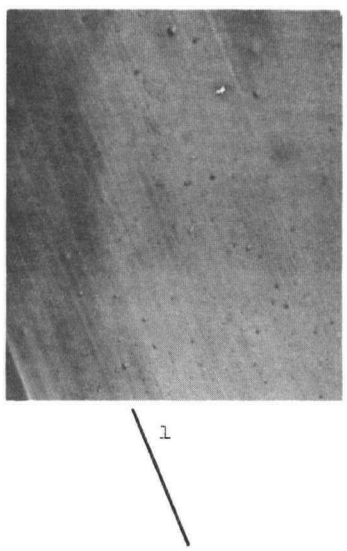

19.B.3

Figure 19. Photomicrographs of typical slip traces on orthogonal faces A and B where A ~(201) and B ~(0$\bar{1}$0); X 100

were created by edge dislocations tracing the paths of screws and the long straight traces were formed by screw dislocations tracing the motion of edges. Slip trace development is sketched in Figure 21. These observations are very similar to slip traces observed in Nb single crystals[1, 45] and appear analogous to those of slip-bands in Fe-3.2% Si crystals[50] revealed by etching. The presence of the short, wavy traces suggests that the screw dislocations travel over relatively short distances before they either cross-slip onto other planes or stop, while the long, straight traces imply that the edges travel over quite long distances.

At 77°K it is apparent that three systems are operative, although system 1 dominates, Figure 19.1, while at higher temperatures only one system operates. Schematic pairing is illustrated under each photomicrograph in Figure 19. Because of the profuse waviness of face A traces it was decided to characterize the respective markings by a narrow wedge rather than a line; in this way they could be realistically paired with the straight B traces and then analyzed. Markings labelled 2 in Figure 19.2 will be discussed in section 2.5.2 under the title of deformation bands.

At temperatures above 77°K, it was found that the slip surfaces are non-crystallographic planes (i.e. high index) in the [001] zone and that the macroscopic slip plane varied with temperature. The results of these analyses, including the range, are given in Table 5 under column Ψ. At 77°K (Figure 19.1) the dominant slip plane was found to be a non-crystallographic plane in the [100] zone lying within 3 or 4 degrees of (011) and therefore could not be expressed in terms of Ψ as it is presently defined; trace -2, is a non-crystallographic plane in the [001] zone which can be expressed in terms of the slip plane parameter Ψ and is given in Table 5. Since the slip direction must be parallel to the zone

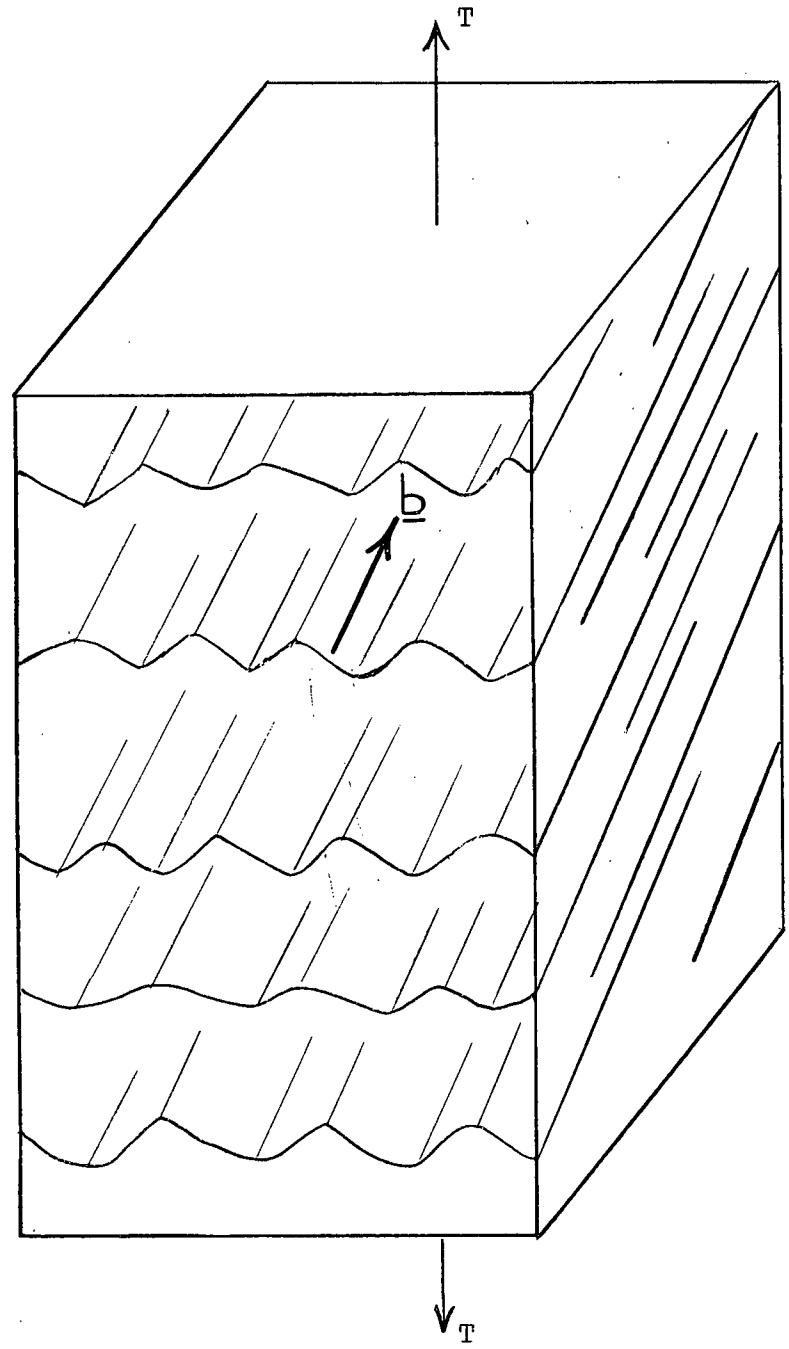

Figure 21. A sketch of slip trace development on orthogonal surfaces when one surface is parallel to the Burgers vector $\underline{b}$ of the mobile dislocations; T is the tensile axis.

axis, the Burgers vectors of dislocations giving rise to primary deformation are parallel to [100] at 77°K and parallel to [001] at higher temperatures. These results are in agreement with the primary slip direction determined from axial rotations during plastic deformation, section 2.4.4.

TABLE 5

Results of Slip Trace Analyses of Temperature Effect on Slip Plane Parameter Ψ ($\dot{\gamma} = 2.5 \times 10^{-3}$/sec.)

Orientation (Figure 18)			Test No.	Test Temp. °K	Ψ (deg.)
No.	χ	ξ			
1	20	24	153	77	5 - 6
			155	140	13 - 17
			146	293	24 - 29
			135	293	22 - 27
			157	398	29 - 37
			156	473	40 - 50
2	6	42	130	77	1 - 2
			132	210	3 - 5
			127	453	11 - 15
			133	475	13 - 17

Prior to discussing the variation in Ψ with temperature, one further feature of the 77°K deformation traces must be noted. The pole of trace-3 in Figure 19.1 lies within two degrees of (011), the most highly stressed plane of the $\{110\}\langle 111\rangle$ system for the given orientation. An examination of the back-reflection Laue photograph obtained from the surface in Figure 19.A.1 revealed two distinct branches of asterism, Figure 22,

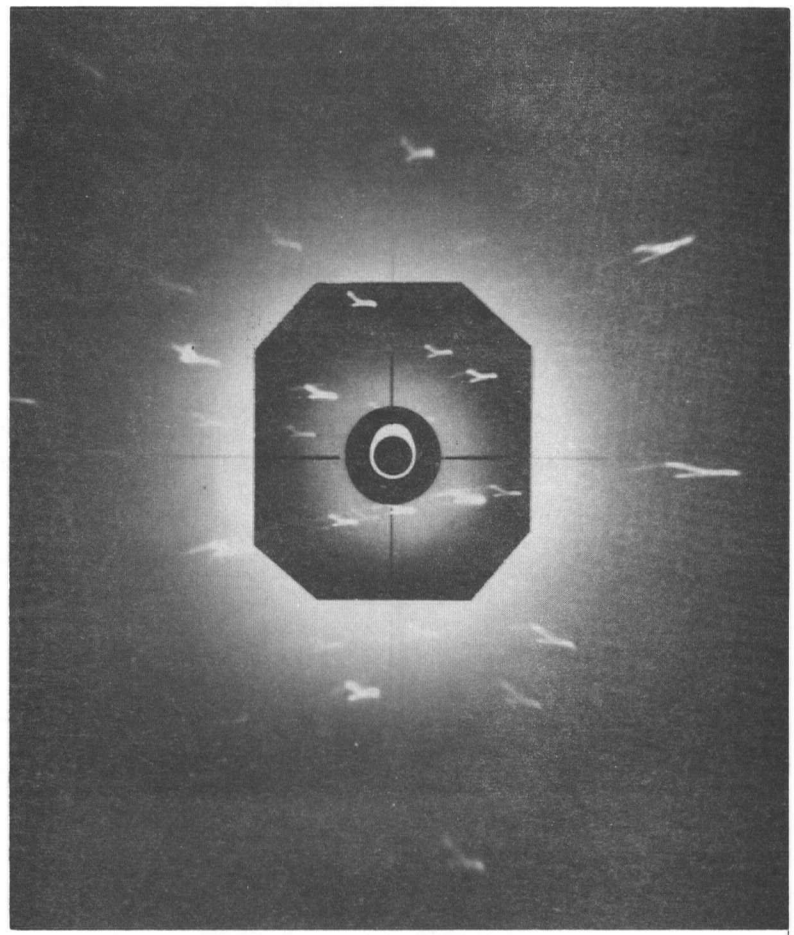

Figure 22. Back-reflection Laue X-ray pattern from surface shown in Figure 19.A.1. Note two branches of asterism.

indicating that deformation on two systems has occurred. The Taylor rotational axis for each branch is determined in Appendix 4 where it is shown that the axes are consistent with slip on the two systems, (011)[100] which is very close to the primary system 1 and (011) $[1\bar{1}1]$, which probably defines system 3. It appears, therefore, that at 77°K, slip wanders slightly in the $[1\bar{1}1]$ direction from strict [100] slip. An examination of Figure 19.A.1 reveals that the straight trace-3 lines are in fact branches of the wavy trace -1 lines.

The variation in the macroscopic slip plane with temperature can now be considered further. It is observed that if the slip plane parameter ψ is plotted against the absolute temperature T, a fairly good straight line connects the points and goes through the origin, Figure 23. It can be seen, too, that if an error of ± 3 degrees was incurred in indexing the slip planes, suitable adjustment would give an even better straight line. In any case several features are worth noting:

(1) The slip surface is generally a non-crystallographic plane in the [001] zone;

(2) The slip surface is not the most highly stressed plane in the [001] zone, except at approximately 220°K, where $\psi = \chi$ for both orientations 1 and 2. Clearly, more information must be gained before it is known with any certainty whether or not the temperature at which $\psi = \chi$ is unique and independent of orientation;

(3) The temperature sensitivity of the slip plane parameter is an increasing function of χ.

In section 2.4.5.3 it will be shown that the slip plane is not a function of ξ, thereby validating comparison (3).

To the author's knowledge, the above results represent the

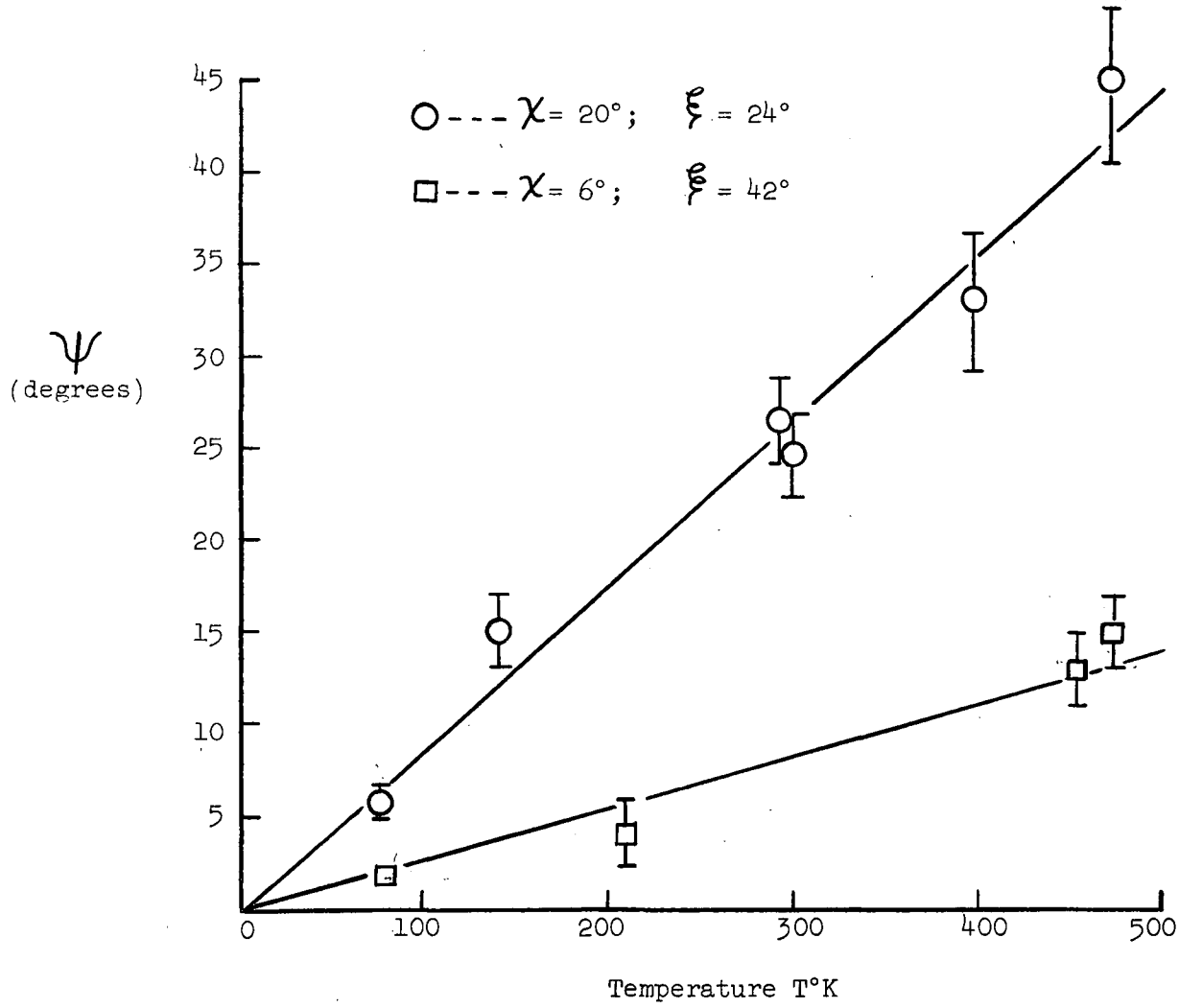

Figure 23. Showing the variation of slip plane parameter ψ with temperature T. ($\dot{\gamma} = 2.5 \times 10^{-3}$/sec)

first documented study of temperature effects in a material exhibiting non-crystallographic slip. Although it is known that bcc metals deform on planes in the $\langle 111 \rangle$ zone and tend to slip on $\{110\}$ planes at low temperatures,[51] the $\psi(T)$ curves have never been reported. A possible reason for this oversight may be that because of the wavy nature of non-crystallographic traces, authors believed that slip traces close to $\{110\}$, $\{321\}$ and $\{211\}$ were actually these planes, since the angle between the planes is quite small (19° and 11° respectively).

2.4.5.2 Strain Rate Dependence

Specimens from orientation 1 were prepared from the same as-grown crystal used in the temperature study and strained a few percent at room temperature at two additional strain rates, $\dot{\gamma} = 1 \times 10^{-5}$/sec and $\dot{\gamma} = 2.5 \times 10^{-1}$/sec, corresponding to cross-head speeds of 0.0002 and 5.0 inch per minute respectively. The slip traces were analyzed and the results are listed in Table 6 which includes for comparison sake the room temperature results from the previous tests where $\dot{\gamma} = 2.5 \times 10^{-3}$/sec. It is readily apparent that the slip plane parameter is strain rate sensitive. As $\dot{\gamma}$ increases, ψ decreases, similar to the effect of decreasing temperature.

TABLE 6

Results of Slip Trace Analyses of Strain Rate Effect on Slip Plane Parameter ψ (T = 293°K)

Orientation (Figure 18) No.	χ	ξ	Test No.	$\dot{\gamma}$ (sec^{-1})	ψ (deg.)
1	20	24	180	1×10^{-5}	33 - 36
			146	2.5×10^{-3}	24 - 29
			135	2.5×10^{-3}	22 - 27
			143	2.5×10^{-1}	20 - 23

Slip plane dependence on strain rate has been observed in Fe- 3% Si single crystals[52] tested at room temperature under three-point bending. At strain rates above 10/sec. only {110} slip was observed whereas at lower strain rates, slip occurred on the most highly stressed plane in the ⟨111⟩ zone. In AuZn it is apparent that the most highly stressed plane in the ⟨001⟩ zone is the slip plane only at intermediate strain rates of approximately 2.5×10^{-1}/sec.

2.4.5.3 Orientation Dependence

The slip plane dependence on orientation has been studied at room temperature and at a strain rate of 2.5×10^{-3}/sec for the specimen orientations shown in Figure 24.

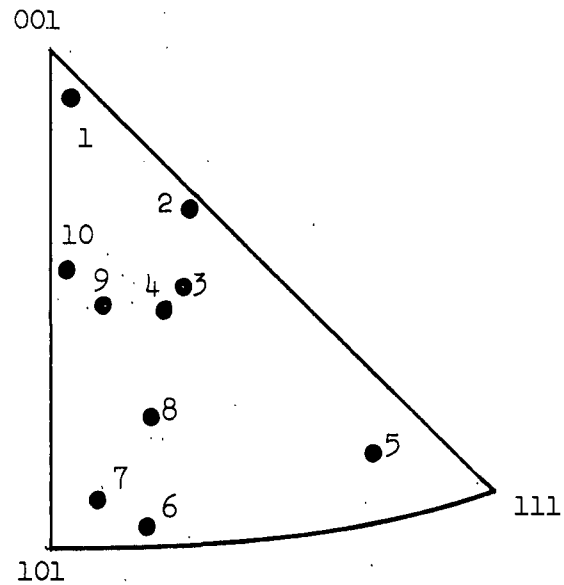

Figure 24. Showing specimen orientations used in slip plane analysis.

For all orientations except No. 1, the primary slip surface was found to be a non-crystallographic plane in the [001] zone. The results of the two-

surface analyses are given in Table 7.

On comparing the slip plane parameters for two orientations of constant χ but differing ξ values (for instance No. 6 and 9, Figure 24) it appears that ψ is independent of ξ, implying that the stress normal to the macroscopic slip plane has negligible effect on the slip surface. The results in Table 7 were therefore plotted as ψ versus χ, Figure 25. The dashed line represents an ideal case of non-crystallographic slip where the macroscopic slip surface is the plane of highest resolved shear stress in the [001] zone. It appears that for orientations near both the [001]-[111] and [001]-[101] boundaries, ideal behaviour is approached whereas for other orientations (approximate limits: $5° < \chi < 40°$) macroscopic slip occurs on less highly stressed planes.

Slip plane dependence on orientation in both tension and compression has been studied in Fe-3% and Fe-6.5% Si single crystals at room temperature,[46,53] in Fe-3% Si at 77°K[47] and in Nb single crystals[45] at 295°K. With reference to slip planes in the <111> zone inclined at an angle ψ' to a reference $\{110\}$ plane, the Fe-Si alloys displayed $\psi'(\chi')$ curves similar to those observed in AuZn but Nb showed preference for either $\{211\}$ or $\{110\}$ slip.

TABLE 7

Results of Slip Plane Analyses of Orientation Effect on Slip Plane Parameter (T=293°K; $\dot{\gamma} \sim 2.5 \times 10^{-3}$/sec.)

Test	Orientation (Ref. Fig. 24)	χ (deg.)	ξ (deg.)	ψ (deg.)
147	2	2	18	2 - 4
-	5	6	42	7*
144	3	15	23	22 - 28
135	4	20	24	24 - 29
146	4	20	24	22 - 27
152	8	28	34	30 - 36
123	6	32	44	34 - 39
138	9	32	22	32 - 37
148	7	38	39	38 - 40
150	10	41	19	41

* Extrapolated from Figure 23.

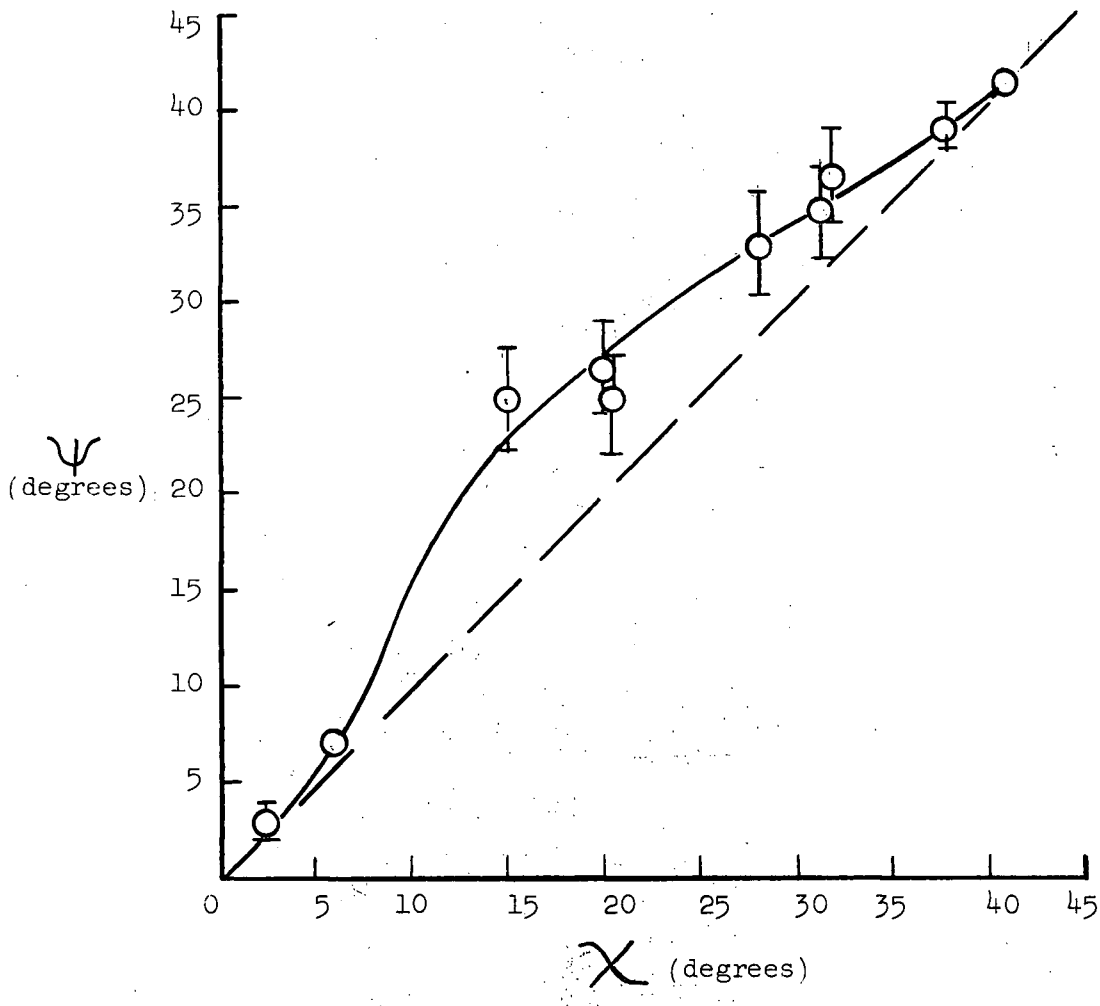

Figure 25. Showing the variation of slip plane parameter ψ with orientation χ. ($T = 293°K$; $\dot{\gamma} = 2.5 \times 10^{-3}$/sec)

Two slip systems, shown in Figure 26, were operative in orientation 6 which is close to the [101]-[111] boundary. On analysis it was found that trace -2 belonged to the [001] zone and consequently the corresponding slip plane parameter, ψ = 34 to 39 degrees, was listed in Table 7; trace -1 belonged to the [100] zone, falling ~39 degrees from (011) and 6 degrees from (001). The reason both [001] and [100] zonal slip

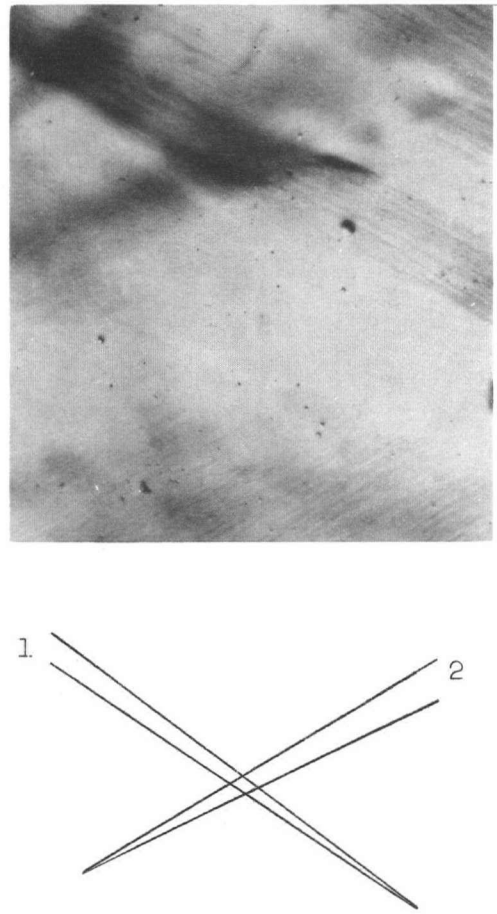

Figure 26. Showing duplex slip in crystal oriented along 101-111 boundary. (orientation 6, Figure 24)

occurs along the boundary [101]-[111] and single [001] slip occurs along [001]-[111] becomes apparent when one considers the variation in Schmid factor on systems of the form $\{110\}\langle 001\rangle$. Although this system is a special case of non-crystallographic $\langle 001\rangle$ slip, it can be considered to illustrate the point at hand if it is assumed that the fundamental planes on which dislocations move are of this form.

Unlike the case of $\{111\}\langle 110\rangle$ slip in fcc metals a specific system of the form $\{110\}\langle 001\rangle$ is not limited to orientations within one of the 24 primary stereographic triangles; instead, each system operates within two adjacent triangles equivalent to a stereographic quadrangle, Figure 27. It can be seen that along the [001]-[111] tie-line, (110)[001] is the most highly stressed system giving rise to the observed traces of that form. Along [101]-[111] both (110)[001] and (011)[100] are equally stressed which is consistent with the observation that both [001] and [100] zonal slip is active in these orientations.

The remaining primary slip systems to be reported are those active in the near [001] orientations. Multiple slip shown in Figure 28 has been observed in orientation 1 and is of a completely different nature from that observed in other orientations. Strain markings are coarse and not as evenly spread throughout the gauge section as were those in other orientations. The markings shown in Figure 28 are typical of a localized area near the middle of the gauge. From two-surface analysis, it was found that the most prominent set, trace -1, was within 2 degrees of $(\bar{1}\bar{1}2)$. Because of uncertainties in pairing, the extra traces were indexed from single surface analyses; trace -2 was found to be consistent with either $\{211\}$ or $\{110\}$ and trace -3, with $\{321\}$. To determine the slip direction associated with the most prominent markings, a cylindrical specimen was

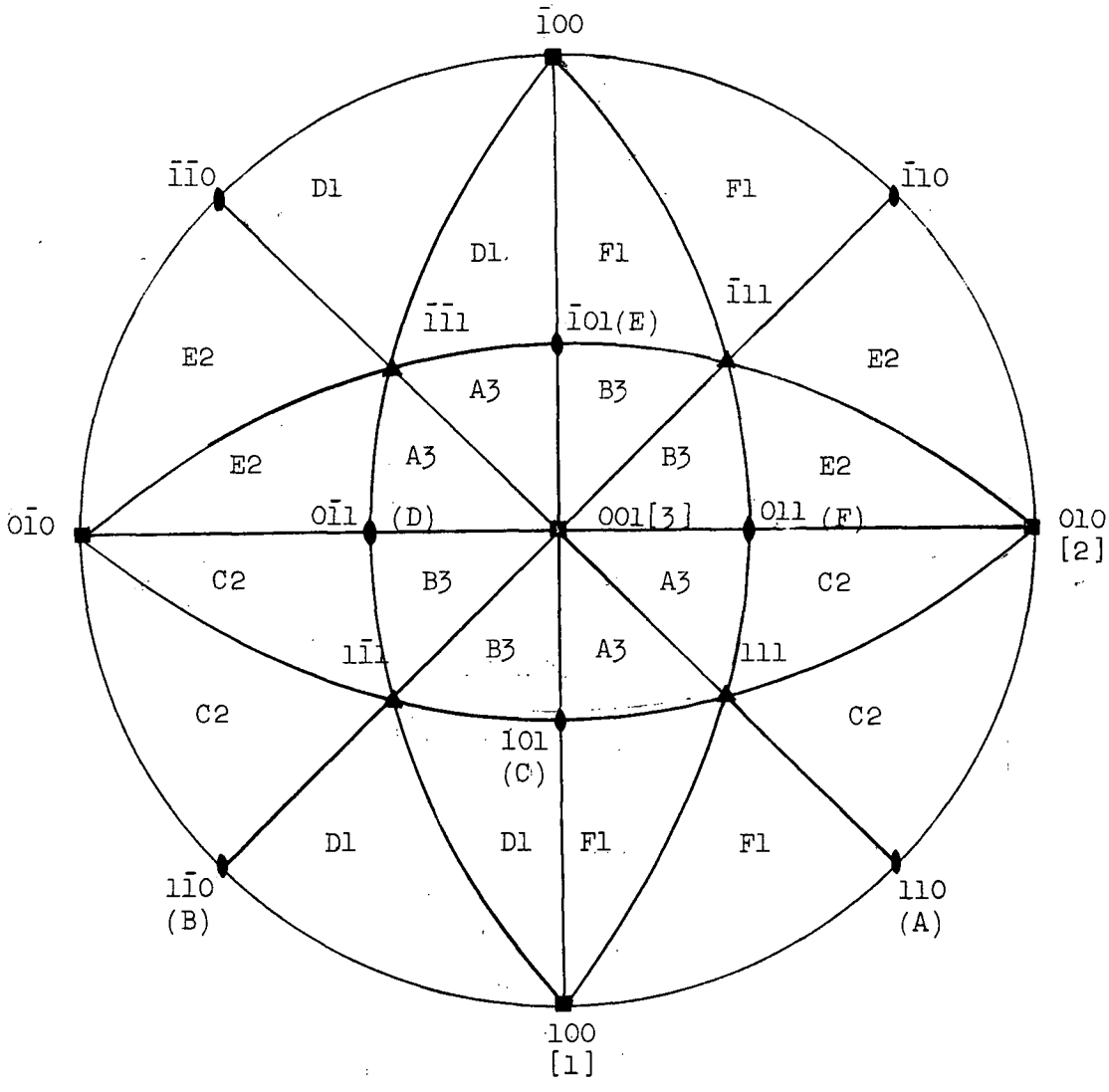

Planes		Directions	
A	(110)	1	[100]
B	($1\bar{1}0$)	2	[010]
C	(101)	3	[001]
D	($0\bar{1}1$)		
E	($\bar{1}01$)		
F	(011)		

Figure 27. A (001) stereographic projection showing the most highly stressed system of the form {110} <001> as a function of orientation.

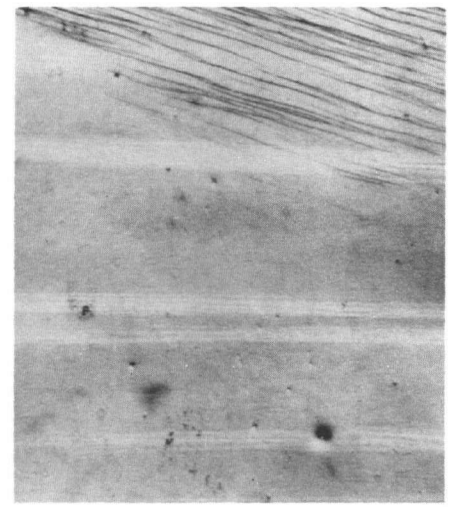

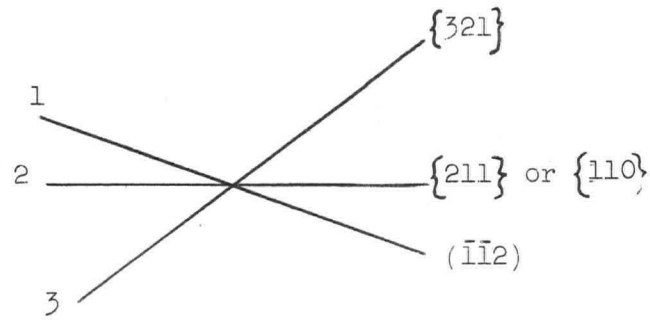

Figure 28. Multiple slip observed in near [001] orientations. (No. 1, Figure 24)

prepared and strained until $(\bar{1}\bar{1}2)$ traces were easily detected. The position round the specimen axis at which the slip traces disappeared was noted then indexed from a back-reflection Laue X-ray pattern since in this position the Burgers vector lying in $(\bar{1}\bar{1}2)$ is parallel to the specimen surface. The cross product of the slip-plane normal $[\bar{1}\bar{1}2]$ and the specimen-surface normal $[1\bar{1}0]$ gave the slip direction, i.e.

$$[\bar{1}\bar{1}2] \times [1\bar{1}0] = [111]$$

It is therefore concluded that the most prominent slip system in orientation 1 is $(\bar{1}\bar{1}2)[111]$. It should be noted that these traces are rather wavy suggesting that $(\bar{1}\bar{1}2)$ may not be an elementary plane on which dislocations move but a macroscopic slip plane made up of composite slip on other, more fundamental, [111] zonal planes.

2.4.5.4 Composition Dependence

Although a complete study of composition effects on the slip plane parameter ψ was not undertaken, a few experiments were performed on Au-rich (51.0 at % Au) and Zn-rich (49.0 at % Au) crystals. Essentially no composition dependence was detected, and therefore, further experiments were abandoned. Composition effects have been reported in Fe-Si alloys where increased Si content from 3.0 to 6.5 wt. % increased the tendency for $\{110\}\langle 111\rangle$ crystallographic slip.[53] However, because of an ordering reaction reported in Fe-Si at approximately 5.5% Si,[54] the nature of the composition effect is not known.

2.4.6 Discussion

It is now possible to compare the primary deformation modes in β' AuZn with those operative in systems of different and similar structures. The non-crystallographic nature of the $\langle 001\rangle$ zonal slip is

distinctly different from the octahedral {111}<110> slip systems observed in fcc metals and ordered alloys Cu_3Au[55] and Ni_3Al,[56] different from cube {100}<110> slip observed in Al[57] and Ni_3Al[56], and different from the generally observed {321}<111>,[26,38,39] {211}<111>[40] and {110}<111>[40] crystallographic slip in the bcc ordered alloy AgMg. The observed non-crystallographic slip closely resembles the <111> zonal slip in bcc metals CuZn,[44] Ta[9,48], Cr[23] W,[58] Fe,[11] Fe-Si alloys, partially ordered FeCo[36] and ordered Fe_3Al,[59] and is very much the same as the {210}, {310} and {100} dislocation traces observed in thin films of NiAl during transmission electron microscopy studies.[29] The systems {211}<111> and {110}<111> observed in AuZn under the special testing conditions mentioned are typical of the more commonly reported slip modes in bcc metals and ordered alloys. Both <001> and <111> zonal slip will now be considered in more detail.

2.4.6.1 <001> Zonal Slip

The immediate task arising from the observation of non-crystallographic slip is to distinguish between the macroscopic slip planes, which are the planes observed under the optical microscope, and the fundamental slip planes, which should be the planes on which individual dislocations move. In bcc metals three views are prevalent; first, elementary slip planes are generally non-crystallographic;[60] second, they are only {110} planes and different macroscopic slip planes are the result of composite slip on {110} planes;[61] and third, the elementary planes are {110} as well as {211} planes and different macroscopic slip planes are the result of composite slip on both types of crystallographic planes.[62,51] Adopting the third approach Kroupa and Vitek[51] have quite successfully calculated the $\psi(\chi)$ curve for an Fe- 3% Si alloy based on a thermally activated cross-slip model of dissociated screw dislocations. Considering

screw dislocation partials lying in sessile configurations on {110} and {211} planes, they show that the thermal energy necessary to transform the sessile configurations into glissile ones, bowed out onto {211} and {110} glide planes decreases as the force on the partials, due to an applied shear stress, increases. In this way, as the position of the tensile axis varies, so does the force on individual partials and as a result, some recombinations are more likely than others. Consequently, the macroscopic slip plane, which is believed to be governed by the motion of recombined screw dislocations, is orientation sensitive.

Ball and Smallman[29] have suggested that the {210}, {310} and {100} slip traces observed in NiAl are the result of continual cross-slip of screw dislocations on orthogonal {110} planes, shown schematically in Figure 29. Combining this general description of non-crystallographic <001> slip with the dissociated screw dislocation concept of Kroupa and Vitek, an attempt will be made to obtain a more detailed account of <001> zonal slip in β'AuZn. That {110} planes are believed to be the elementary slip planes was deduced from the observations that ψ degenerates to zero at very low temperatures (and presumably high strain rates) and small χ values; that thermally activated cross-slip of screw dislocations governs the macroscopic slip plane is concluded from the pronounced influence of temperature and deformation rate on the slip plane parameter ψ.

The possibility of splitting of <001> dislocations in bcc metals has recently been discussed by Vitek.[63] Using isotopic elasticity theory, he found that dissociations of the dislocation <001> according to the reaction:

$$a\langle 001\rangle = a/8\langle 0\bar{1}1\rangle + a/8\langle 017\rangle \qquad (15)$$

are stable for an arbitrary orientation of the dislocation line in all bcc metals studied, ranging from Li and β brass with anisotropy ratios A (where

A is defined[31] as the ratio of the shear modulus on the $\{100\}\langle 001\rangle$ system to that in $\{110\}\langle 110\rangle$ and is given as $2C_{44}/(C_{11}-C_{12})$ of 9.4 and 8.8 respectively to Nb with a ratio of 0.5. Furthermore, Vitek found that dissociations of the type:

$$a\langle 001\rangle = a/8\langle 1\bar{1}0\rangle + a/4\langle 1\bar{1}2\rangle + a/4\langle \bar{1}12\rangle + a/8\langle \bar{1}10\rangle \qquad (16)$$

are stable only for an edge dislocation; for an arbitrary orientation of the dislocation line they are stable only in Li, β-brass, Na and K; i.e., those metals which possess an extremely high anisotropy factor. Since the anisotropy factor for β' AuZn is 3.3 (calculated from elastic stiffness constants given by Schwartz and Muldawer[64]), reaction(15)applies but reaction(16)for the case of screw dislocations is doubtful. Reactions(15) and(16)are sketched in Figure 30.

Considering reaction(15)in more detail it is seen that the extended dislocation defines a fault on a $\{100\}$ plane. Since the fundamental slip plane is believed to be a $\{110\}$ plane, dissociation(15)renders dislocations sessile with respect to $\{110\}$ motion. In order to find the average motion of screw dislocations which governs the slip geometry it is then necessary to study the transformation of the sessile dislocation into a dislocation glissile on $\{110\}$ planes as a thermally activated event in a stress field. The important parameters that must be determined are the activation energy for the sessile-glissile transformation and the distance travelled by the dislocation during an activation event.

If the sessile-glissile transformation is considered as the reverse of reaction(15)plus the bowing out of the recombined length on a $\{110\}$ glide plane, then the activation energy is the sum of the constriction energy U_c, the recombination energy U_r and the increase in the line energy due to bowing of the dislocation ΔU_L minus the work done by the

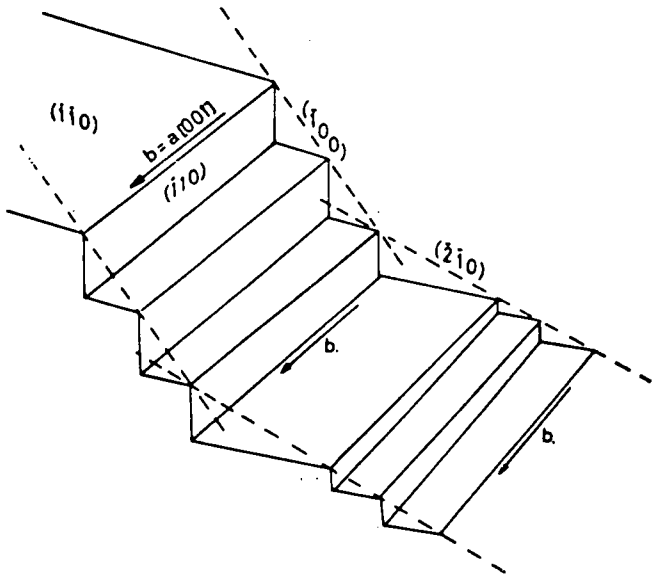

Figure 29. Schematic representation of continual cross-slip on orthogonal {110} planes. (After Ball and Smallman[29])

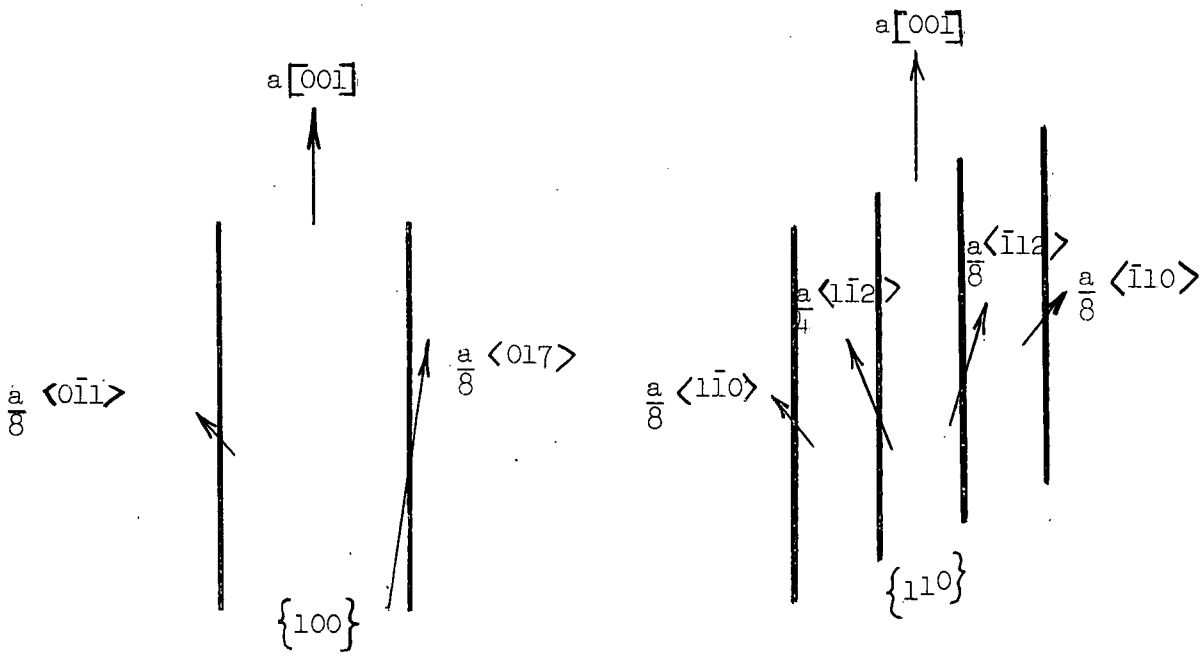

Reaction (15)

$$a\langle 001\rangle = \frac{a}{8}\langle 0\bar{1}1\rangle + \frac{a}{8}\langle 011\rangle$$

Reaction (16)

$$a\langle 001\rangle = \frac{a}{8}\langle 1\bar{1}0\rangle + \frac{a}{4}\langle 1\bar{1}2\rangle + \frac{a}{4}\langle \bar{1}12\rangle + \frac{a}{8}\langle \bar{1}10\rangle$$

Figure 30. Schematic representation of dissociation reactions (15) and (16).

local stress $\tau^{*} = (\tau_a - \tau_H)$ acting on the $\{110\}$ plane in the direction of the Burgers vector, where τ_a is the resolved shear stress and τ_H is the back stress acting on the glide plane. Entropy assistance is neglected. The transformation sequence is illustrated in Figure 31. Because the glissile dislocation is believed to be a $\langle 001 \rangle$ unstable dislocation, it is assumed that the distance of glide on the $\{110\}$ plane will be equal to the bowing-out distance. Consequently it is assumed that the transformations of the sessile into the glissile configuration and vice versa are continually repeated for the occurrence of plastic flow.

In the [001] zone, the most probable elementary glide plane, either (110) or $(1\bar{1}0)$, will be determined by the activation energy necessary for cross slip from the (100) and (010) planes onto the (110) and $(1\bar{1}0)$ planes which in turn depends on the effective stress acting on the glide planes. The probability p for activation is given by:[65]

$$p = e^{-\Delta G/kT} \tag{17}$$

where ΔG is the Gibbs free energy of activation and k and T have their usual meaning. ΔG is that energy which must be supplied by a thermal fluctuation of the dislocation before the transformation is completed. The average number of activation events $\bar{N}$ on the (110) plane before an event occurs on the $(1\bar{1}0)$ plane is then given by the probability ratio:

$$\bar{N} = \frac{p_{110}}{p_{1\bar{1}0}} = e^{-[\Delta G_{110} - \Delta G_{1\bar{1}0}]/kT} \tag{18}$$

where subscripts 110 and $1\bar{1}0$ refer to the two planes of interest.

The average motion of the screw dislocations can then be considered to be composed of $\bar{N}$ units of slip on the (110) plane followed by one unit of slip on the $(1\bar{1}0)$ plane. The unit of slip on each plane is

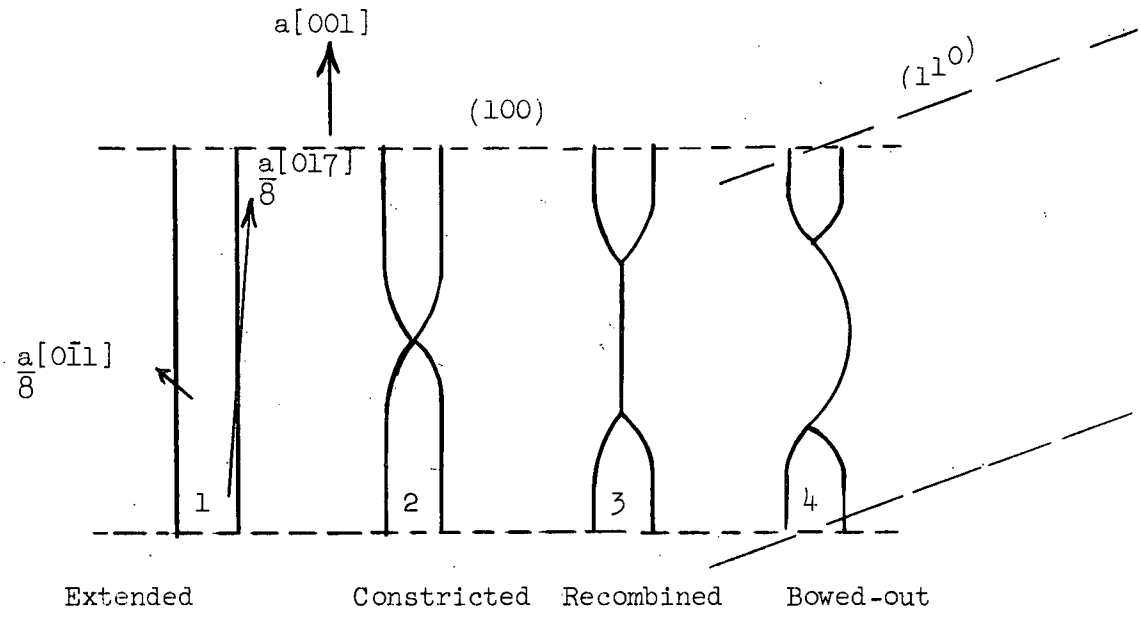

Figure 31. A sketch of the sessile to glissile transformation sequence.

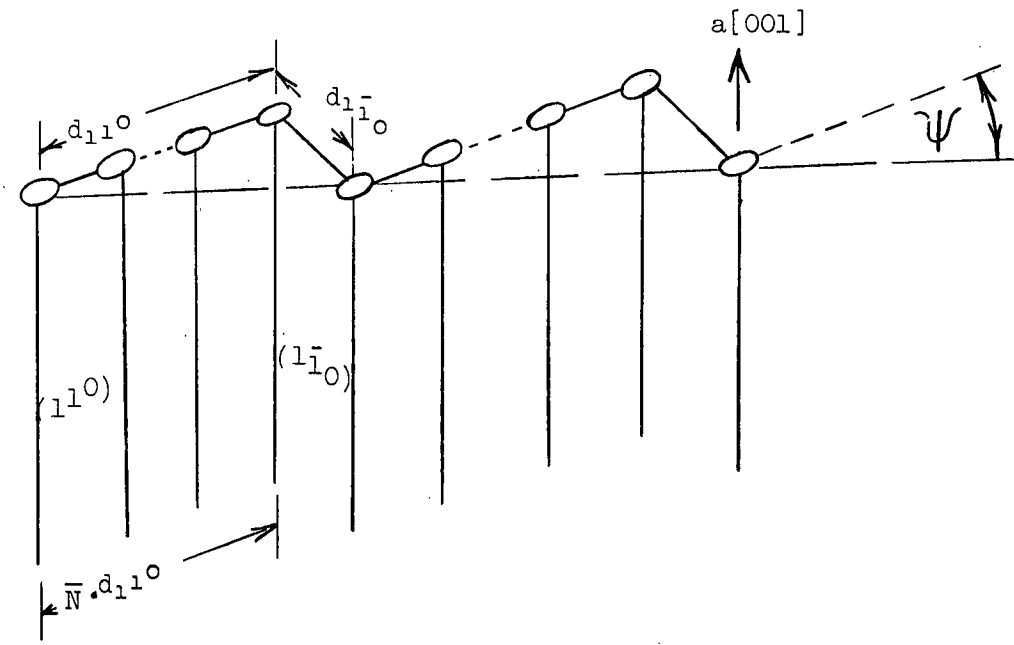

Figure 32. Schematic illustration of the continual cross-slip cycle defining the slip plane parameter ψ. The circled regions represent the transformation sites (i.e. sessile to glissile and vice versa).

given by the bowing-out distance d, which is related to the local stress on the two planes. This "cycle" is shown diagramatically in Figure 32, where it is apparent that the slip plane parameter ψ can be given by the relationship:

$$\tan\psi = \frac{d_{1\bar{1}0}}{\bar{N}\cdot d_{110}} \tag{19}$$

In order to account for the dependence of ψ on temperature, strain rate and orientation, the parameters $\bar{N}$ and d must be expressed in terms of T, $\dot{\gamma}$ and χ. (Note: χ specifies the orientation dependence since ξ was observed to have negligible effects.) Because the effects of temperature and strain rate are believed to be similar, ψ need be expressed only as a function of temperature and orientation.

It can be shown that the free energy of activation for the sessile-glissile transformation critical for the nucleation of cross slip is given by the expression:[65]

$$\Delta G = U_c^{**} + \frac{1}{\tau^* b}\, 2\left((\Gamma_g - \Gamma_s)^3\, \Gamma_g\right)^{\frac{1}{2}} \tag{20}$$

where b is the Burgers vector of the screw dislocation [001], Γ_g is the line tension of the perfect dislocation and Γ_s is the line tension of the extended dislocation. It should be noted that since an entropy term does not appear in equation (20), ΔG is really an activation enthalpy. The corresponding value of d is given by the expression:[65]

$$d = \frac{\Gamma_g - \Gamma_s}{\tau^* b} \tag{21}$$

On substituting (18), (20) and (21) into (19) it is found that:

$$\tan\psi = \frac{\tau^*_{1\bar{1}0}(\chi)}{\tau^*_{\bar{1}\bar{1}0}(\chi)}\, e^{\frac{-A}{T}\left[\frac{1}{\tau^*_{1\bar{1}0}} - \frac{1}{\tau^*_{\bar{1}\bar{1}0}}\right]} \tag{22}$$

where A is a constant equal to $(2[\Gamma_g - \Gamma_s]^3\, \Gamma_g)^{\frac{1}{2}}$, and

U_c^{**} is the constriction energy

where $\tau^*_{1\bar{1}0}(\chi) = \tau_a^M \cos\chi - \tau_{\eta\,1\bar{1}0}$ (23)

and $\tau^*_{1\bar{1}0}(\chi) = \tau_a^M \sin\chi - \tau_{\eta\,1\bar{1}0}$ (24)

in which τ_a^M is defined as the resolved shear stress acting on the most highly stressed plane on the [001] zone. Since the back stresses $\tau_{\eta\,1\bar{1}0}$ and $\tau_{\eta\,1\bar{1}0}$ are not known, it is difficult to test the validity of equation (22) quantitatively. Qualitatively, however, it is in agreement with the experimental observations. As temperature decreases, $\tan\psi$ and hence ψ tends to zero for a constant value of χ; the exact $\psi(T)$ behaviour cannot be stated since the variation of the local stresses with temperature is not known. As χ increases and approaches 45° the applied stresses and hence the local effective stresses $\tau^*_{1\bar{1}0}$ and $\tau^*_{1\bar{1}0}$ become equal so that $\tan\psi$ approaches unity and ψ approaches 45°. Since $\tau^*_{1\bar{1}0}$ tends to zero as χ approaches zero, equation (22) becomes undefined in this limit and hence cannot be compared with the observation that ψ tends to zero.

The essential feature in this description is the assumption of dissociated screw dislocations. Since stacking fault energies in bcc metals are considered generally to be higher than those in fcc metals, it is likely that fault energies in ordered bcc alloys will be even higher. Consequently the extent of partial dislocation separation may be very small, in which case an anisotropic dislocation core would develop instead of a true faulted plane. Whether or not an anisotropic core offers significant resistance to dislocation motion is not known; the above description assumes it does. The attractive feature, however, is that the description appears to account for the observations.

2.4.6.2 {hkl} <111> Slip

Using a method given by Groves and Kelly[66] for determining the number of independent slip systems in crystals, Ball and Smallman[29] have

recently shown that the continual cross-slip process on orthogonal {110} planes of the <001> zone does not increase the number of independent slip systems in NiAl, leaving only three independent {110}<001> systems to operate. The same result applies to AuZn. Whereas the total ductility to fracture in polycrystalline NiAl decreases abruptly to less than three percent at temperatures below 0.45 Tm,[25,67] total ductility in polycrystalline AuZn remains in excess of ten percent at temperatures as low as 77°K (0.077 Tm).[12] On single surface analyses of slip traces in AuZn grains, general {hko} traces were evident within the grains, and {211} and {321} traces were observed near the boundaries. Since general plasticity of a polycrystalline aggregate necessitates the operation of at least five independent deformation modes,[68] the ductility of polycrystalline AuZn was attributed to slip on the extra {211} and {321} planes.

The single crystal observations are direct proof for the operation of {211}<111> and {110}<111> slip systems in AuZn; the {321} trace is also believed to be associated with <111> slip. Examination of NiAl single crystals compressed along <001> axis revealed no extra slip modes; instead, evidence of kinking was observed[25] similar to that in the iso-structural compounds CsI[69] and CsBr.[69,70] It appears, therefore, that for crystal orientations in which the Schmid factors on the {110}<001> systems are near zero (i.e. the near <001> orientations) CsCl type compounds either slip on <111> zonal planes or undergo kinking. If <111> slip occurs the corresponding polycrystalline aggregates are ductile, but if kinking occurs, the aggregates are brittle.

It remains to be shown whether or not <111> slip can be explained in terms of the three models reviewed earlier, viz. those based on ordering energy per atomic bond, dislocation line energy and atom size

ratio. As pointed out by Rachinger and Cottrell[25] (RC) the fact that ⟨111⟩ slip occurs in a CsCl type superlattice implies that $\frac{a}{2}$ ⟨111⟩ superlattice partials are present connected by a ribbon of stacking fault wider than about one lattice spacing. Obviously, AuZn is a near borderline case between "metallic" and "ionic" bonding nature since the crystal slips in both the "metallic" ⟨111⟩ and "ionic" ⟨001⟩ directions under special testing conditions (77°K; near ⟨001⟩ orientations). AuZn, then, is an almost ideal compound in which to evaluate the RC criterion which states that compounds with ordering energies greater or less than 0.06 ev. per atomic bond slip along ⟨001⟩ or ⟨111⟩ respectively and conversely, those with energies of ~0.06 ev. slip in both directions. However since accurate ordering energies (not estimates using $\frac{kT_{mp}}{4}$) for AuZn are not known at present, the true evaluation of the RC criterion remains to be performed. Therefore, it is impossible to state whether or not ⟨111⟩ slip in the AuZn superlattice can be explained in terms of the critical ordering energy criterion.

It is interesting to compare heats of formation, electronegativity differences and slip directions for several CsCl type compounds, Table 8. If it is assumed that the heats of formation and the electronegativity difference between component species is an indication of the strength of the A-B bond, then it can be seen that bond strength has a direct effect on the slip direction. As a very rough estimate, it appears that compounds having heats of formation greater than ~6000 cal/mole and electronegativity differences (on the A-R scale) in excess of ~0.24, slip along ⟨001⟩ lattice directions whereas those with lower heats of formation and associated electronegativity differences slip along ⟨111⟩. The transition range in which both ⟨001⟩ and ⟨111⟩ slip may occur appears to lie somewhere between formation energies of 4500 to 6000 cal/mole and electronegativity differences of 0.21 to 0.24. Anomalous in this respect is AuCd

TABLE 8

Correlation of Slip Direction with Heats of Formation and Electronegativity Differences in CsCl Type Compounds

Compound	Electronegativity* Difference $\Delta\chi$	Heat of Formation (cal/mole)	ref.	Slip Direction uvw	ref.
NiAl	.28	14000	105	001	29
LiTl	.47	6400	106	001	26
AuZn	.24	6150	107	001 , 111	26, present work
MgTl	.21	5000 to 6500	106	001	26
AuCd	.04	4660	106	001 and possibly 111	26
AgMg	.19	4380	108	111	26, 39, 40
CuZn	.09	2900	106	111	26

*Allred-Rochow[112] Electronegativities for component species used to determine $\Delta\chi$.

with $\Delta\chi \sim 0.04$. Since the Allred-Rochow electronegativity scale is only one of many (used here because it gives the best $\Delta\chi$ -slip direction correlation), it was found that on other scales (Pauling,[109] Mulliken[110]) $\Delta\chi$ for AuCd fell close to AuZn. Qualitative though it is, the above comparison does lend some support to the basic idea of Rachinger and Cottrell that bond strengths play a very important role in determining slip directions in CsCl type compounds.

If the line energy model of Ball and Smallman[29] is to account for both $\langle 001 \rangle$ and $\langle 111 \rangle$ slip directions, then it must be shown that the total energy of the superdislocation (i.e. self-energies of both $\frac{a}{2}\langle 111 \rangle$ partials plus the interaction energy between the partials plus the energy of the stacking fault linking the partials) as well as mobility are very

near the values for the <001> dislocations (Table 4). Accurate computations necessarily require a knowledge of stacking fault energy and width, which are not known for AuZn. Again, quantitative assessments between theory and experiment cannot be performed.

As noted earlier, the relative atom size model of Lautenschlager et al[34] predict <001> slip directions when $\frac{R_A}{R_B}$ approaches 0.732, but <111> when the ratio approaches unity. Clearly there is an intermediate ratio where the model predicts both <001> and <111> slip. Lautenschlager et al calculated $\frac{R_A}{R_B}$ for a series of CsCl type compounds, including AuZn, in the following manner. Given the atomic and ionic radii of each component, lattice parameters for the ordered bcc structures may be calculated assuming both species, in one case, are present as ions and in a second case, as atoms. The measured lattice parameter is then compared with the calculated "ionic" and "atomic" parameters. Assuming a linear relationship between $\frac{R_A}{R_B}$ and lattice parameter, the effective ratio is determined since $\left(\frac{R_A}{R_B}\right)_{ionic}$ and $\left(\frac{R_A}{R_B}\right)_{atomic}$ are known. Calculated in this fashion $R_{Zn/R_{Au}} \sim 0.92$. From their measured variation of $d_\perp$ (defined in section 2.4.1) against R_{A/R_B}, it appears that both <111> and <001> slip directions are favourable when the ratio is in the vicinity of 0.9. The occurrence of both <001> and <111> slip in AuZn is therefore consistent with the predictions based on the atom size ratio.

One further crystallographic feature of <111> slip must be noted. At both 77°K and in near <001> orientations at room temperatures (conditions under which <111> slip was detected) the operative slip plane was close to the maximum resolved shear stress plane in the <111> zone. The Schmid factor was ~0.49 for both the (011) $[1\bar{1}1]$ system operative at 77°K and

the $(\bar{1}\bar{1}2)$ [111] system operative at room temperature. Combined with the fact that the $(\bar{1}\bar{1}2)$ traces were somewhat wavy (Figure 28) these observations tentatively suggest that slip occurs on non-crystallographic planes in the $\langle 111 \rangle$ zone.

2.5 WORK-HARDENING BEHAVIOUR

2.5.1 Flow Parameters

The work-hardening parameters as defined in section 2.2.2 are compiled in Tables 9, 10 and 11 for Au-rich, stoichiometric and Zn-rich crystals respectively (Figures 6, 7, and 8) and Table 12 for Au-rich crystals tested at room temperature in various orientations (Figure 11). The following discussions centre on the variation of the hardening parameters with temperature, composition and orientation.

2.5.1.1 Yield Stress

The temperature dependence of τ_o is illustrated in Figure 33. Points denoted as crosses were obtained from multiple tests on one crystal by subtracting the total work-hardening due to straining at prior temperatures from the yield stress at the test temperature. There is good agreement between yield stresses determined from the work-hardening curves and those determined from multiple tests on one specimen. τ_o for stoichiometric AuZn decreases slightly above 220°K but approximately triples between 220°K and 77°K. For the non-stoichiometric crystals, the general shape of the τ_o-T curve is different. Two regions of weak temperature-sensitivity exist, above approximately 300°K and below about 140°K. From 300°K to 140°K τ_o increases about three times for the Zn-rich crystals but less than two times for the Au-rich alloy. It is also seen that yield stress for Zn-rich crystals displays a second region of temperature sensitivity above approximately 400°K. Similar temperature dependence of yield stress has been found in polycrystalline AuZn.[12]

If the data shown in Figure 33 are used to compare the

TABLE 9

Work-Hardening Parameters for 51.0 at. %Au β' AuZn Single Crystals
($\dot{\gamma} = 2.5 \times 10^{-3}$/sec)

Test	Temp °K	τ_0	τ_1	τ_{11}	τ'_{11}	τ_{111}	τ_m	γ_1	γ_{11}	γ'_{11}	γ_{111}	γ_m	γ_f	θ_1	θ_{11}
		psi						%						psi	
71	77	6700	-	-	-	-	21100	-	-	-	-	-	50	-	20000
72		6400	-	-	-	-	18600	-	-	-	-	-	42	-	17500
79	141	6000	-	-	-	-	17800	-	-	-	-	-	54	-	10800
80		6500	-	-	-	-	21700	-	-	-	-	-	72	-	9300
87	181	5650	10150	14100	-	-	16300	44	106	-	-	-	152	3750	-
88		5140	10150	14300	-	-	17700	50	116	-	-	-	178	3550	-
77	217	3340	8800	12800	13900	-	20700	56	160	202	-	-	270	2500	10000
86		5080	9800	14200	15300	-	23200	44	152	190	-	-	280	2930	8800
84	260	4150	8500	11900	13000	-	22800	46	148	198	-	-	308	2300	8730
85		4020	8500	11900	13000	-	21700	46	148	198	-	-	292	2300	9140
60	293	4220	7600	10500	11600	-	18000	42	152	211	-	-	302	1900	7000
61		3720	7300	10300	11700	-	17500	40	158	232	-	-	312	1900	7180
75	373	3230	7100	8300	8600	11100	11300	29	116	146	194	209	220	1000	5160
76		3410	7100	8300	8500	11000	11100	30	126	150	198	209	228	1000	5260
82	403	3430	6300	7350	7550	9300	9550	14	43	52	76	85	144	2370	7200
83		3800	6600	7700	7800	8900	9250	20	45	49	64	83	97	2500	7000
81	433	3130	-	-	-	7808	8000	-	-	-	-	-	47	-	-
73	488	3100	-	-	-	-	5700	-	-	-	-	-	60	-	-
74		3400	-	-	-	-	5900	-	-	-	-	-	50	-	-

TABLE 10

Work-Hardening Parameters for Stoichiometric β' AuZn Single Crystals
($\dot{\gamma} = 2.5 \times 10^{-3}$/sec)

Test	Temp. °K	τ_o	τ_I	τ_{II}	τ'_{II}	τ_{III}	τ_m	γ_I	γ_{II}	γ'_{II}	γ_{III}	γ_m	γ_f	θ_I	θ_{II}
		psi						%						psi	
7	77	5900	-	-	-	-	16000	-	-	-	-	-	46	-	22400
8	77	5800	-	-	-	-	19700	-	-	-	-	-	70	-	23200
9	153	2880	5000	9000	-	-	14500	30	72	-	-	-	154	4700	-
10	153	2530	4000	8000	-	-	12000	20	60	-	-	-	110	5600	-
183	183	2300	4800	7150	8700	-	12700	30	86	147	-	-	195	2500	-
3	223	1960	3600	4400	5300	18700	21400	16	60	90	258	-	316	2000	7700
4	223	1410	2500	4600	5200	17000	20900	20	90	120	260	-	340	2200	8500
5	293	1880	3300	4500	5100	9400	13100	14	50	65	144	-	292	2900	5170
6	293	1540	2400	4500	5000	8700	12500	10	70	87	158	-	352	3000	5120
20	373	1890	-	-	-	5800	7500	12	-	-	94	250	290	-	2300
21	373	1780	-	-	-	5700	8000	10	-	-	88	220	243	-	2400
18	443	1830	-	-	-	-	4900	-	-	-	-	80	122	-	-
19	443	1820	-	-	-	-	4600	-	-	-	-	80	160	-	-

TABLE 11

Work-Hardening Parameters for 51.0 at.% Zn β' AuZn Single Crystals
($\dot{\gamma} = 2.5 \times 10^{-3}$/sec)

Test	Temp. °K	τ_0	τ_1	τ_{II}	τ'_{II}	τ_{III}	τ_m	γ_1	γ_{II}	γ'_{II}	γ_{III}	γ_m	γ_f	θ_1	θ_{II}
		psi						%						psi	
95	77	8200	-	-	-	-	24500	-	-	-	-	-	18	-	-
96	77	8850	-	-	-	-	24600	-	-	-	-	-	18	-	-
101	140	8510	-	-	-	-	28300	-	-	-	-	-	80	-	16700
102	140	7670	-	-	-	-	23800	-	-	-	-	-	50	-	16500
99	192	5190	10600	14700	-	-	19700	52	110	-	-	-	190	3700	-
100	192	4130	10400	14300	-	-	16500	52	98	-	-	-	140	3890	-
97	243	4420	10000	10600	10800	16200	17700	40	94	-	180	247	256	2000	7300
98	243	4370	12000	12500	-	17800	19000	50	-	-	140	200	222	-	10000
89	293	3220	7800	8500	-	13100	14300	26	70	-	218	260	274	290	3870
90	293	4000	8200	8500	-	14700	15100	20	70	-	224	240	245	420	4050
103	348	2780	6600	7600	7600	9450	10200	28	79	80	104	138	156	1200	7780
104	348	3040	6500	7400	7400	9450	9850	42	78	80	106	122	132	1100	7700
91	373	2510	5200	5900	6050	8200	9200	14	40	52	64	90	150	1620	17000
92	373	3320	6500	7100	7400	9700	10000	12	38	55	72	90	146	1640	13600
105	408	2840	-	-	-	-	6200	-	-	-	-	22	175	-	-
106	408	3250	-	-	-	-	5700	-	-	-	-	20	152	-	-
93	473	2510	-	-	-	-	3450	-	-	-	-	12	225	-	-
94	473	2240	-	-	-	-	3500	-	-	-	-	12	218	-	-

TABLE 12

Work-Hardening Parameters as a Function of Orientation for β' AuZn Single Crystals
(T = 293°K; $\dot{\gamma}$ = 2.5 x 10^{-3}/sec; 51.0 at.%Au)

Test	Orientation (Fig. 11)	χ	ξ	τ_0	τ_I	τ_{II}	τ_{II}'	τ_{III}	τ_m	γ_I	γ_{II}	γ_{II}'	γ_{III}	γ_m	γ_f	θ_I	θ_{II}
				psi						%						psi	
115	1	6	46	3700	8300	11700	14000	-	23800	56	120	210	-	-	340	2720	7920
116				4120	8500	12200	14000	-	24000	56	140	210	-	-	340	2740	7920
121	2	13	49	4160	-	-	-	18500	20400	-	-	150	220	-	300	-	-
122				3910	-	-	-	16400	21400	-	-	100	126	-	250	-	-
119	3	30	46	3650	-	-	-	12000	17100	-	-	-	35	-	124	-	-
120				3700	-	-	-	11300	19800	-	-	80	24	-	152	-	-
117	4	36	44	4000	-	-	-	12800	19400	-	-	86	24	-	160	-	-
118				3740	-	-	-	11700	16200	-	-	-	35	-	185	-	-
60	5	14	26	4220	7600	10500	11600	-	18000	42	152	211	-	-	302	1900	7000
61				3720	7300	10300	11700	-	17500	40	158	232	-	-	312	1900	7180
25	6	18	31	3900	7800	10600	11200	-	17000	54	148	180	-	-	280	1800	5800
137	7	32	23	3000	7400	9400	9800	13600	14400	34	110	132	214	260	285	1850	5000
67	8	12	12	3980	7500	10100	10200	-	15300	30	62	66	-	-	158	3900	5850
68				3980	7400	10000	10100	-	15200	30	62	66	-	-	158	3900	5850
139	9	16	10	3700	6400	8000	8300	11800	12500	14	50	60	126	154	164	3600	5600
69	10	15	5	33500	-	-	-	-	45000	-	-	-	-	-	10	-	-
70				36500	-	-	-	-	49500	-	-	-	-	-	18	-	38500

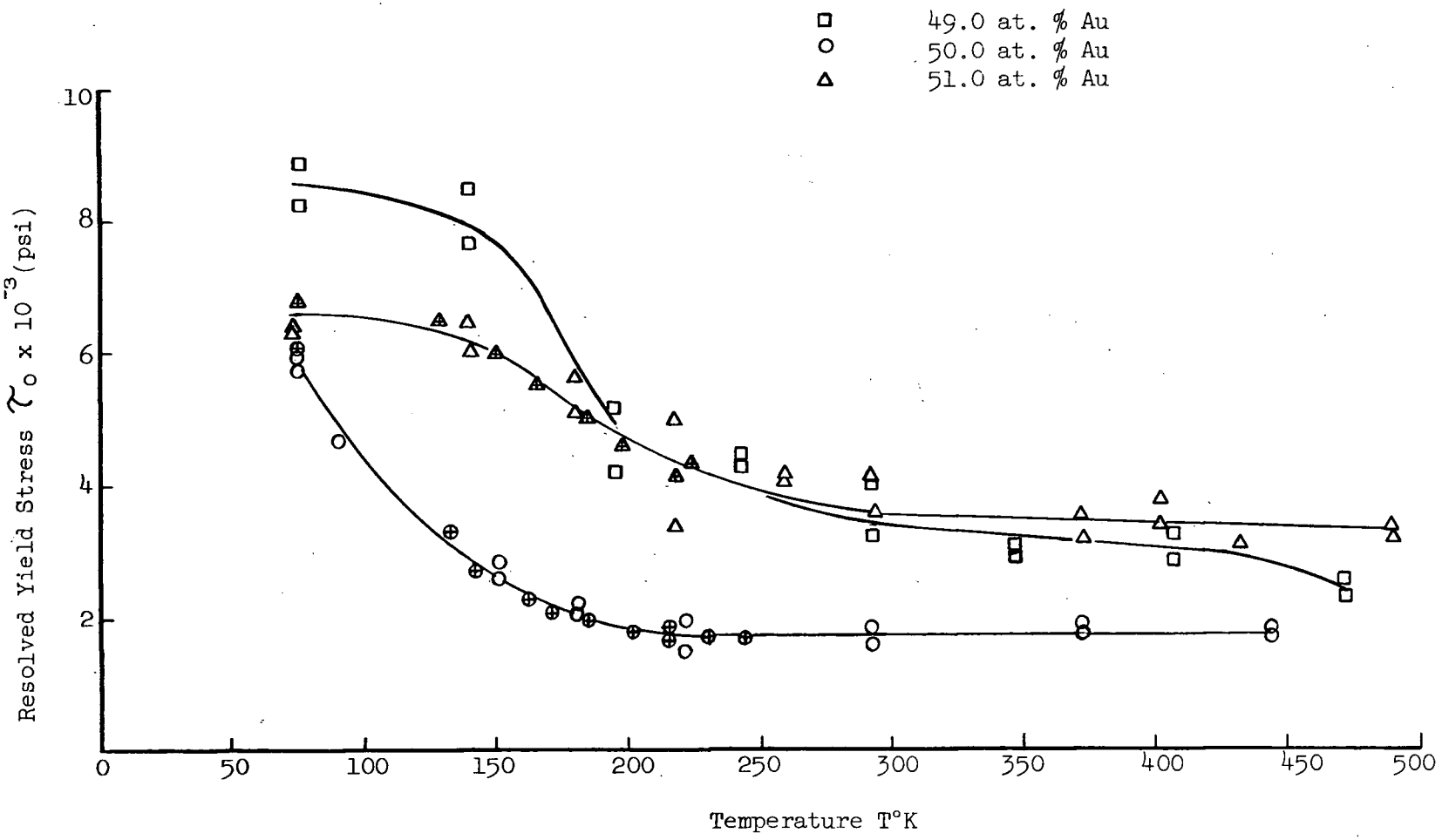

Figure 33. Showing the variation of yield stress with temperature for Au-rich, Stoichiometric and Zn-rich β' AuZn single crystals.
($\dot{\gamma}$ = 2.5 x 10^{-3}/sec; $\varphi \sim 26°$, $\chi \sim 20°$)

strengthening effect of the excess Au and Zn, it is seen that at temperatures above approximately 200°K both species impart similar hardening of ~1700 psi/at. % whereas below 200°K Zn appears to be the more potent strengthening agent. For example, at 150°K, $\Delta\tau$/at. % deviation is ~5100 psi for Zn-rich crystals and 3400 psi for Au-rich while at 77°K, is ~2700 for Zn-rich and only 500 psi for Au-rich. In polycrystalline material, Causey[12] found that hardening above 133°K was approximately equal on both sides of stoichiometry with $\frac{\Delta\sigma}{\Delta C}$ ~9000 psi/at.% for Zn-rich alloys and ~7500 psi/at. % for Au-rich alloys; at 77°K a pronounced minimum exists at ~50.5 at. % Au so that the hardening per at. % deviation from stoichiometry is considerably less for Au-rich than Zn-rich alloys. It appears, therefore, that the effects of deviations from stoichiometry on yield stress are the same in single and polycrystalline AuZn.

Since the absolute melting point of AuZn is 998°K the homologous temperature is directly proportional to temperature in degrees K. Over the same range of homologous temperatures 0.08 T_m to 0.5 T_m single crystals of stoichiometric AgMg[100,101] and NiAl[25,37] were observed to display yield stress variations similar to AuZn increasing approximately three times in the temperature interval .25 T_m to .08 T_m. Polycrystalline AgMg[13,38], NiAl[25,67] and NiTi[67] exhibited comparable yield stress temperature dependence. In general the behaviour is similar to bcc metals (for review see Conrad[94]) although the dependence is not quite as strong. The temperature dependence of yield will be further considered in the light of thermally activated deformation mechanisms, Section 2.6 of the thesis.

The orientation dependence of τ_o resolved on the macroscopic slip plane in the [001] direction is shown in Figure 34. Although some scatter in the results is evident, it appears that τ_o is approximately

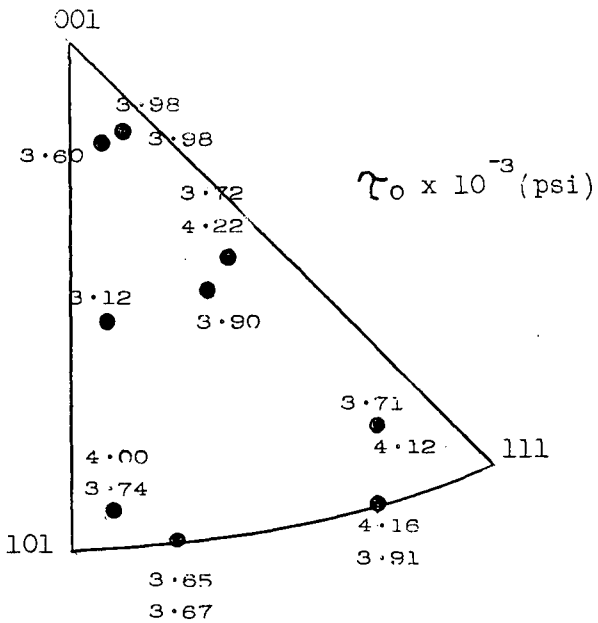

Figure 34. Showing the resolved yield stress dependence on orientation. (51.0 at. % Au; T = 293°K)

independent of orientation and may be given as ~3850 psi. The significance of these observations and their relation to the variation in slip plane parameter Ψ with orientation is discussed in section 2.5.4.1.

The value of τ_o in orientation 10 (Figure 11) was resolved on the operative $(\bar{1}\bar{1}2)[111]$ system and found to be ~35000 psi which is about nine times higher than τ_o for $\{hko\}\langle 001\rangle$ slip. It is believed that the (hko)[001] deformation mode that might be expected to operate was suppressed in orientation 10 because of the geometry of the test specimens. In Figure 35 it is shown that for the given specimen diameter/gauge length ratio of 0.1 grip constraints do not allow [001] slip for orientations in which ξ is less than approximately 6°. In orientation 10 where ξ is 5°, [001] slip is thus restricted. It can be seen, too, from Schmid factor and resolved shear-stress calculations that slip on the second most highly stressed $\{hko\}\langle 001\rangle$ system, namely (okl)[100], was not as favourable as slip on the observed system. For the given orientation 10 the Schmid factor on a representative (okl)[100] system taken as (011)[100] is 0.05 while the factor on $(\bar{1}\bar{1}2)[111]$

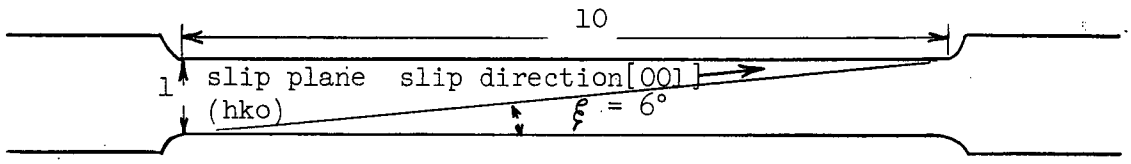

Figure 35. Showing effect of specimen geometry on inhibiting (hko)[001] slip.

is 0.48, a difference of 9.5 times. This is greater than the difference of about 9 times in critical resolved shear stress for slip on the two systems. Although $(\bar{1}\bar{1}2)[111]$ is the most prominent system it was observed in Figure 28 that some $\{110\}$ slip may have occurred as well. The occurrence of this extra mode can most likely be accounted for by the fact that stress on the (011)[100] system probably becomes critical in the initial hardening stages past yield.

2.5.1.2 The Work-Hardening Rate in Stage I, θ_1

The work-hardening rates during stage I deformation θ_1, are shown in Figure 36 for the three compositions tested where the results are plotted as θ_1/μ, where μ is the shear modulus characteristic of the operative slip system $\{hko\}\langle 001\rangle$. Shear modulii have been calculated as a function of slip system in Appendix 5. It is apparent that θ_1 is a minimum at intermediate temperatures of $\sim$210°K, 295°K and 370°K for the stoichiometric, Zn-rich and Au-rich crystals respectively. The variation of θ_1 with temperature appears to be linear for the non-stoichiometric crystals. In fcc metals, stage I hardening rates have been observed to either increase slightly,[16,83] remain constant[135,139] or decrease slightly[140] in a monotonic

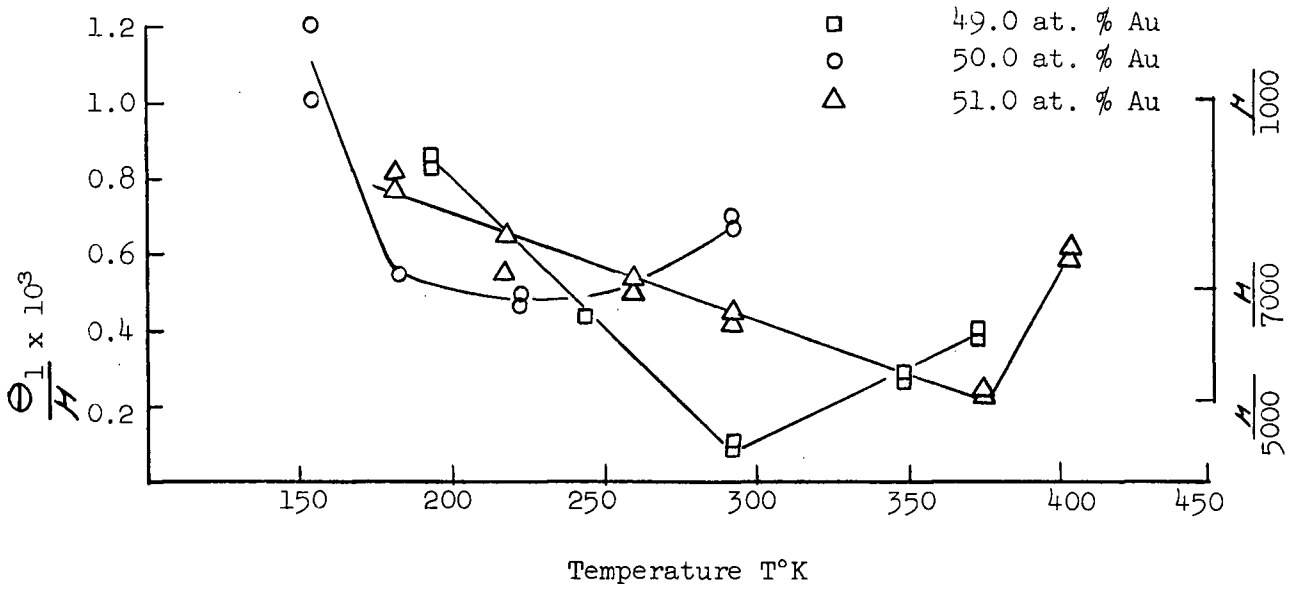

Figure 36. Showing the variation in stage I work-hardening rate Θ_1 with temperature.

fashion with increasing temperature, while in bcc crystals Nb[1] and Ta[9], Θ_1 was found to increase with increasing temperature, from near zero at ~.08 T_m. The slope of the Θ_1-T curves in AuZn crystals is similar to Nb and Ta and considerably stronger than fcc metals. The occurrence of a minimum hardening rate at intermediate temperature appears to be unique.

The very low values of Θ_1 about room temperature for Zn-rich crystals is believed responsible for the wavy nature of the corresponding flow curves (Figure 8). What probably happens is that early in the test, some part of the gauge section deforms at a slightly faster rate than the rest. The cross-sectional area in this region becomes slightly smaller than in the rest of the specimen giving rise to a corresponding increase in the shear stress. Since the rate at which slip planes harden with increasing strain is low, then continued slip in this reduced section will occur more easily than in the remainder of the specimen. In this manner localized

thinning occurs along the gauge analogous to a necking mechanism. Once the primary slip planes harden to such an extent that further slip requires an applied tensile stress greater than is necessary to promote new slip packets, deformation in the localized area ceases. A new "neck, is formed and the procedure repeats itself until the gauge section is uniformly thinned.

The dependence of Θ_1 on initial orientation is shown in Figure 37. While insufficient experiments were performed to permit unambiguous comments on orientation effects, it is noted that the hardening rate near the

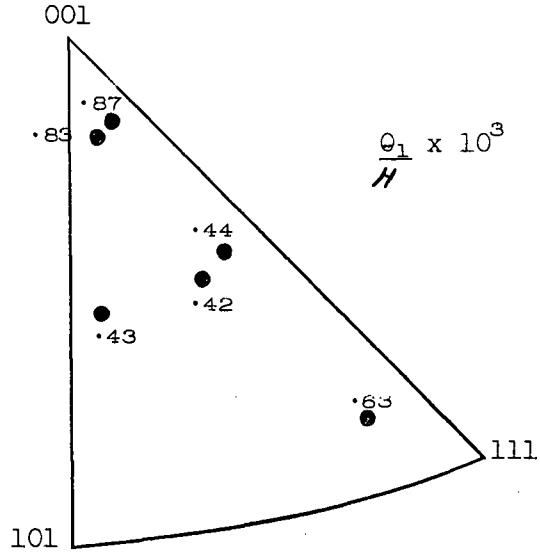

Figure 37. Showing the variation in stage I work-hardening rate with orientation. (51.0 at. % Au; T = 293°K)

[001] corner is approximately two times greater than that near the middle of the stereographic triangle.

2.5.1.3 The End of Stage I

The strain at the end of easy glide γ_{11} is shown in Figure 38. The extent of stage I is considerably greater for non-stoichiometric compositions by the approximate ratios of 2:1$\frac{1}{2}$:1 for Au-rich, Zn-rich and stoichiometric crystals respectively. Similar effects have been observed on

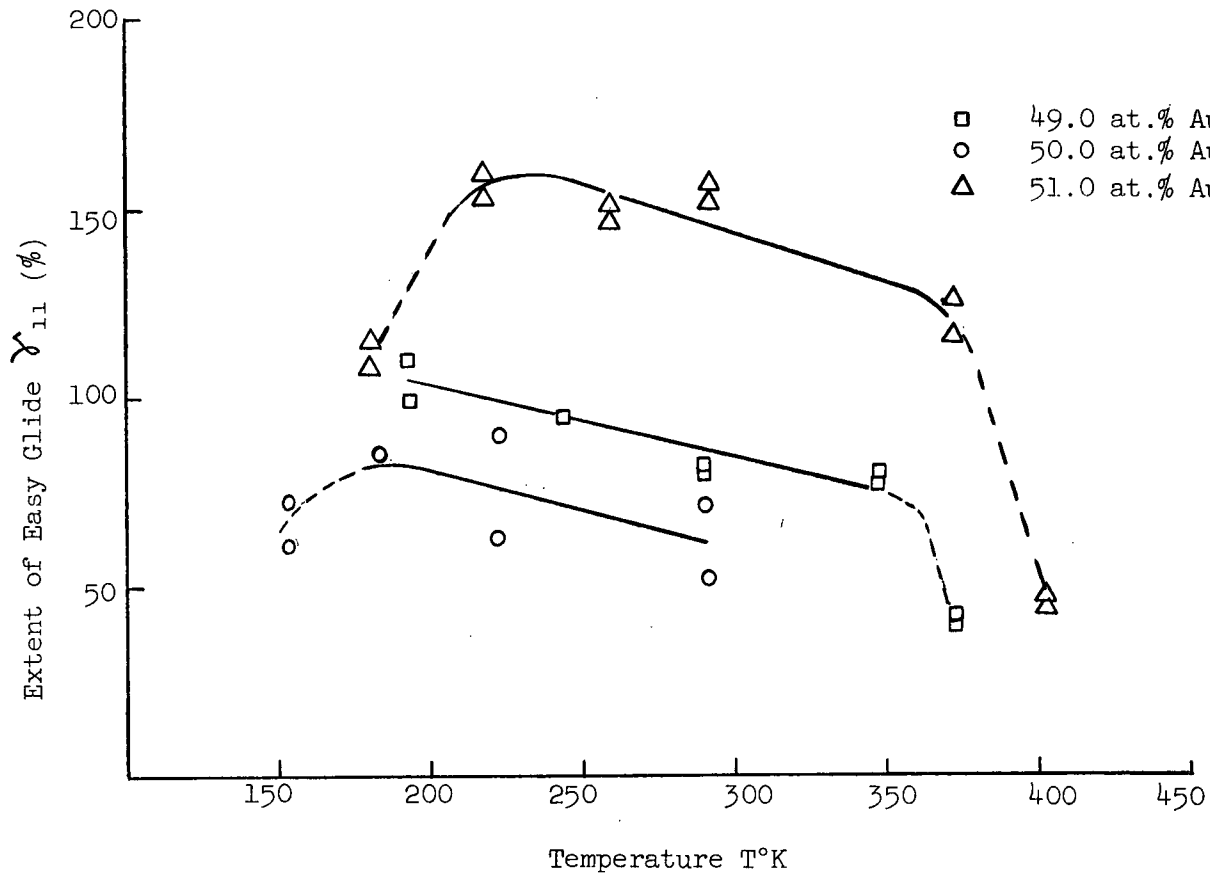

Figure 38. Showing the effect of temperature and composition on the extent of easy glide.

adding solute elements to fcc metals.[16,17,141] An explanation[141] is based on the assumption that easy glide ends when the stress concentration around clusters of dislocations on the primary slip plane are sufficiently large to initiate slip on crystallographically similar secondary systems. Since the yield stress is raised on both sides of stoichiometry, the clusters need greater stress fields to move secondary dislocations and since the work hardening rates are about the same, then easy glide must be more extensive to effect the larger clusters. Thin foil transmission electron microscopy studies (section 2.5.3) verify the assumption that dislocation clusters are present on primary slip planes and suggest that clusters give rise to the macroscopically detected deformation bands (section 2.5.2) in the vicinity of which localized secondary slip is detected near the end of stage I.

Except at temperatures below ~200°K, the extent of easy glide increases with decreasing temperature, which is similar to the effect of deviations from stoichiometry and can be explained in a similar manner. Since the yield stress increases with decreasing temperature (Figure 33) larger clusters and hence more extensive easy glide is necessary to initiate secondary slip.

The effects of temperature and composition on the stress at the end of easy glide τ_{11} are shown in Figure 39. For the stoichiometric

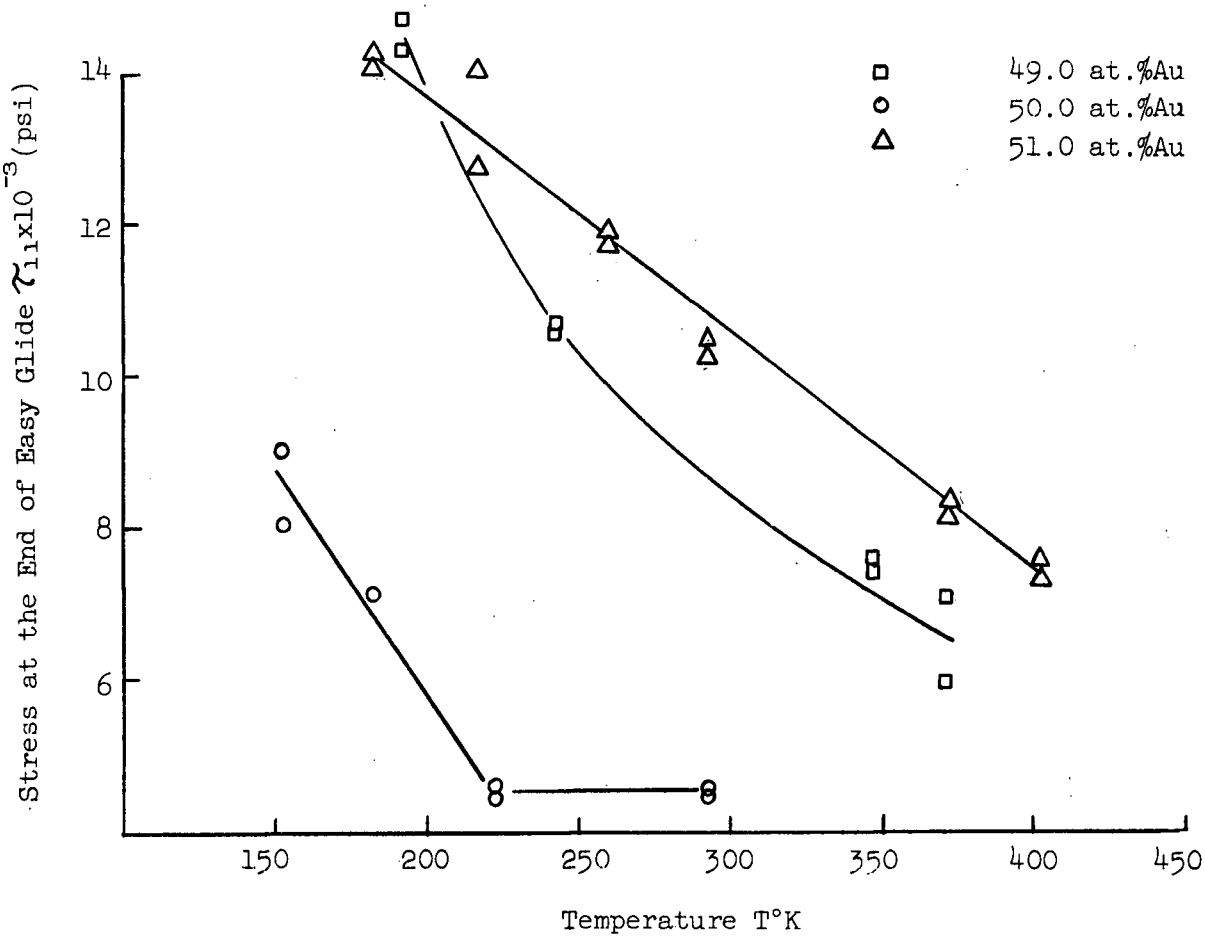

Figure 39. Showing the effects of temperature and composition on the stress at the end of easy glide.

crystals it is seen that τ_{11} increases ~ 2.5 times between 220°K and 150°K but remains constant at temperatures above 220°K, similar to the yield stress temperature variation. Non-stoichiometric alloys display a monotonic variation

in τ_{11} with temperature, decreasing by ~2 times over the range 180°K to 400°K.

An interesting result is obtained when one calculates the stress ratios τ_{11}/τ_o for the three compositions at various temperatures and orientations, Table 13. It is found that the average ratio is 2.4 ± 0.2, 2.9 ± 0.2 and 2.7 ± 0.4 for the Zn-rich, stoichiometric and Au-rich alloys respectively; within the limits stated τ_{11}/τ_o appears to be independent of temperature, composition and orientation suggesting that the work hardening mechanism is unchanged over this range of temperature, composition and orientation.

TABLE 13

τ_{11}/τ_o as a Function of Temperature, Composition and Orientation

Table 13.1

T°K	192	243	293	348	373	Avg. τ_{11}/τ_o
τ_{11}/τ_o	2.8	2.4	2.4	2.7	2.3	
Zn-Rich	3.5	-	2.1	2.4	2.1	2.4 ± .2

Table 13.2

T°K	153	183	223	293	Avg. τ_{11}/τ_o
τ_{11}/τ_o	3.1	3.1	2.2	2.4	
Stoichiometric	3.1	-	3.2	2.9	2.9 ± .2

Table 13.3

T°K	181	217	260	293	373	403	Avg. τ_{11}/τ_o
τ_{11}/τ_o	2.5	3.8	2.9	2.5	2.6	2.2	
Au-Rich	2.8	2.8	2.0	2.8	2.4	2.0	2.7 ± .4

Table 13.4

Orientation (Figure 11)	1	5	6	7	8	9	Avg. τ_{11}/τ_o
τ_{11}/τ_o	3.1	2.5	2.7	3.1	2.5	2.2	
Au-Rich	3.0	2.8	-	-	2.5	-	2.7 ± .4

The effect of orientation on the extent of easy glide is shown in Figure 40. It is apparent that γ_{11} increases as ξ increases,

consistent with the observations that Θ_1 decreases with increasing ξ while τ_{11} remains approximately unchanged.

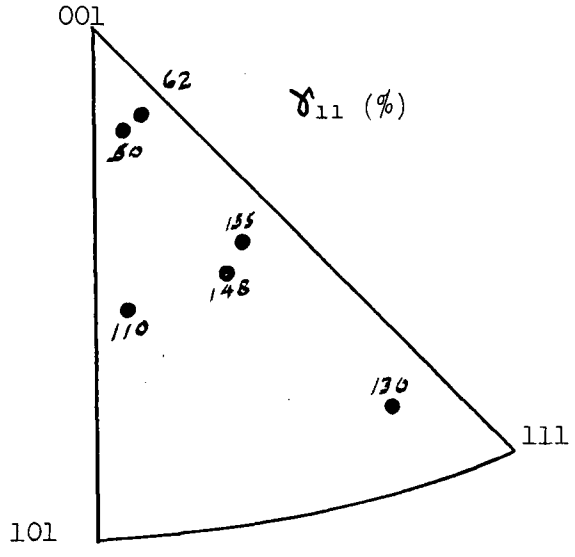

Figure 40. Showing the variation in the extent of easy glide with orientation. (51.0 at. % Au; T = 293°K)

2.5.1.4 The Work-Hardening Rate in Stage II, Θ_{II}

The temperature and composition dependence of stage II work-hardening rate is shown in Figure 41 where the results are given in terms of $\frac{\Theta_{II}}{\mu}$. Sample flow curves from which Θ_{II} values were reliably taken are also shown. Since para-linear type hardening was observed at temperatures below ~150°K it was questionable whether or not the slope Θ_l of the linear segment of the flow curve could be related to stage II hardening. This difficulty was partially resolved by studying the variation in slip line structure during straining. The results of this study are reported in a later section of the thesis where it will be shown that multiple slip occurs continually at 77°K, but only in minor amounts during stage II at higher temperatures. Para-linear hardening was then believed to be related, in part at least, to stage II hardening rates since both types of deformation are manifestations of multiple slip processes. The corresponding linear work-

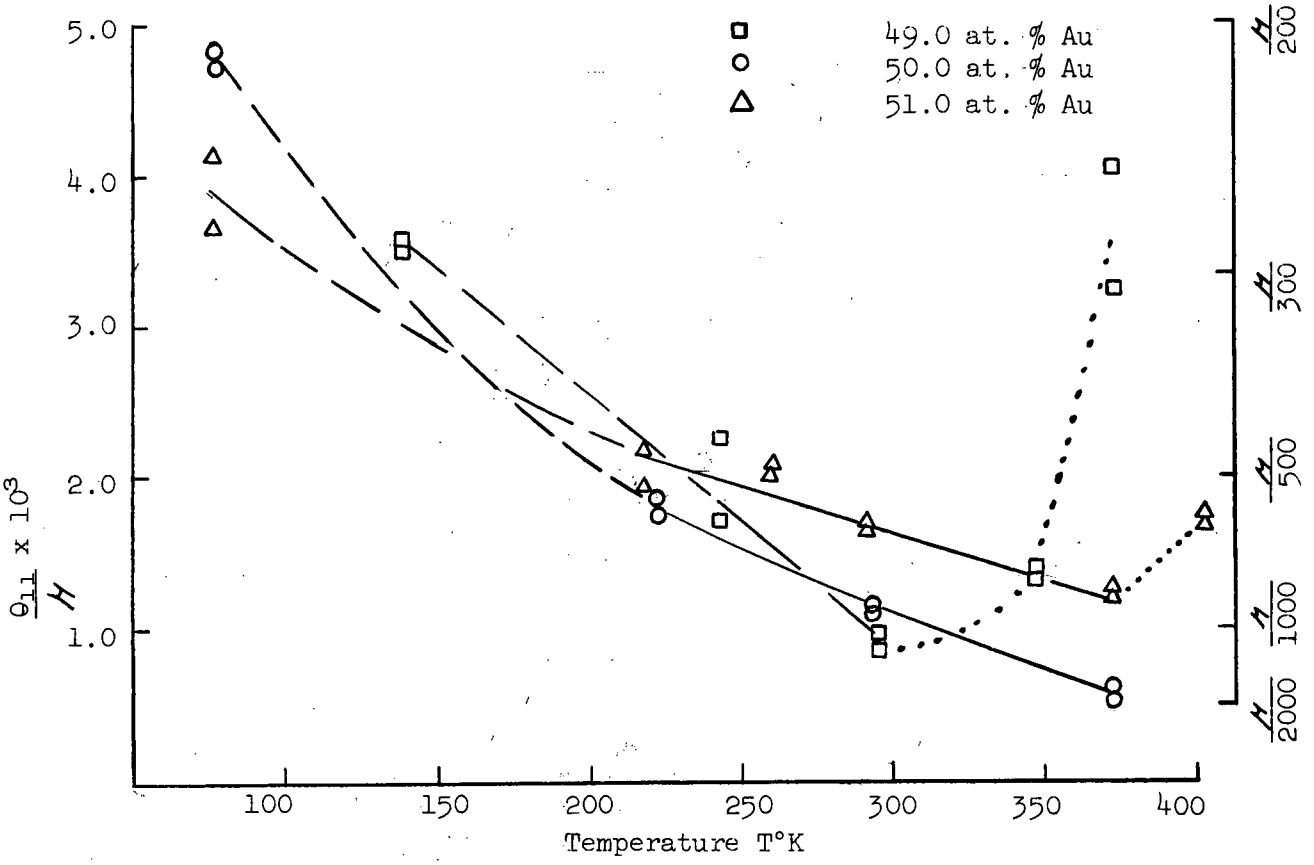

Figure 41.1. Showing the variation of stage II work-hardening θ_{11} rate with temperature.

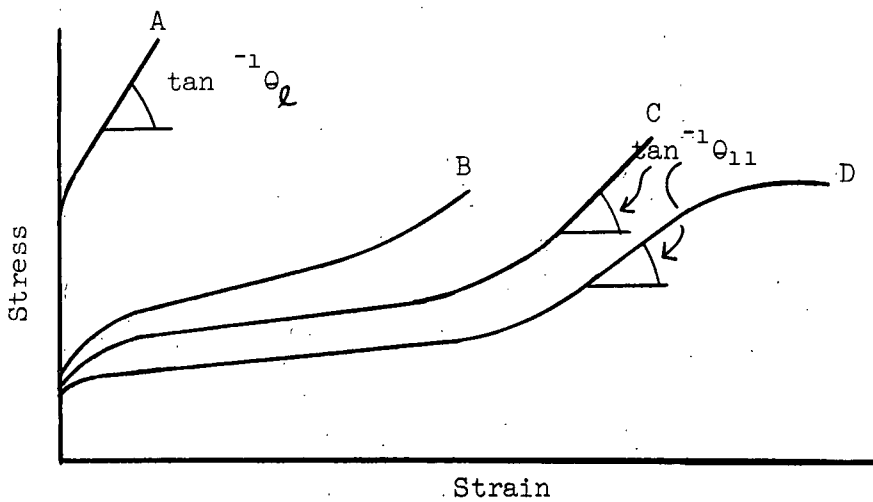

Figure 41.2. Schematic flow curves. Type A analyzed for linear hardening rates and Types C and D for stage II hardening rates; Type B not analyzed.

hardening rates at 77°K are plotted, therefore, in Figure 41 where they are connected with the θ_{II} values by a dashed line. An explanation of the higher work-hardening rates during para-linear flow is given in section 2.5.4.

Over the temperature range 225°K to 350°K in which θ_{II} could be reliably evaluated, it is apparent that hardening rates during stage II decrease by 2.5 times from $\frac{\mu}{500}$ to $\frac{\mu}{1200}$ with increasing temperature. This behaviour is different from the very minor decrease with temperature in fcc metals and alloys, but resembles the quite pronounced decrease above 0.27 T_m in Cd.[142,143] It is also interesting to note that θ_{II} is strain rate sensitive, decreasing with decreasing strain rate. The flow curves in Figure 9 were analyzed for this feature and the results are given in Table 14.

TABLE 14

Variation in Stage II Hardening Rate with Strain Rate
($T = 293°K$, $\xi = 26°$, $\chi = 20°$)

Test	$\dot{\gamma}$ (sec.$^{-1}$)	θ_{II} (psi)	$\theta_{II}/\mu \times 10^3$
112	2.5×10^{-4}	5900	1.36
60, 61	2.5×10^{-3}	7100	1.63
110	2.5×10^{-2}	9100	2.09

It appears, therefore, that thermally activated recovery processes can take place concurrent with plastic deformation.

Below 350°K, the effect of composition on θ_{II} is very small, similar to fcc systems.[16,17,141] At higher temperatures, however, non-stoichiometric crystals exhibit an unusual sudden rise in hardening rate, which is somewhat similar to behaviour of bcc metals[1,9] near .1 T_m. These results suggest that the work-hardening mechanism is probably the same

for all compositions below 350°K, but differs for stoichiometric and non-stoichiometric crystals above this temperature.

The dependence of Θ_{11} on crystal orientation is shown in Figure 42. It can be seen that Θ_{11} decreases as the specimen orientation approaches the [001]-[101] boundary (i.e. as χ increases) which is similar to the effect of increasing temperature and decreasing strain rate.

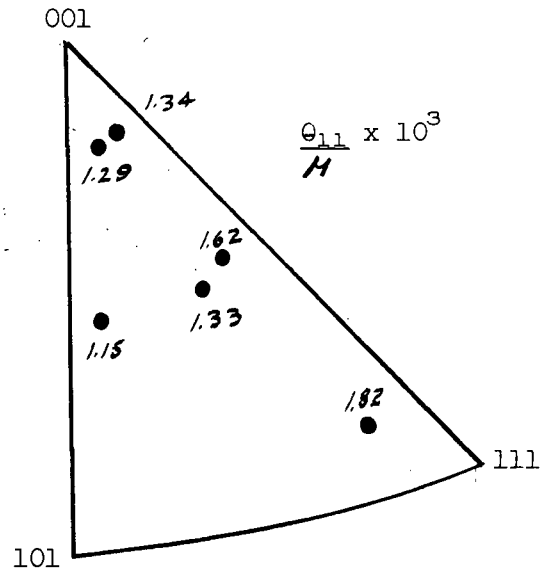

Figure 42. Showing the orientation dependence of stage II work-hardening rate (51.0 at. % Au; T = 293°K)

An intimate relationship between temperature, strain rate and orientation was noted earlier in the discussion on deformation modes. It was shown that the slip plane parameter ψ increases with increasing temperature, increasing χ and decreasing strain rate which was interpreted in terms of an increasing tendency for cross-slip of screw dislocations. It is once more apparent that these variables are related through their combined effect on stage II hardening rates. With increasing temperature, increasing χ and decreasing strain rate, Θ_{11} decreases. It is not known if the observed variation in Θ_{11} is simply a manifestation of the changing slip plane and hence a property of the macroscopic slip plane per se, or if it

suggests that cross-slip plays a dual role in the deformation of AuZn, active as a dynamic recovery mechanism as well as governing the choice of slip plane.

Work-hardening rates in specimens oriented near the [001] corner (Figure 11, orientation 10) must be discussed separately. As already noted, in these orientation $\{hko\}\langle 001\rangle$ systems no longer serve as the primary slip modes; instead slip occurs on a $\{211\}\langle 111\rangle$ system. Secondary systems, probably $\{321\}\langle 111\rangle$ and $\{110\}\langle 001\rangle$, operate as well (Figure 28) but observations at fracture show that their contribution to the total ductility is negligible with respect to the $\{211\}\langle 111\rangle$ primary slip. It is to be concluded therefore that the very high work-hardening rate and limited ductility are direct results of $\langle 111\rangle$ slip. The linear hardening slopes θ_ℓ were analyzed giving values of $\sim 38{,}500$ psi. In terms of shear modulus, this is equal to $\frac{\mu}{60}$ where μ was calculated from the relationship $\mu_{\{211\}\langle 111\rangle} = \frac{1}{3}(c_{11}-c_{12}+c_{44})$, Appendix 5. The elastic constants c_{11}, c_{12} and c_{44} were taken from the data of Muldawer and Schwartze[64]. It is immediately apparent that hardening rates resulting from $\langle 111\rangle$ slip are over 10 times greater than those associated with general $\{hko\}\langle 001\rangle$ slip modes. The reason for this unusually high value must in some way be associated with antiphase boundaries created by the motion of $\frac{1}{2}a\langle 111\rangle$ type superlattice partial dislocations. Possible superdislocation hardening mechanisms are discussed in section 2.5.4.

It is significant that the linear hardening rate $\theta_\ell \sim \mu/15$ observed in polycrystalline AuZn[12] is considerably nearer the value $\frac{\mu}{60}$ in single crystals undergoing $\langle 111\rangle$ slip than the values $\frac{\mu}{500}$ to $\frac{\mu}{1200}$ in crystals deforming along $\langle 001\rangle$ direction. (It should be noted that $\theta_\ell \sim \mu/8$ quoted in reference 12 was obtained using the shear modulus for $\{211\}\langle 111\rangle$ slip rather than for $\{hko\}\langle 001\rangle$) While slip on the $\{hko\}\langle 001\rangle$ systems is

believed to account for most of the plasticity observed in polycrystalline material, {211} and {321} traces were observed in the vicinity of grain boundaries, suggesting that <111> slip does occur under rather high stress conditions. In view of the very high hardening rate associated with <111> slip in single crystals it appears as though the rapid hardening in polycrystalline material below ~300°K is controlled by dislocation motion on {hkl} <111> systems. Hence, grain boundary hardening, rather than hardening within the grain is believed to control the flow stress. This is consistent with the Hall-Petch behaviour of AuZn[12], where the Petch slope k_f relating the flow stress to the reciprocal of the square root of the grain size is observed to increase with increasing strain.

2.5.1.5 Stage III

Stage III is characterized by rapidly decreasing values of work-hardening rate with increasing strain. In Figure 43 it is shown that the stress τ_{111} at the end of stage II decreases with increasing temperature, suggesting that a thermally activated recovery mechanism is responsible for the breakdown of linear hardening. Since only a few orientations investigated gave rise to three-stage work-hardening curves, it is difficult to comment with certainty on the quantitative effects of specimen orientation on τ_{111}. There is some evidence to suggest that τ_{111} decreases as χ increases, but until further experiments can be carried out, this must remain as a tentative observation only.

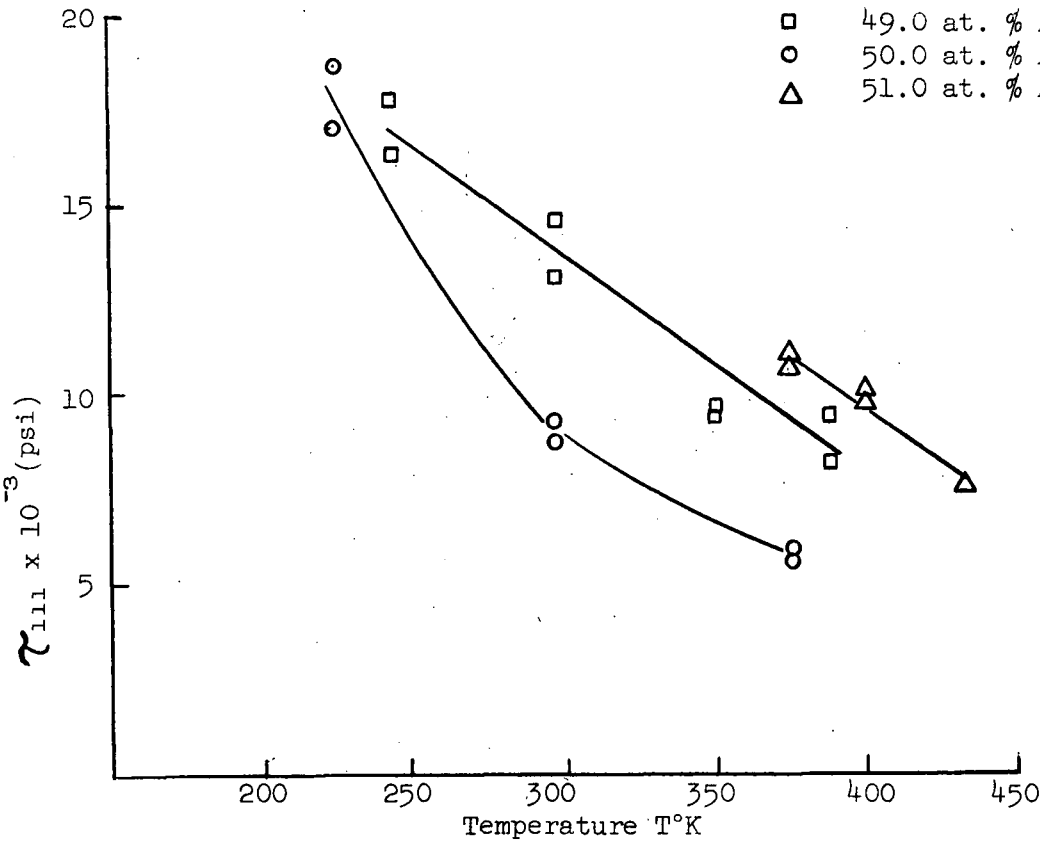

Figure 43. Showing the effect of temperature on the stress at the end of stage II.

2.5.1.6 Maximum Shear Stress and Ductility

The maximum shear-stress τ_m and total shear-strain to fracture γ_f are shown in Figures 44 and 45 as functions of temperature and composition. τ_m tends to decrease with increasing temperature except over the intermediate temperature range 200°K to 300°K where a peak is detected. Polycrystalline AuZn[12] shows exactly the same variation in ultimate tensile strength versus temperature. In both polycrystalline and single crystal material, the maximum flow stress decreases by about 5 times between 77°K and 500°K. Although τ_m increases with deviations from stoichiometry in both materials, the effect is not nearly as pronounced as it is on the yield stress.

The shear strain to fracture γ_f may be taken as a measure of

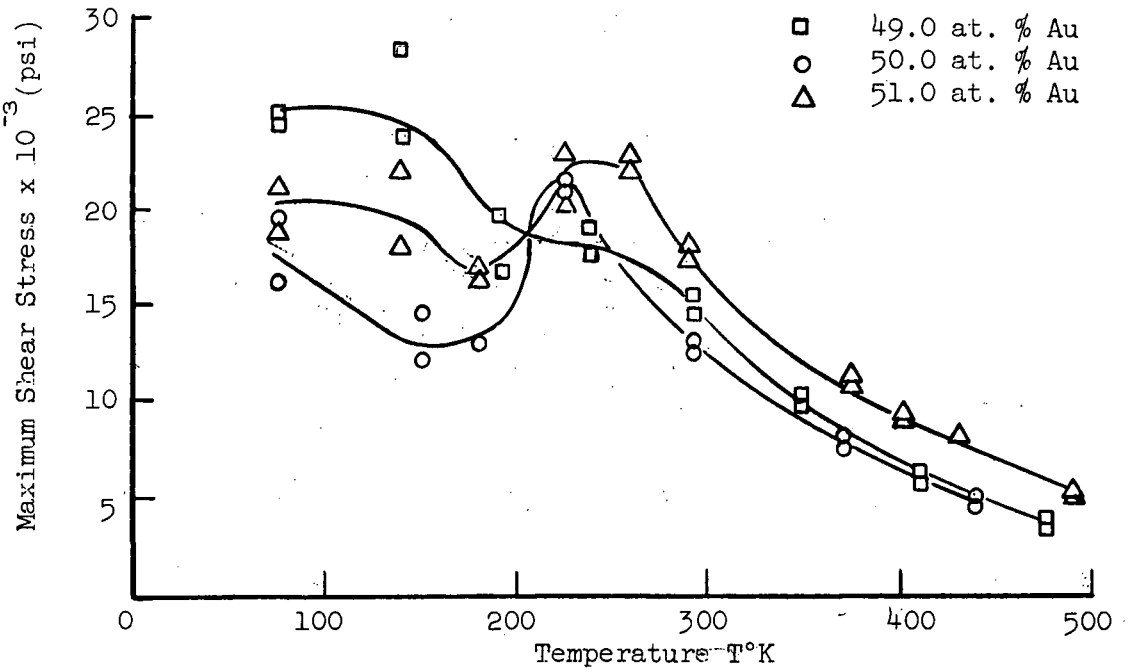

Figure 44. Showing the variation of maximum shear stress with temperature.

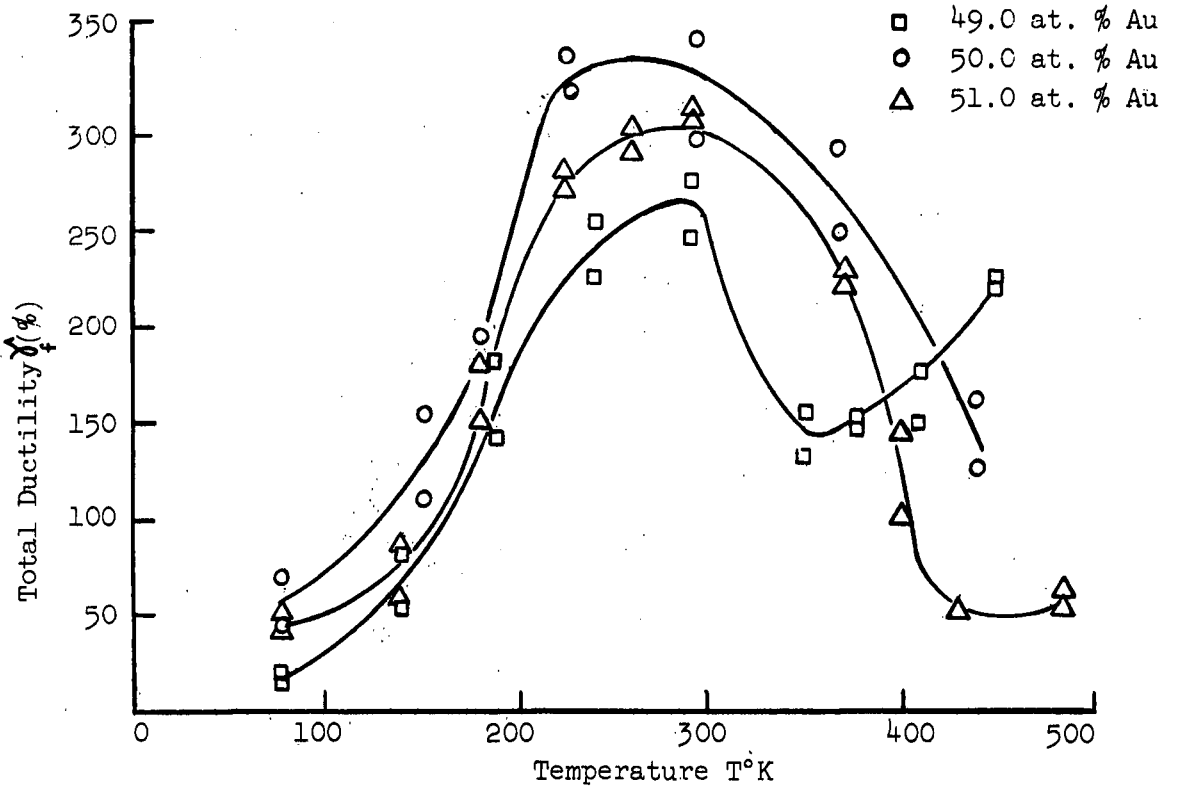

Figure 45. Showing the variation of total ductility with temperature.

ductility in single crystals. From Figure 45 it can be seen that the temperature dependence of ductility may be divided into three distinct regions: (A) from 77°K to 250°K, in which γ_f increases by about 6 to 10 times depending on composition; (B) from 250°K to 400°K where γ_f decreases by ~2 times for Zn-rich crystals and about 5 times for stoichiometric and Au-rich alloys; (C) above 400°K where ductility appears to increase in both Zn-rich and Au-rich crystals. Over the temperature ranges A and B, stoichiometric crystals are most ductile and Zn-rich crystals are the least ductile, but in region C, Zn-rich alloys display greatest ductility. The temperature range of maximum ductility is coincident with the peak flow stress. Polycrystalline ductility[12] exhibits identical behaviour over the same temperature range suggesting that similar mechanisms may be responsible for fracture. Until some crystallographic aspects of single crystal fracture are presented in section 2.5.2, further discussion is terminated.

2.5.2 Slip Line Variation During Deformation

In addition to the direct evaluation of work-hardening rates, supplementary studies are often performed to arrive at possible hardening models. Slip line studies on the surfaces of deformed crystals, transmission electron microscopy in thin films, X-ray diffraction, electrical resistivity and magnetic properties of ferromagnetic materials are useful experiments from this viewpoint. Indeed detailed studies of the first two types have led to the development of two very prominent work-hardening theories of stage II deformation, the long range hardening theory of Seeger[144,145] and the pile-up theory of Hirsch.[146] Consequently information from both surface slip line variation during deformation and the corresponding dislocation structure in thin films is believed to be of utmost importance in understanding the general deformation behaviour of metal crystals. Both surface

slip line studies and transmission electron microscopy experiments were carried out during the present investigations and the results are reported in their respective sections 2.5.2 and 2.5.3. While these studies were not intended to give a detailed account of the work-hardening mechanisms, they were designed to add information which would aid in understanding the plastic behaviour of β' AuZn single crystals.

2.5.2.1 Procedure

Specimen preparation for slip line analyses has been given in section 2.4. Crystals of orientation 1 in Figure 18 previously used to determine primary slip traces versus temperature have been used to study the variation of slip lines during tensile deformation at temperatures between 77°K and 473°K. Specimen surfaces were examined optically under oblique filtered lighting with the Reichert metallograph.

2.5.2.2 Observations

In presenting photomicrographs showing the development of slip lines, it was decided for the purposes of comparison to include the series already presented in section 2.4 since they are characteristic of the slip line appearance during initial flow. Slip traces on orthogonal faces A and B (identified in section 2.4) are shown as a function of strain at 77°K, 140°K, 293°K, 398°K and 473°K in Figures 46 to 50 respectively. Schematic flow curves noting the strains at which observations were made are also shown. Because of the non-crystallographic nature of slip traces, systems are indexed with respect to approximate $\{hko\}$ planes in the $\langle 001 \rangle$ zone. For easy comparison, comments on the observations are summarized in Table 15. The results are discussed in the context of a general discussion on work-hardening, section 2.5.4.2.

46.A.1

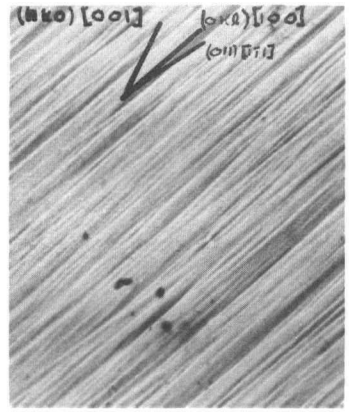

γ = 10%

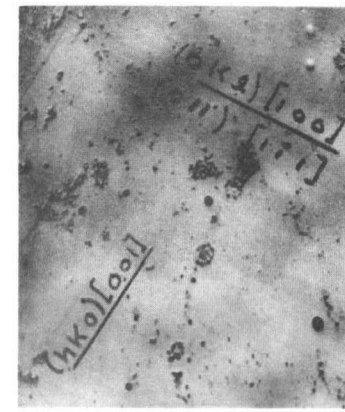

46.B.1

46.A.2

γ = 44%

46.B.2

46.A.3

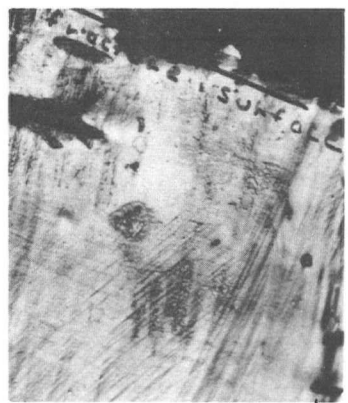

γ = 62%

46.B.3

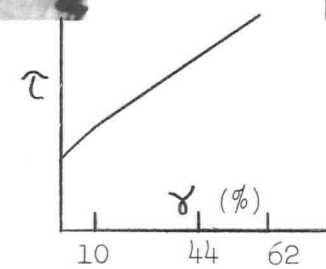

Figure 46. Variation in slip line structure with strain at 77°K.
X 100

47.A.1

γ = 20%

47.B.1

47.A.2

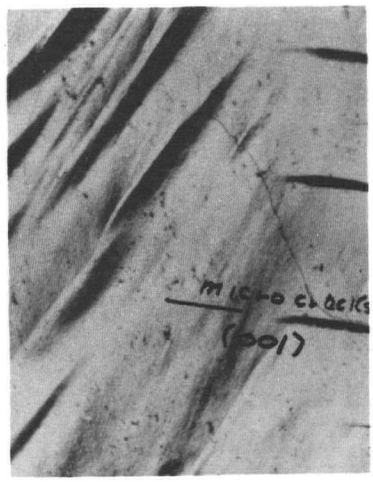

γ = 120%

47.B.2

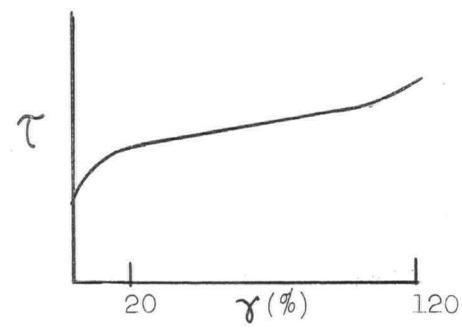

Figure 47. Variation in slip line structure with strain at 140°K.
X 100

48.A.1

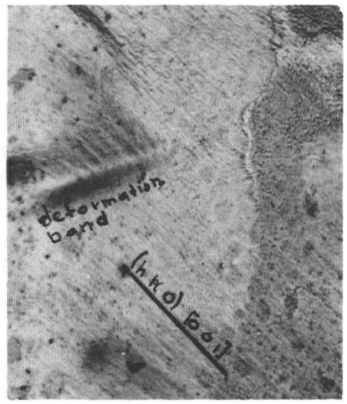

γ = 20%

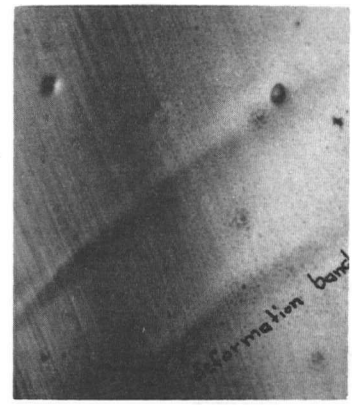

48.B.1

48.A.2

γ = 120%

48.B.2

48.B.3

(X200)

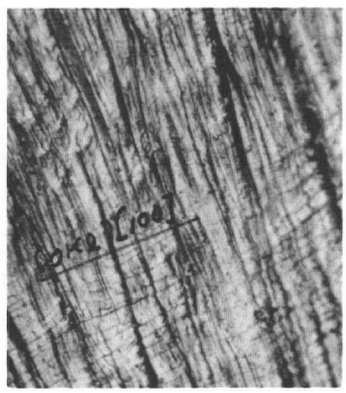

γ = 230%

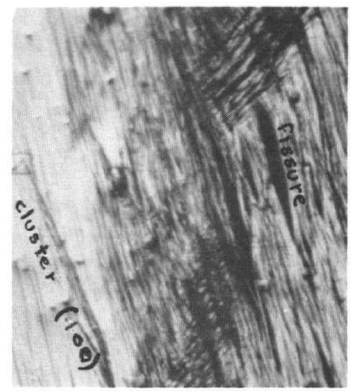

γ = 300%

48.B.4

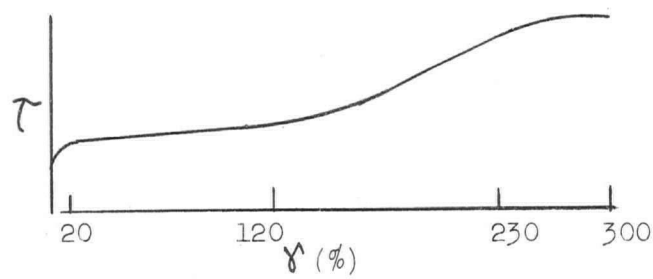

Figure 48. Variation in slip line structure with strain at 293°K; X 100 (except where noted).

49.A.1

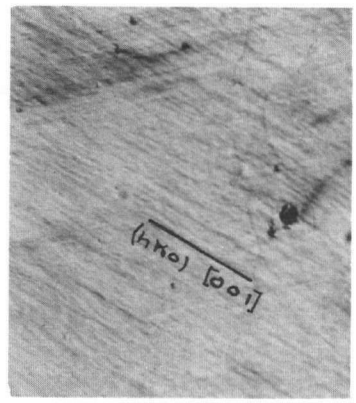

γ = 9%

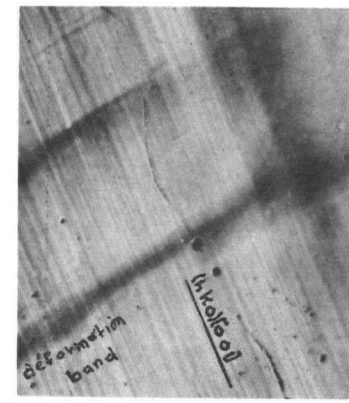

49.B.1

49.A.2
X 25

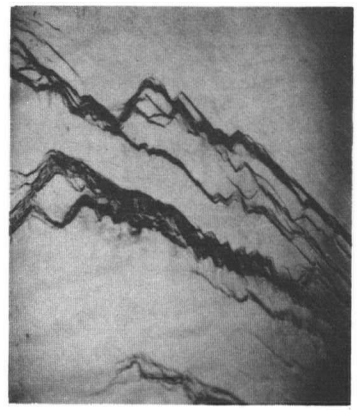

γ = 44%

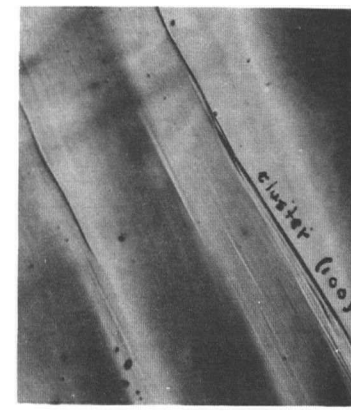

49.B.2

49.A.3
X 25

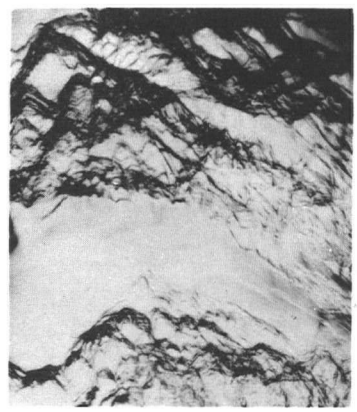

γ = 100%

49.B.3
X 25

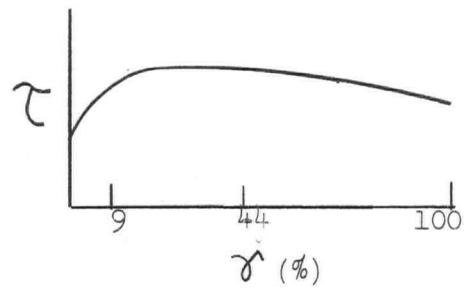

Figure 49. Variation in slip line structure with strain at 398°K. X 100 (except where noted)

50.A.1

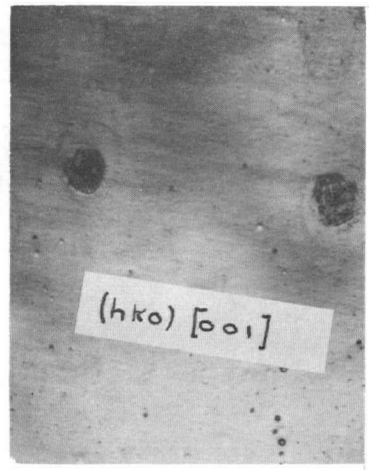

γ = 15%

50.B.1

50.A.2

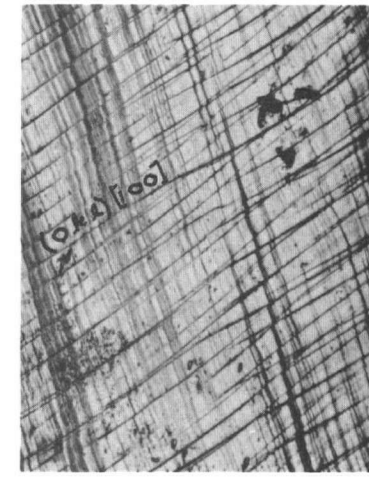

50.B.3

γ = 71%

γ = 145%

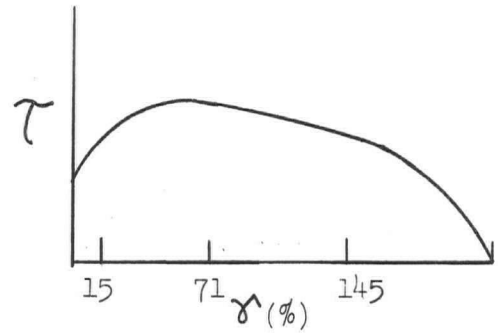

Figure 50. Variation in slip line structure with strain at 473°K. X 100

TABLE 15

Comments on Slip Line Variation During Deformation

Temp. °K	Ref. Fig.	Primary Slip System: System (approximate with respect to plane)	Primary Slip System: Description: Initial	Primary Slip System: Description: Variation with Strain	Secondary Slip System: Yes No	Secondary Slip System: First Detected	Secondary Slip System: Description: Systems	Secondary Slip System: Description: Initial	Secondary Slip System: Description: Variation with Strain	Contribution to Total Strain *: ξ final (degree): Measured	Contribution to Total Strain *: ξ final (degree): Calculated	Contribution to Total Strain *: Amount
77	46	(011)[100]	face A-coarse, slightly wavy; face B-fine, straight	coarsen on both faces A and B	Yes	at yield	(011)[111] (110)[001]	minor amount " "	coarsen slightly coarsen and increase in number	54 (from [100])	51 (from [100])	~10%
140	47	(210)[001]	on both A and B, banded slip lines	development of fine traces between "bands"	Yes	during last few percent strain	{321} and {211}	short, straight detected near shadowed areas parallel to microcracks	remain fine, straight, widely spaced	14	15	Negligible
293	48	(310)[001]	wavy on A and straight on B; relatively fine	face A traces coarsen, become wavy on a large-scale with wave traces lying close to (100); traces B adopt slight wavy appearance	Yes	at end of stage I	(021)[100]	short, curved appearance, occurring in localized regions in vicinity of deformation bands	coarsen, new traces develop around smaller deformation bands	11	10	Negligible
398	49	(510)[001]	increased waviness of face A traces; straight traces on face B and finely spaced	both traces A and B coarsen while traces A become profusely wavy	No	-	-	-	-	-	-	-
473	50	(100)[001]	increased waviness of face A traces; face B traces remain straight and finely spaced	"	Yes	at ~50% strain (i.e. at peak flow stress)	(010)[100]	long, slightly wavy, coarse	remain approximately constant in number, but coarsen	-	-	~50%

* See note, p.109

TABLE 15 (Continued)

Temp. °K	Other Crystallographic Features				Fracture Appearance
	Type	First Detected	Plane	Variation with Strain	
77	micro-cracks	at 40%	(001) within 5 degrees	apparent increase in length	fracture surface parallel to microcracks
140	micro-cracks	during last few percent strain	(001) within 5 degrees	-	fracture surface parallel to microcracks
	deformation bands	yield	Section 2.5.2.3		
293	slip line clusters visible on face B	onset of stage III	(100) within 5 degrees	coarsen	fracture surface parallel to fissures, which appear at begining of stage III in vicinity of slip clusters
	deformation bands	yield	Section 2.5.2.3		
398	slip line clusters visible on face B	40% (near maximum flow stress)	(100) within 5 degrees	coarsen; at fracture gauge section "saturated" with clusters	fracture plane parallel to cluster
	deformation bands	yield	Section 2.5.2.3		
473	-	-	-	-	-

Note re Table 15:

Contribution of secondary systems to total strain was estimated by calculating specimen reorientations assuming various amounts of secondary slip, then comparing the calculated with the measured values. Reorientation calculations were performed using the relationship:[49]

$$\text{Sin } \chi_i = \frac{l_o}{l_i} \text{ Sin } \chi_o$$

where the suffixes o and i refer to the original and instantaneous values of gauge length l and angle χ between the tensile axis and the slip direction.

2.5.2.3 Deformation Bands

2.5.2.3.1 Characteristics

A fairly common feature of the surface appearance of the deformed crystals is the occurrence of a series of markings traversing the primary slip traces, termed deformation bands. The bands can be described as striations which can be seen under very low magnification; at high magnification, they seem to disappear. Deformation bands were detected in all orientations at room temperature, except those near the [001] corner where $(\bar{1}\bar{1}2)[111]$ slip predominates, and at all temperatures between 140°K and 398°K for a constant orientation near the middle of the stereographic triangle.

Bands form in the very early stages of deformation. Their variation in appearance during straining is best illustrated in the room temperature observations, Figure 48. Although the distance between any two is not quite uniform, the average spacing is approximately 0.2 to 0.3 mm. and the average width about 0.03 to 0.04 mm. As strain increases, the bands increase in intensity and become wavy (Figure 48.B.2), while the average separation appears unchanged. It can be seen that the primary slip traces crossing deformation bands change their direction, slightly at first (Figure 48.B.1), but quite markedly at higher strains (Figure 48.B.2). The appearance of the slip lines suggests a change of elevation at the band site and the change in slip line direction indicates that the material within the band lags behind the matrix during lattice reorientations. These markings closely resemble similar structures observed in aluminum single crystals.[147]

2.5.2.3.2 Crystallographic Nature

During the early stages of deformation, the boundaries of the bands may be defined as plane surfaces. Two surface trace analyses were subsequently performed and the results are shown stereographically in Figure 51.

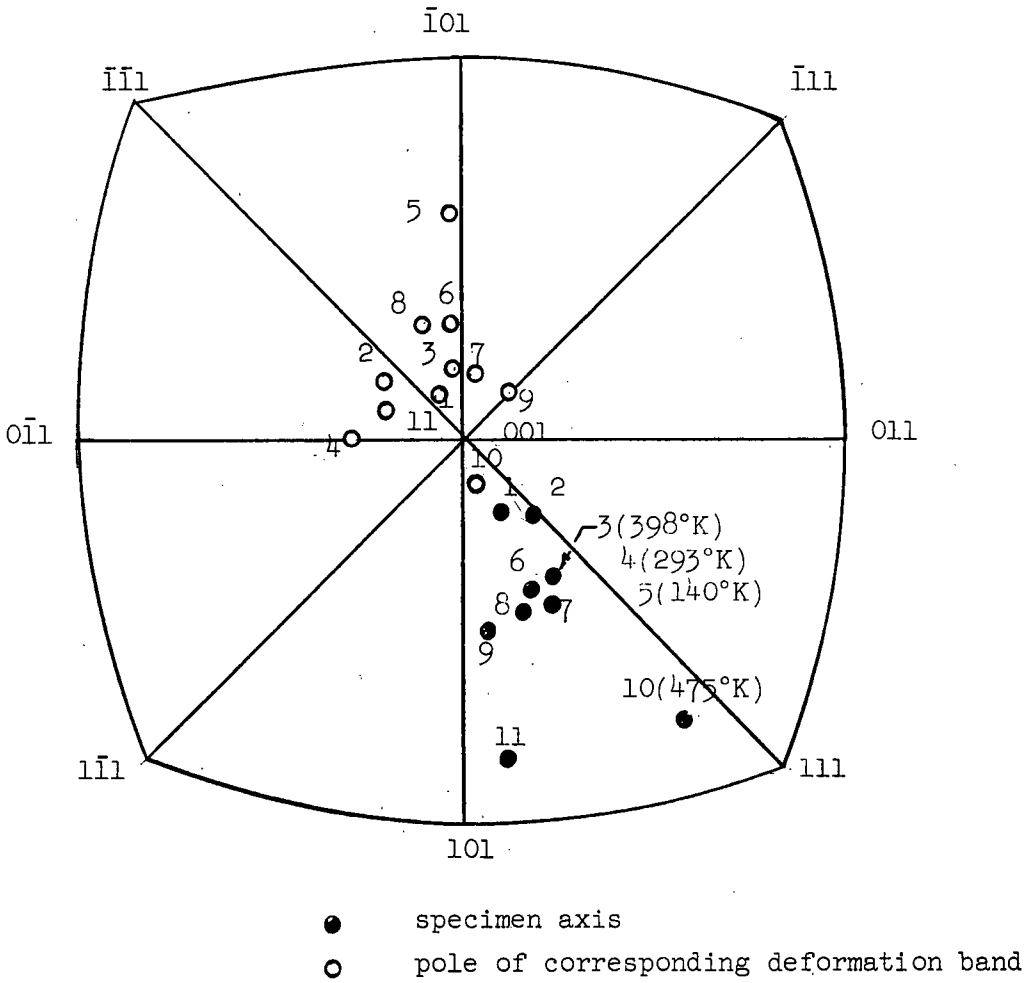

Figure 51. Stereographic projection of deformation band poles versus crystal orientation and test temperature.

It is apparent that the poles cluster round the [001] slip direction to within an average of ~8°, suggesting that the slip direction plays an important role in deformation band formation. No systematic effects of orientation or temperature were detected.

2.5.2.3.3 Mechanism of Formation

Deformation bands are a fairly common feature of the deformation of cubic crystals. Two explanations have been advanced to account for their formation. From a macroscopic aspect[147,148,149] it is believed that bands are caused by bending which occurs as a result of constraints at the specimen loading grips, or by inhomogeneous lattice rotations where one section of the crystal slips more than its neighbours. The band planes produced move in the direction of slip until two of opposite sign meet and become stuck. A planar obstacle is consequently formed against which later dislocations pile up and create the deformation band. This explanation accounts for the observed scale, but does not explain the fundamental dislocation processes by which bend planes are formed.

Mott[150] has proposed a more detailed theory to account for band formation. His idea of the dislocation arrangement within a band is shown in Figure 52. Walls of positive edge dislocations are pushed by the applied shear stress and arrive from the right while walls of edge disloca-

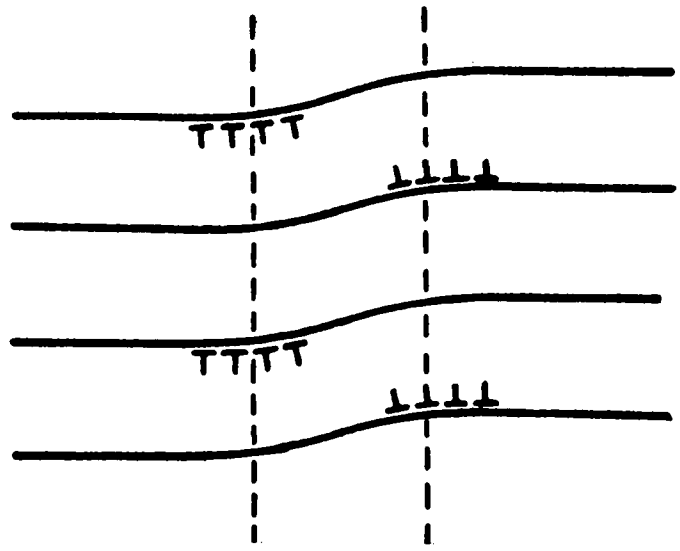

Figure 52. Schematic representation of dislocations in deformation bands. (after Mott[150])

tions of opposite sign and roughly equal strength arrive from the left, thereby forming a deformation band. The positive wall causes the lattice to tilt downward while the negative wall effects an upward curvature. The mutual attraction of positive and negative dislocations makes these configurations fairly stable.[151]

Mott's edge dislocation wall-model necessarily implies that the deformation bands are perpendicular to the slip direction. In aluminum[147,148] deformation bands lie along (110) planes perpendicular to the slip direction in support of Mott's theory. In AuZn it was shown that although the bend planes are not quite perpendicular to the [001] slip direction, they tend to adopt orientations centered about this pole. The view is taken therefore, that a mechanism similar to that proposed by Mott can account for the band formation in β'AuZn.

2.5.2.4 Microcracks

The nucleation and propagation of microcracks along {100} planes is a commonly observed fracture mode in bcc metals deformed at low temperatures.[152,153,154] In considering the initiation of a crack in bcc structures, Cottrell[155] has suggested that the formation of dislocations with a[001] Burgers vectors is an important step. According to the reaction:

$$\frac{1}{2}a[\bar{1}\bar{1}1] + \frac{1}{2}a[111] = a[001] \qquad (25)$$

an edge dislocation of Burgers vector a[001] can form from a combination of two dislocations with Burgers vectors $\frac{1}{2}a[\bar{1}\bar{1}1]$ and $\frac{1}{2}a[111]$ gliding in the (101) and $(10\bar{1})$ planes respectively. The product dislocation lies along [010] and is a pure edge with glide plane (100). Since a[001] dislocations are normally not mobile in bcc lattices, Cottrell suggests that they act as barriers against which other dislocations pile up and eventually nucleate a

crack. Cottrell's mechanism is not likely to be responsible for crack nucleation in β' AuZn since slip trace analyses show that [001] dislocations are highly mobile.

The crystallographic similarity between the high temperature deformation bands and the low temperature microcracks (i.e. both are approximately coincident with (001) planes) suggests that similar edge dislocation wall mechanisms may be responsible for their formation. Whereas stress concentrations resulting from wall formation may be relieved through the operation of secondary $\{hko\}\langle 001\rangle$ slip systems at 293°K (Figure 48.B.2), they appear to be relieved through crack formation at low temperatures, presumably because the increased critical shear stress for $\{hko\}\langle 001\rangle$ slip renders secondary slip unfavourable. The increasing susceptibility for crack formation at low temperatures, therefore, probably accounts for the decreasing ductility, region A in Figure 45.

2.5.3 Transmission Electron Microscopy of Thin Films

2.5.3.1 Introduction

Considerable dispute has arisen in the literature concerning the degree to which dislocation arrangements observed in thin films are representative of configurations in the bulk material.[144,172,173] Seeger[144] has criticized the use of thin film microscopy observations to support work-hardening theories on the grounds that long-range stress fields present in the cold-worked state and extending over distances large with respect to the usual foil thickness are to a large extent relaxed during the process of preparing a foil from the bulk, since the surface of the foils must be stress-free. The relaxation in stresses must then effect a change in the dislocation arrangement. The degree of rearrangement is believed to depend on the stacking fault energy of a material being greater the higher the energy. Hirsch,[173] on the other hand, takes the view that since dislocation distributions obtained from etch-pit studies are in sufficiently good agreement with the results of thin film microscopy, the latter may be regarded as being reasonably representative of the bulk, at least as regards the overall dislocation distribution.

In recent years more elaborate specimen preparation techniques have been established in attempts to preserve the dislocation arrangements that are truly characteristic of crystals undergoing plastic deformation. Dislocation arrays have been pinned by both precipitation techniques[174] and neutron irradiation exposures. In the case of Cu crystals[175,176] irradiation pinning did not significantly affect the dislocation arrangement since similar structures were observed in foils prepared in the more conventional manner.[164] Until more experiments of this nature are carried

out, it must be assumed that the unpinned structure is fairly characteristic of the pinned bulk arrays. What must also be evaluated is the effect of irradiation and subsequent point defect creation on dislocation structure.

The purpose of the present study is to examine the dislocation distribution in annealed and deformed AuZn single crystals tested at room temperature. Irradiation experiments were not carried out and it is therefore not possible to estimate the degree to which the foil structure is characteristic of the bulk. Recently, martensitic transformation products have been observed near the edges of Zn-saturated (53.9 at. % Zn) AuZn foils[177] similar to the twin-like marking observed by Causey[12]. In the present study, however, similar markings were not detected for any foil orientation. Any rearrangements that occurred during thinning, therefore, could not be attributed to stress fields of a transformation product.

2.5.3.2 Procedure

Because of difficulties experienced in preparing thin foils from 3 mm. diameter crystals, large 5 mm. diameter Au-rich (51.0 at.% Au) crystals oriented near the middle of the stereographic triangle were employed to study dislocation distribution. The room temperature work-hardening behaviour of the larger crystals agreed well with the small crystal behaviour. Specimens were mounted in epoxy resin and strained in the usual manner.

To obtain information about the three-dimensional nature of dislocation distributions in deformed crystals, it is necessary to examine foils of several orientations. Specimens of three orientations were obtained from deformed crystals by spark machining discs $\sim$1mm. in thickness:

(1) parallel to the (hko) glide plane and parallel to the [001]

Burgers vector, termed (hko) section;

(2) parallel to the (110) plane and parallel to the Burgers vector, called (110) section;

and (3) perpendicular to the glide plane and parallel to the Burgers vector, termed perpendicular (hko) section.

Discs were cut using surface slip traces as a guide; the orientation of sections (2) and (3) was checked with the back-reflection Laue X-ray technique.

Thinning was achieved by repeatedly jet-machining and electro-chemically polishing[178] the discs in a mixture of 45% hydrochloric acid, 50% ethyl alcohol and 5% glycerine at -20°C and 12 volts. The electrolyte was contained in a pyrex beaker cooled in a bath of methyl alcohol and solid CO_2. To avoid straining the foil during thinning the usual technique of lacquering the outer rim of the specimen was abandoned. After thinning, specimens were thoroughly washed in distilled water then rinsed in ethyl alcohol and kept in a dessicator until examined.

Observations were made on a Hitachi Hu 11A electron microscope operated at 100 KV. Contrast was varied by tilting the specimens through $\sim 10°$ during examination. A selected area diffraction pattern was obtained from each area photographed to permit subsequent analyses of dislocation arrangements relative to prominent crystal directions.

2.5.3.3 Observations

2.5.3.3.1 As-Grown Structure

Dislocation structures observed in foils prepared from as-grown crystals are shown in Figure 53. Dislocation density in as-grown

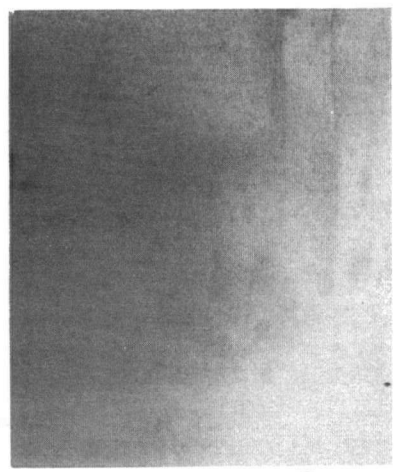

53.1

53.2

Figure 53. Electron micrographs of dislocation structure in as-grown crystals.

crystals is estimated as $\sim 10^{7}$ cm/cm^{3} since on the whole only a few dislocations were visible in any photomicrograph corresponding to a foil area of $\sim 10^{-7}$ cm^{2}. Figure 53.1 represents the most commonly observed as-grown structure, showing rather long, straight dislocations, while Figure 53.2 represents a less commonly observed zig-zag dislocation structure similar to equilibrium configurations found in β-brass.[179,180] The unusually high density seen in Figure 53.2 is not to be associated with zig-zag dislocations since similar shapes were observed in other low density areas.

In an elastically isotropic crystal with no applied stress, the concept of dislocation line tension implies that the equilibrium position of a dislocation running between pinning points (for instance, foil surfaces) is a straight line, similar to the structures in Figure 53.1. On the other hand, zig-zagged dislocations are considered to be a direct result of crystal anisotropy.[179] A straight dislocation which is in a high energy direction may be unstable with its total energy decreasing if

it changes to a zig-zag shape. Calculated from Zener's[31] relationship $A = \frac{2\,C_{44}}{(C_{11}-C_{12})}$ and using that data of Schwartz and Muldawer,[64] the degree of elastic anisotropy A in β'AuZn is 3.3, which is probably high enough to render certain dislocations unstable, and hence account for their zig-zag shape.

2.5.3.3.2 Variation in Dislocation Structure During Deformation at 293°K

2.5.3.3.2.1 (hko) Section

The effect of room temperature deformation on dislocation structure in foils cut approximately parallel to the glide plane and containing the [001] Burgers vector is shown in Figures 54 and 55. The structures shown are typical of those observed in several foils prepared from crystals strained 35% to the beginning of easy glide, Figure 54, and 130% to the end of easy glide, Figure 55. The most outstanding characteristic of the dislocation structure is the long, generally straight arrays of dislocation bundles. With increasing deformation, the dislocation content of the bundles increases while the average distance between any two appears to decrease slightly from ~2 to 1.5 microns. At the end of stage I, several areas along neighbouring bundles appear bridged by dislocations parallel to those within the bundle, giving rise to a rectangular shaped cell structure. Structural developments were not followed into stage II because of the increasing difficulty experienced in preparing satisfactory foils from the more heavily work-hardened crystals.

Crystallographic reference directions are shown on most electron micrographs. It is readily apparent that the direction of the bundles is perpendicular to the operative slip direction [001] suggesting that the dislocations comprising the arrays possess predominantly edge

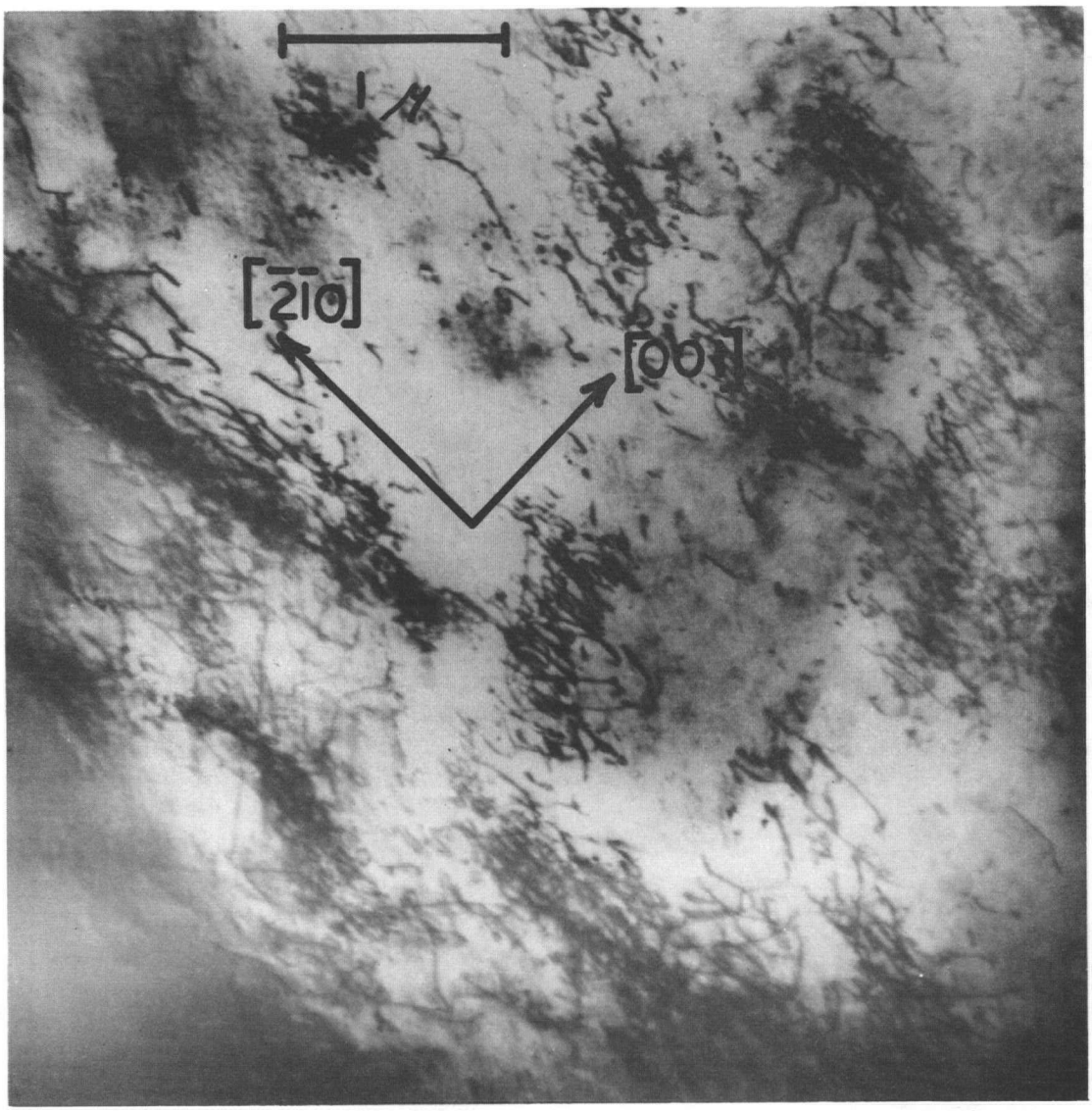

Figure 54.1

Figure 54. Electron micrographs of dislocation structure at the beginning of easy glide; (hko) sections parallel to macroscopic slip plane. (γ = 35%)

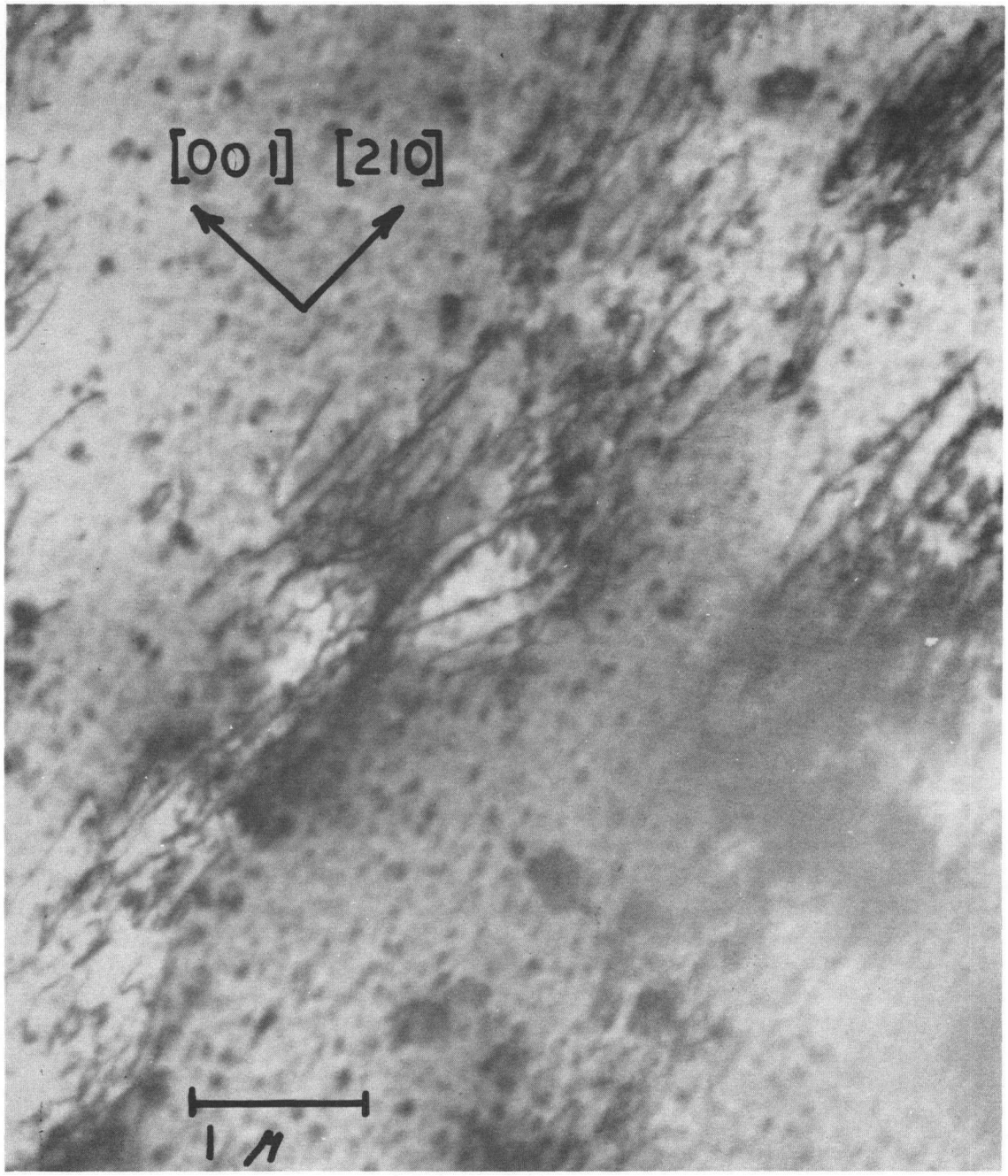

Figure 54.2

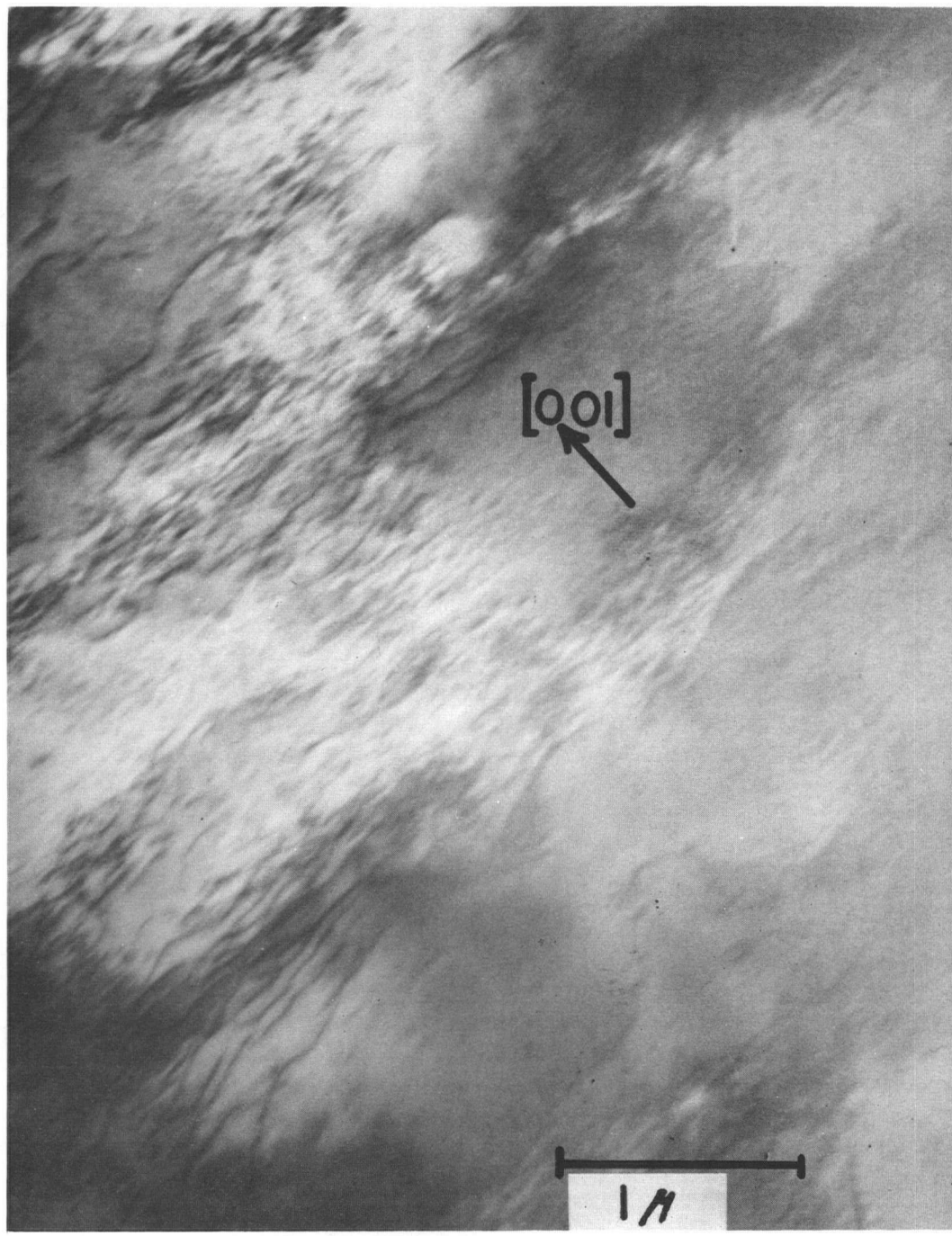

Figure 55.1

Figure 55. Electron micrographs of dislocation structure at the end of easy glide; (hko) section parallel to macroscopic slip plane. (γ = 130%)

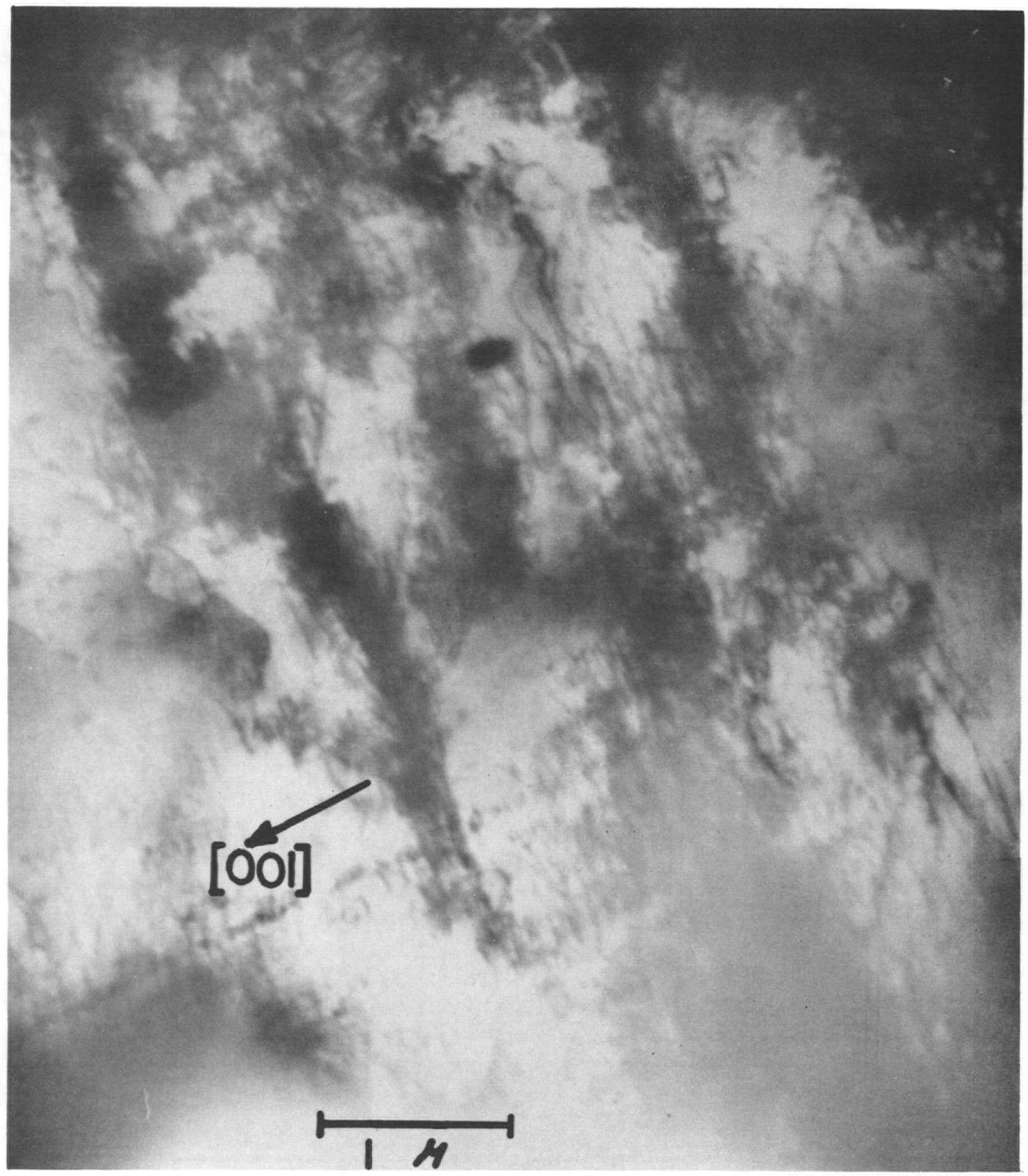

Figure 55.2

character. The absence of screw dislocations is noticeable in all micrographs. Analysis of dark field patterns employing the $\underline{g}\cdot\underline{b} = 0$ invisibility criterion[181], where $\underline{g}$ is the diffraction vector responsible for the dislocation contrast and $\underline{b}$ is the Burgers vector, showed that the Burgers vector of the dislocations in the bundles was consistent with [001]. However, detailed Burgers vector analysis to determine possible non-[001] dislocations in the clusters was not carried out since high resolution dark field photographs could not be obtained with the existing facilities.

2.5.3.3.2.2 (110) Section

Because of the non-crystallographic nature of the macroscopic slip plane, sections parallel to the fundamental (110) glide plane containing the slip direction [001] were also examined. Typical structures seen after 35% deformation are shown in Figure 56. It can be seen that no major differences exist between the dislocation structures on the macroscopic and fundamental glide planes, although the length of the clusters (bundles) on the (110) plane appears slightly greater than on the (hko) glide plane suggesting that the edge array may lie along $[1\bar{1}0]$ directions. The observation that the bundles penetrate the foil should not be taken as evidence against this suggestion, since even infinitely long bundles would pass through the foil which deviated slightly ($\sim 4°$) from (110). Because of this deviation the length of the bundle in the parent crystal is uncertain. During examination in the microscope, foils tilted to bring many (110) reciprocal lattice spots into reflection showed considerably longer bundles than are shown in Figure 56, often strung over distances of $\sim 15\mu$, suggesting that the bundles are at least this long.

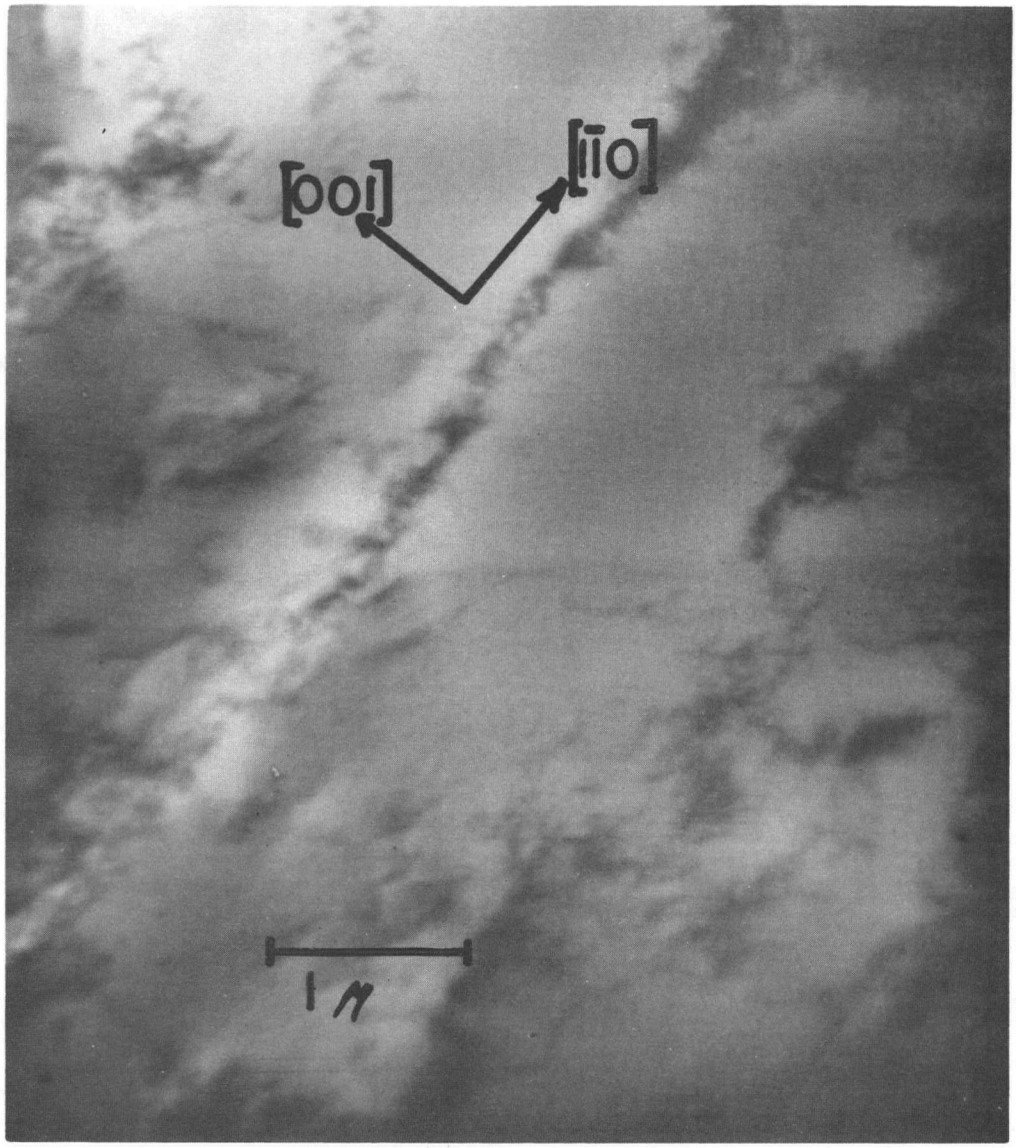

Figure 56. Electron metallograph of dislocation structure at the beginning of stage I; (110) section containing the Burgers vector [001].

2.5.3.3.2.3 Perpendicular (hko) Section

Sections perpendicular to the macroscopic slip planes and containing the [001] slip direction were examined to determine the extent to which these two-dimensional bundles formed walls perpendicular to the glide plane. Typical structures observed after 35% strain are shown in Figure 57. In comparison with the bundled arrays on the glide planes, contrast effects from the perpendicular sections are due to dislocations passing almost vertically through the foils. The piercing character of the dislocations was verified by tilting the specimen stage and observing the decreasing projected length of dislocation onto the film plane, Figure 58, as the foil approached a reflecting position effectively perpendicular to the (110) glide plane. From these sections dislocation density at the start of easy glide is estimated as $\sim 10^{9}$ cm/cm^{3}.

In Figure 57 it can be seen that the [001] slip direction is perpendicular to the dislocations, again suggesting that predominantly edge dislocations are present in the foil. In Figure 57.1 dislocations are observed to be along rows approximately parallel to both [210] and [001]. The same trend is evident in Figure 57.2, although the rows appear shorter. These observations suggest that the two-dimensional bundle arrays are in fact low walls ($\sim 2\mu$ high) of edge dislocations. Since the projected dislocation length decreased near the (110) reflections it is believed that the walls are perpendicular to the (110) fundamental glide plane. The [001] rows suggest that some of the bundles may be narrow carpets of dislocations lying in the glide plane.

2.5.3.4 Discussion

Three points must be explained: (1) the nature of the bundled

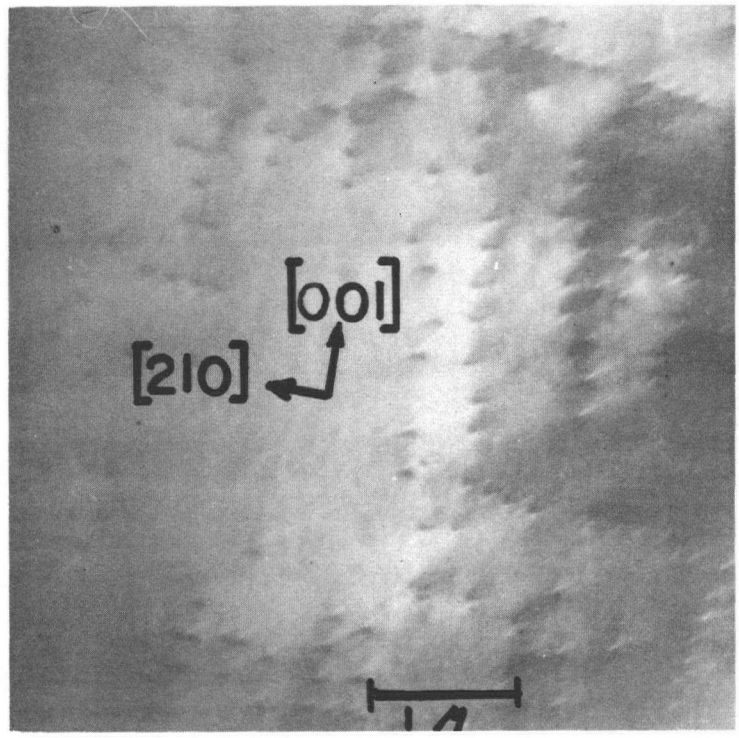

57.1

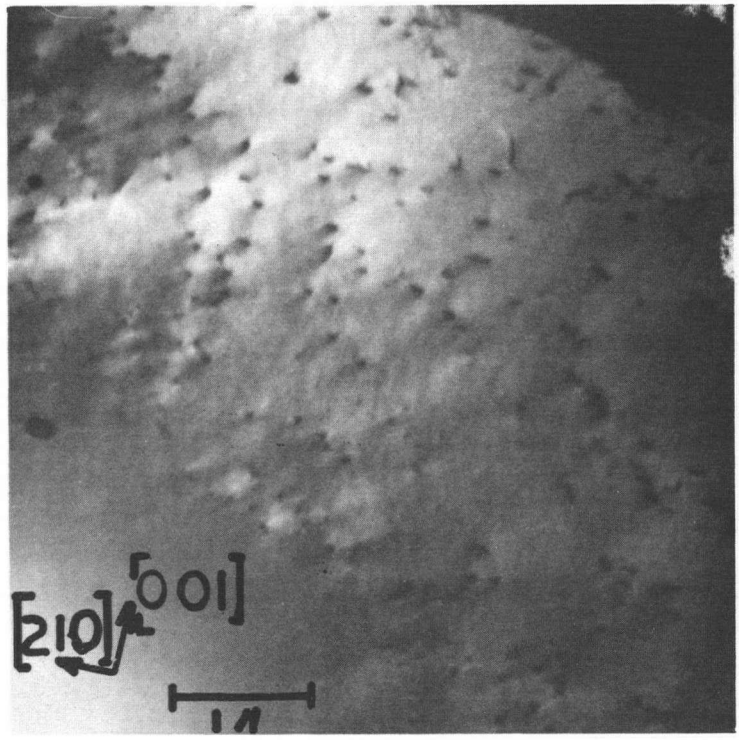

57.2

Figure 57. Electron micrographs of dislocation structure at the beginning of stage I; section perpendicular to the macroscopic slip plane and contains the [001] Burgers vector.

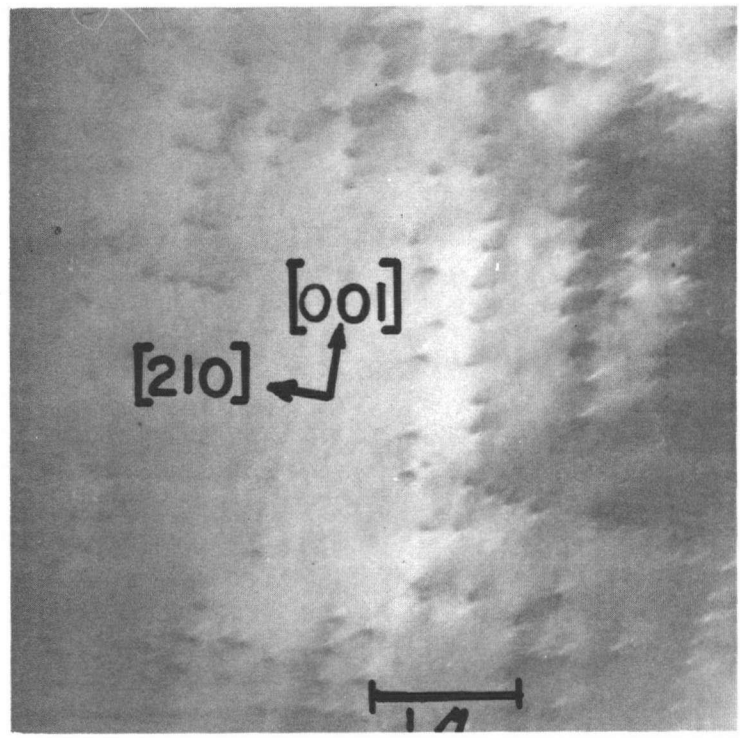

57.1

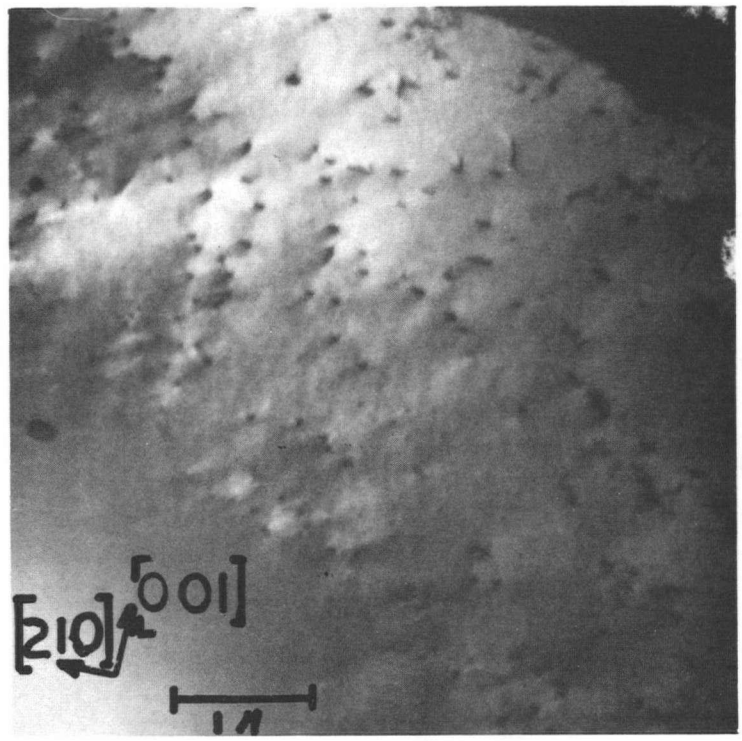

57.2

Figure 57. Electron micrographs of dislocation structure at the beginning of stage I; section perpendicular to the macroscopic slip plane and contains the [001] Burgers vector.

Figure 58. Electron micrograph of dislocation structure at the beginning of stage I; approximately perpendicular to (110).

array, (2) the mechanism of the wall formation, and (3) the absence of screw dislocations. These points will be considered in order.

Edge dislocation bundles ("clusters", "strands" or "braids") are a common feature of the stage I dislocation structure on the primary slip plane in many metal crystals of fcc[144,164,165,182], bcc[7,8,160] and hcp[167,183] structures. Characteristic, too, is the absence of screw dislocations. The edge clusters are usually arrays of dislocation dipoles, i.e. close pairs of dislocations of opposite sign lying along roughly parallel planes that may be frequently linked to form narrow closed loops of dislocation line. The bundles observed in AuZn are also believed to be comprised almost entirely of dislocation dipoles which often link to form closed loops as is seen particularly well in Figure 54. The bundles are comprised of approximately equal numbers of edge dislocations of opposite sign, as no net contrast changes are observed across the arrays, even at the higher stresses near the end of stage I.

A model for dipole formation in Mg crystals has been given by Hirsch and Lally.[167] Assuming that approaching edge dislocations of opposite signs on parallel slip planes trap one another, bands of dipoles form if the distance between the slip plane is less than a certain critical distance. This model is believed to account for dipole formation in AuZn as well. Assuming that slip occurs in part through the operation of Frank-Read sources, then at higher stresses when more sources operate, the distance between active slip planes decreases. Once the applied stress reaches a critical value, thought to be near the stress at the onset of stage I, sufficient slip planes are active and edge trapping may begin, forming the first dipoles. With increasing deformation, clusters of dipoles are expected to develop in the vicinity of the originals, giving

rise to an increased density of dislocations within the clusters, and subsequent wall growth.

The similarity between the crystallographic nature of the previously reported macroscopic deformation bands and the microscopically observed edge dislocation walls suggests that the mechanism of formation of both structures may be similar. If edge dislocation trapping can account for both structures, as suggested, the difference in scale between the bands and clusters may be explained if it is assumed that periodically extra-heavily populated clusters form which can give rise to an overall lattice tilt, large enough to be detected optically.

Whether or not screw dislocation annihilation by cross-slip as suggested by Hirsch and Lally[167] can account for the apparent absence of screws in AuZn is not known since sections inclined to the Burgers vector were not studied. Because of the ease with which cross-slip occurs in AuZn and since the foils examined were all parallel to the Burgers vector of the primary dislocations, it is highly probable that screw dislocations escape by cross-slip during the thinning process as suggested by Seeger.[144]

The foregoing discussion presupposes that the dipoles are formed in the bulk of the crystal during deformation. Evidence for this has been observed in Cu crystals where it was shown[175] that dislocation dipoles are present in foils prepared from specimens subjected to neutron irradiation pinning while still under stress. Clearly, similar irradiation under load of AuZn crystals is necessary before it can be ascertained whether or not the dipole structure is truly representative of the bulk arrangements, or whether it forms, in larger part, due to a relaxation of stresses within the foils during thinning.

2.5.4 Discussion

2.5.4.1 Yield Stress Variation with Orientation

It was shown that the yield stress resolved on the macroscopic slip system {hko} ⟨001⟩ is apparently independent of orientation (section 2.5.1.1), while the slip plane is orientation sensitive (section 2.4.5.3). However, the slip plane is not always the most highly stressed plane in the ⟨001⟩ zone suggesting that the yield stress on non-crystallographic planes should be a continuous function of their position in the zone. To resolve this apparent paradox, an attempt will be made to predict the relative variation of yield stress with orientation and then to note to what extent the apparent yield stress "invariance" with orientation is consistent with the predictions. This treatment is based on the Taylor analysis[44] used recently to analyze non-crystallographic slip in Fe-3% Si[46] and Ta[48] single crystals.

The resolved shear stress $\tau(\psi)^{\gamma}$ necessary for the onset of plastic flow on the potential macroscopic slip plane is given by the expression (Appendix 3):

$$\tau(\psi)^{\gamma} = \sigma \sin \xi_0 \cos \xi_0 \cos(\chi - \psi) \qquad (26)$$

where σ is the tensile stress at yield (ψ, χ and ξ are defined (in section 2.4.3). Assuming that $\tau(\psi)^{\gamma}$ is independent of ξ, as suggested by Figure 34, then on differentiating (26) with respect to ψ and rearranging, it is found that:

$$\frac{d\tau(\psi)^{\gamma}}{\tau(\psi)^{\gamma}} = \tan(\chi - \psi) \qquad (27)$$

which gives the variation of the shear resistance with the angle ψ. Integrating (27) between the limits 0 and ψ gives the espression:

$$\ln\left|\frac{\tau(\psi)^2}{\tau_{110}^2}\right| = \int_0^{\psi} \tan(\chi - \psi)\, d\psi \qquad (28)$$

where τ_{110}^2 is the resistance to shear on the (110) plane. From the experimentally determined ψ (χ) relationship, Figure 25, equation (28) was solved for $\frac{\tau(\psi)^2}{\tau_{110}^2}$ by employing Simpson's method for graphical integration. The resulting curve is shown in Figure 59 and is compared with the experimentally determined values of yield stress versus orientation from Figure 34. The experimental values are given relative to the yield stress for (110) slip, taken as 3850 psi.

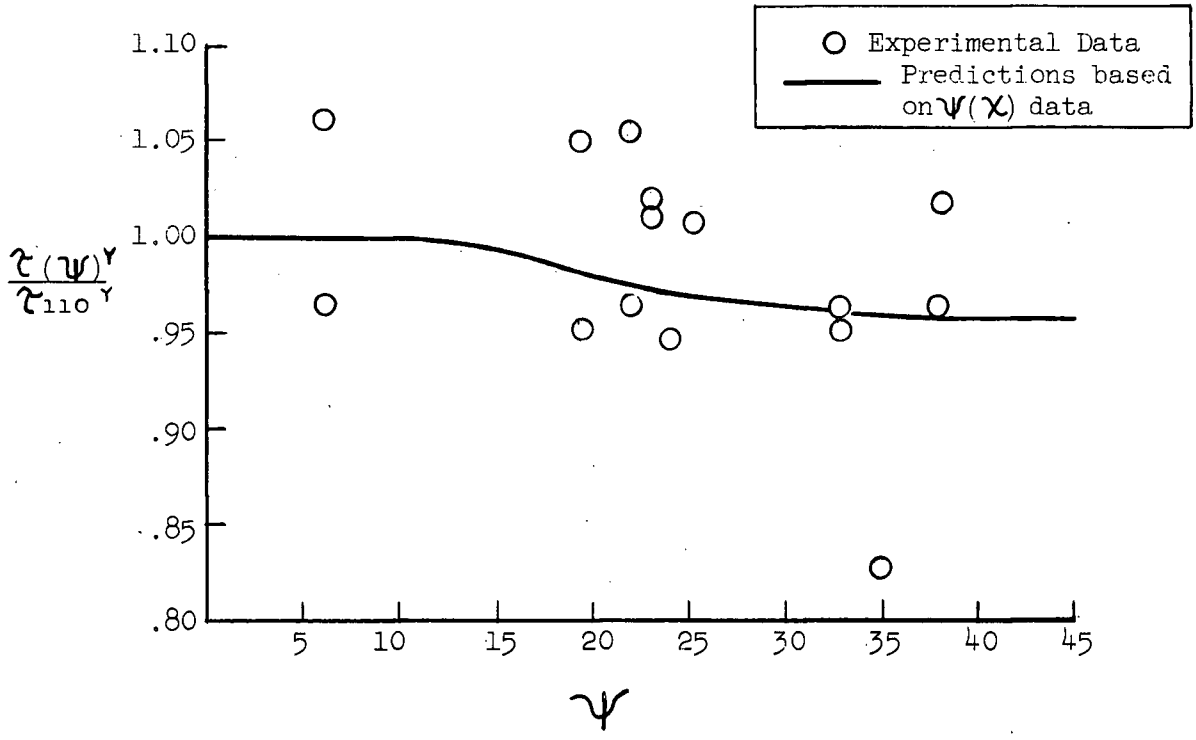

Figure 59. Showing the experimental compared with the predicted values of critical resolved yield stress ratio versus ψ.

Since the predicted orientation dependence of the relative yield stress varies by less than 5% over the orientation range $0 \leq \psi \leq 45°$ it is difficult to ascertain whether or not the somewhat scattered experi-

mental results display a similar trend. The apparent "invariance" in yield stress with orientation is therefore not in disagreement with the predictions. Clearly, before definite statements can be made concerning the yield stress dependence on orientation, experiments giving highly reproducible results must be performed.

If it is assumed that the fundamental glide system is (110)[001] as suggested earlier in the discussion of non-crystallographic slip (section 2.4.6.1), then the present results imply that as χ increases the critical resolved shear stress for (110)[001] slip decreases. For constant χ and varying ξ, the critical resolved shear stress on (110)[001] is constant. This may be explained by considering again the concept of dissociated screw dislocations contained on the (100) planes (section 2.4.6.1). As χ increases, so does the ratio of the shear stress resolved on (100)[001] to that on (110)[001] implying an increasing tendency for dislocation recombination relative to that for bowing-out in the sessile to glissile transformation process (Figure 31). Consequently, if recombination is the mechanism controlling the yield stress, then the critical resolved shear stress for (110)[001] slip should decrease with increasing χ, as observed. Since $\tau_{(100)[001]}/\tau_{(110)[001]}$ is independent of ξ, then the tendency for recombination relative to the bowing-out process is unchanged and the yield stress resolved on (110)[001] should be constant, again in agreement with experiment.

2.5.4.2. Work Hardening

It was shown that the form of the work hardening curves of β' AuZn single crystals changes markedly over the temperature range 77°K to 473°K from para-linear at low temperatures (below $\sim .15\ T_m$) to multi-

stage at intermediate temperatures (~.20 to .35 T_m) and then to parabolic followed by work-softening at higher temperatures (above ~.4 T_m). In this respect AuZn is entirely different from fcc and hcp crystals which are known to display multi-stage work-hardening curves at temperatures as low as 4°K. Recently deformation studies on crystals of bcc metals Nb[1] and Ta[9,10] have shown that the form of the work-hardening curves in these materials is also highly temperature sensitive, varying in much the same fashion as AuZn. The temperature range of three-stage hardening in Ta[9] corresponds to T_m ~ 0.10 to 0.18 while in Nb[1] to ~ 0.10 to 0.25, only slightly lower than the multi-stage hardening range in AuZn. The apparent likeness in the deformation behaviour of the ordered bcc compound and ordinary bcc metals suggests that similar hardening mechanisms may be controlling the flow stress in both instances.

The occurrence of cross-slip immediately upon the onset of plastic flow and the formation of dislocation dipole clusters on the primary glide planes during easy glide are features common to both AuZn and bcc metals, signifying a fundamental similarity in dislocation behaviour during deformation. Since dipole clusters have been observed in fcc and hcp crystals as well then it is believed that the fundamental AuZn-bcc metal relationship is linked mainly through the common continual cross-slip of screw dislocations. The motion of screw dislocations is known to be thermally activated. Consequently, the exact path along which screws move will depend on temperature and the extent to which temperature influences this motion could very well be the critical factor in subsequent work-hardening behaviour.

Since observations of three-stage hardening in bcc metals are relatively new, authors are concerned primarily with noting the rather

specific conditions of temperature, strain rate, orientation and impurity level under which multiple stage flow occurs. Effort is also being directed at studying the general work-hardening characteristics and attempts are being made to correlate dislocation structure observed in thin-foils with stage I and stage II hardening rates.[7,8,160,161] However, detailed models to account for stage I and stage II hardening such as those presented for the classically studied fcc and hcp metals have not been proposed. Based predominantly on electron metallography observations in thin foils, the general concensus of opinion seems to be that work-hardening in bcc metals can be explained in a similar way to fcc metals since analogous dislocation clusters and subsequent cell formation are common structural features of the work-hardened state. However because Θ_{II}, for instance, is approximately half that for fcc metals (Nb $\sim \mu/600$[2,7,8], Ta $\sim \mu/600$[9,10] Fe $\sim \mu/400$ to $\mu/900$[162] compared with $\Theta_{II} \sim \mu/200$ to $\mu/300$) and because it is quite strongly temperature dependent, it is probable that some important differences exist in hardening mechanisms for the two structures. Certainly, any model for stage II hardening in bcc metals must differ from fcc models by including temperature sensitive parameters.

Flow curves from crystals of the highly ordered bcc compounds AgMg[40] and NiAl[25,37] show essentially para-linear type hardening, although crystals of NiAl[37] compressed at 25°C in ⟨111⟩ and ⟨112⟩ orientations tend to deform in a two-stage manner. Work-hardening was not discussed. Some discussion, however, has arisen on the work-hardening mechanism in polycrystalline bcc ordered AgMg[38] and FeCo[125] which undergo ⟨111⟩ slip. Based on the creation of anti-phase boundaries resulting from the motion of superlattice partial dislocations $\frac{1}{2}$ a ⟨111⟩ these mechanisms predict an unusually high hardening rate, since as well as interacting with each other, superlattice dislocations, on intersecting, disorder the lattice

which alone is enough to increase the flow stress substantially.[125,127] This mechanism probably accounts for the exceptionally high work-hardening rate observed in AuZn crystals oriented near the [001] corner which deform on the {211} ⟨111⟩ system ($\theta_\ell \sim \mu/60$ compared with $\theta_{11} \sim \mu/500$ in orientations near the middle of the triangle.) It may also account for the higher linear hardening rate in specimens tested at 77°K ($\theta_\ell \sim \mu/200$) which are believed to undergo a minor amount of ⟨111⟩ slip. The disordering mechanism, however, is not applicable to AuZn tested under conditions giving rise to a ⟨001⟩ slip since this vector does not disorder the lattice.

The mechanisms of work-hardening in ordered bcc crystals undergoing ⟨001⟩ slip are in all likelihood, as complex, if not more so because of the two atom types, as in bcc metals and close-packed structures. To avoid speculation, a model will not be proposed. It will simply be shown where the present observations fit the framework of existing hardening theories. As shown stage I deformation is characterized by hardening rates in the order of $\mu/5000$ to $\mu/1000$ which are not greatly different from those in easy glide of fcc crystals[163] ($\sim 10^{-4}\,\mu$). Slip occurs on a single non-crystallographic system giving rise to dislocation dipoles which form walls perpendicular to the primary (110) glide plane. With increasing deformation the dislocation density within the walls increases and the average wall spacing tends to decrease slightly. These observations are very similar to those reported in fcc metals[144,164,165] and bcc Nb[7,8,160] suggesting that similar mechanisms may be responsible for the observed hardening.

Two principal theories have been proposed to explain work-hardening during easy glide in close packed crystals, that of Seeger et al[166] and of Hirsch and Lally.[167] The essential difference between the theories

is that of dislocation distribution. Based on slip line studies, Seeger et al consider that hardening arises chiefly from the long range interactions of the stress fields of individual dislocations randomly arranged in the lattice, while Hirsch and Lally rely on electron metallography observations and take the opposite view that stress fields associated with dislocation clusters present the dominant barrier to dislocation motion. If the clustered arrays observed in β' AuZn can be taken as truly representative of the work-hardened structure, then it would appear that the latter description is consistent with the observations.

The nature of stage II hardening is perhaps one of the most disputed topics in deformation theory today. Several mechanisms have been proposed in which the flow stress is controlled either by long range stresses from dislocations piled up at insurmountable obstacles,[144,168] by interactions with forest dislocations,[169] by sessile jogs on gliding dislocations,[170] by bowing-out of dislocation loops[171] or by dislocations piling-up at long continuous barriers whose effectiveness varies with distance from them.[172] The view is taken here that any of these models could probably account for the flow stress in AuZn, since essential to them all are elastic interactions between primary and secondary dislocations which are manifested in AuZn through slip on secondary systems detected at the end of stage I. The detailed differences between dislocation interactions probably accounts for the quite low values of θ_{11} in AuZn compared with fcc metals (μ /500 to μ /1200 compared with μ /200 to μ /300). Essential to a deeper understanding of hardening mechanisms in AuZn is a knowledge of the Burgers vectors of dislocations comprising the clusters. Since unequivocal Burgers vector analyses were not performed during these investigations possible dislocation interactions will not be speculated upon.

Stage III hardening also remains to be explained. The decrease in work-hardening rate at the onset of stage III in fcc metals is explained by the occurrence of thermally activated cross-slip of screw dislocations. Although thermal activation does play a role as evidenced by τ_{111} decreasing with increasing temperature, it is not known whether the cross-slip explanation applies to AuZn in which cross-slip occurs continually throughout deformation. It is possible, as suggested by Mitchell et al[1] for Nb, that either large-scale cross-slip or the breakdown of dislocation barriers causes the onset of stage III. Slip line observations did, in fact, show that large-scale cross-slip occurs quite early in the deformation of AuZn crystals (i.e. near the end of stage I), and becomes profuse during stage III, suggesting that this may be the dynamic recovery mechanism.

It was shown that specimens oriented along the [101]-[111] boundary of the stereographic triangle work harden in a parabolic or semi-two-stage manner, similar to the stage II-stage III region of flow exhibited by crystals oriented well within the triangle. Subsequent metallographic examination of deformed [101]-[111] crystals revealed that duplex slip occurs throughout deformation, thereby accounting for the absence of easy glide. Since the two systems operating are of the same general form as the primary and secondary stage II systems, viz. (hko)[001] and (okl)[100], similar dislocation interaction mechanisms are probably responsible for the high hardening rates in both the early stages of parabolic flow and stage II deformation. Whether the hardening results from long-range interactions of a[001] and a[100] dislocations or from obstacles created by reactions of the type a[001] + a[100] $\rightarrow$ a[101] against which dislocations pile up, is not known. It might be expected, though, that since the Burgers

vectors of the mobile dislocations are mutually perpendicular, the long-range interaction may be weak and hence not an effective hardening mechanism.

2.6 THERMALLY ACTIVATED YIELD

2.6.1 Introduction

Plastic deformation is now generally recognized as a dynamic, i.e. time dependent, process that may be thermally activated. Since plastic flow occurs through the movement of dislocations, it is believed that during the course of passage through the lattice, dislocations periodically contact obstacles that, unless overcome, cause the dislocation to stop. Obstacles are essentially of two types, short range, extending over distances in the order of ten atomic diameters and long range that possess stress fields of the order ten atomic diameters or greater. Thermal energy is able to assist the applied stress in pushing the dislocation past short range obstacles but, because of their extent, cannot aid in getting dislocations past the stronger long range obstacles. Hence the names thermal and athermal barriers to flow. At sufficiently high temperatures, all thermal barriers become transparent and dislocations pass through the lattice unimpeded once the applied stress has overcome the athermal barriers. At lower temperatures, however, thermal barriers are present and must be overcome by the assistance of stress and thermal energy if an applied strain rate is to be maintained. Usually several thermal barriers are encountered, the strongest of which determines the rate at which dislocations can move under the given conditions of temperature, stress and strain rate.

Assuming that thermally activated processes occur sequentially, i.e. one after another, and assuming that the same event is rate controlling throughout the lattice, then it is generally accepted that the macroscopic shear strain rate $\dot{\gamma}$ may be expressed by the relationship:[87]

$$\dot{\gamma} = \dot{\gamma}_o \, e^{-\frac{\Delta G}{kT}} \tag{29}$$

where $\dot{\gamma}_o$ is a parameter which depends on the number and arrangement of the dislocations and their vibrational frequency, ΔG is the change in Gibbs free energy of the system during an activated event and k and T have their usual significance. The process having the highest "activation energy" ΔG therefore controls the strain rate. If, on the other hand, thermally activated processes occur independently and the rate controlling step is not the same at all points in the lattice then the shear strain rate is given as:[65]

$$\dot{\gamma} = \sum \dot{\gamma}_i = \sum \dot{\gamma}_{oi} \, e^{-\frac{\Delta G_i}{kT}} \tag{30}$$

where i refers to the $i^{\underline{th}}$ kind of mechanism. In this case the application of activation theory for the purposes of identifying the rate controlling mechanism is not possible since one can no longer extrapolate macroscopic thermodynamic measurements to a single activated event occurring in a specific region of the lattice.

Schoeck[87] has recently obtained an expression for ΔG which has been modified slightly by Risebrough[89] and stands presently as:

$$\Delta G = \frac{\Delta H + T \, \frac{\partial \mu}{\partial T} \, \frac{\tau^*}{\mu} \, v^*}{1 - \frac{T}{\mu} \frac{\partial \mu}{\partial T}} \tag{31}$$

where μ is the shear modulus on the slip plane in the slip direction, and ΔH is the activation enthalpy , given by:

$$\Delta H = \frac{-kT^2 \left(\partial \ln \dot{\gamma}/\dot{\gamma}_o \right)}{\partial \tau^*}_T \left(\frac{\partial \tau^*}{\partial T} \right)_{\dot{\gamma}/\dot{\gamma}_o} , \text{ and} \tag{32}$$

v^* is the activation volume defined as:

$$v^* = -\left(\frac{\partial \Delta G}{\partial \tau^*} \right)_T = kT \left(\frac{\partial \ln \dot{\gamma}/\dot{\gamma}_o}{\partial \tau^*} \right)_T \tag{33}$$

and τ^* is the stress component effective in assisting the thermal energy in pushing the dislocation past the largest thermal obstacle and is defined[88] as the difference between the applied stress τ_a and the long range stress τ_μ acting in the vicinity of the barrier. The concept of activation volume arises when one considers the work W done on the system during an activation event, by the stress τ^* pushing a dislocation segment of length l^* a distance d^*:

$$W = \tau^* b\, l^*\, d^* \tag{34}$$

where b is the Burgers vector of the dislocation. Activation volume, then, is simply the term $b\, l^*\, d^*$.

To account for the temperature dependence of yield Seeger[88] postulated that the applied stress τ_a consists of two (previously defined) components τ^* and τ_μ such that:

$$\tau_a = \tau^* + \tau_\mu \tag{35}$$

For an ideal system in which the rate controlling thermally activated mechanism does not change below a critical temperature T_c (above which, thermal obstacles are transparent), the components of τ_a may be illustrated schematically, Figure 60. Since the rate controlling mechanism is no longer thermally activated above T_c, yield is only slightly dependent on temperature, decreasing through the small temperature changes in the shear modulus. Below T_c, however, the decreasing amount of thermal energy available for assisting the overcoming of short range barriers necessitates an increase in the effective stress term τ^* and hence a rise in yield stress. τ_μ varies through changes in the shear modulus.

To evaluate the activation parameters ΔG, ΔH and v^* it is necessary to evaluate the partial differentials $\left(\frac{\partial \tau^*}{\partial T}\right)_{\dot\gamma/\dot\gamma_o}$ and $\left(\frac{\partial \ln \dot\gamma/\dot\gamma_o}{\partial \tau^*}\right)_T$ at a constant structure, i.e. density, arrangement and

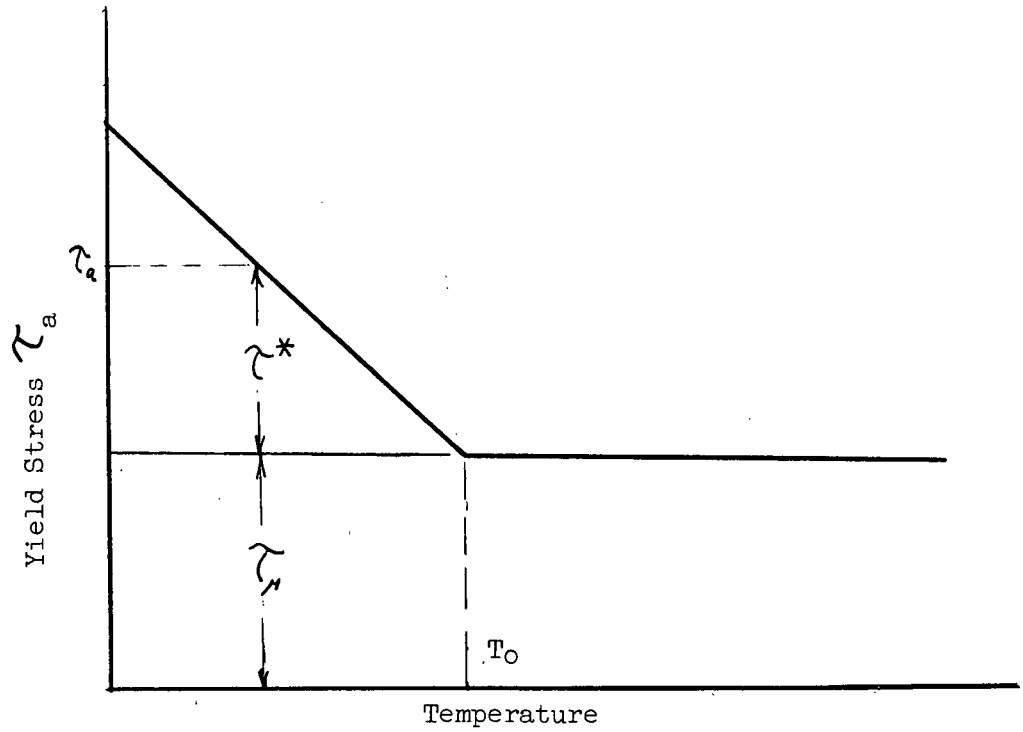

Figure 60. Illustrating the athermal τ_μ and thermal τ^* components of the yield stress τ_a. (after Seeger[88])

the number of mobile dislocations remaining essentially constant. Assuming the yield stress to be governed by the same thermally activated mechanism over the range of temperatures of interest, then one can consider that the structure is relatively constant at yield.[86] Hence, on subtracting τ_μ from τ_a (Figure 60) a plot of τ^* against temperature is realized and the slope $\left(\frac{\Delta\tau^*}{\Delta T}\right)_T$ may be taken as $\left(\frac{\partial\tau^*}{\partial T}\right)_T$. Likewise plots of τ_a versus $\dot{\gamma}$ at constant temperature can be adjusted (by subtracting τ_μ which is not strain rate sensitive, assuming a constant mechanism) to give τ^* against $\dot{\gamma}$ and hence allow $\left(\frac{\partial \ln \dot{\gamma}/\dot{\gamma}_o}{\partial\tau^*}\right)_T$ to be evaluated. Instead of studying strain rate effects on yield stress it is common practice to perform differential strain rate change tests on a single specimen during flow at a fixed temperature then to extrapolate to zero strain to evaluate the second partial.

The object of the experiments reported here was to measure the activation parameters in AuZn single crystals then to suggest a possible rate controlling mechanism responsible for the temperature dependence of yield (section 2.5.1.1). The discussion will be limited to stoichiometric crystals oriented near the middle of the stereographic triangle.

2.6.2 Activation Volume and Effective Stress

Flow stress differences accompanying instantaneous changes of strain rate may be taken as variations in effective stress $\Delta\tau^*$ with $\dot{\gamma}$ if it is assumed that the structure remains constant during the instant of change. Differential tests corresponding to strain rate changes from 10^{-4} to 10^{-2} per sec were carried out by varying the cross-head speed on the Instron from 0.002 to 0.20 inch per minute, and vice versa, using a push-button speed selector. Experiments were performed at temperatures ranging from 77°K to 213°K, i.e. over the temperature interval corresponding to temperature sensitive yield (Figure 33). Typical flow curve variations accompanying a strain rate change are shown schematically in Figure 61. In principle, both stress increments and decrements may be taken as $\Delta\tau^*$. However, because of less uncertainty in measurement, stress increments were taken in this work, by subtracting the flow stress τ_1 at the lower strain rate from the flow stress τ_2 at the higher rate. τ_2 was taken at the first deviation from linearity, following Basinski and Christian.[90]

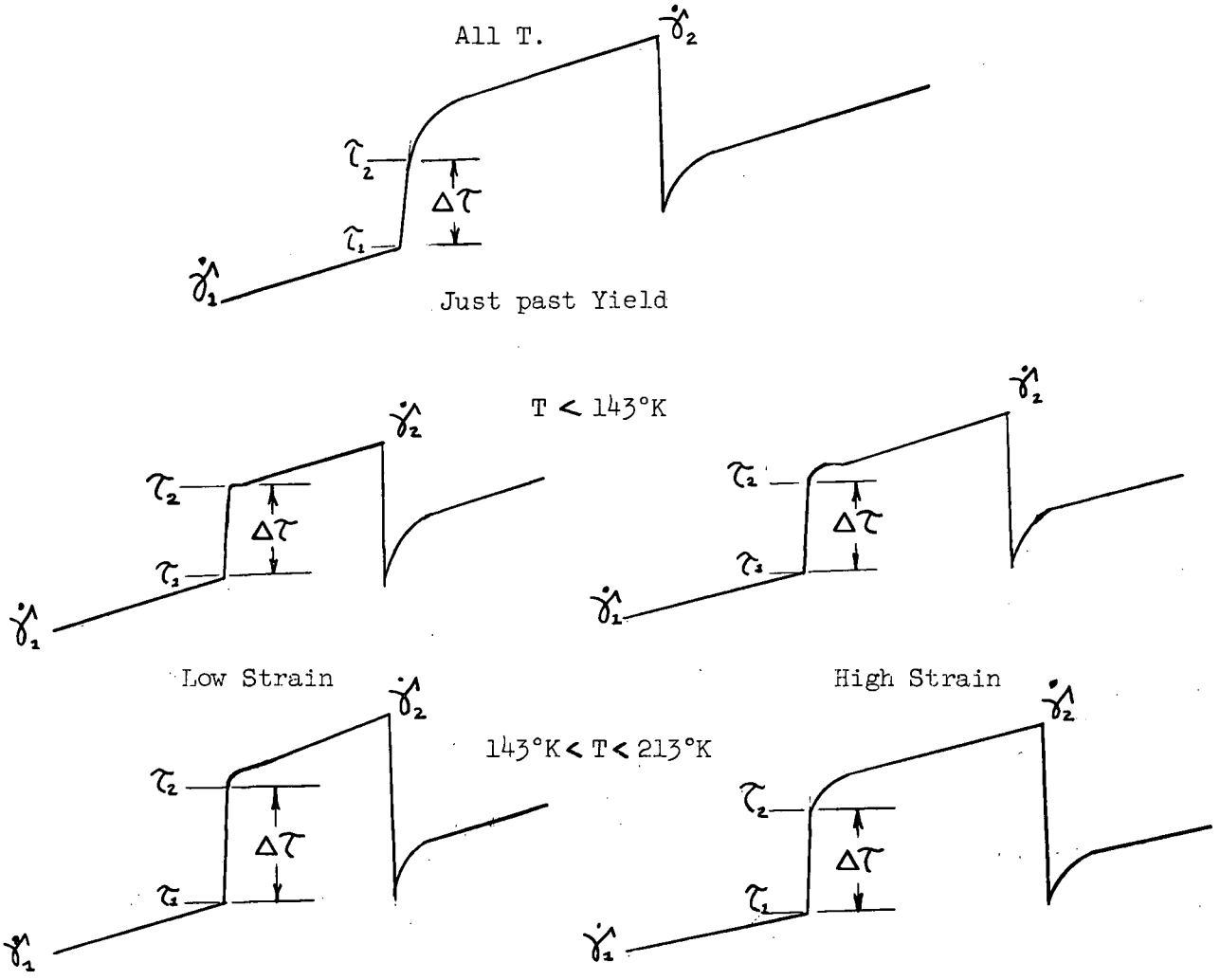

Figure 61. Schematic representation of changes in the flow curve accompanying strain rate change tests.

From the relationship presented in 2.6.1, activation volumes were calculated from:

$$v^* = kT\left(\frac{\ln \dot{\gamma}_2/\dot{\gamma}_1}{\Delta\tau}\right)_T \qquad (36)$$

and are plotted in Figure 62 (in units of b^3) as a function of shear strain; b is the Burgers vector of the mobile [001] dislocations and was taken as the lattice parameter 3.14×10^{-8} cm.[12] At 77°K the activation volume at yield, v^*_o, is $\sim 30b^3$ and is constant within $5b^3$ throughout deformation. As the temperature increases, v^*_o also increases and at the same time, becomes somewhat more strain (stress) sensitive, decreasing with increasing strain. At 213°K for instance, v^*_o decreases from $325b^3$ at

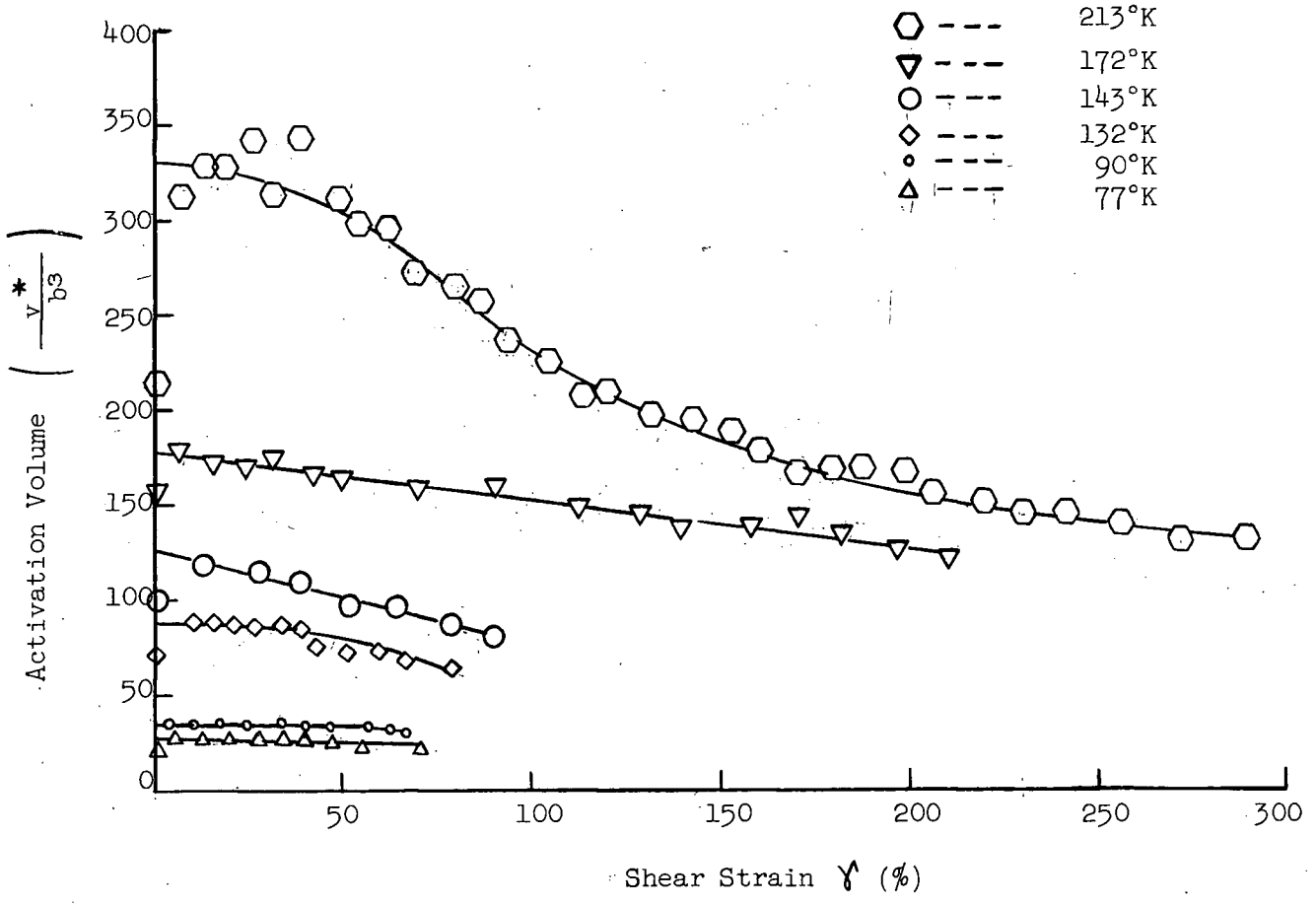

Figure 62. Activation volume against shear strain at temperatures between 77°K and 213°K.

yield to $130b^3$ at fracture.

In Figure 62 it can be seen that activation volumes determined just past yield at all temperatures are slightly lower than those obtained by extrapolating later values to zero strain. In all likelihood, the initially lower volumes are associated with uncertainties in determining $\Delta\tau$ since the departure from linearity with a strain rate increase just past yield is not nearly as marked as it is at higher strains (Figure 61). For the purposes of comparison and for calculating activation energies in section 2.6.3 activation volumes v_o^* extrapolated to zero strain will be employed.

Activation volumes are commonly plotted against the effective stress τ^*. To separate τ^* from the applied stress, the athermally attributed linear portion of the yield stress-temperature curve for stoichiometric crystals (Figure 33) was extrapolated to 0°K and at each temperature of interest below the critical temperature $T_c \sim 220°K$ the corresponding athermal stress component was subtracted from the yield stress. The subsequent τ^* - T results are plotted in Figure 63 and extrapolated to 0°K for future reference. Activation volumes, then, versus τ^* are shown in Figure 64. Also shown are the variations for polycrystalline AuZn and the bcc metals (V, Nb, Ta, Cr, Mo, W, Fe) over the same range of τ^* taken from the compiled data of Conrad and Hayes.[91] It is apparent that single and polycrystalline AuZn display exactly the same $v_o^* - \tau^*$ behaviour that falls within the range for the bcc transition metals, suggesting that similar mechanisms may be rate controlling.

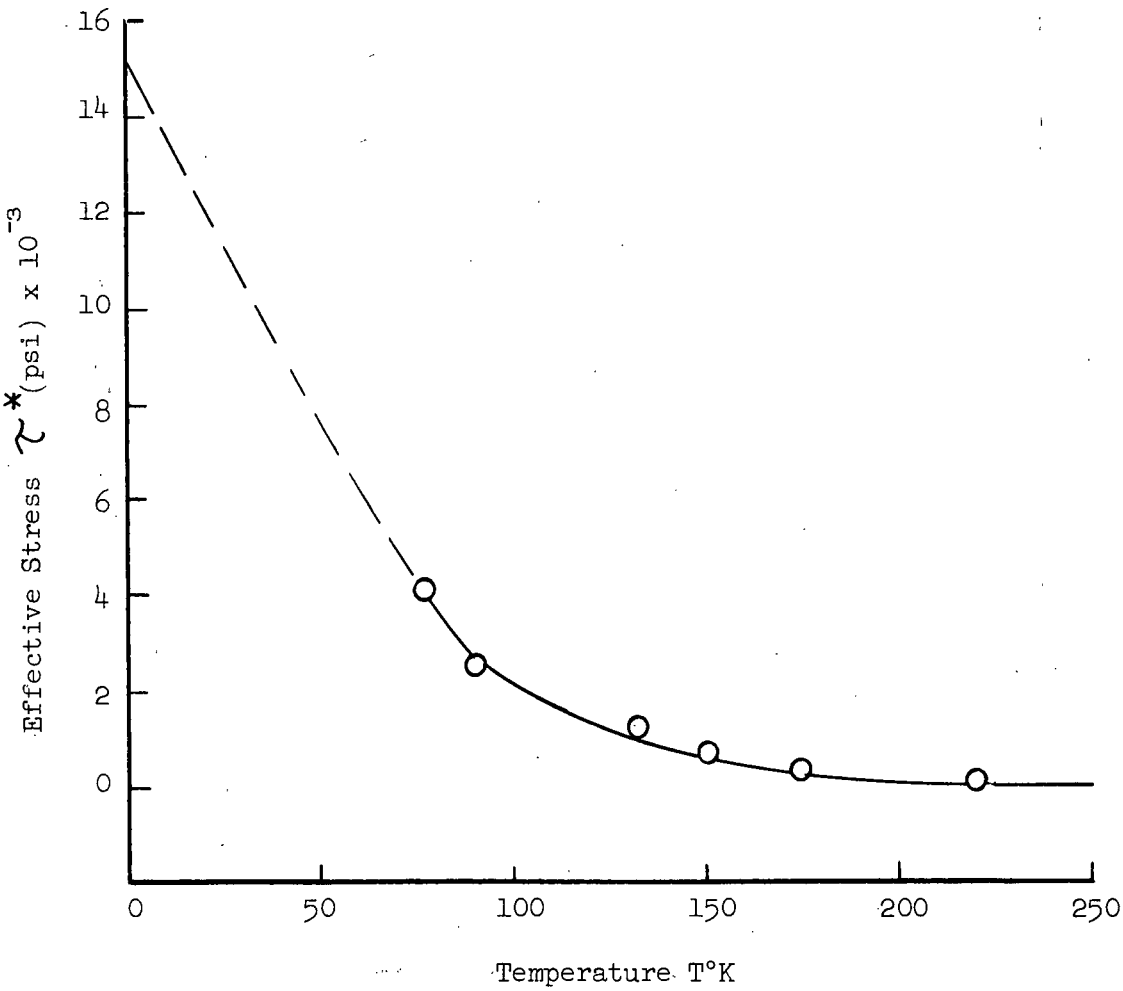

Figure 63. Showing the variation in effective stress with temperature.

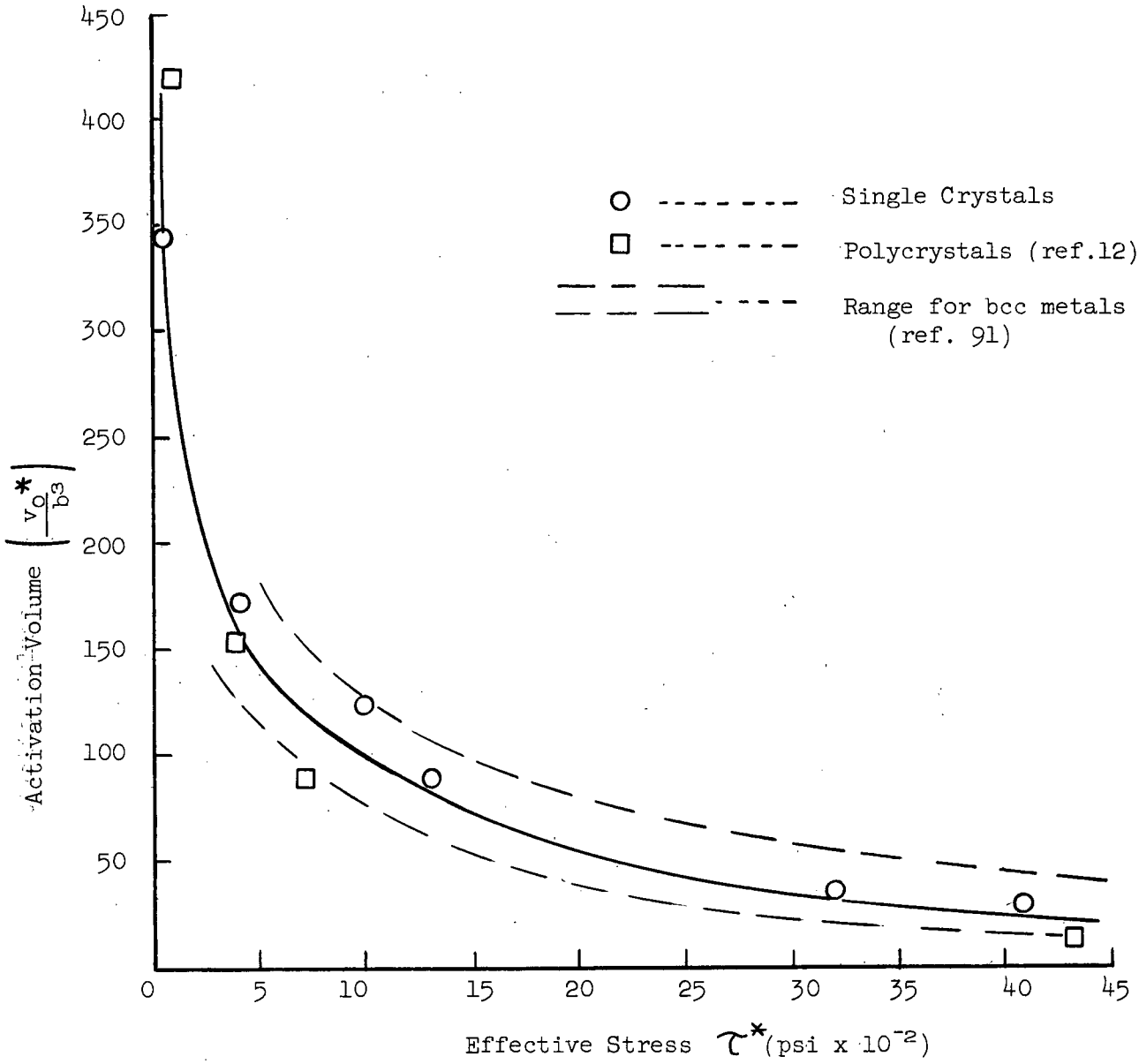

Figure 64. Showing the variation of activation volume with effective stress for β' AuZn and bcc metals.

2.6.3 Activation Energy

The expression given for the activation free energy ΔG in equation(31)when rewritten to include the terms for ΔH and v^*, gives the relationship:

$$\Delta G = -kT^2 \left(\frac{\partial \ln \dot{\gamma}/\dot{\gamma}_o}{\partial \tau^*}\right)_T \frac{\left[\left(\frac{\partial \tau^*}{\partial T}\right)_{\dot{\gamma}/\dot{\gamma}_o} - \frac{\partial \mu}{\partial T}\frac{\tau^*}{\mu}\right]}{1 - \frac{T}{\mu}\frac{\partial \mu}{\partial T}} \qquad (37)$$

It is assumed that the temperature variation of the elastic stiffness constants in AuZn is small implying that changes in shear modulus with temperature are also small. This assumption is justified on the basis that τ_μ, which is related to the shear modulus variation with temperature, increases only approximately 10 percent from 300°K to 0°K. Hence, the term $\frac{\partial \mu}{\partial T}\frac{\tau^*}{\mu}$ in equation(37)will be small and may be neglected with respect to the larger term $\partial\tau^*/\partial T$ giving the effective stress variation with temperature. ΔG may then be approximated as ΔH; i.e.:

$$\Delta G \approx - v^* T \left(\frac{\partial \tau^*}{\partial T}\right)_{\dot{\gamma}/\dot{\gamma}_o} = \Delta H \qquad (38)$$

As a measure of activation energy, therefore, activation enthalpies were calculated rather than activation free energies and are reported in Table 16 The term $\left(\frac{\partial \tau^*}{\partial T}\right)_{\dot{\gamma}/\dot{\gamma}_o}$ at different temperatures was evaluated from the slope of the τ^* - T curve, Figure 63.

To determine the height of the rate controlling thermal barrier, ΔH_o, it is necessary to measure ΔH when τ^* is zero.[91-94] Figure 65 shows ΔH versus τ^* and, when extrapolated to zero stress, gives $\Delta H_o \sim 0.9$ ev. For bcc metals,[91-94] ΔH_o is approximately $0.1\mu b^3$. On this basis, the controlling energy barrier in AuZn crystals is $\sim 0.15\mu b^3$ (where $b = a\langle 001\rangle = 3.14 \times 10^{-8}$ cm and $\mu = C_{44} = 3.0 \times 10^{11}$ dynes/cm^2)

and, therefore, of the same order of magnitude as the pure bcc metals, again suggesting that similar mechanisms may be rate controlling.

TABLE 16

Activation Parameters ΔH and v_o^* at Temperatures between 77°K and 175°K for Stoichiometric Crystals

T (°K)	v_o^*/b^3 (from Fig.69)	τ^*(psi) (from Fig.63)	ΔH (ev.) (from Equation 38)
77	30	4100	.23
90	33	3200	.29
100	50	2600	.35
125	76	1600	.46
132	90	1300	.49
143	125	1000	.66
150	137	800	.73
172	170	400	.72
175	200	350	.79

In polycrystalline AuZn, it was found[12] that $\Delta H_o \sim 0.43$ ev., about half of the single crystal value. Since activation volumes for both systems are in good agreement, part of the discrepancy may lie in the certainty of measuring $\left(\frac{\Delta\tau^*}{\Delta T}\right)_T$. In both instances the partial was measured from the slope of the corresponding yield stress-temperature curve. In polycrystals only five temperatures were used to establish the shape of the yield stress curve over the range of interest below ~250°K, whereas in single crystals yield stresses were measured more frequently giving a total of 13 points over the same temperature range, interjecting a greater degree of certainty in the measured $\left(\frac{\Delta\tau^*}{\Delta T}\right)_T$ terms.

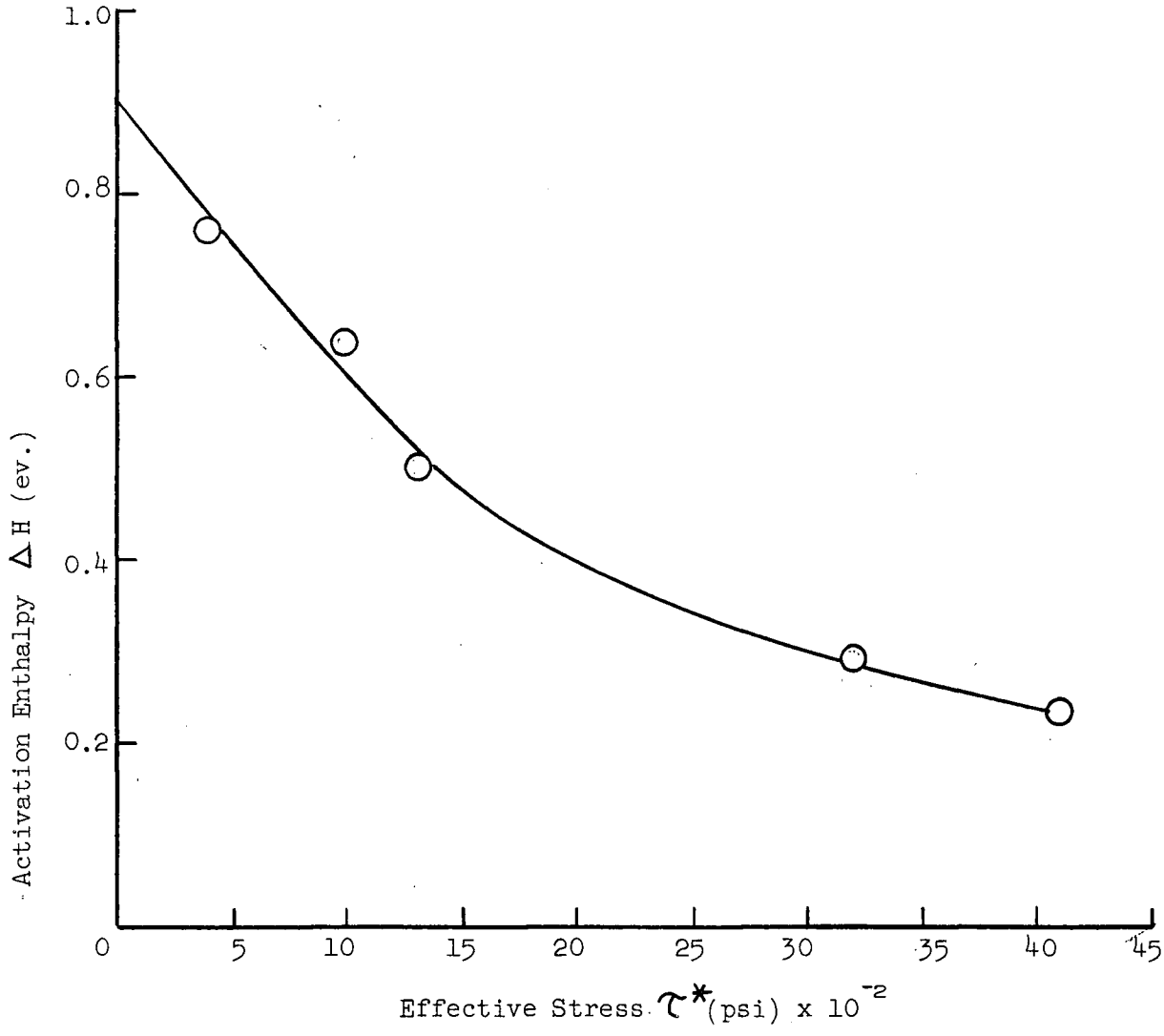

Figure 65. Showing the variation of activation enthalpy with effective stress.

2.6.4 Discussion

Since the present activation parameters are in accord with the results for bcc metals suggesting that similar mechanisms may be responsible for yield of AuZn, the commonly discussed bcc rate controlling mechanisms will be reviewed.

2.6.4.1 Impurity Obstacles

In view of the rather high interstitial content (Oxygen plus Nitrogen ~300 ppm Appendix 1), it is possible that dislocation-interstitial interactions could be controlling the yield stress. Assuming that the dislocation is bent to make nearest neighbour contacts with the impurity atom, then the distance l^* between obstacles is related to the impurity concentration C through the Burgers vector[97], $\frac{b}{l^*} \sim C^{\frac{1}{2}}$. For an impurity content of 300 ppm the shear stress necessary to push the dislocation between the obstacles, given by $\tau^* = \frac{\mu b}{l^*}$, is approximately $\mu/50$, which is equivalent to ~90,000 psi. On extrapolating the τ^* - T curve to 0°K (Figure 63) it was found that $\tau_o^* \sim 15{,}000$ psi which is considerably less than the stress necessary to push dislocation through impurity obstacles spaced 50b in the slip plane. Assuming that the dislocation makes three-dimensional nearest-neighbour contacts, then[98] $\frac{b}{l^*} \sim C^{\frac{1}{3}}$ and the corresponding stress necessary to push the dislocations through the obstacle field is $\mu/15$ and is greater than the theoretical shear strength of the lattice. In the light of an impurity model, it would also be difficult to explain the increase in activation volume with increasing temperature.

2.6.4.2 Peierls Nabarro (PN) Mechanism

It has been the conclusion of a great many workers that the rate controlling mechanism in bcc metals[91,94,95,96,99] and ordered alloy

AgMg[100,101] is the overcoming of the Peierls-Nabarro barrier to flow, i.e. the inherent lattice energy barrier that a dislocation, lying along close packed rows of atoms, overcomes as it moves from one equilibrium "valley" to the next. In surmounting the Peierls "hills" the configuration of atoms at the dislocation core is altered which therefore increases the dislocation energy. Hence the energy of a straight dislocation is a function of its displacement from the bottom of a "valley" and has the periodicity of the spacing between the parallel rows of atoms.

The critical step in the PN mechanism is the thermally activated nucleation of a pair of kinks that will subsequently move apart bringing the dislocation into its next equilibrium position, Figure 66.

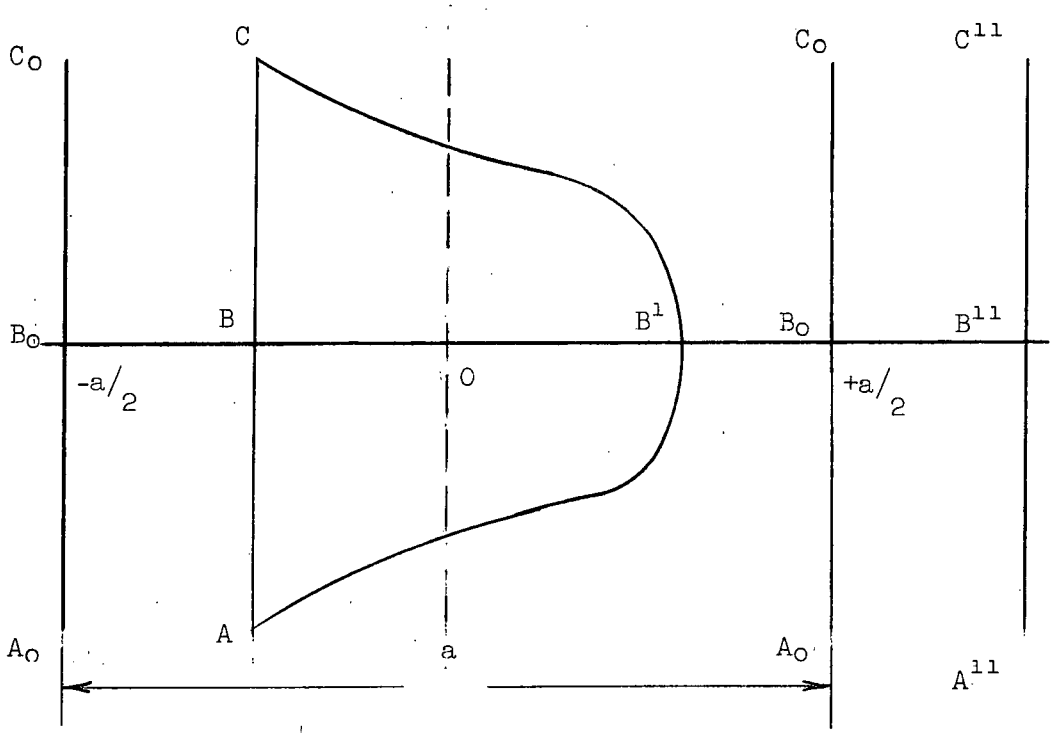

Figure 66. Schematic illustration of the PN mechanism.

The dislocation line initially lies along $A_oB_oC_o$ in an equilibrium position in the Peierls "valley". Under the action of an effective stress τ^* the dislocation moves from its equilibrium position to a new position ABC part way up the "hill". Thermal fluctuations occasionally supply enough energy to assist τ^* in pushing a dislocation segment AB'C over the "hill" thereby creating a double kink, AB' and B'C, which on moving apart, brings the dislocation into a new position A"B"C" ready for the next activated event.

On the basis of a line energy model of a dislocation, Dorn and Rajnak[103] have recently derived an expression for the energy U_k to nucleate a kink. Assuming that the Peierls "hill" is sinusoidal:

$$U_k = \frac{2\Gamma_o a}{\pi}\left(\frac{2\tau_p a b}{\pi\Gamma_o}\right)^{\frac{1}{2}} \qquad (39)$$

where Γ_o is the dislocation line energy per unit length in the low energy position $A_oB_oC_o$, a is the spacing between parallel rows of closely spaced atoms in the slip plane, τ_p the Peierls stress (the stress necessary, in the absence of thermal energy, to push the dislocation over the barrier) and b the Burgers vector. For a quasi-parabolic "hill", Guyot and Dorn[102] have derived the following expression for U_k:

$$U_k = \frac{\pi^{3/2}\Gamma_o a}{8}\left(\frac{2\tau_p a b}{\pi\Gamma_o}\right)^{\frac{1}{2}} \qquad (40)$$

The sinusoidal and quasi-parabolic profiles are shown in Figure 67.

Figure 67. Schematic illustration of the sinusoidal and quasi-parabolic Peierls "hill" profiles.

To evaluate the kink energy in AuZn, values for Γ_o and τ_p are necessary. Assuming that $\Gamma_o \sim 3.0 \times 10^{-4}$ ergs/cm (Table 4 ; {110}<001> system) and that τ_p at 0°K may be approximated as 15,000 psi (obtained by extrapolating τ^*- T to 0°K) the kink energy is then given as ~ 0.24 ev. When $\tau^* = 0$ thermal fluctuations must supply enough energy to nucleate a double kink, i.e. 2 $U_k \sim 0.48$ ev. If it is assumed that the PN mechanism is rate controlling over the whole range of temperature sensitivity of yield, i.e. below 220°K, then ΔH_o (i.e. at 220°K) should be equivalent to ~0.48 ev. Clearly the value 0.9 ev. obtained earlier is considerably larger than the energy estimated to nucleate a double kink. It appears therefore, that if the PN mechanism acts as a rate controlling process, it operates over a lower temperature range.

It is assumed that the PN mechanism is rate controlling below a critical temperature T_{cp} where T_{cp} may be estimated by noting the temperature at which the experimentally determined activation enthalpy is approximately 0.48 ev. From the data in Table 16, ΔH is plotted against T, Figure 68. Assuming that a straight line through the origin joins the points then $T_{cp} \sim 125$°K.

The plausibility of a PN mechanism controlling yield at tempera-

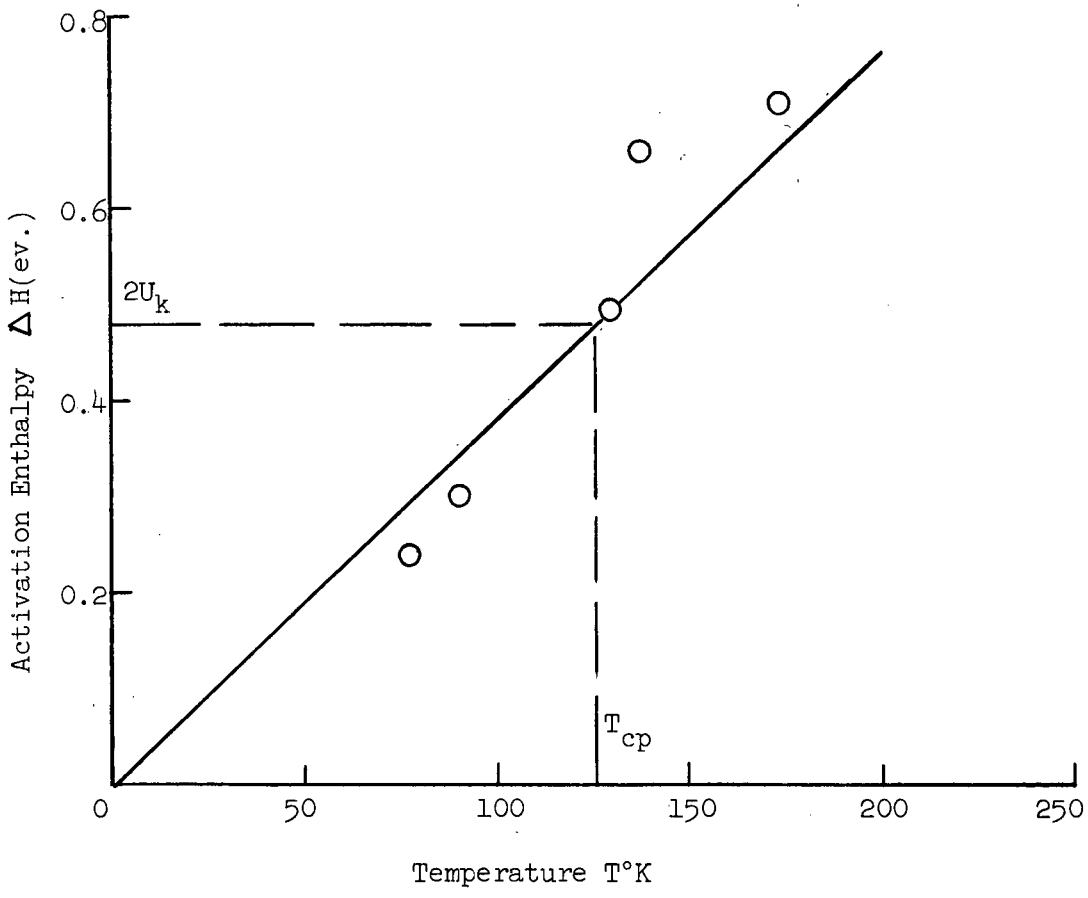

Figure 68. Showing the variation in activation enthalpy with temperature.

tures below ~125°K becomes apparent when one examines the activation volumes. Guyot and Dorn[102] have given an expression for the width w of the critical sized loop forming the embryonic kinks:

$$w = \frac{\pi}{2}\left(\frac{2a\,\Gamma_o}{b\,\tau_p}\right)^{\frac{1}{2}} \qquad (41)$$

where all parameters have the same meaning as defined earlier. The activation volume for the PN process is then expressed as: (42)

$$v^* = w\,a\,b$$

which upon substitution for Γ_o, T_p, a and b gives $v_o^* \sim 40b^3$, similar to the activation volume in AgMg[100,101] below 250°K. On comparing the calculated with the experimentally determined values plotted against temperature in Figure 69, it is apparent that below ~120°K, $v_o^* \sim 30\text{-}40b^3$ and is not strongly temperature sensitive, agreeing well with the dictates of a PN process. Above 120°K, v_o^* increases linearly with temperature suggesting that a different mechanism becomes rate controlling. It is noted that the critical temperature for a PN process estimated from the activation volume measurements is in good agreement with that deduced from the activation enthalpy calculations. That PN may be rate controlling below ~125°K is further evidenced by the fact that activation volume remains approximately constant during deformation (Figure 62). Analysis of polycrystalline data[12] was consistent with the dictates of a PN mechanism controlling yield below a critical temperature of approximately 150°K, a critical temperature slightly higher than the present temperature of ~125°K but in quite good agreement in view of the uncertainties in determining T_{cp}.

2.6.4.3 Cross Slip

In view of the extensive cross slip occurring continually during the deformation of AuZn, the possibility that it may control the

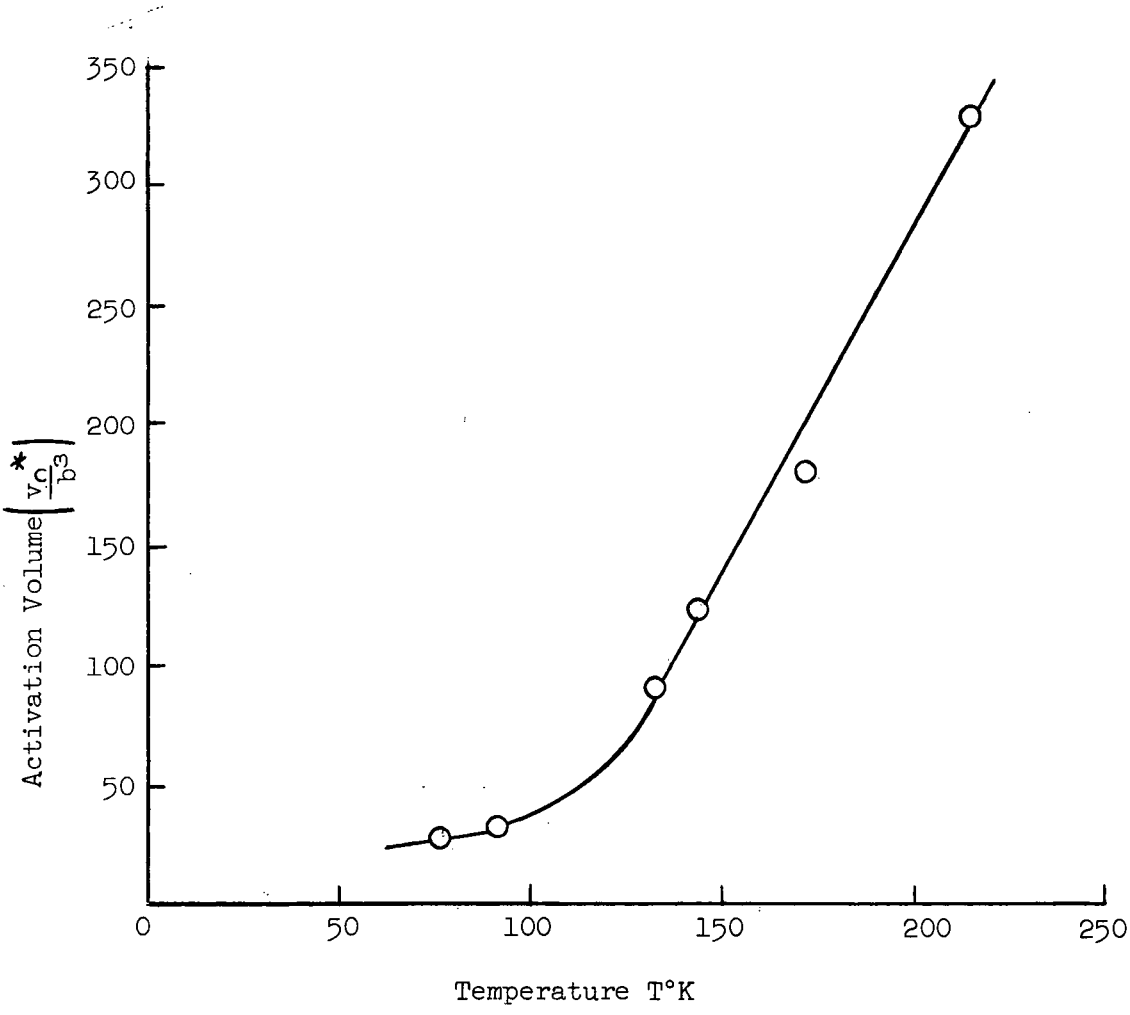

Figure 69. Showing the variation in activation volume with temperature.

deformation rate will be considered. The analysis will be a qualitative one, based on the experimentally determined activation volumes. Considering activation volume as the product of the activated length l^*, the activated distance d^* and the Burgers vector b and employing expressions given by Dorn[65] for the parameters d_c^* and l_c^* for the cross slip process, one arrives at an expression relating activation volume to effective stress:

$$v^* = \frac{A}{(\tau^*)^2} \qquad (43)$$

where A is a constant incorporating the line tension of the bowing-out dislocation and its Burgers vector. Since $v^* \propto \frac{1}{(\tau^*)^2}$, then qualitatively, activation volume should increase with decreasing τ^* (i.e. increasing temperature), as observed. On plotting ln v_o^* against ln τ^* in Figure 70, two regions of behaviour are apparent, from 77°K to ~150°K in which $v_o^* \propto \frac{1}{(\tau^*)^{1.5}}$ and from ~150°K to 213°K over which $v_o^* \propto \frac{1}{(\tau^*)^{0.5}}$. It appears, therefore, that below 150°K the activation volume variation follows quite closely the dictates of the cross slip mechanism suggesting that cross slip may be an alternative to the PN mechanism controlling yield at low temperatures.

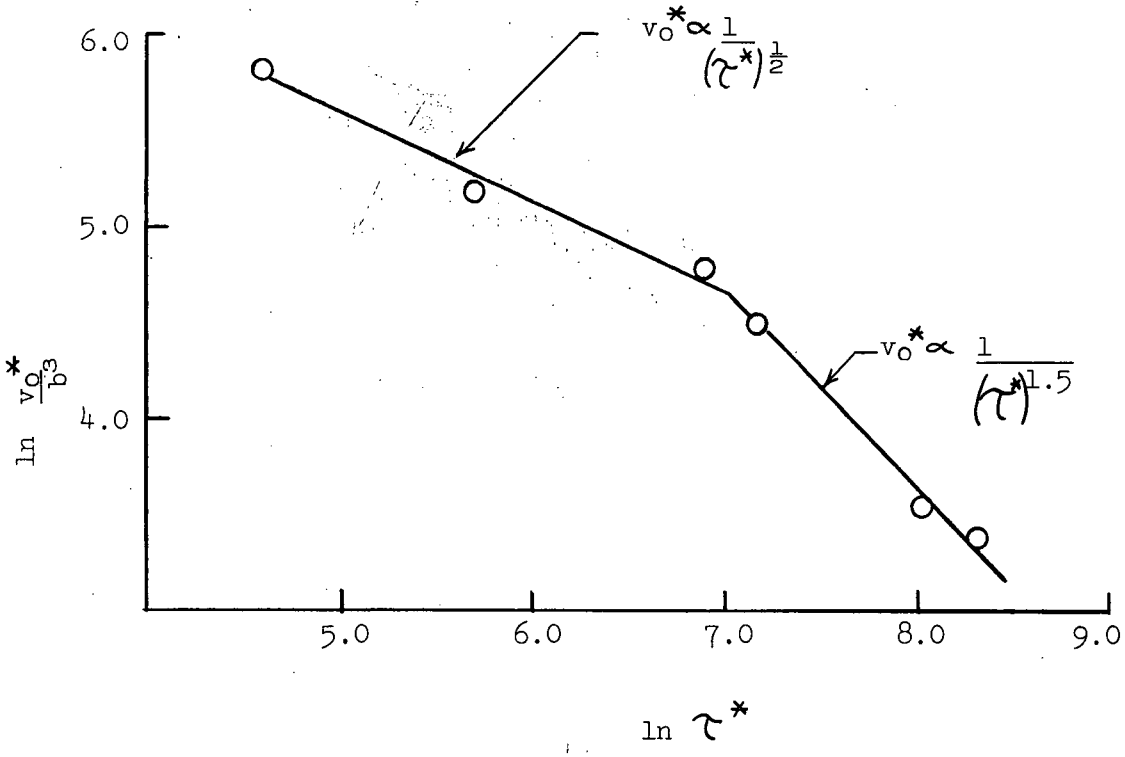

Figure 70. Showing the functional dependence of activation volume on effective stress.

3. SUMMARY AND CONCLUSIONS

1. The primary slip surface is a non-crystallographic plane (hko) in the zone of the slip direction [001]. With increasing temperature, decreasing strain rate and increasing distance of the tensile axis from the [001]-[111] boundary, the slip plane varies from (110) to (100). This phenomenon was interpreted in terms of continual cross-slip of screw dislocations on orthogonal planes (110) and $(1\bar{1}0)$.

2. Slip line observations indicate that edge dislocations can slip over large distances on $\{110\}$ planes while screw dislocations slip over much smaller distances. These observations are consistent with the continual cross-slip mechanism proposed to explain non-crystallographic slip.

3. Multi-stage work-hardening and associated large ductility as high as 300% shear strain has been observed for Au-rich (51.0 at.% Au), stoichiometric and Zn-rich (51.0 at.% Zn) crystals in the approximate temperature range $0.2 \lesssim T/T_m \lesssim 0.35$ and for all orientations within the standard stereographic triangle except near the [001] corner.

4. Following a short transition region (stage 0), stage I easy glide begins, characterized by relatively low hardening rates ($\mu/1000$ to $\mu/5000$). Transmission electron microscopy studies revealed walls of edge dislocations perpendicular to the primary glide plane which are believed to be the main cause of stage I hardening.

5. The principal effects of deviations from stoichiometry are to increase the flow stress and lengthen the extent of stage I.

6. The end of easy glide is coincident with slip on secondary systems of

the form (okl)[100] in localized regions of the crystal near deformation bands. The contribution of the secondary system to the overall deformation is negligible.

7. Stage II deformation commences after a fairly slow transition and the development of the secondary system probably accounts for the high work-hardening rate. θ_{11} is nearly independent of composition, but is somewhat sensitive to the other experimental variables, increasing with decreasing temperature, increasing strain rate and decreasing distance of the specimen axis from the [001]-[111] boundary. $\theta_{11} \sim \mu/500$, about half that for fcc metals.

8. The onset of stage III is coincident with slip line cluster formation all along the gauge section which is believed to result from large-scale cross-slip of screw dislocations.

9. At temperatures below ~150°K, para-linear hardening is observed. The onset of minor amounts of (011)[1$\bar{1}$1] slip at 77°K (as detected from Taylor analysis of asterism in a back-reflection Laue photograph) is believed to be responsible for the high linear hardening rate.

10. Increasing susceptibility to crack formation along (001) planes is believed to be responsible for decreasing ductility below ~250°K.

11. Above ~350°K, parabolic type hardening occurs followed by work softening and total strain to fracture decreases. This behaviour was explained in terms of increasing propensity for large-scale cross-slip.

12. Ductility increases with temperature above ~450°K, coincident with the operation, to about the same extent, of two slip systems of the general forms (hko)[001] and (okl)[100].

13. In orientations near the [001] corner of the stereographic triangle, $(\bar{1}\bar{1}2)[111]$ slip occurs. Hardening rates are very high ($\mu/60$) and ductility is low ($\sim$20% shear strain), presumably due to the disordering of the lattice resulting from the motion of superdislocation partials $\frac{a}{2}[111]$. The yield stress is about ten times greater than for $(hko)[001]$ slip.

14. Serrated flow was detected at temperatures between 293°K and 400°K for non-stoichiometric crystals and is attributed to a dislocation-solute atom interaction.

15. Deformation bands roughly parallel to (001) planes were detected in all orientations at temperatures above 140°K. It is suggested that the bands are a manifestation of the formation of edge dislocation walls of opposite sign.

16. It was found that the yield stress is approximately orientation insensitive and was shown to be consistent with predictions based on the observed variation of slip plane with orientation. These results were interpreted in terms of decreasing critical resolved shear stress for glide on (110)[001] with increasing distance from the [001]-[111] boundary, arising from the increasing ease of recombination of dissociated screw dislocations lying on (100) planes.

17. The temperature sensitivity of yield in stoichiometric crystals below ~220°K was subjected to thermal activation analysis. The dictates of either the Peierls-Nabarro mechanism or cross-slip of screw dislocations are consistent with the experimentally determined activation volumes and activation enthalpies below 150°K.

4. SUGGESTIONS FOR FUTURE WORK

The following questions arise from this work and can be considered as the most natural extensions of it:

1. What are the effects of a wider range of temperature and orientation on non-crystallographic slip and hence on the shape of the $\psi(\chi)$ and $\psi(T)$ curves? At constant strain rate, is the temperature at which the slip surface coincides with the most highly stressed plane in the <001> zone independent of χ?

2. Assuming fundamental (110)[001] slip, how will the critical resolved shear stress-orientation relationship $\tau(\psi)$ vary with temperature and strain rate?

3. What are the dislocation reactions leading to stage II work-hardening as revealed by detailed Burgers vector analysis of dislocation clusters using high resolution dark field techniques. Also, does <111> slip contribute to general deformation for orientations other than those near <001> and at temperatures above 77°K?

4. For near <001> orientations, is the slip plane in the zone of the slip direction <111> temperature sensitive? How does the critical resolved shear stress for <111> slip vary with temperature and strain rate?

5. Is serrated yielding a phenomenon inherent in the deformation of non-stoichiometric β' AuZn at intermediate temperatures and strain rates or is it a manifestation of dislocation-impurity atom interactions?

APPENDIX I

Crystal Homogeneity

A.1.1 Chemical Analysis and Composition Gradients

Specimens of approximately 300 mg. were accurately weighed then dissolved in 15 cc of warmed aqua regia. The solution was boiled to remove NO_2 then diluted to 200 cc with distilled water and warmed again. Hydrazine sulphate was carefully added to precipitate gold. The solution was left over night then subsequently filtered and the residue ashed at 600°C after drying at 150°C. The gold was carefully weighed and the zinc was determined by difference.

Crystals of three different nominal compositions, 49.0, 50.0 and 51.0 at % Au were grown and analyzed chemically for Au at five points along their length. The results are given in Table A1.1 and are plotted in Figure A1.1. All analyses were in duplicate and are accurate to within ~0.04 at %. To a first approximation, the average composition over the first two-thirds of the crystal to solidify deviates only slightly from the nominal composition.

In all crystals a region of high zinc content is noted over approximately the last third to solidify. In view of the large density difference between gold and zinc (ρ_{Au} = 19.3 g/cc; ρ_{Zn} = 7.1 g/cc) and the high vapour pressure of zinc at melt temperatures (775°C), it is not surprising that the last end to freeze should be zinc rich. Attempts to reduce the composition gradients by homogenizing the as-grown crystals in reduced pressure at a temperature sufficiently high for rapid diffusivity of zinc vapour met with no success.

TABLE A1.1

Chemical Analysis of As-Grown Crystals

Nominal Comp. (at. % Au)	Distance along the crystal (inch)	Composition (wt. % Au)
51.0	0.5	75.90
		75.89
	3.6	75.88
		75.85
	9.8	75.85
		75.84
	14.2	75.73
		75.70
	18.0	75.38
		75.45
50.0	0.8	75.00
		75.15
	2.4	75.16
		75.12
	7.0	75.13
		74.99
	11.6	75.06
		74.97
	14.2	74.42
		74.33
49.0	0.3	74.63
		74.61
	3.5	74.45
		74.62
	9.8	74.38
		74.32
	14.4	74.32
		74.29
	17.5	73.90
		73.88

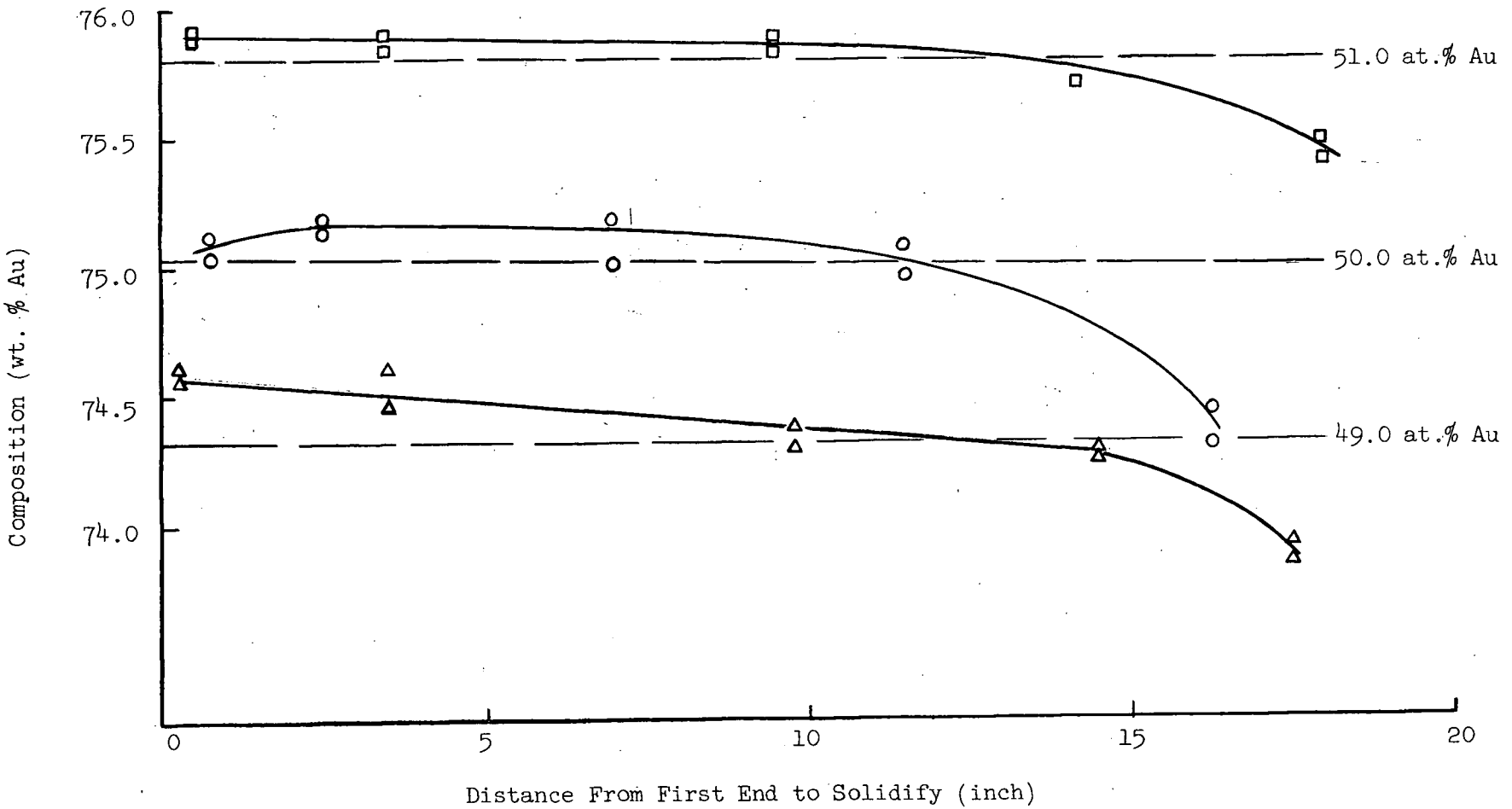

Figure A1. Showing composition gradients in as-grown β' AuZn single crystals.

A.1.2 Interstitials and Trace Elements

Results are given in Table A.1.2 for interstitial and trace element content in a typical β' AuZn tensile specimen, analyzed by Ledoux Analysts, Teaneck, New Jersey.

TABLE A.1.2

Impurity Analysis in Typical β' AuZn Tensile Specimen

Interstitial Element	Content (ppm)
Carbon	8
Oxygen	195
Nitrogen	127
Hydrogen	1
Trace Elements	Not Detected

APPENDIX 2

Evaluation of Machining Damage

Evidence that the cold-worked surface layers of the tensile specimens could be completely removed by polishing and annealing was obtained from back-reflection Laue diffraction patterns and room temperature tensile tests on stoichiometric specimens. The surface layers were removed in fresh 5% KCN solution. The variation in asterism with amount polished from the surface, Δd, is shown in Figures A2.1, A2.2 and A2.3. Tensile strength versus Δd for two series of experiments is shown in Figure A2.4 and the effect of annealing time and temperature on the yield strength of two different crystals is reported in Table A.2.1. For these latter tests, each specimen was strained just past yield then re-annealed and tested again. It is apparent that removing a surface layer 0.005 inch and annealing at 300°C for one hour renders the tensile specimens free from machining damage.

TABLE A.2.1

Effect of annealing temperature and time on the strength of two tensile specimens relative to the unannealed condition

Specimen	Δd (inch)	Annealing Temp.(°C)	Annealing Time (hr.)	Tensile Load at Yield (lb.)
E-1-7	0.0100	-	-	129
	"	300	1 h.	103
	"	300	3 h.	104
D-1-5	0.0094	-	-	42
	"	300	1 h.	35
	"	300	3 1/2	35
	"	425	1	34

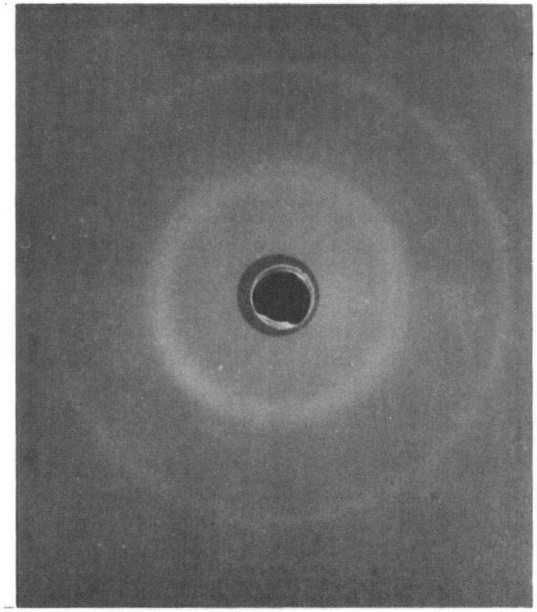

$\Delta d = 0$

A2.1

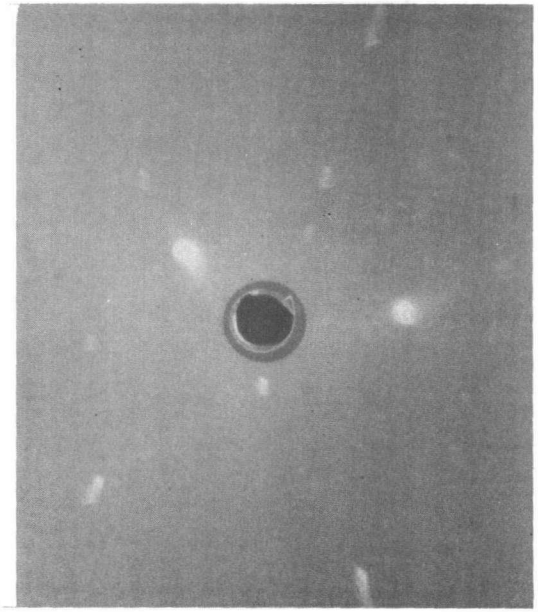

$\Delta d = 0.0033$ inch

A2.2

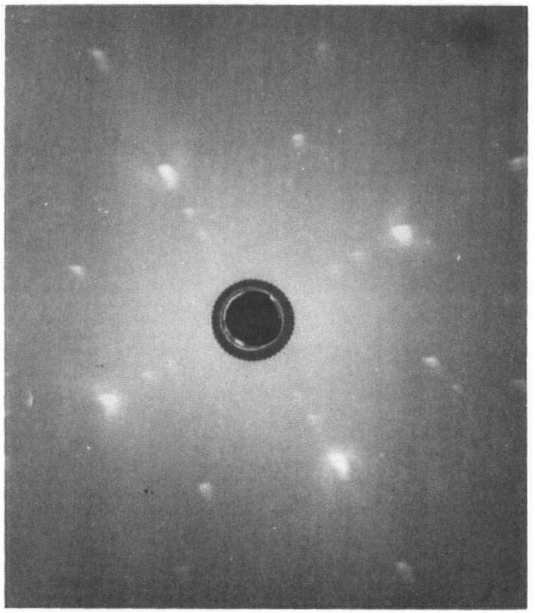

$\Delta d = 0.0098$ inch

A2.3

Figures A2.1, A2.2, A2.3. Showing the variation in degree of asterism with reduction of diameter of machined tensile specimens.

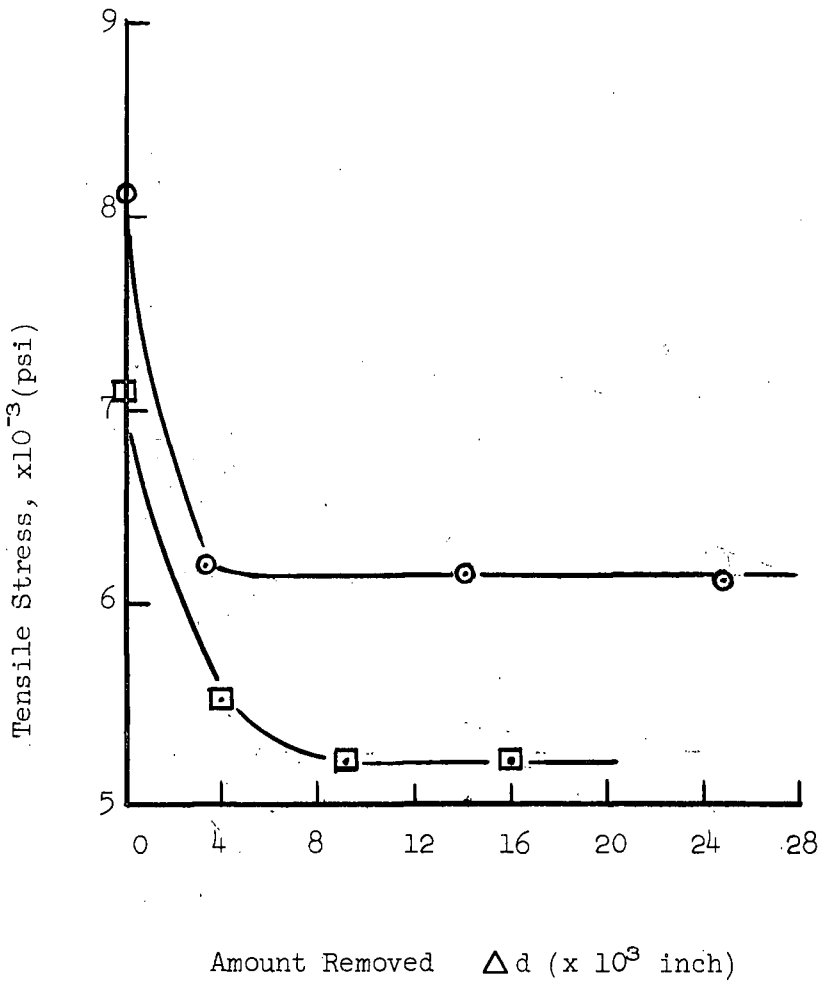

Figure A2.4. Showing tensile strength of machined crystal versus amount removed from the specimen diameter.

APPENDIX 3

Equations: Resolved Shear Stress $\tau(\psi)$ and Resolved Shear Strain $\gamma(\psi)$

The equations used in computing resolved shear stress $\tau(\psi)$ and resolved shear strain $\gamma(\psi)$ on the operative slip plane defined by the parameter ψ (section 2.4) were obtained in the following manner. From Schmid and Boas[49], the resolved shear stress and resolved shear strain acting on the operative slip system are given as:

$$\tau = \frac{P}{A_o} \operatorname{Sin}(90 - \phi_o) \frac{l_o}{l} \left[\left(\frac{l}{l_o} \right)^2 - \operatorname{Sin}^2 \xi_o \right]^{\frac{1}{2}} \tag{1}$$

and

$$\gamma = \frac{1}{\operatorname{Sin}(90-\phi_o)} \left(\left[\left(\frac{l}{l_o} \right)^2 - \operatorname{Sin}^2 \xi_o \right]^{\frac{1}{2}} - \operatorname{Cos} \xi_o \right) \tag{2}$$

where P is the instantaneous tensile load on the crystal, A_o the initial cross sectional area of the specimen, l_o and l the initial and instantaneous gauge lengths respectively, ξ_o the initial angle between the slip direction and the tensile axis and $(90-\phi_o)$ the initial angle between the slip plane and the tensile axis. The angle ϕ may be written in terms of the parameters ψ, χ and ξ (section 2.4) characterizing slip modes in β'AuZn. With the aid of Figure A3.1 and applying the cosine law from spherical trigonometry, it is found that:

$$\operatorname{Cos} \phi_o = \operatorname{Cos}(\chi - \psi) \operatorname{Sin} \xi_o \tag{3}$$

Therefore, in terms of the known parameters ξ_o, χ and ψ, τ and γ from (1) and (2) may be rewritten in the form:

$$\tau(\psi) = \frac{P}{A_o} \operatorname{Sin} \xi_o \operatorname{Cos}(\chi - \psi) \frac{l_o}{l} \left[\left(\frac{l}{l_o} \right)^2 - \operatorname{Sin}^2 \xi_o \right]^{\frac{1}{2}} \tag{4}$$

and

$$\gamma(\psi) = \frac{1}{\operatorname{Sin} \xi_o \operatorname{Cos}(\chi - \psi)} \left(\left[\left(\frac{l}{l_o} \right)^2 - \operatorname{Sin}^2 \xi_o \right]^{\frac{1}{2}} - \operatorname{Cos} \xi_o \right) \tag{5}$$

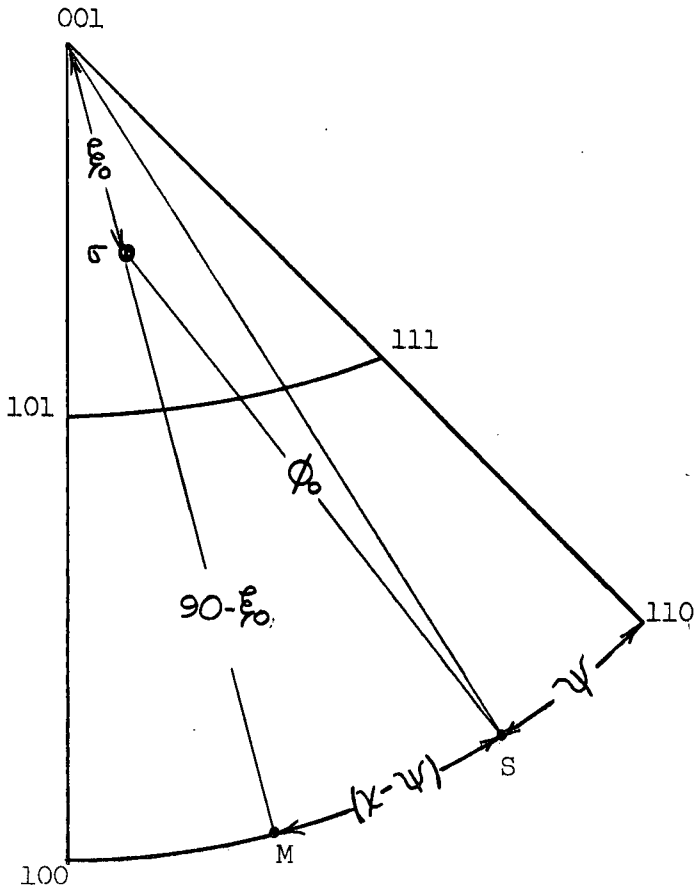
001
ε_0
S
111
101
ϕ_0
$90-\varepsilon_0$
110
ψ
$(\chi-\psi)$
S
M
100

Figure A3.1.

APPENDIX 4

Taylor Rotation Axes

(Re: Asterism at 77°K, Figure 22)

The Taylor rotation axis lies in the slip plane and is perpendicular to the slip direction. It is that axis about which the lattice rotates during slip on a given system. The identification of rotation axes from asterism on back-reflection X-ray photographs of deformed crystals is a commonly used technique for identifying slip systems.[156,157,158] Asterism shown in Figure 22 was assumed to arise from the operation of two slip systems operating simultaneously. It is known that asterism may also arise from deformation bands (for review, see Hirsch)[159], but this origin was ruled out since bands were not detected at 77°K. A typical branch from Figure 22 is illustrated schematically in Figure A4.1.

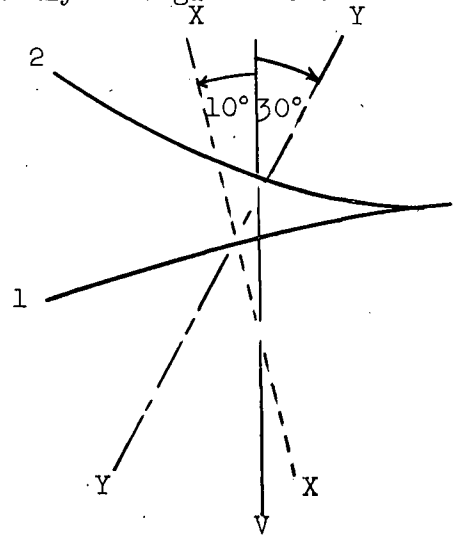

Figure A4.1. Sketch of asterism from Figure 22. V is the vertical axis in the film plane; X-X and Y-Y are associated with branches 1 and 2 respectively and are the projections of the rotation axes R_1 and R_2 onto the film plane.

The primary slip system at 77°K was found to be a non-crystallographic plane in the [100] zone lying ~6° from (011); a secondary

trace was coincident with the most highly stressed plane of the $\{110\}\langle 111\rangle$ system, namely (011). Representing the primary system as (011)[100] and assuming that the secondary system is (011)[1$\bar{1}$1], the Taylor rotation axes are then given as [01$\bar{1}$] and [21$\bar{1}$]respectively. To check the assumption all $\{110\}$ and $\{211\}$ poles are plotted stereographically in Figure A4.2 relative to the indexed diffraction spots from Figure 22. Also plotted are X-X and Y-Y, the film plane projections of the rotation axes R_1 and R_2 respectively, along which the poles of the axes must lie. It is seen that [01$\bar{1}$]lies on the Y-Y projection implying that slip on the (011)[100] system gave rise to asterism branch 2. The pole [21$\bar{1}$] is seen to lie along X-X, and thereby consistent with the assumption that one of the branches of asterism in Figure 22 (i.e. branch 1) is the result of (011)[1$\bar{1}$1] slip.

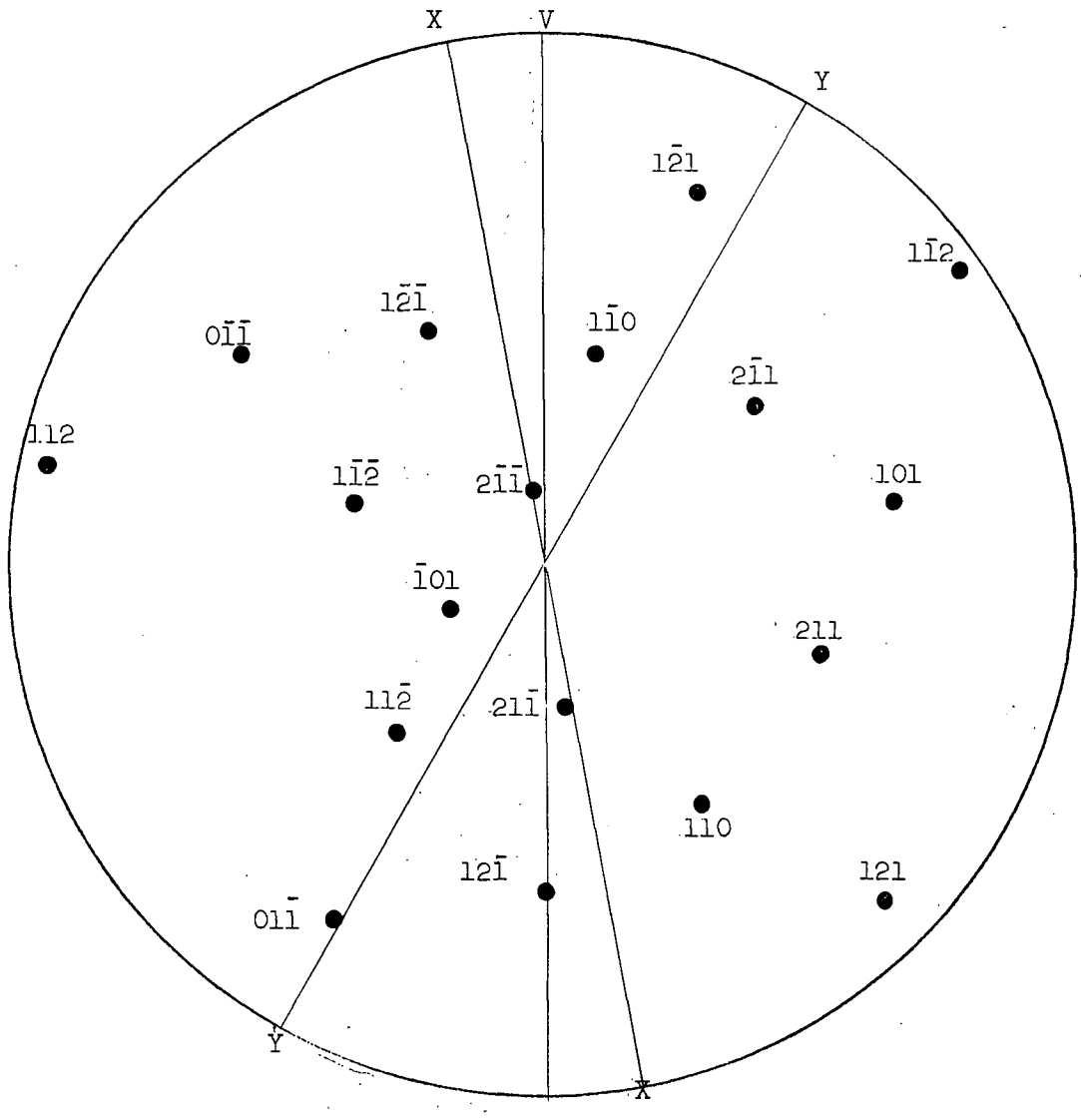

Figure A4.2. Stereographic projection of all {110} and {211} poles plotted with respect to indexed diffraction spots from Figure 22. The base circle represents the film plane. Rotation axes R_1 and R_2 lie on the great circles X-X and Y-Y respectively.

APPENDIX 5

Shear Modulus as a Function of Slip System

The work-hardening parameters τ_0, θ_1 and θ_{11} are often expressed in terms of the unitless quantities $\frac{\tau_0}{\mu}$, $\frac{\theta_1}{\mu}$ and $\frac{\theta_{11}}{\mu}$ where μ is the shear modulus characteristic of a given slip system. Expressed in this way, the quantities can be readily compared with similar terms characterizing work-hardening in other systems. During the course of the present investigations, similar quantities were obtained only after a general method had been established for evaluating μ as a function of slip system $\{hkl\}\langle uvw\rangle$. The method employed will be outlined in its general and hence most useful form using standard second order tensor notation and the repeated suffix convention.

The components of the stress tensor τ_{mn} relative to a right-handed set of orthogonal axes x_1, x_2, x_3 is given by the expression:

$$\tau_{mn} = C_{mnpq} \epsilon_{pq} \; ; \; (m, n = 1, 2, 3) \qquad (1)$$

where C_{mnpq} represent the elastic stiffness constants of the material and ϵ_{pq} is the corresponding strain tensor. Equation (1) defines completely the stress state relative to the $x_i (i=1,2,3)$ reference frame. In calculating shear modulii for a slip system defined by the unit vectors $\underline{n}$ and $\underline{\beta}$ (given in the x_i frame) where $\underline{n}$ is parallel to the normal of the $\{hkl\}$ slip plane and $\underline{\beta}$ is parallel to the slip direction $\langle uvw\rangle$, it is necessary to change the reference frame from x_i to a new set of orthogonal axes $\bar{x}_i$. The new frame is oriented relative to the old frame in such a manner that $\bar{x}_1$ is parallel to $\underline{\beta}$ and $\bar{x}_2$ is parallel to $\underline{n}$; $\bar{x}_3$ is then given by the vector $\underline{\beta} \times \underline{n}$ to form a right-handed system, Figure A5.1. Relative to the new system of axes the stress tensor $\bar{\tau}_{ij}$ is given by the second order tensor

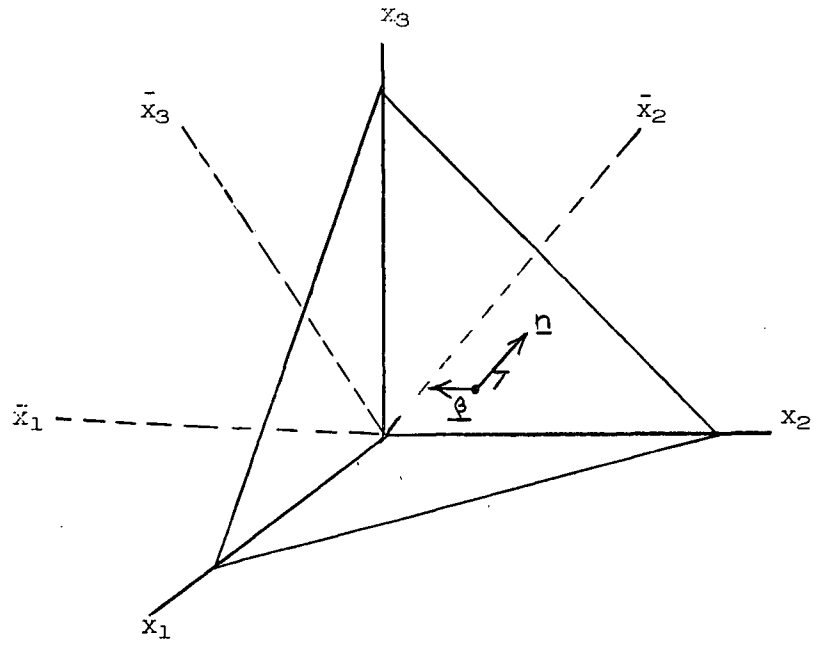

Figure A5.1. Showing the $\bar{x}_i$ reference frame relative to the x_i frame.

transformation law:

$$\bar{\tau}_{ij} = a_{im}\, a_{jn}\, \tau_{mn} \qquad (2)$$

where a_{ij} is the transformation matrix which relates the new frame to the old. In order to expand equation (2) into a term consisting of elastic constants and strain, it is necessary to express the strain tensor ϵ_{pq} in terms of a strain tensor in the new frame $\bar{\epsilon}_{kl}$ by employing the reverse transformation method for second order tensors:

$$\epsilon_{pq} = a_{kp} a_{lq}\, \bar{\epsilon}_{kl} \qquad (3)$$

where a_{pq} denotes the transformation matrix relating the old frame to the new. Combining equations (1), (2) and (3), the stress tensor in the new system is given by the expression:

$$\bar{\tau}_{ij} = a_{im} a_{jn} a_{kp} a_{lq} C_{mnpq}\, \bar{\epsilon}_{kl} \qquad (4)$$

The component of $\bar{\tau}_{ij}$ which is of special interest in determining $\mu(\underline{n}, \underline{\beta})$ corresponds to the stress acting on face $\bar{x}_2$ in direction $\bar{x}_1$; i.e. $\bar{\tau}_{21}$ which is given by:

$$\bar{\tau}_{21} = a_{2m} a_{1n} a_{kp} a_{lq} C_{mnpq}\, \bar{\epsilon}_{kl} \qquad (5)$$

Equation (5) will be considered again.

If it is assumed that lattice rotations within a body can be neglected as infinitesimal, then the stress tensor is symmetric regardless of the reference frame, i.e. $\tau_{mn} = \tau_{nm}$ and $\bar{\tau}_{ij} = \bar{\tau}_{ji}$. Symmetry then effects a reduction in the number of elastic constants characteristic of a general material from 81 to 36. The stress state can then be written in terms of a shortened notation:

$$\tau_m = C_{mn} \epsilon_n; \quad (n=1,2,\ldots 6) \tag{6}$$

The relationship between τ_m and τ_{mn} is seen by comparing the tensor τ_{mn} with the vector in six-space τ_m:

$$\tau_{mn} = \begin{vmatrix} \tau_{11} & \tau_{12} & \tau_{13} \\ \tau_{21} & \tau_{22} & \tau_{23} \\ \tau_{31} & \tau_{32} & \tau_{33} \end{vmatrix} = \begin{vmatrix} \tau_{11} & \tau_{12} & \tau_{13} \\ \tau_{12} & \tau_{22} & \tau_{23} \\ \tau_{13} & \tau_{23} & \tau_{33} \end{vmatrix} = \begin{vmatrix} \tau_1 & \tau_6 & \tau_5 \\ \tau_6 & \tau_2 & \tau_4 \\ \tau_5 & \tau_4 & \tau_3 \end{vmatrix} = \tau_m$$

Equation (5) will now be evaluated for the special case of cubic symmetry. Use will be made of the fact that all but 12 of the 36 elastic constants C_{mn} are zero, and of the 12 non-zero terms, only 3 are independent, namely c_{11}, c_{12} and c_{44}. The elastic constant matrix is then given as:

$$C_{mn} = \begin{pmatrix} C_{11} & C_{12} & C_{13} & 0 & 0 & 0 \\ C_{21} & C_{22} & C_{23} & 0 & 0 & 0 \\ C_{31} & C_{32} & C_{33} & 0 & 0 & 0 \\ 0 & 0 & 0 & C_{44} & 0 & 0 \\ 0 & 0 & 0 & 0 & C_{55} & 0 \\ 0 & 0 & 0 & 0 & 0 & C_{66} \end{pmatrix} = \begin{pmatrix} C_{11} & C_{12} & C_{12} & 0 & 0 & 0 \\ C_{12} & C_{11} & C_{12} & 0 & 0 & 0 \\ C_{12} & C_{12} & C_{11} & 0 & 0 & 0 \\ 0 & 0 & 0 & C_{44} & 0 & 0 \\ 0 & 0 & 0 & 0 & C_{44} & 0 \\ 0 & 0 & 0 & 0 & 0 & C_{44} \end{pmatrix}$$

From the greatly reduced number of non-zero elastic constants it can be seen that C_{mnpq} is non-zero only for the suffixes given in Table A5.1.

TABLE A5.1

Non-Zero Suffixes

C_{mn}	C_{mnpq}	Suffixes m	n	p	q
C_{11}	C_{1111}	1	1	1	1
C_{12}	C_{1122}	1	1	2	2
C_{13}	C_{1133}	1	1	3	3
C_{21}	C_{2211}	2	2	1	1
C_{22}	C_{2222}	2	2	2	2
C_{23}	C_{2233}	2	2	3	3
C_{31}	C_{3311}	3	3	1	1
C_{32}	C_{3322}	3	3	2	2
C_{33}	C_{3333}	3	3	3	3
C_{44}	C_{2323}	2	3	2	3
	$=C_{3232}$	3	2	3	2
	$=C_{2332}$	2	3	3	2
	$=C_{3223}$	3	2	2	3
C_{55}	C_{1313}	1	3	1	3
	$=C_{3131}$	3	1	3	1
	$=C_{1331}$	1	3	3	1
	$=C_{3113}$	3	1	1	3
C_{66}	C_{1212}	1	2	1	2
	$=C_{2121}$	2	1	2	1
	$=C_{1221}$	1	2	2	1
	$=C_{2112}$	2	1	1	2

By substituting values of C_{mnpq} and the appropriate suffixes from Table A5.1 into equation (5) an expression for $\bar{\tau}_{21}$ is obtained in terms of the independent elastic constants c_{11}, c_{12} and c_{44} and the direction cosines between the x_i and $\bar{x}_i$ reference frames. Following this procedure it was found that $\bar{\tau}_{21}$ is given by the relationship:

$$\begin{aligned}\bar{\tau}_{21} &= C_{11}\left[(a_{11}a_{21})^2 + (a_{22}a_{12})^2 + (a_{13}a_{23})^2 \right] \\ &+ 2C_{12}\left[a_{11}a_{12}a_{21}a_{22} + a_{11}a_{21}a_{13}a_{23} + a_{12}a_{13}a_{22}a_{23} \right] \\ &+ C_{44}\left[(a_{13}a_{22})^2 + (a_{12}a_{23})^2 + (a_{21}a_{12})^2 + (a_{13}a_{21})^2 + (a_{11}a_{23})^2 \right. \\ &\quad + (a_{11}a_{22})^2 + 2a_{22}a_{13}a_{23}a_{12} + 2a_{21}a_{13}a_{23}a_{11} \\ &\quad \left. + 2a_{21}a_{12}a_{22}a_{11} \right] \bar{\epsilon}_{21} + \text{other strain terms} \qquad (7) \\ &\quad (\bar{\epsilon}_{kl},\ k \neq 2,\ l \neq 1)\end{aligned}$$

The shear modulus $\mu(\underline{n}, \underline{\beta}) = \dfrac{\partial \bar{\tau}_{21}}{\partial \bar{\epsilon}_{21}}$ is computed directly from the coefficients of $\bar{\epsilon}_{21}$ in equation (7).

Consider the shear modulus for the $\{110\}\langle 001\rangle$ system. The transformation matrix is given as (Figure A5.2)

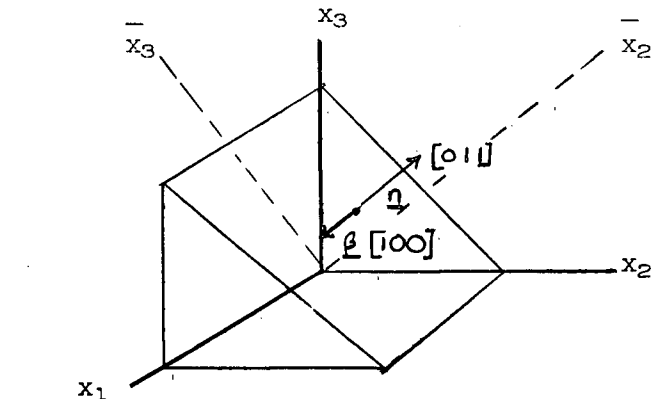

Figure A5.2.

$$a_{ij} = \begin{pmatrix} 1 & 0 & 0 \\ 0 & \frac{1}{\sqrt{2}} & \frac{1}{\sqrt{2}} \\ 0 & \frac{-1}{\sqrt{2}} & \frac{1}{\sqrt{2}} \end{pmatrix}$$

(It should be noted that the components of the first row of a_{ij}, namely a_{1j} are the components of a unit vector along $\bar{x}_1$ relative to the x_i frame. Likewise a_{2j} and a_{3j} are the components of unit vectors along $\bar{x}_2$ and $\bar{x}_3$ respectively. In a similar fashion the components of the first, second and

third columns of a_{ij}, namely a_{i1}, a_{i2} and a_{i3}, are the components of unit vectors along x_1, x_2 and x_3 respectively, relative to the $\bar{x}_i$ frame.) On substituting values of a_{ij} from the above matrix into equation (7) it is seen that:

$$\mathcal{M}\{110\}\langle 001\rangle = C_{44} \tag{8}$$

For the sake of completion, shear modulii were calculated on other possible slip systems in cubic structures and are given in Table A5.2.

TABLE A5.2

Shear Modulii for Various Slip Systems in Cubic Structures

Cubic Slip System	$\mathcal{M}(\underline{n}, \underline{\beta})$
$\{hko\}\langle 001\rangle$	C_{44}
$\{001\}\langle 110\rangle$	C_{44}
$\{110\}\langle 110\rangle$	$1/2\ (C_{11}-C_{12})$
$\{110\}\langle 111\rangle$	$1/3\ (C_{11}-C_{12}+C_{44})$
$\{111\}\langle 110\rangle$	$1/3\ (C_{11}-C_{12}+C_{44})$
$\{211\}\langle 111\rangle$	$1/3\ (C_{11}-C_{12}+C_{44})$

Since the transformation matrix is symmetrical with respect to $\underline{n}$ and $\underline{\beta}$, the modulus characteristic of plane $\underline{n}$ and direction $\underline{\beta}$ is the same as that characteristic of plane $\underline{\beta}$ in direction $\underline{n}$.

Note added in proof: Equation (4) could be obtained directly from equation (1) by noting that C_{mnpq} is a fourth order tensor and subjecting it to the transformation law for fourth order tensors, i.e.

$$\tau_{mn} = C_{mnpq}\,\epsilon_{pq}$$

$$\bar{\tau}_{ij} = \bar{C}_{ijkl}\,\bar{\tau}_{kl}$$

$$\bar{C}_{ijkl} = a_{im}a_{jn}a_{kp}a_{lq}C_{mnpq}$$

BIBLIOGRAPHY

1 T.E.Mitchell, R.A.Foxall and P.B.Hirsch, Phil. Mag. 8, 1895, (1963).

2 A.Seeger, "Dislocations and Mechanical Properties of Crystals, (Wiley, New York) p.243, (1957).

3 L.M.Clarebrough and M.E.Hargreaves, Prog. Met. Phys. 8, 1, (1959).

4 F.R.N.Nabarro, Z.S.Basinski and D.B.Holt, Advances in Physics, 13, 193, (1964).

5 F.Guiu and P.L.Pratt, Phys. Stat. Sol. 15, 539, (1966).

6 A.S.Keh, Phil. Mag. 12, 9, (1965).

7 P.A.Foxall, M.S.Duesbery and P.B.Hirsch, Can. J. Phys., 45, 607, (1967).

8 D.K.Bowen, J.W.Christian and G.Taylor, Can. J. Phys., 45, 903, (1967).

9 T.E.Mitchell and W.A.Spitzig, Acta Met. 13, 1169, (1965).

10 R.J.Arsenault, Phil. Mag. 15, 549, (1967).

11 A.S.Keh and Y.Nakada, Can. J. Phys., 45, 1101, (1967).

12 A.R.Causey, Ph.D. Thesis, University of British Columbia, (1967).

13 D.L.Wood and J.H.Westbrook, Trans. A.I.M.E. 224, 1024, (1962).

14 E.P.Lautenschlager, D.A.Kiewit, and J.O.Brittain, Trans. A.I.M.E., 233, 1297, (1965).

15 V.I.Syutkina and E.S.Yakovleva, Soviet Physics Solid State, 4, 125, (1963).

16 T.E.Mitchell and P.P.Thornton, Phil. Mag. 8, 1127, (1963).

17 H.Kronmuller, Z. Physik, 154, 574, (1959).

18 H.Pops and T.B.Massalski, Trans. A.I.M.E. 233, 728, (1965).

19 A.S.Argon and S.R.Maloof, Acta Met. 14, 1449, (1966).

20 D.F.Stein, Can. J. Physics, 45, 1063, (1967).

21 T.E.Mitchell and P.L.Raffo, Can. J. Phys., 45, 1047, (1967).

22 E.S.Greiner and D.M.Boulin, Trans. A.I.M.E., 239, 965, (1967).

23 C.N.Reid, A.Gilbert and G.T.Hahn, Trans. A.I.M.E. 239, 467, (1967).

24 R.M.Rose, D.P.Ferris and J.Wulff, Trans. A.I.M.E., 224, 981, (1962).

25 A.Ball and R.E.Smallman, Acta Met. 14, 1349, (1966).

26 W.A.Rachinger and A.H.Cottrell, Acta Met. 4, 109, (1956).

27 F.R.N.Nabarro, Advances in Physics, 1, 269, (1952).

28 W.L.Bragg and E.J.Williams, Proc. Roy. Soc. A151, 540, (1935).

29 A.Ball and R.E.Smallman, Acta Met., 14, 1517, (1966).

30 A.J.E.Foreman, Acta Met., 3, 322, (1955).

31 C.Zener, "Elasticity and Anelasticity of Metals", Chicago Univ. Press, 16, (1948).

32 A.K.Head, Phys. Stat. Sol., 5, 51, (1964).

33 J.D.Eshelby, Phil. Mag., 40, 903, (1949).

34 E.P.Lautenschlager, T.Hughes and J.O.Brittain, Acta Met., 15, 1347, (1967).

35 A.J.Dekker, "Solid State Physics", Prentice Hall, New Jersey, p.126, (1962).

36 N.S.Stoloff and R.G.Davies, Acta Met., 12, 473, (1964).

37 R.J.Wasilewski, S.R.Butler and J.E.Hanlon, Trans. A.I.M.E., 239, 1357, (1967).

38 J.C.Terry and R.E.Smallman, Phil. Mag., 8, 1827, (1963).

39 A.K.Mukherjee and J.E.Dorn, Trans. A.I.M.E., 230, 1065, (1964).

40 V.B.Kurfman, Trans. A.I.M.E., 236, 1050, (1966).

41 F.Laves, Naturwissenschaften, 30, 546, (1952).

42 M.J.Marcinkowski and R.M.Fisher, J. App. Phys. 34, 2135, (1963).

43 C.S.Barrett, "Structure of Metals", McGraw-Hill, p.40, (1952).

44 G.I.Taylor, Proc. Roy. Soc., A118, 1, (1928).

45 M.S.Duesbery, R.A.Foxall, and P.B.Hirsch, J. De Physique, 27, C3-193, (1966).

46 T.Taoka, S.Takeuchi and E.Furubayashi, J. Phys. Soc. Japan, 19, 701, (1964).

47 B.Sestak, N.Zarubova, and V.Sladek, Canad. J. Phys. 45, 1031, (1967).

48 J.F.Byron and D.Hull, J.Less.Common Metals, 13, 71, (1967).

49 E.Boas and W.Schmid, "Plasticity of Crystals", Hughes, London, 1950.

50 J.R.Low and R.W.Guard, Acta Met. 7, 171, (1959).

51 F.Kroupa and V.Vitek, Canad. J. Phys. 45, 945, (1967).

52 B.Sestak and S.Libovicky, "Relation Between the Structure and Mechanical Properties of Metals", N.P.L. Symposium, Tedington, 158, (1963).

53 B.Sestak and N.Zarubova, Phys. Stat. Sol. 10, 239, (1965).

54 A.Gemperle, communicated by F.Kroupa and V.Vitek, Discussion, Canad. J. Phys. 45, 971, (1967).

55 B.H.Kear, Acta Met., 12, 555, (1964).

56 S.M.Copley and B.H.Kear, Pratt and Whitney Aircraft, North Haven, Conn. Report 66-026, (1966).

57 R.T.Holt, M.Sc. Thesis, London University, (1964).

58 J.L.Taylor, Trans. A.I.M.E., 236, 464, (1966).

59 M.J.Marcinkowski and N.Brown, Acta. Met. 9, 764, (1961).

60 G.I.Taylor and C.F.Elam, Proc. Roy. Soc. A112, 337, (1926).

61 R.Maddin and N.K.Chen, Prog. Met. Phys., 5, 53, (1954).

62 R.P.Steijn and R.M.Brick, Trans. A.S.M., 46, 1406, (1954).

63 V.Vitek, Phys. Stat. Sol. 15, 557, (1966).

64 M.Schwartz and L.Muldawer, J.App. Phys., 29, 1561, (1958).

65 J.E.Dorn, Symposium, University of Denver, (1962).

66 G.W.Groves and A.Kelly, Phil. Mag. 8, 877, (1963).

67 A.G.Rozner and R.J.Wasilewski, J. Inst. Metals, 94, 169, (1966).

68 R.von Mises, Z. angew. Math. Mech., 8, 161, (1928).

69 M.V.Klassen-Neklyudova, "Mechanical Twinning of Crystals", Consultants' Bureau, N.Y., (1964).

70 L.D.Johnson and J.A.Pask, J. Amer. Cer. Soc., 47, 437, (1964).

71 B.Russell, Phil. Mag., 8, 615, (1963).

72 G.F.Bolling and R.H.Richman, Acta Met. 13, 723, (1965).

73 R.J.Wasilewski, Trans. A.I.M.E., 233, 1691, (1965).

74 E.Hornbogen, A.Segmuller, and G.Wasserman, Z. Metallkunde, 48, 379, (1957).

75 G.W.Ardley and A.H.Cottrell, Proc. Roy. Soc. 219A, 328, (1953).

76 G.W.Ardley, Acta Met., 3, 525, (1955).

77 A.Portevin and F.LeChatelier, Compte Rendu Acad. Sci., 176, 507, (1923).

78 R.H.Ham and D.Jaffrey, Phil.Mag. 15, 247, (1967).

79 A.H.Cottrell, "Dislocations and Plastic Flow in Crystals", Oxford Press, p.136, (1953).

80 A.H.Cottrell, Phil. Mag., 44, 829, (1953).

81 R.R.Vandervoort, A.K.Mukherjee and J.E.Dorn, Trans. A.S.M., 59, 930, (1966).

82 T.Boncszewski and G.C.Smith, Acta Met. 11, 165, (1963).

83 J.Diehl and R.Berner, Z.Metallk., 51, 522, (1960).

84 W.M.Charnock, private communication, University of British Columbia, (1967).

85 K.Mukherjee, D.S.Lieberman and T.A.Read, J.App. Phys., 36, 857, (1965).

86 H.Conrad, J. of Metals, 16, 582, (1964).

87 G.Schoeck, Phys. Stat. Sol., 8, 499, (1965).

88 A.Seeger, "Conference on Defects in Crystalline Solics", Phys. Soc., London, (1954).

89 N.R.Risebrough, Ph.D. Thesis, University of British Columbia, (1965).

90 Z.S.Basinski and J.W.Christian, Aust. J. Phys., 13, 299, (1960).

91 H.Conrad and W.Hayes, Trans. Quart. A.S.M. 56, 249, (1963).

92 H.Conrad, R.Armstrong, H.Wiedersich and G.Schoeck, Phil. Mag., 6, 177, (1961).

93 H.Conrad and H.Wiedersich, Acta Met., 8, 123, (1960).

94 H.Conrad, "The Relation Between the Structure and Mechanical Properties of Metals", N.P.L. Symposium, Tedington, p.475, (1963).

95 S.S.Lau, S.Ranji, A.K.Mukherjee, G.Thomas and J.E.Dorn, Acta Met., 15, 237, (1967).

96 G.Schoeck, Acta Met., 9, 382, (1961).

97 J.W.Christian and B.C.Masters, Proc. Roy. Soc., 281, 240, (1964).

98 B.L.Mordike and P.Haasen, Phil. Mag., 7, 459, (1962).

99 P.Wynblatt and J.E.Dorn, Trans. A.I.M.E., 236, 1451, (1966).

100 A.K.Mukherjee and J.E.Dorn, Trans. A.I.M.E., 230, 1065, (1964).

101 A.K.Mukherjee, W.G.Ferguson, W.L.Barmore and J.E.Dorn, J. App. Phys., 37, 3707, (1966).

102 P.Guyot and J.E.Dorn, Can. J. Physics, 45, 983, (1967).

103 J.E.Dorn and S.Rajnak, Trans. A.I.M.E., 230, 1052, (1964).

104 A.H.Cottrell, "Dislocations and Plastic Flow in Crystals", Oxford Press, p.38, (1953).

105 O.Kubaschewski, Trans. Faraday Soc., 54, 814, (1958).

106 R.Hultgren, R.L.Orr, P.D.Anderson and K.K.Kelley, "Selected Values of Thermodynamic Properties of Metals and Alloys", Wiley, N.Y., (1962).

107 R.W.Carpenter, R.L.Orr and R.Hultgren, Trans. A.I.M.E., 239, 107, (1967).

108 P.M.Robinson and M.B.Bever, Trans. A.I.M.E., 230, 1487, (1964).

109 L.Pauling, "Nature of the Chemical Bond", Cornell University Press, (1948).

110 R.S.Mulliken, J. Chem. Physics, 2, 782, (1934); 3, 573, (1935).

111 F.Seitz, Advanc. Phys. 1, 43, (1952).

112 A.L.Allred and E.G.Rochow, J. Inorg. and Nuclear Chem., 5, 264, 269, (1958).

113 N.S.Stoloff and R.G.Davies, Prog. Matls. Sci. 13, No. 1, (1966).

114 W.L.Bragg, Proc. Phys. Soc., 52, 105, (1940).

115 E.P.Lautenschlager, T.C.Tisone and J.O.Brittain, Phys. Stat. Sol., 20, 443, (1967).

116 S.G.Cupschalk and N.Brown, Acta Met., 15, 847, (1967).

117 T.Saburi, S.Nenno and H.Kido, J. Phys. Soc. Japan, 21, 1216, (1966).

118 B.H.Kear, Acta Met., 12, 555, (1964).

119 D.E.Mikkola and J.B.Cohen, Acta Met., 14, 105, (1966).

120 M.J.Marcinkowski and L.Zwell, Acta Met., 11, 373, (1963).

121 M.J.Marcinkowski and H.Brown, "Proc. European Regional Conf. on Electron Microscopy", Delft, p.400, (1960).

122 J.H.Westbrook (Editor), "Mechanical Properties of Intermetallic Compounds", Wiley, N.Y., p.1, (1960).

123 R.G.Davies and N.S.Stoloff, Phil. Mag., 12, 297, (1965).

124 B.H.Kear, Acta Met., 12, 555, (1964).

125 M.J.Marcinkowski and H.Chessin, Phil. Mag., 10, 837, (1964).

126 N.S.Stoloff, R.G.Davies and R.C.Ku, Trans. A.I.M.E., 233, 1500, (1965).

127 N.S.Stoloff and R.G.Davies, Acta Met., 12, 473, (1964).

128 N.Brown, Phil. Mag., 4, 693, (1959).

129 R.G.Davies and N.S.Stoloff, Acta Met., 11, 1187, (1963).

130 A.Lawley, A.E.Vidoz and R.W.Cahn, Acta Met., 9, 287, (1961).

131 P.A.Flinn, Trans. A.I.M.E., 218, 145, (1960).

132 R.G.Davies and N.S.Stoloff, Trans. A.I.M.E., 233, 714, (1965).

133 S.M.Copley and R.H.Kear, report No. 66-026, Pratt and Whitney Aircraft, Conn., September, (1966).

134 E.M.Grala, "Mechanical Properties of Intermetallic Compounds", Wiley, N.Y., p.358, (1959).

135 J.H.Westbrook and D.L.Wood, J. Inst. Metals, 91, 174, (1963).

136 A.U.Seybolt and J.H.Westbrook, Acta Met., 12, 449, (1964).

137 E.A.Owen and J.G.Edmunds, Proc. Roy. Soc. (London(, 50, 389, (1938).

138 E.N.Andrade and D.A.Aboav, Prog. Roy. Soc. A240, 304, (1957).

139 P.Haasen, Phil. Mag., 3, 284, (1958).

140 F.D.Rosi and C.H.Mathewson, Trans. A.I.M.E., 188, 1159, (1950).

141 J.Garstone and R.W.K.Honeycombe, "Dislocations and Mechanical Properties of Crystals", Wiley, N.Y., p.391, (1957).

142 N.R.Risebrough and E.Teghtsoonian, Can. J. Physics, 45, 591, (1967).

143 M.Bocek, P.Lukac, B.Smula and M.Svobava, Phys. Stat. Sol. 7, 173, (1964).

144 A.Seeger, "The Relation Between the Structure and Mechanical Properties of Metals", N.P.L. Symposium, Tedington, H.M.S.O., p.4, (1963).

145 A.Seeger, Discussions Faraday Soc., 38, 163, (1964).

146 P.B.Hirsch, Discussions Faraday Soc., 38, 111, (1964).

147 N.K.Chen and C.H.Mathewson, Trans. A.I.M.E., 191, 653, (1951).

148 R.W.K.Honeycombe, J.Inst. Metals, 80, 45, (1951).

149 P.L.Pratt, Acta Met., 1, 103, (1953).

150 N.F.Mott, Proc. Phys. Soc., B64, 792, (1951).

151 J.Friedel, "Dislocations", Oxford, New York, Pergamon Press, p.252, (1964).

152 A.S.Argon and S.R.Maloof, Acta Met., 14, 1463, (1966).

153 M.Gell, Acta Met., 14, 1625, (1966).

154 A.N.Stroh, "Fracture", p.117, Wiley, N.Y., (1959).

155 A.H.Cottrell, Trans. A.I.M.E., 212, 192, (1958).

156 R.Maddin and N.K.Chen, Prog. Met. Phys., 5, 70, (1954).

157 A.A.Barenko, Phys. Met. and Metallog., 21, 97, (1966).

158 E.S.Greiner and D.M.Boulin, Trans. A.I.M.E., 239, 965, (1967).

159 P.B.Hirsch, Prog. Met. Phys., 6, 296, (1056).

160 G.Taylor and J.W.Christian, Phil. Mag., 15, 893, (1967).

161 W.A.Spitzig and T.E.Mitchell, Acta Met., 14, 1311, (1966).

162 A.S.Keh, Phil. Mag., 12, 9, (1965).

163 P.M.Hazzledine, Can. J. Phys. 45, 765, (1967).

164 J.W.Steeds, Proc. Roy. Soc., A292, 343, (1966).

165 D.M.Moon and W.H.Robinson, Can. J. Phys., 45, 1017, (1967).

166 A.Seeger, H.Kronmuller, H.Mader and H.Trauble, Phil. Mag., 6, 639, (1961).

167 P.B.Hirsch and J.S.Lally, Phil. Mag., 12, 595, (1965).

168 A.Seeger, Handb. Phys., 7, 2, (1958).

169 Z.S.Basinski, Phil. Mag., 4, 393, (1959).

170 N.F.Mott, Trans. A.I.M.E., 218, 962, (1960).

171 D.Kuhlmann-Wilsdorf, Trans. A.I.M.E., 224, 1047, (1962).

172 P.B.Hirsch and T.E.Mitchell, Can. J. Phys., 45, 663, (1967).

173 P.B.Hirsch, "Relation Between the Structure and Mechanical Properties of Metal", N.P.L. Symposium, Tedington, H.M.S.O., p.40, (1963).

174 R.K.Ham, Phil. Mag., 7, 1177, (1962).

175 U. Essmann, Phys. Stat. Sol., 3, 932, (1963).

176 U. Essman, Phys. Stat. Sol., 12, 707 and 723, (1965).

177 A.Ball and R.E.Smallman, Acta Met., 13, 1011, (1965).

178 P.B.Hirsch, A.Howie, R.B.Nicholson, P.W.Pashley and M.J.Whelan, "Electron Microscopy of Thin Crystals", Butterworths, London, (1965).

179 A.K.Head, Phys. Stat. Sol., 19, 185, (1967).

180 A.K.Head, H.M.Loretto and P.Humble, Phys. Stat. Sol., 20, 505 and 521, (1967).

181 P.B.Hirsch, A.Howie, and M.J.Whelan, Phil. Trans. R. Soc., 252A, 499, (1960).

182 S.Mader, "Electron Microscopy and Strength of Crystals", G.Thomas and J.Washburn, (Editors), Wiley, N.Y., 183, (1963).

183 J.V.Sharp, M.J.Makin and J.W.Christian, Phys. Stat. Sol., 11, 845, (1965).